

Measurements of top quark production with the CMS detector at the LHC

Jeson Abe Jacob

September 2015



A dissertation submitted to the University of Bristol in accordance with the requirements for award of the degree of Doctor of Philosophy in the Faculty of Science, School of Physics, September 2015.

≈24,900 words

Abstract

The CMS detector at the LHC has collected proton-proton data since 2010, enabling analysts to study the properties of the top quark, the heaviest known fundamental particle, in great detail. Starting with a description of the CMS detector and an overview of the Standard Model of particle physics, this thesis goes on to present a measurement of normalised differential cross sections of $t\bar{t}$ production in the electron+jets and muon+jets channels with respect to global event variables. 5.0 fb^{-1} of proton-proton collision data collected with the CMS experiment at $\sqrt{s}=7 \text{ TeV}$, and 19.7 fb^{-1} of data collected at $\sqrt{s}=8 \text{ TeV}$ are used. The measurement is performed in bins of the following global event variables: missing transverse energy (E_T^{miss}), the scalar sum of jet transverse momenta (H_T), the scalar sum of the transverse momenta of all objects in the event (S_T), the transverse momentum (p_T^W) and the transverse mass (M_T^W) of the leptonically decaying W boson from the $t\bar{t}$ decay.

The datasets used in the electron channel were obtained using an electron+jets trigger in 2011 and a single electron trigger in 2012. Muon datasets were obtained using a single muon trigger during both data taking periods. Following the application of selection criteria on the datasets and Monte Carlo simulation to obtain a $t\bar{t}$ signal sample, and background samples from single top, $W/Z + \text{jets}$ and QCD multi-jet processes, a fit of the simulated samples to data is carried out in each bin and in each channel to obtain a $t\bar{t}$ event yield. The number of signal events is then unfolded to remove detector and selection effects. Combining the result from the two channels, the calculation of the normalised differential cross sections is performed. Comparison with common Monte Carlo generators, including with different modelling parameters, confirms previous CMS findings of a softer measured transverse momentum distribution than in simulations, but otherwise there is general consistency between generator predictions and data.

Declaration

I declare that the work in this dissertation was carried out in accordance with the requirements of the University's Regulations and Code of Practice for Research Degree Programmes and that it has not been submitted for any other academic award. Except where indicated by specific reference in the text, the work is the candidate's own work. Work done in collaboration with, or with the assistance of, others, is indicated as such. Any views expressed in the dissertation are those of the author.

Signed:

Date:

Contents

1	Introduction	1
2	The Standard Model of Particle Physics	5
2.1	Introduction	5
2.1.1	Gauge Principle	7
2.1.2	Quantum Electrodynamics	8
2.1.3	Electroweak Theory	10
2.1.4	Quantum Chromodynamics	12
2.1.5	Spontaneous Symmetry Breaking	14
2.2	Incompleteness of, and physics beyond, the SM	16
3	Top Physics at the LHC	19
3.1	Introduction	19
3.1.1	Top Quark Production and Decay	19
3.1.2	Single Top background	23
3.1.3	W/Z+jets background	24
3.1.4	QCD background	25
3.2	Monte Carlo Simulation	26
3.2.1	MadGraph	26
3.2.2	MC@NLO	27
3.2.3	PYTHIA	27
3.2.4	POWHEG	28
3.3	Theoretical Systematics	28
3.3.1	Factorisation and Renormalisation Scale & Matching Threshold	28
3.3.2	Detector Simulation (GEANT)	29
4	The CMS Detector at the LHC	31
4.1	Introduction to the LHC	31
4.2	Overview of CMS	33
4.3	Sub-Detectors	35
4.3.1	Tracker	35
4.3.2	Electromagnetic Calorimeter	38
4.3.3	Hadronic Calorimeter	40
4.3.4	Superconducting Magnet	40
4.3.5	Muon Chambers	42
4.3.6	Trigger and Data Acquisition	44
4.4	Upgrades	46
5	CMS Computing and Offline	49
5.1	CMS Computing	49
5.2	Event Data Model	50
5.3	Object Reconstruction and Identification	51
5.3.1	Track Reconstruction	51

5.3.2	Pileup Subtraction	52
5.3.3	Electron Reconstruction	53
5.3.4	Muon Reconstruction	56
5.3.5	Jet Reconstruction	58
6	b-tagging Study	61
6.1	Observables used in b-tagging algorithms	61
6.2	b-tagging algorithm descriptions	64
6.2.1	Track Counting	64
6.2.2	Jet Probability	64
6.2.3	Soft Muon	64
6.2.4	Simple Secondary Vertex	65
6.2.5	Combined Secondary Vertex	65
6.3	Performance Comparison	66
6.4	Efficiency	67
6.5	Algorithm Comparison	68
7	Differential Cross Sections: Data, Simulation and Selection	71
7.1	Outline and Motivation	71
7.2	Data and Simulated Samples	73
7.2.1	Data	73
7.2.2	Simulated Samples	75
7.3	Selection	81
7.3.1	Preselection	81
7.3.2	Electron channel selection	82
7.3.3	Muon channel selection	83
7.3.4	Jets selection	83
7.3.5	Multi-jet background selection	84
7.4	Data-MC scale factors	88
7.4.1	Pileup	88
7.4.2	b-tagging	90
7.4.3	Jet Energy Scale	90
7.4.4	Missing Transverse Energy Corrections	91
7.4.5	Trigger, Lepton ID and Isolation Efficiencies and Corrections	92
8	Differential Cross Sections: Fitting, Unfolding and Measurement	97
8.1	Data-MC Comparison	97
8.2	Binning Choice	103
8.3	Maximum Likelihood Fit	107
8.3.1	Choice of templates	108
8.3.2	Fit Results	114
8.4	Fit cross-checks	123
8.5	Background Subtraction	123
8.6	Unfolding	123
8.6.1	Measurement	129
9	Differential Cross Sections: Systematic Uncertainties and Results	133
9.1	Systematic uncertainties	133

9.1.1	Experimental Uncertainties	134
9.1.2	Theoretical Uncertainties	137
9.1.3	Systematic Uncertainty Tables	139
9.2	Results	142
10	Summary and Outlook	151
A	b-tagging Study Plots	155
B	$t\bar{t}$ differential cross section	157
B.1	Datasets in differential cross section analysis	157
B.2	Data - Monte Carlo corrections	158
B.3	Binning in the muon+jets channel	161
B.4	Fitting Variable Distributions	164
B.5	Fit Results Tables	165
B.6	Fit correlations	176
B.7	Systematic Uncertainties	177
B.8	Results	188
B.8.1	7 TeV	188
B.8.2	8 TeV	191
References		195

List of Figures

1		
1.1	Map of LHC location.	2
2		
2.1	Elementary electromagnetic processes.	8
2.2	The Higgs field potential.	15
2.3	Invariant mass in $H \rightarrow \gamma\gamma$ (left) and $H \rightarrow ZZ$ (right) channels.	15
2.4	Summary of Higgs boson mass measurements from CMS, ATLAS and combined CMS+ATLAS analyses in the $H \rightarrow \gamma\gamma$ and $H \rightarrow ZZ$ channels.	16
2.5	The composition of the universe showing the amounts of dark matter, dark energy and ordinary matter.	18
3		
3.1	Feynman diagrams of leading order $t\bar{t}$ production processes.	20
3.2	$t\bar{t}$ production cross sections at 1.96 TeV at CDF and D \emptyset at the TeVatron and at 7 TeV and 8 TeV at CMS and ATLAS at the LHC.	20
3.3	Proton parton distribution functions at $Q^2 = 10 \text{ GeV}^2$	21
3.4	Feynman diagram of the electron+jets semi-leptonic $t\bar{t}$ decay channel.	22
3.5	Relative branching ratios of the $t\bar{t}$ system	23
3.6	Feynman diagrams of leading order single top production processes.	24
4		
4.1	Schematic of LHC and experiments.	31
4.2	Cumulative luminosity delivered to CMS during 2010, 2011 and 2012.	33
4.3	Diagrammatic sectional view of the CMS detector.	34
4.4	Cross sectional diagram of the CMS strip tracker.	36
4.5	Diagram of the ECAL showing barrel supermodules, endcaps and preshower detectors.	39
4.6	A longitudinal schematic of the CMS HCAL.	41
4.7	Bore of the CMS solenoid magnet in vertical position in the CMS assembly hall, SX5.	42
4.8	Schematic representation of a quarter of the CMS muon system.	43
4.9	Single muon HLT rates at low and high luminosities.	46
5		
5.1	Muon transverse momentum resolution using muon system and the tracking system.	57
6		
6.1	Graphical representation of a secondary vertex.	62
6.2	Graphical representation of a track impact parameter.	63
6.3	Discriminator values produced by the Combined Secondary Vertex algorithm after normalisation.	67

6.4	b-tagging efficiencies of non-b-jets as a function of b-tagging efficiency for b-jets for the CSV algorithm.	68
6.5	udsjet efficiencies as a function of b-jet efficiencies for all algorithms.	69
7		
7.1	Comparison of QCD selections in the electron+jets channel at $\sqrt{s} = 7 \text{ TeV}$ and at $\sqrt{s} = 8 \text{ TeV}$	86
7.2	PF relative isolation distributions in the muon+jets channel at $\sqrt{s} = 7 \text{ TeV}$ and $\sqrt{s} = 8 \text{ TeV}$	87
7.3	Distributions of the number of reconstructed vertices in an event in the electron+jets channel before and after implementing pileup reweighting at $\sqrt{s} = 7 \text{ TeV}$ and $\sqrt{s} = 8 \text{ TeV}$	89
7.4	Distributions of the number of b-tags in an event in the electron+jets channel before and after applying b-tag scale factors at $\sqrt{s} = 7 \text{ TeV}$ and $\sqrt{s} = 8 \text{ TeV}$	91
7.5	Fits of the invariant mass distribution of all tag-and-probe pairs and tag-and-probe pairs in which the probe satisfies the identification and isolation criteria.	93
7.6	Identification and isolation efficiencies as a function of η and p_T in data and $t\bar{t}$ Monte Carlo simulation.	94
8		
8.1	Comparison of Monte Carlo simulation to data in the electron+jets channel after final selection at $\sqrt{s} = 7 \text{ TeV}$	99
8.2	Comparison of Monte Carlo simulation to data in the muon+jets channel after final selection at $\sqrt{s} = 7 \text{ TeV}$	100
8.3	Comparison of Monte Carlo simulation to data in the electron+jets channel after final selection at $\sqrt{s} = 8 \text{ TeV}$	101
8.4	Comparison of Monte Carlo simulation to data in the muon+jets channel after final selection at $\sqrt{s} = 8 \text{ TeV}$	102
8.5	Graphical representation of bin purity and stability.	103
8.6	Generated versus reconstructed distributions of the primary variable at $\sqrt{s} = 7 \text{ TeV}$	105
8.7	Generated versus reconstructed distributions of the primary variables at $\sqrt{s} = 8 \text{ TeV}$	106
8.8	Normalised distributions of the templates for the three fit variables, inclusive across all primary variable bins at $\sqrt{s} = 7 \text{ TeV}$	110
8.9	Normalised distributions of the QCD templates for the three fit variables in E_T^{miss} bins at $\sqrt{s} = 8 \text{ TeV}$	112
8.10	Normalised distributions of the V+jets templates for the three fit variables in E_T^{miss} bins.	113
8.11	Comparison of Monte Carlo simulation to data distributions of primary variables in the electron+jets channel after fitting at $\sqrt{s} = 7 \text{ TeV}$	115
8.12	Comparison of Monte Carlo simulation to data distributions of primary variables in the muon+jets channel after fitting at $\sqrt{s} = 7 \text{ TeV}$	116
8.13	Comparison of Monte Carlo simulation to data distributions of primary variables in the electron+jets channel after fitting at $\sqrt{s} = 8 \text{ TeV}$	117
8.14	Comparison of Monte Carlo simulation to data distributions of primary variables in the muon+jets channel after fitting at $\sqrt{s} = 8 \text{ TeV}$	118

8.15	Comparison of Monte Carlo simulation to data distributions of kinematic event variables in the electron+jets channel after fitting at $\sqrt{s} = 7 \text{ TeV}$	119
8.16	Comparison of Monte Carlo simulation to data distributions of kinematic event variables in the muon+jets channel after fitting at $\sqrt{s} = 7 \text{ TeV}$	120
8.17	Comparison of Monte Carlo simulation to data distributions of kinematic event variables in the electron+jets channel after fitting at $\sqrt{s} = 8 \text{ TeV}$	121
8.18	Comparison of Monte Carlo simulation to data distributions of kinematic event variables in the muon+jets channel after fitting at $\sqrt{s} = 8 \text{ TeV}$	122
8.19	Correlation between fit processes for the E_T^{miss} variable in the electron+jets channel at $\sqrt{s} = 8 \text{ TeV}$	124
8.20	$\log d_i $ plots at $\sqrt{s} = 8 \text{ TeV}$	127
8.21	Unfolding closure tests for the E_T^{miss} variable at $\sqrt{s} = 8 \text{ TeV}$	128
8.22	Pull distribution using toy Monte Carlo datasets for the E_T^{miss} variable using a k value of 3 for the E_T^{miss} variable at $\sqrt{s} = 8 \text{ TeV}$	130
9		
9.1	Diagrams of semi-leptonic and dileptonic τ events.	135
9.2	Comparison of the signal and fake distributions in the E_T^{miss} variable from semi-leptonic $t\bar{t}$ events in the electron+jets channel at $\sqrt{s} = 8 \text{ TeV}$	136
9.3	Comparison of the E_T^{miss} distributions in the nominal measurement and in the tau energy down variation in data and in simulation.	137
9.4	E_T^{miss} and electron $ \eta $ shape comparison of W+jets templates in $\sqrt{s} = 7 \text{ TeV}$ and $\sqrt{s} = 8 \text{ TeV}$ in the electron+jets channel.	138
9.5	Comparison of the measured normalised differential cross section with respect to E_T^{miss} , H_T and S_T to different Monte Carlo generators and predictions at $\sqrt{s} = 7 \text{ TeV}$	146
9.6	Comparison of the measured normalised differential cross section with respect to p_T^W and M_T^W to different Monte Carlo generators and predictions at $\sqrt{s} = 7 \text{ TeV}$	147
9.7	Comparison of the measured normalised differential cross section with respect to E_T^{miss} , H_T and S_T to different Monte Carlo generators and predictions at $\sqrt{s} = 8 \text{ TeV}$	148
9.8	Comparison of the measured normalised differential cross section with respect to p_T^W and M_T^W to different Monte Carlo generators and predictions at $\sqrt{s} = 8 \text{ TeV}$	149
A		
A.1	Discriminator distributions produced by CMS b-tagging algorithms.	155
A.2	c-jet, g-jet and uds-jet efficiencies as a function of b-jet efficiency for CMS b-tagging algorithms.	156
B		
B.1	Distributions of the number of reconstructed vertices in an event in the muon+jets channel before and after implementing pileup reweighting at $\sqrt{s} = 7 \text{ TeV}$ and $\sqrt{s} = 8 \text{ TeV}$	158
B.2	Distributions of the number of b-tags in an event in the muon+jets channel before and after applying b-tag scale factors at $\sqrt{s} = 7 \text{ TeV}$ and $\sqrt{s} = 8 \text{ TeV}$	159
B.3	Fits of the invariant mass distribution of tag-and-probe electron pairs.	160
B.4	Trigger efficiencies as a function of η and p_T in data and $t\bar{t}$ Monte Carlo simulation.	160

B.5 Generated versus reconstructed distributions of the primary variables at $\sqrt{s} = 7\text{ TeV}$ in the muon+jets channel.	161
B.6 Generated versus reconstructed distributions of the primary variables at $\sqrt{s} = 8\text{ TeV}$ in the muon+jets channel.	162
B.7 Normalised distributions of the templates for the three fit variables inclusive across all primary variable bins at $\sqrt{s} = 8\text{ TeV}$	164
B.8 Correlation between fit processes for the $E_{\text{T}}^{\text{miss}}$ variable in the electron+jets channel at $\sqrt{s} = 7\text{ TeV}$	176
B.9 Comparison of the measured normalised differential cross section, with background subtraction results, with respect to $E_{\text{T}}^{\text{miss}}$, H_{T} , S_{T} , p_{T}^{W} and M_{T}^{W} to different Monte Carlo generators and predictions at $\sqrt{s} = 7\text{ TeV}$	190
B.10 Comparison of the measured normalised differential cross section, with background subtraction results, with respect to $E_{\text{T}}^{\text{miss}}$, H_{T} , S_{T} , p_{T}^{W} and M_{T}^{W} to different Monte Carlo generators and predictions at $\sqrt{s} = 8\text{ TeV}$	193
B.11 Comparison of the measured normalised differential cross section, with background subtraction results, with respect to $E_{\text{T}}^{\text{miss}}$, H_{T} , S_{T} , p_{T}^{W} and M_{T}^{W} to different Monte Carlo generators and predictions at $\sqrt{s} = 8\text{ TeV}$	194

List of Tables

2		
2.1	Fundamental fermions, split into their three generations, and bosons of the Standard Model. The graviton is currently only hypothesised. Particle properties taken from [99].	6
3		
3.1	SM $t\bar{t}$ and single top production cross sections in pb at next-to-next-to-leading order at the LHC.	21
3.2	Threshold transverse energy for matching systematic uncertainty	29
7		
7.1	7 TeV data sets by run period with the corresponding integrated luminosities (\mathcal{L}_{int}) and run numbers.	74
7.2	8 TeV data sets by run period with the corresponding integrated luminosities (\mathcal{L}_{int}) and run numbers.	74
7.3	7 TeV Monte Carlo signal datasets used for this analysis.	76
7.4	8 TeV Monte Carlo signal datasets used for this analysis.	76
7.5	7 TeV Monte Carlo background datasets used for this analysis. All samples are generated inclusively if not marked otherwise (* generator cut on in-flight-decays of b- and c-hadrons, \ominus enriched in conversion electrons; l means all leptonic decays: $l = e, \mu, \tau$; • generator cut on $m_{Z/\gamma} > 50$ GeV).	77
7.6	8 TeV Monte Carlo background datasets used for this analysis. All samples are generated inclusively if not marked otherwise (* generator cut on in-flight-decays of b- and c-hadrons, \ominus enriched in conversion electrons; l means all leptonic decays: $l = e, \mu, \tau$; • generator cut on $m_{Z/\gamma} > 50$ GeV).	78
7.7	7 TeV Monte Carlo systematic datasets used for this analysis. All samples are produced with the MADGRAPH generator. W + jets and Z + jets samples were not available and so have been scaled from available 8 TeV samples.	79
7.8	8 TeV Monte Carlo systematic datasets used for this analysis. All samples are produced with the MADGRAPH generator.	80
7.9	Summary of event selection steps.	81
8		
8.1	Expected and observed event yields at several stages of the electron+jets selection (upper) and the muon+jets channel selection (lower) at $\sqrt{s}=7$ TeV.	98
8.2	Expected and observed event yields at several stages of the electron+jets selection (upper) and the muon+jets selection (lower) at $\sqrt{s}=8$ TeV.	98
8.3	Optimal k -values for all primary variables at both 7 and 8 TeV.	127
9		
9.1	Typical systematic uncertainties in percent (median values) for the normalised $t\bar{t}$ differential cross section measurement at $\sqrt{s} = 7$ TeV (combination of electron and muon channels). Typical values of the total systematic uncertainty are also shown.	140

9.2	Typical systematic uncertainties in percent (median values) for the normalised $t\bar{t}$ differential cross section measurement at $\sqrt{s} = 7$ TeV (combination of electron and muon channels). Typical values of the total systematic uncertainty are also shown.	141
9.3	Typical systematic uncertainties in percent (median values) for the normalised $t\bar{t}$ differential cross section measurement at $\sqrt{s} = 8$ TeV (combination of electron and muon channels). Typical values of the total systematic uncertainty are also shown.	141
9.4	Typical systematic uncertainties in percent (median values) for the normalised $t\bar{t}$ differential cross section measurement at $\sqrt{s} = 8$ TeV (combination of electron and muon channels). Typical values of the total systematic uncertainty are also shown.	142

B

B.1	HLT Triggers used in 2011 and 2012 data in the electron+jets and muon+jets channels.	157
B.2	JSON files used for the 2011 and 2012 data taking periods.	157
B.3	Fit results for the E_T^{miss} variable at a centre-of-mass energy of 7 TeV (electron channel).	165
B.4	Fit results for the E_T^{miss} variable at a centre-of-mass energy of 7 TeV (muon channel).	165
B.5	Fit results for the H_T variable at a centre-of-mass energy of 7 TeV (electron channel).	166
B.6	Fit results for the H_T variable at a centre-of-mass energy of 7 TeV (muon channel).	166
B.7	Fit results for the S_T variable at a centre-of-mass energy of 7 TeV (electron channel).	167
B.8	Fit results for the S_T variable at a centre-of-mass energy of 7 TeV (muon channel).	167
B.9	Fit results for the p_T^W variable at a centre-of-mass energy of 7 TeV (electron channel).	168
B.10	Fit results for the p_T^W variable at a centre-of-mass energy of 7 TeV (muon channel).	169
B.11	Fit results for the M_T^W variable at a centre-of-mass energy of 7 TeV (electron channel).	170
B.12	Fit results for the M_T^W variable at a centre-of-mass energy of 7 TeV (muon channel).	170
B.13	Fit results for the E_T^{miss} variable at a centre-of-mass energy of 8 TeV (electron channel).	171
B.14	Fit results for the E_T^{miss} variable at a centre-of-mass energy of 8 TeV (muon channel).	171
B.15	Fit results for the H_T variable at a centre-of-mass energy of 8 TeV (electron channel).	172
B.16	Fit results for the H_T variable at a centre-of-mass energy of 8 TeV (muon channel).	172
B.17	Fit results for the S_T variable at a centre-of-mass energy of 8 TeV (electron channel).	173

B.18 Fit results for the S_T variable at a centre-of-mass energy of 8 TeV (muon channel).	173
B.19 Fit results for the p_T^W variable at a centre-of-mass energy of 8 TeV (electron channel).	174
B.20 Fit results for the p_T^W variable at a centre-of-mass energy of 8 TeV (muon channel).	174
B.21 Fit results for the M_T^W variable at a centre-of-mass energy of 8 TeV (electron channel).	175
B.22 Fit results for the M_T^W variable at a centre-of-mass energy of 8 TeV (muon channel).	175
B.23 Systematic uncertainties for the normalised $t\bar{t}$ cross section measurement with respect to E_T^{miss} variable at a centre-of-mass energy of 7 TeV (combination of electron and muon channels).	178
B.24 Systematic uncertainties for the normalised $t\bar{t}$ cross section measurement with respect to H_T variable at a centre-of-mass energy of 7 TeV (combination of electron and muon channels).	179
B.25 Systematic uncertainties for the normalised $t\bar{t}$ cross section measurement with respect to S_T variable at a centre-of-mass energy of 7 TeV (combination of electron and muon channels).	180
B.26 Systematic uncertainties for the normalised $t\bar{t}$ cross section measurement with respect to p_T^W variable at a centre-of-mass energy of 7 TeV (combination of electron and muon channels).	181
B.27 Systematic uncertainties for the normalised $t\bar{t}$ cross section measurement with respect to M_T^W variable at a centre-of-mass energy of 7 TeV (combination of electron and muon channels).	182
B.28 Systematic uncertainties for the normalised $t\bar{t}$ cross section measurement with respect to E_T^{miss} variable at a centre-of-mass energy of 8 TeV (combination of electron and muon channels).	183
B.29 Systematic uncertainties for the normalised $t\bar{t}$ cross section measurement with respect to H_T variable at a centre-of-mass energy of 8 TeV (combination of electron and muon channels).	184
B.30 Systematic uncertainties for the normalised $t\bar{t}$ cross section measurement with respect to S_T variable at a centre-of-mass energy of 8 TeV (combination of electron and muon channels).	185
B.31 Systematic uncertainties for the normalised $t\bar{t}$ cross section measurement with respect to p_T^W variable at a centre-of-mass energy of 8 TeV (combination of electron and muon channels).	186
B.32 Systematic uncertainties for the normalised $t\bar{t}$ cross section measurement with respect to M_T^W variable at a centre-of-mass energy of 8 TeV (combination of electron and muon channels).	187
B.33 Normalised $t\bar{t}$ cross section measurement with respect to E_T^{miss} variable at a centre-of-mass energy of 7 TeV (combination of electron and muon channels). The errors shown are combined statistical, fit and unfolding errors (\dagger) and systematic uncertainty (*).	188

B.34 Normalised $t\bar{t}$ cross section measurement with respect to H_T variable at a centre-of-mass energy of 7 TeV (combination of electron and muon channels). The errors shown are combined statistical, fit and unfolding errors (\dagger) and systematic uncertainty (*).	188
B.35 Normalised $t\bar{t}$ cross section measurement with respect to S_T variable at a centre-of-mass energy of 7 TeV (combination of electron and muon channels). The errors shown are combined statistical, fit and unfolding errors (\dagger) and systematic uncertainty (*).	189
B.36 Normalised $t\bar{t}$ cross section measurement with respect to p_T^W variable at a centre-of-mass energy of 7 TeV (combination of electron and muon channels). The errors shown are combined statistical, fit and unfolding errors (\dagger) and systematic uncertainty (*).	189
B.37 Normalised $t\bar{t}$ cross section measurement with respect to M_T^W variable at a centre-of-mass energy of 7 TeV (combination of electron and muon channels). The errors shown are combined statistical, fit and unfolding errors (\dagger) and systematic uncertainty (*).	189
B.38 Normalised $t\bar{t}$ cross section measurement with respect to E_T^{miss} variable at a centre-of-mass energy of 8 TeV (combination of electron and muon channels). The errors shown are combined statistical, fit and unfolding errors (\dagger) and systematic uncertainty (*).	191
B.39 Normalised $t\bar{t}$ cross section measurement with respect to H_T variable at a centre-of-mass energy of 8 TeV (combination of electron and muon channels). The errors shown are combined statistical, fit and unfolding errors (\dagger) and systematic uncertainty (*).	191
B.40 Normalised $t\bar{t}$ cross section measurement with respect to S_T variable at a centre-of-mass energy of 8 TeV (combination of electron and muon channels). The errors shown are combined statistical, fit and unfolding errors (\dagger) and systematic uncertainty (*).	192
B.41 Normalised $t\bar{t}$ cross section measurement with respect to p_T^W variable at a centre-of-mass energy of 8 TeV (combination of electron and muon channels). The errors shown are combined statistical, fit and unfolding errors (\dagger) and systematic uncertainty (*).	192
B.42 Normalised $t\bar{t}$ cross section measurement with respect to M_T^W variable at a centre-of-mass energy of 8 TeV (combination of electron and muon channels). The errors shown are combined statistical, fit and unfolding errors (\dagger) and systematic uncertainty (*).	192

1 | Introduction

Particle physics research over the last century or so has provided us with our current basic understanding of the fundamental particles that have made up the universe since its origin, and their interactions with each other. This is summarised by the Standard Model (SM) of particle physics, which has been developed incrementally in recent decades and has stood up well to scientific scrutiny. The Large Hadron Collider (LHC) at the Organisation Européenne pour la Recherche Nucléaire (CERN) near the Swiss city of Geneva (Figure 1.1) was constructed with the aim of investigating the SM. Areas of current interest including electroweak symmetry breaking, the Higgs mechanism and physics beyond the SM (BSM) such as supersymmetry (explained in further detail in Section 2), require the acceleration of particles to high energies (of the order of several TeV). The start of data-taking from proton-proton collisions at the LHC in 2009 ushered in a new era in terms of energies at particle colliders, taking over as the highest energy particle collider from the TeVatron at Fermilab, near Chicago, U.S.A. In 2010 and 2011 the LHC collected data at a centre-of-mass energy of 7 TeV (5.1 fb^{-1}), followed by 8 TeV (21.8 fb^{-1}) in 2012 and currently in 2015, after the first long shutdown, at 13 TeV.

The Compact Muon Solenoid (CMS) general-purpose detector is one of the four main detectors located around the LHC (the others being ATLAS, LHCb and ALICE), approximately 100 m below ground level.

This thesis presents an analysis based on the full proton-proton collision data from the CMS experiment in 2011 and 2012. The analysis investigates the top-antitop ($t\bar{t}$) differential cross section with respect to global level event variables, specifically in semileptonic $t\bar{t}$ decays in the electron+jets and muon+jets channels. This investigation is motivated primarily by the importance of understanding $t\bar{t}$ events, since they are a significant background in many new physics analyses. The understanding of event generators and QCD events provided by

1. Introduction

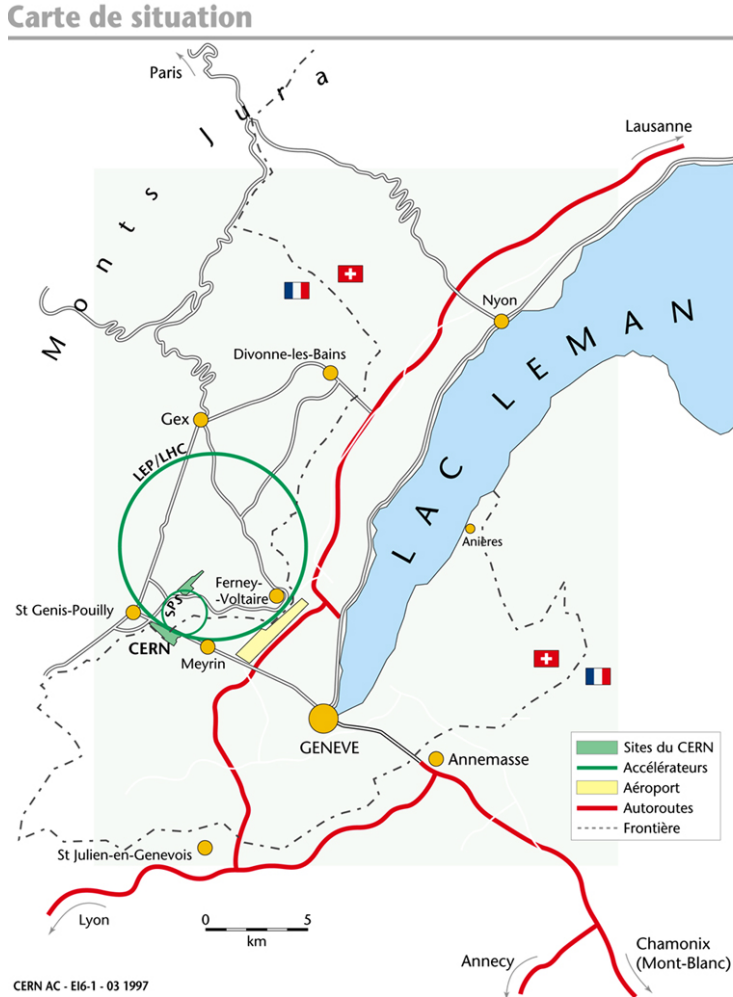


Figure 1.1: Map of LHC location.

studies such as this is also helpful for other physics analyses. Furthermore, rare Standard Model processes and new physics scenarios could be detected in the distributions of the global variables under investigation.

The work presented here was carried out in collaboration with Emrys Clement, Lukasz Kreczko, Sergey Senkin and Philip Symonds under the supervision of Professors Joel Goldstein and Greg Heath. The main contribution of the author to these studies lay in development of the physics analysis, implemented in a C++ and Python software framework, playing the leading role in producing the combined 7 TeV and 8 TeV analysis described in Chapters 7, 8 and 9. Areas of focus regarding physics included event selection synchronisation of the event selection, distribution comparison between 7 TeV and 8 TeV data, and implementing details such as selection criteria, b-tagging, trigger efficiencies, jet energy resolution and fitting, in

addition to maintaining up-to-date particle object definitions, corrections, efficiencies and prescription recommendations from working groups within CMS.

Chapters 4 and 5 describe the LHC and the CMS detector, including information about the object reconstruction process based on detector readout, to represent particles produced in collisions. Chapter 2 provides an overview of the Standard Model theory and some of its shortcomings, followed by a review of physics of the top quark at the LHC in Chapter 3. A small study investigating the b-tagging algorithms used in CMS is described in Chapter 6, and the main $t\bar{t}$ differential cross section analysis is then covered in Chapters 7, 8 and 9. To conclude, Chapter ?? contains a summary and outlook to the future. Additional data, tables and plots from the presented analyses are given in Appendices A and B.

From the outset, natural units are used throughout this thesis, unless otherwise specified, so that

$$\hbar = c = 1, \quad (1.1)$$

meaning that mass, momentum and energy all have the same units of electronVolts (eV).

1. Introduction

2 | The Standard Model of Particle Physics

2.1 Introduction

The Standard Model (SM) is the name given to the theory developed during the course of the 20th century that describes the elementary particles that make up all known, observable matter and the three fundamental forces by which they interact (electromagnetic, weak and strong). The SM does not, however, describe the gravitational force as it is not known how to model it mathematically at a quantum scale. The SM puts forward twelve fermions, with a spin quantum number of $1/2$, as the matter particles. These are split into two groups of six quarks and six leptons, all of which are split into three generations. The six quarks are classified according to their charge and flavour: up, down, charm, strange, top and beauty quarks. The leptons are in turn classified similarly: electron, muon or tau leptons, together with their corresponding neutrinos. Neutrinos, although originally thought to be massless, are now known to carry mass due to the observation of the oscillation of neutrinos between different flavours. Table 2.1 shows these particles of the Standard Model in their respective generations. All of these particles have a respective antiparticle which has identical quantum numbers with the exception of opposite electric charge.

All known, observable matter in the universe is composed of the aforementioned twelve fermions or their antiparticles. All stable matter is composed of protons, neutrons and electrons. All other particles are unstable and decay; they are produced only in particle colliders such as the LHC, or in cosmic radiation. Quarks also carry the charge of the strong force, termed ‘colour’, of red, green or blue. The only quark which does not form bound colourless states (hadronise) is the top quark which has a very short lifetime of $\approx 5 \times 10^{-25}$ s [99]

2. The Standard Model of Particle Physics

Generation	Flavour	Charge / e	Spin	Mass / MeV
Leptons				
I	electron (e)	-1	$\frac{1}{2}$	0.511
	electron neutrino (ν_e)	0	$\frac{1}{2}$	$< 2 \times 10^{-6}$
II	muon (μ)	-1	$\frac{1}{2}$	105.66
	muon neutrino (ν_μ)	0	$\frac{1}{2}$	$< 2 \times 10^{-6}$
III	tau (τ)	-1	$\frac{1}{2}$	$(1.777 \pm 0.16) \times 10^3$
	tau neutrino (ν_τ)	0	$\frac{1}{2}$	$< 2 \times 10^{-6}$
Quarks				
I	up (u)	$+\frac{2}{3}$	$\frac{1}{2}$	$2.3^{+0.7}_{-0.5}$
	down (d)	$-\frac{1}{3}$	$\frac{1}{2}$	$4.8^{+0.5}_{-0.3}$
II	charm (c)	$+\frac{2}{3}$	$\frac{1}{2}$	$(1.275 \pm 0.025) \times 10^3$
	strange (s)	$-\frac{1}{3}$	$\frac{1}{2}$	95 ± 5
III	top/truth (t)	$+\frac{2}{3}$	$\frac{1}{2}$	$(173.21 \pm 0.51 \pm 0.71) \times 10^3$
	bottom/beauty (b)	$-\frac{1}{3}$	$\frac{1}{2}$	$(4.18^{+0.03}_{-0.03}) \times 10^3$
Bosons				
Force	Gauge Boson(s)	Charge / e	Spin	Mass / GeV
Weak	W^+/W^-	+1/-1	1	80.385 ± 0.015
Weak	Z^0	0	1	91.188 ± 0.002
Electromagnetic	photon (γ)	0	1	0
Strong	gluon (g)	0	1	0
Gravitation	graviton	0	2	0
-	Higgs (H)	0	0	125.7 ± 0.4

Table 2.1: Fundamental fermions, split into their three generations, and bosons of the Standard Model. The graviton is currently only hypothesised. Particle properties taken from [99].

due to its large mass, and therefore decays before it can hadronise.

These fermions interact via the integer spin (spin 1) gauge bosons of the three fundamental forces. Electron, muon and tau leptons interact via the electromagnetic and weak forces; their neutrinos, since they carry no electric charge, interact only via the weak force; and the quarks interact via the electromagnetic, weak and strong forces. Each of the forces are mediated by gauge bosons that are the ‘force carriers’. The mediator of the strong force is known as the gluon, that of the electromagnetic force is the photon and those of the weak force are the W^+ , W^- and Z bosons. Table 2.1 shows the gauge bosons and their properties.

The strength of the fundamental forces is quantified by their coupling strength, denoted α . Taking the strength of the strong force as the baseline, the relative strength of the electromagnetic force is 10^{-2} , that of the weak force is 10^{-5} and the strength of the gravitational force is 10^{-39} , though the notion of relative strength is dependent on the energy scale, so different relative strengths are often quoted, in particular for the weak force [104, 76]. The electromagnetic coupling strength, also known as the fine-structure constant, is defined as $\alpha_{em} = \frac{e^2}{4\pi}$, which at low energies is $\approx \frac{1}{137}$. Although the strong force is the strongest force, it has a limited range of only $\sim 10^{-15}$ m, and the weak force has an estimated range of $\sim 10^{-18}$ m, while the electromagnetic and gravitational forces have infinite range.

The discovery of the Higgs boson was announced in July 2012 by the CMS and ATLAS experiments at the LHC, and is a major component of the Standard Model [45, 14]. The mechanism of electroweak symmetry breaking through which other particles acquire mass is due to the Higgs field, and is described in Section 2.1.5.

2.1.1 Gauge Principle

The underlying mathematical model of the Standard Model is a Quantum Field Theory (QFT) combining special relativity and quantum mechanics. All interactions in the SM must conserve the kinematic quantities energy and momentum, in addition to electric charge. The electromagnetic and strong forces also conserve the dynamic quantities colour, strangeness, spin, baryon number, lepton number and quark flavour. The weak force, if mediated by a charged propagator (W^\pm), can allow the violation of quark flavour, meaning a quark can decay into another flavour quark.

The laws of conservation occur as a result of underlying symmetries in the theories. For instance, energy conservation stems from time symmetry and angular momentum conservation is a result of rotational symmetry. In addition to these classical symmetries, a quantum field theory can also possess gauge symmetries. The principle of gauge invariance refers to field theories in which the Lagrangian, which summarises the dynamics of the system, is invariant under local transformations (transformations that are a function of a field,

and therefore different at all space-time points within the field). If the collection of all such gauge transformations is commutative, i.e. any order of application of the symmetry transformations produces the same result, the theory is termed Abelian. Conversely, if the group is non-commutative, the theory is non-Abelian. Each group of transformations has an associated generator, and each generator has a corresponding vector field, or gauge field, whose purpose is ensuring invariance under local transformations. The quanta of these fields are the gauge bosons of the Standard Model. Note that the converse of local transformations are global transformations, in which the transformation takes place instantaneously at all space-time points.

Group transformations can be represented as groups of $n \times n$ matrices which possess properties such as unitarity (U) and orthogonality (O). A group of matrices with determinant 1 is called ‘special’ (S), leading to further groups $SU(N)$ and $SO(N)$. The Standard Model is comprised of electroweak theory (combining electromagnetism and weak theory), with a gauge symmetry of $SU(2) \times U(1)$, and the theory of strong interactions, described by the gauge group $SU(3)$.

2.1.2 Quantum Electrodynamics

Quantum electrodynamics (QED) is a component theory of the Standard Model that governs the interactions of electrically charged particles. The simplest electromagnetic process is shown in Figure 2.1a, and all real processes are made of some number of these processes combined together, such as electron-positron annihilation shown in Figure 2.1b.

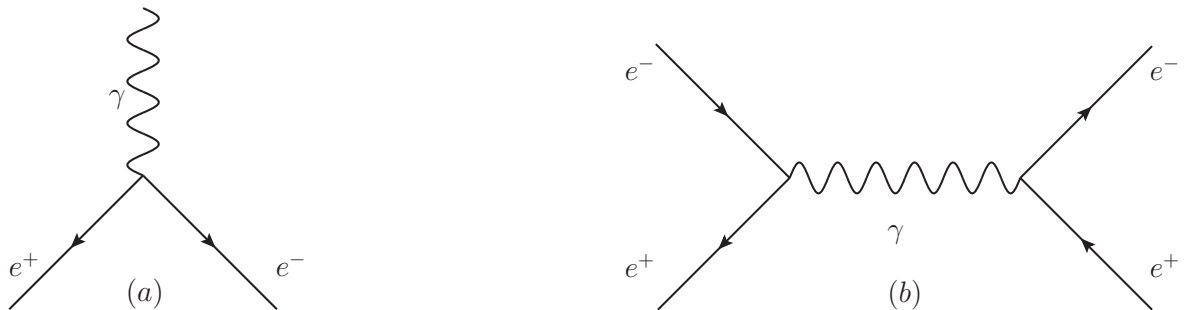


Figure 2.1: (a) the elementary electromagnetic process of an electron emitting a photon and (b) electron-positron annihilation.

Any such real process is represented by the sum of all possible orders of Feynman diagrams for the interaction. In practice, since each vertex contributes a factor of α , higher-order Feynman diagrams with more than a few vertices contribute negligibly to the process and are often ignored.

The coupling strength of a force can be further explained in terms of vacuum polarisation. Regarding the electromagnetic force, this refers to the phenomenon of electron-positron pairs and photons being spontaneously created and absorbed by an electron. These virtual particles, which would be represented in Feynman diagrams as closed loops, shield the original electron leading to the electron charge being measured at a lower value than its true charge. This measured value is called the effective, or 'screened', charge. As a result, the coupling strength of the electromagnetic force is said to be a 'running' coupling constant, due to the fact that it decreases as a function of distance.

The mathematical formulation of QED stems from the Dirac equation, which describes the Lagrangian for a spin-half (Fermionic) field ψ [65]:

$$\mathcal{L} = i(\hbar c)\bar{\psi}\gamma^\mu\partial_\mu\psi - (mc^2)\bar{\psi}\psi \quad (2.1)$$

Here, \hbar is the reduced Planck's constant, μ are the Lorentz indices and γ^μ are the gamma (or Dirac) matrices. Under a global transformation of the field by a phase $i\alpha$, this Lagrangian is invariant (i.e. under a global transformation of the $U(1)$ group, since this is equivalent to multiplication of the field ψ by a 1×1 unitary matrix). However, under a local gauge transformation by a phase of $i\alpha(x)$, the symmetry no longer holds meaning the Lagrangian is not invariant:

$$\mathcal{L} \rightarrow \mathcal{L} - \bar{\psi}(x)\gamma^\mu\psi(x)[\partial_\mu\alpha(x)]. \quad (2.2)$$

Local symmetry can be maintained in this case if a new gauge field, A_μ , is introduced to the Lagrangian by means of a covariant derivative D_μ . If the partial derivatives in the Dirac equation are now replaced with the covariant derivatives, the invariant Lagrangian is

obtained:

$$\mathcal{L} = i(\hbar c)\bar{\psi}\gamma^\mu\partial_\mu\psi - e\bar{\psi}\gamma^\mu\psi A_\mu - (mc^2)\bar{\psi}\psi - \frac{1}{4}F^{\mu\nu}F_{\mu\nu}. \quad (2.3)$$

In this way, the principle of local gauge invariance under the $U(1)$ group is used to introduce additional fields to a Lagrangian in order to make it invariant under local transformations. This final Lagrangian is that of quantum electrodynamics. The physical interpretation of the gauge field A_μ is the photon, which couples to charged particles (electrons and positrons) with a coupling strength proportional to the charge. The term $\frac{1}{4}F^{\mu\nu}F_{\mu\nu}$ is an additional term to account for the kinetic energy of the free particle of the new gauge field, i.e. the photon; and there is no term denoting the photon mass.

2.1.3 Electroweak Theory

The unification of the electromagnetic and weak forces in the 1960s provided a more complete theory of fundamental particles. This unification takes the form of an $SU(2) \times U(1)$ gauge group combining the electromagnetic and weak forces, and can be constructed in a similar way to the QED formalism in Section 2.1.4.

First, it is necessary to define isospin, I , an abstract fundamental property of fundamental particles that is conserved in all interactions. Similarly, weak hypercharge, Y , is also a quantum property, defined as $Y_W = 2(Q - I_3)$, where Q represents the charge of the particle and I_3 is the third component of isospin. I_3 takes a value of $1/2$ for left-handed fermions.

It has been shown empirically that the weak interaction exhibits violation of parity (P) and interacts only with left-handed particles via the charged gauge bosons (W^\pm). Hence, the fields representing fermions are split into left handed and right handed components by defining a left handed doublet containing the left handed electron and left handed neutrino, and a right handed singlet containing the right handed electron.

Four additional massless fields and their associated currents are introduced in order to impose gauge-invariance: W_μ^1 , W_μ^2 , W_μ^3 and B_μ . The W_μ fields are introduced for gauge invariance of the $SU(2)$ group, and interact with the third isospin component I_3 . The B_μ

field similarly transforms by the unitary group $U(1)$, and interacts with the weak hypercharge Y . These additional fields lead to the construction of three weak isospin currents and a weak hypercharge current.

Requiring local gauge invariance under an $SU(2) \times U(1)$ group, the covariant derivative is

$$D_\mu = \partial_\mu + \frac{i}{2}g_W \vec{\tau} \cdot \vec{W}_\mu + ig' \frac{Y}{2} B_\mu. \quad (2.4)$$

The vectors W_μ^1 , W_μ^2 , W_μ^3 have coupling strengths of g_W to the three isospin currents and B_μ couples to the hypercharge current with a strength of g' . These four bosons relate to the quanta of the new fields. A linear superposition of the W_μ^1 and W_μ^2 states gives the W^\pm bosons, while the neutral states W_μ^3 and B_μ undergo a mixing related by the weak mixing angle, θ_W , to give the neutral Z^0 and γ bosons. (The weak mixing angle relates the coupling constants of the electromagnetic and weak forces by $\tan \theta_W = \frac{g'}{g_W}$).

It has been experimentally observed that both the W bosons and the Z boson have mass. Indeed, the strength of the electromagnetic force is of the same order as the weak force, but as a result of the weak gauge bosons having mass, the weak force appears weaker and has a shorter range. However, the local gauge invariance would be broken if terms to give the bosons mass were to be included. The theory of spontaneous breaking of the symmetry underlying the $SU(2) \times U(1)$ group addresses this problem, as explained in Section 2.1.5.

The weak force has been shown to change the flavour of quarks in an interaction, meaning flavour conservation is broken. The quarks, like leptons, come in the form of left handed doublets within each generation,

$$\begin{pmatrix} u_L \\ d'_L \end{pmatrix}, \begin{pmatrix} c_L \\ s'_L \end{pmatrix}, \begin{pmatrix} t_L \\ b'_L \end{pmatrix} \quad (2.5)$$

with isospin $\frac{1}{2}$. Note that the lower quarks of the doublets are denoted with primes as they indicate a rotated state of the quark, called Cabibbo-rotated states, which are superpositions

of the physical quarks. This means that in, for example, the decay of a down quark to an up quark via emittance of a W^- , the down quark to which the W^- couples is actually a superposition of ‘down type’ quarks, i.e. down, charm and beauty quarks. The Cabibbo-Kobayashi-Maskawa (CKM) matrix, relates the weak interaction mixed states to the physical quark states. This is the degree of quark mixing between the different generations, and results in the measured values (see equation 2.6) of $|V_{12}|$ for the probability of a transition from quark 1 to quark 2 in a weak interaction [99]. In reference to top physics, the $|V_{tb}|$ value of almost 1 means that the top quark almost always decays to a W boson and a b-quark.

$$\begin{pmatrix} V_{ud} & V_{us} & V_{ub} \\ V_{cd} & V_{cs} & V_{cb} \\ V_{td} & V_{ts} & V_{tb} \end{pmatrix} = \begin{pmatrix} 0.974 & 0.225 & 0.004 \\ 0.225 & 0.973 & 0.041 \\ 0.009 & 0.041 & 0.999 \end{pmatrix} \quad (2.6)$$

2.1.4 Quantum Chromodynamics

In the theory of quantum chromodynamics (QCD), the charge of the strong force is colour, and the force is independent of other particle properties such as charge and flavour. Empirical data has led to the conclusion that there are three colour charges: red, green and blue [76]. Colour conservation is a requirement of strong processes (cf. charge conservation in QED), although the colour of an individual quark can be changed in a strong interaction. The mediators of the strong force, gluons, carry a positive and a negative colour charge themselves, and so can interact directly with other gluons. The coupling constant of the strong force is a running coupling constant. At small distances of the order of the size of the proton (~ 0.1 fm), α_S is small and becomes smaller as distance decreases, leading to quarks and gluons being essentially free particles and interacting weakly with each other when confined within colourless bound states (though this interaction is still stronger than the electromagnetic force). This phenomenon is termed asymptotic freedom.

The previously mentioned colourless bound quark states are called hadrons. The process in which free gluons and quarks form bound colourless states is called hadronisation, and at

high momenta manifests as a cone of particles, termed jets. Hadrons are divided into two types: mesons are composed of a quark and an antiquark with the quark carrying a colour charge and the antiquark carrying the respective anticolour; baryons are composed of three quarks or three antiquarks. Recently, the LHCb experiment at CERN published first results of the observation of a pentaquark state [18].

The proton, a baryon, consists of two u-quarks, one d-quark and gluons binding the quarks together. However, the structure of the proton becomes more complicated, consisting of more particles, as the momentum of the probing particle increases. The aforementioned three-quark-structure of the proton is evident at low momenta, while at higher momenta, virtual pairs of quarks and antiquarks, and gluons are visible. These virtual quarks are termed sea quarks and, together with the gluons, can make up most of the mass of the proton at high energy scales. In any proton, each constituent particle carries some fraction, x , of the overall proton momentum.

The quantum field theory of QCD is determined to have the underlying symmetry of the group $SU(3)$, based on the fact that there are three colour charges. Imposing local gauge invariance, the Lagrangian contains eight generators of the $SU(3)$ group. These generators lead to eight gauge fields, whose physical interpretation are the eight massless gluons that mediate the strong force. Therefore, although in principle there could be nine gluons, since there are three colours and gluons carry a colour and an anticolour charge, the $SU(3)$ symmetry leads to a colour octet and a colour singlet [76].

Any particle that occurs in nature must be a colour singlet, and so the gluons in the colour octet are never seen in nature as free particles. However, although the final gluon is a colour singlet, it has not been observed and is thought not to exist. If it did exist, it would result in a long range strong force, but it is known that the strong force has a short range of action.

2.1.5 Spontaneous Symmetry Breaking

The theory of spontaneous breaking of the electroweak $SU(2)$ symmetry, mentioned in Section 2.1.3, also known as the Higgs mechanism, was put forward in the 1960s [78]. This theory was postulated as a mechanism by which the W^\pm and Z gauge bosons could acquire mass, since the Lagrangian of the electroweak interaction contains no mass term for these particles, and their inclusion would violate local gauge invariance.

The method by which this symmetry is spontaneously broken begins with the inclusion of two new complex scalar ‘Higgs’ fields (so in total there are four components to these two complex fields). These fields are introduced with an additional scalar potential energy term in the Lagrangian, $V(\Phi)$, where Φ represents the newly introduced complex scalar fields. The potential $V(\Phi)$ is chosen to be

$$V(\Phi) = -\mu^2 \Phi^\dagger \Phi + \lambda^2 (\Phi^\dagger \Phi)^2 \quad (2.7)$$

Imposing the requirement of μ^2 and λ both being greater than 0, gives a potential of the geometry shown in Figure 2.2. The minimum of this potential is clearly not at $\Phi = 0$, rather, the minimum has a circular form given by the formula $\Phi^\dagger \Phi = \frac{\mu^2}{2\lambda} = \frac{v^2}{2}$, where $v = \frac{|\mu|}{\sqrt{\lambda}}$, the ‘vacuum expectation value’ of the Higgs field. Since the minimum, i.e. the vacuum, is at a location other than $\Phi = 0$, the new field is said to have a non-zero vacuum expectation value, and the $SU(2) \times U(1)$ symmetry is spontaneously broken. The observed Higgs boson is created as a result of perturbations in the potential about this minimum. In addition to this new particle, introducing the new fields also results in the fields associated with the W^\pm and Z^0 bosons in the Lagrangian acquiring mass.

Terms known as Yukawa coupling terms can be introduced to specify the interactions of Φ with the fermion fields. It is this coupling of the Higgs field to any massive particle that gives them a proportional mass. The top quark, being the heaviest known particle at ~ 173 GeV, has a Yukawa coupling to the Higgs field close to 1.

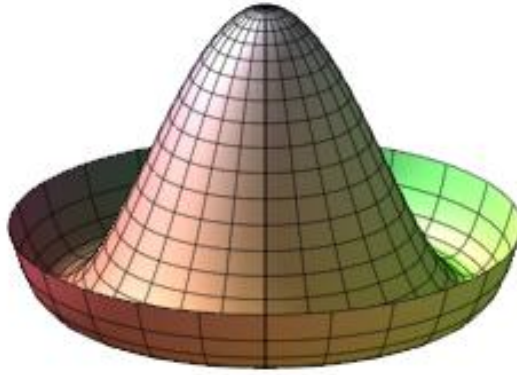


Figure 2.2: The Higgs field potential $V(\Phi)$ [96].

Results published at the discovery of the Higgs boson are shown in Figure 2.3 in the $H \rightarrow \gamma\gamma$ and $H \rightarrow ZZ$ channels. These plots of the invariant masses of the $\gamma\gamma$ and ZZ combinations show a clear excess of events around 125 GeV. The latest results from CMS and ATLAS, shown in Figure 2.4 state a Higgs mass of $125.09 \pm 0.21 \pm 0.11$ GeV [16], where the first uncertainty is statistical and the second is systematic. Since the announcement of the discovery of the Higgs boson in 2012, studies have continued to determine its quantum properties. Thus far, results show it to be in agreement with predictions from the Standard Model [88].

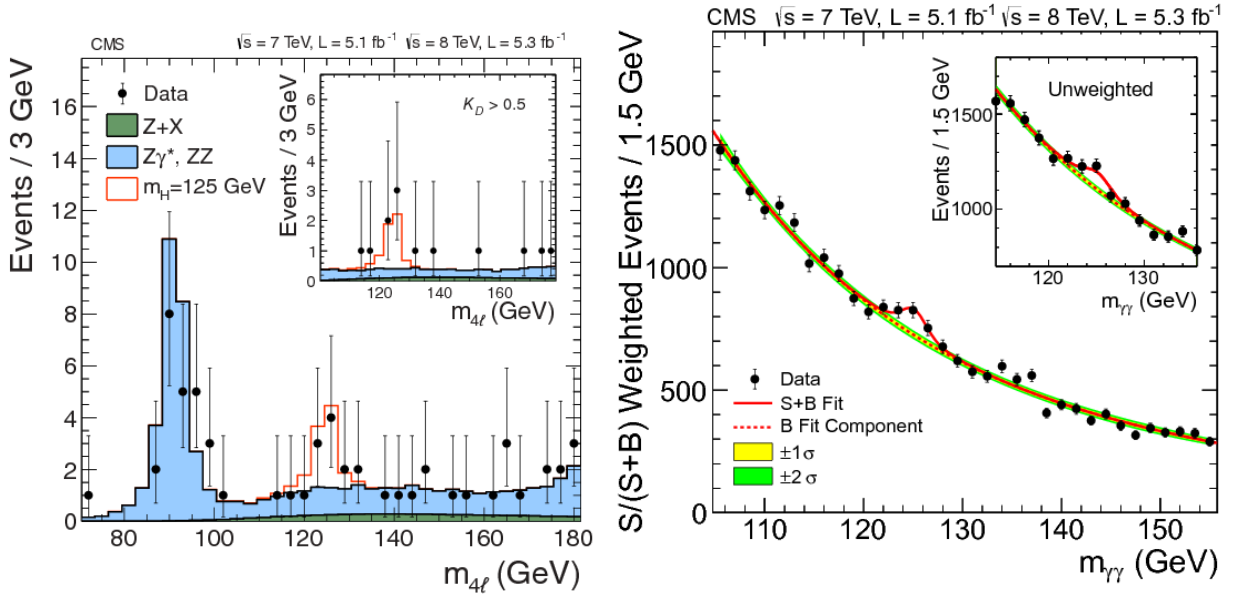


Figure 2.3: Invariant mass in $H \rightarrow \gamma\gamma$ (left) and $H \rightarrow ZZ$ (right) channels [45].

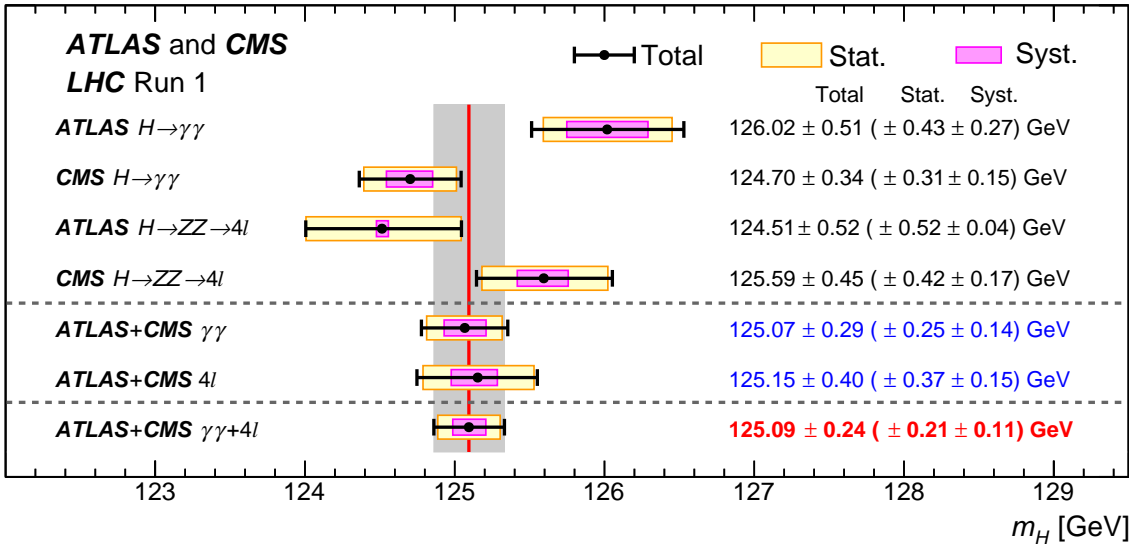


Figure 2.4: Summary of Higgs boson mass measurements from CMS, ATLAS and combined CMS+ATLAS analyses in the $H \rightarrow \gamma\gamma$ and $H \rightarrow ZZ$ channels [16].

2.2 Incompleteness of, and physics beyond, the SM

The Standard Model has proven to be an extremely successful theory thus far. However, its inability to describe many phenomena in the universe lead to it being considered currently incomplete. Indeed, a ‘Grand Unified Theory’ combining the electromagnetic, weak, and strong interactions is considered to be the next step in the quest for a ‘Theory of Everything’ including gravity, with all of these forces being different physical manifestations of one single force.

There are many free parameters in the Standard Model and the very reason why it takes the form it has, with four fundamental forces, six quarks and six leptons, each divided into three generations, is not explained. The gravitational force is also conspicuous by its absence from the SM. The imbalance between matter and anti-matter in the universe, despite the generally accepted view that both were created in equal quantities in the Big Bang, is also not fully explained by the SM. Although the evident matter-antimatter asymmetry in the universe could be partially explained by the observed charge-parity (CP) symmetry violation in weak interactions [52], this is not sufficient to account for the observed excess.

Furthermore, the SM does not provide a theoretical explanation for neutrino mass. Originally thought to be massless, neutrinos are now known to have mass, albeit extremely small, based on observations of neutrino oscillations between different flavours [82, 72].

The hierarchy problem, in terms of the Higgs boson, refers to the fact that the measured Higgs mass is many orders of magnitude smaller than the order of the Planck scale (1.22×10^{19} GeV). The expected quantum corrections to the Higgs mass from higher order interactions should result in a far larger mass. This disagreement suggests that there occurs some ‘fine tuning’ of the bare Higgs mass, to lead to the experimentally observed mass of approximately 125 GeV.

Supersymmetry (SUSY) is one potential solution to hierarchy problem. This theory proposes a symmetry between fermions (spin $\frac{1}{2}$) and bosons (spin 1). Each particle has an associated ‘superpartner’ with identical quantum properties with the exception of spin, which differs by $\frac{1}{2}$, so that all SM fermions have a boson superpartner, and all SM bosons have a fermion superpartner. These super particles, or sparticles, are thought to have higher masses than their SM counterparts since they have not been discovered yet, making supersymmetry a broken symmetry. In many supersymmetry theories, the lightest SUSY particle (LSP) is stable and is a potential candidate to be a dark matter particle.

Another potential solution is the theory of topcolor, an example of a composite model theory that suggests the existence of a top-quark-condensate (a composite field of the top and antitop quarks) that acts effectively like the SM Higgs field [32, 79]. Such a theory would give rise to a... new fundamental interaction between top quarks at high energies resulting in the large top mass. Theories of extra dimensions also exist, in which additional space-time dimensions are postulated in which only gravity propagates [31]. This could provide an explanation for the fact that the Planck scale is far larger than the electroweak force by solving the heirarchy problem.

The Planck experiment, and the WMAP mission before that, provide estimates that the universe is thought to constitute approximately 27 % dark matter, 68 % dark energy and

5 % ordinary matter (Figure 2.5) [22]. The origins and nature of the dark energy and dark matter are currently unknown and they are as yet unobserved, but their existence has been inferred from their gravitational effects on galactic masses composed of stars, gases and dust. The relative amounts of ordinary matter, dark matter and dark energy have been inferred from measurements of the cosmic microwave background radiation which give an indication of the structure and composition of the early universe. The relatively large amounts of dark matter and dark energy hypothesised suggests that they are made up of weakly interacting massive particles.

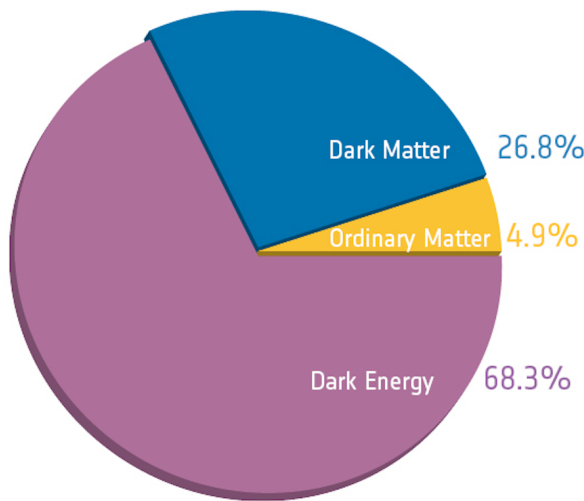


Figure 2.5: The composition of the universe showing the amounts of dark matter, dark energy and ordinary matter based on latest results from Planck/ESA [22]

3 | Top Physics at the LHC

3.1 Introduction

The top quark was discovered by the CDF and D \emptyset collaborations at the Tevatron at Fermilab in 1995 [20, 19] and is still one of the less well studied fundamental particles in the SM. The top quark is the heaviest fermion with its mass currently placed at 173.29 ± 0.23 (stat.) ± 0.92 (syst.) GeV/ c^2 [61]. Since the lifetime of the top quark is very short, approximately 5×10^{-25} s [99], it is the only one of the quarks to decay before it hadronises, meaning that the bare quark properties can be investigated. These unique properties of the top quark within the SM mean it is an interesting focus of study.

3.1.1 Top Quark Production and Decay

Top quarks can be produced either in top-antitop ($t\bar{t}$) production through the strong interaction or single top (t-quark) production through the electroweak mechanism. During Run 1 of data taking at the LHC produced millions of top quark pair events with gluon-gluon fusion or quark-antiquark annihilation being the primary production mechanisms (shown in Figure 3.1). The $t\bar{t}$ production cross section at $\sqrt{s} = 1.96$ TeV was measured by the CDF and D \emptyset collaborations at the TeVatron, while the cross sections at $\sqrt{s} = 7$ TeV and $\sqrt{s} = 8$ TeV have been measured by CMS and ATLAS at the LHC. The measurements are summarised in Figure 3.2. Numerical cross sections values at the LHC, at $\sqrt{s}=7$ TeV, $\sqrt{s}=8$ TeV, $\sqrt{s}=13$ TeV and $\sqrt{s}=14$ TeV are shown in Table 3.1.

At the TeVatron, quark-antiquark annihilation dominated, accounting for 90 % of the $t\bar{t}$ production cross section. At $\sqrt{s} = 7$ TeV, gluon-gluon fusion accounts for approximately 80 % of the $t\bar{t}$ production, increasing to approximately 90 % at $\sqrt{s} = 14$ TeV [99]. Gluon-gluon fusion dominates at the LHC since protons are collided with protons, meaning antiquarks

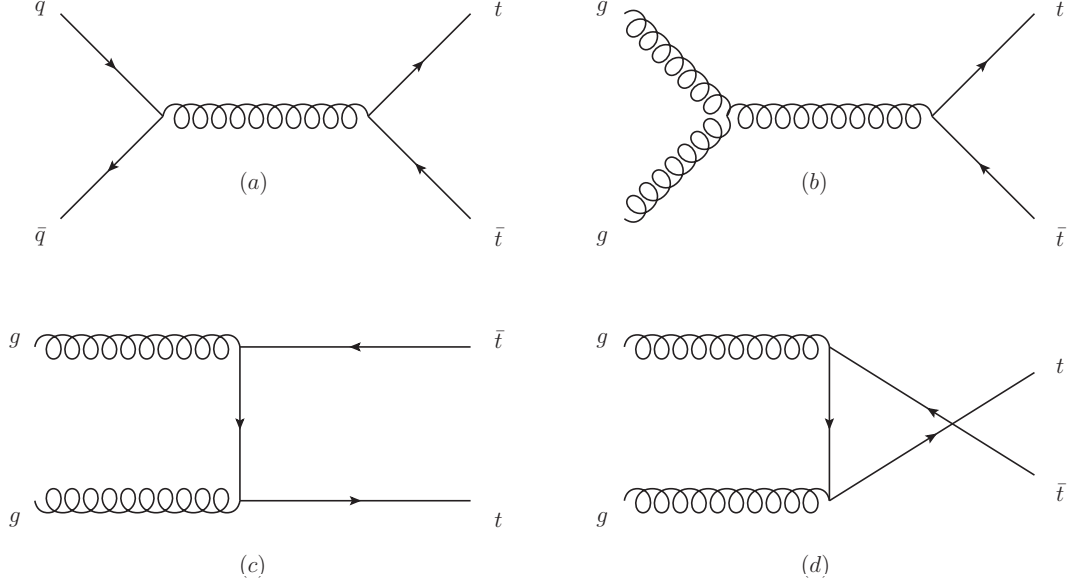


Figure 3.1: Feynman diagrams of leading order $t\bar{t}$ production processes. (a) depicts quark-antiquark annihilation, and (b), (c) and (d) depict gluon-gluon fusion in the s, t and u channels respectively.)

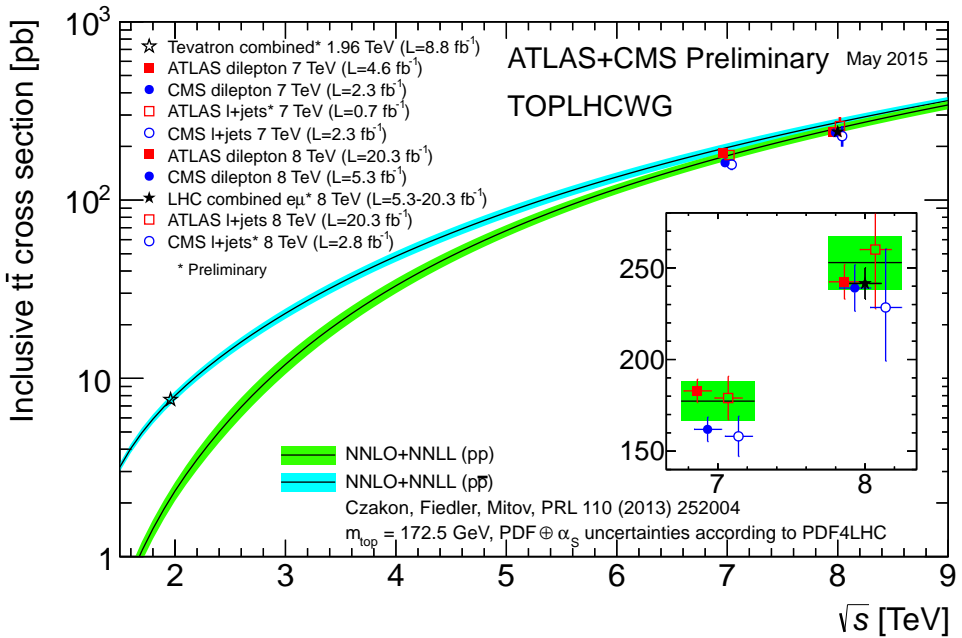


Figure 3.2: $t\bar{t}$ production cross sections at 1.96 TeV at CDF and DØ at the TeVatron and at 7 TeV and 8 TeV at CMS and ATLAS [77].

\sqrt{s}	$t\bar{t}$	Single t s-channel	Single t t-channel	Single t tW-channel
7	177.31	4.29	63.69	15.74
8	252.89	5.24	84.69	22.37
13	831.76	10.32	216.99	71.70
14	984.50	11.39	248.09	84.40

Table 3.1: SM $t\bar{t}$ and single top production cross sections in pb at next-to-next-to-leading order at the LHC.

are only available from sea quarks in the proton. At low momentum fractions, x , the gluon density in the proton is large compared to the sea quarks, and increases towards lower x at a higher rate than that of the sea quarks. Figure 3.3 shows the proton parton distribution functions (PDFs) at a momentum transfer, $Q^2 = 10000 \text{ GeV}^2$, the region relevant for the LHC and of the order required for t/W/Z production. At low x , it can be seen that the sea quarks and gluons dominate, while the valence quarks increase in number at high x .

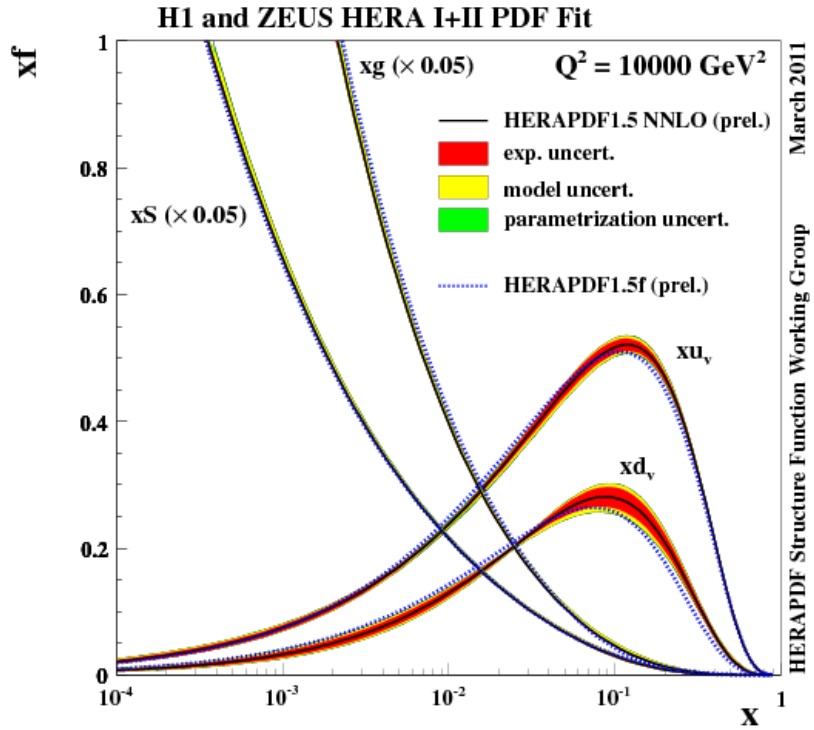


Figure 3.3: Parton distribution functions from HERA as a function of proton momentum fraction for $Q^2 = 10 \text{ GeV}^2$ [102].

Top quarks decay almost 100 % of the time to a W boson and a b flavour jet. The W boson

then decays either hadronically (into two jets) or leptonically (lepton + neutrino). Top pair events are characterised by the decay of the W bosons:

- Leptonic: $t\bar{t} \rightarrow W^+ b W^- \bar{b} \rightarrow l\nu_l b l' \bar{\nu}_{l'} \bar{b}$. Both W bosons decay to a lepton and a neutrino. The event would consist of 2 jets, 2 leptons and 2 neutrinos (which would show up as missing transverse energy (E_T^{miss}) in the event). (10.5 %)
- Hadronic: $t\bar{t} \rightarrow W^+ b W^- \bar{b} \rightarrow q\bar{q} b q \bar{q} \bar{b}$. Both W bosons decay to two jets. The event would consist of 6 jets. (45.7 %)
- Semi-Leptonic: $t\bar{t} \rightarrow W^+ b W^- \bar{b} \rightarrow q\bar{q} b l \nu_l \bar{b}$. One W boson decays to a lepton and a neutrino, the other decays to two jets. The event would consist of 4 jets, 1 lepton and 1 neutrino. This decay is shown in Figure 3.4. (43.8 %)

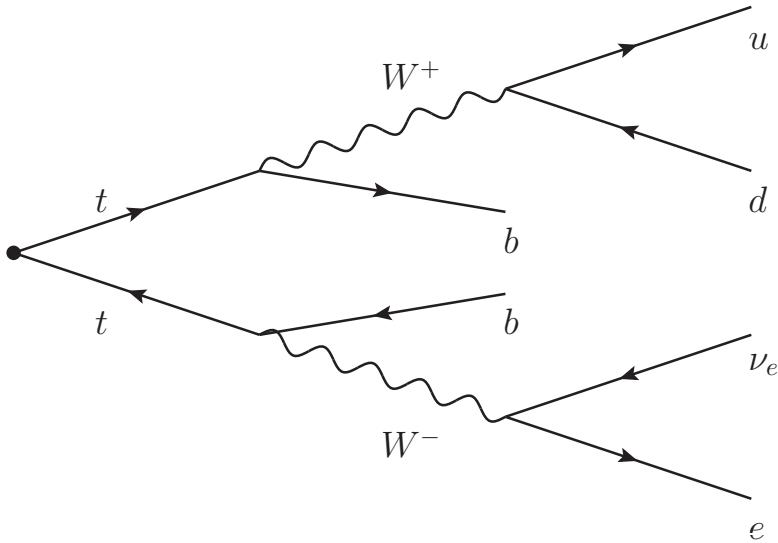


Figure 3.4: Feynman diagram of the electron+jets semi-leptonic $t\bar{t}$ decay channel.

The branching ratios for each decay mode are quoted in brackets [99], and are represented graphically in Figure 3.5. The numbers of jets in the final state of each channel could be higher than the numbers quoted above as a result of higher order processes such as initial state radiation (radiation from the gluons before the $t\bar{t}$ production) or final state radiation. The hadronic decay channel, with multiple jets and no leptons in the final state, is difficult to distinguish from the QCD multijet, W+jets and Z+jets backgrounds. Conversely, the leptonic channel has a very clean signature with two leptons, however the low branching

ratio would limit the available statistics. The semi-leptonic channel, with one lepton and four jets provides a good balance between statistics and event identification. The lepton can be an electron, a muon or a tau. However, top events with taus are difficult to distinguish from genuine semi-leptonic events, hence resulting measurements are generally less precise, and therefore taus are not included in semi-leptonic t-quark studies in general (see Section 9.1.1 for more details regarding taus in semi-leptonic $t\bar{t}$ events).

Top Pair Decay Channels

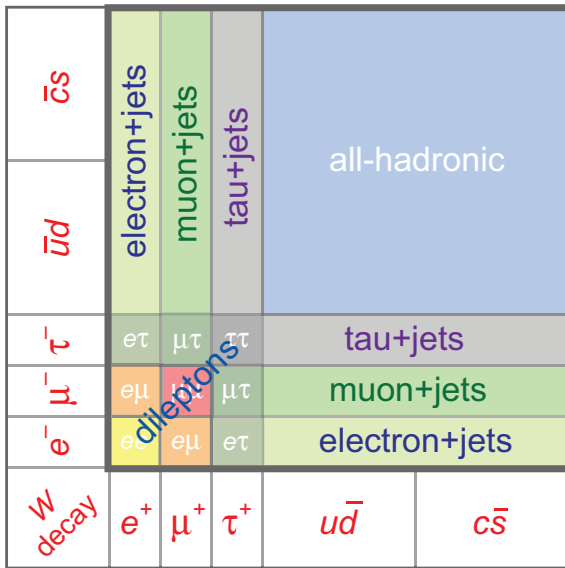


Figure 3.5: Relative branching ratios of the $t\bar{t}$ system

The signal channel for the analysis described in this work is semi-leptonic $t\bar{t}$ decay, also referred to as the lepton+jets channel, where the lepton is either an electron or a muon. These channels have a branching ratio of approximately 14.2 % and 14.4 % respectively [99].

3.1.2 Single Top background

Single top production is one of the backgrounds considered in this analysis, and can occur via the electroweak interaction in one of three channels: s-channel (Figure 3.6 (a)), t-channel (Figure 3.6 (b) and (c)) which both involve the exchange of a virtual W boson, or tW-channel (Figure 3.6 (d) and (e)) which involves the associated production of a W boson and a top quark. Although semi-leptonic $t\bar{t}$ decays have more jets in the final state than these single top

production modes, initial state radiation and final state radiation, where low energy gluons and quarks are produced before and/or after the interaction that produces the single t-quark, can increase the numbers of jets in single top events. This can lead to such events having a similar signature to $t\bar{t}$ events, and providing a non-negligible background. SM production cross sections for single top events are shown in Table 3.1. Comparisons of data to Monte Carlo simulation, and the composition of the backgrounds, including single top events, will be shown in Section 8.1.

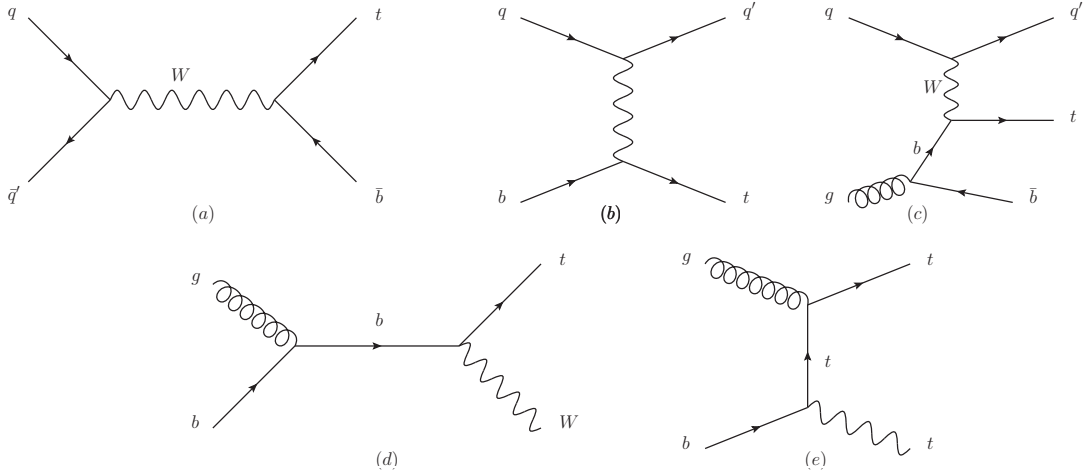


Figure 3.6: Feynman diagrams of leading order single top production processes in the s-channel (a), t-channel (b) and (c), and associated tW production (d) and (e).

3.1.3 W/Z+jets background

$W + \text{jets}$ production presents a significant background to semi-leptonic $t\bar{t}$ analyses. This background consists of events in which a real W boson is produced together with additional jets. Events in which these W bosons decay leptonically can provide a similar event signature after reconstruction to that of a semi-leptonic $t\bar{t}$ decay. In general, these processes can be removed from the signal selection because the final decay products in $W + \text{jets}$ events typically have lower energies than those from semi-leptonic $t\bar{t}$ decays, since the top quark has a high mass. Another characteristic of $W + \text{jets}$ events is that the jets are more likely to be light quark jets and therefore less likely to be b-jets than in $t\bar{t}$ events. Thus, $W + \text{jets}$ events can be separated to a large extent from the $t\bar{t}$ signal by using jet multiplicity, jet p_T and b-jet multiplicity.

Similarly, $Z + \text{jets}$ events can mimic $t\bar{t}$ events where the leptonic decay of a Z boson to a lepton and an anti-lepton takes place. This background can be distinguished from semi-leptonic $t\bar{t}$ decays by vetoing on a second lepton and imposing jet multiplicity requirements. Misidentification and misreconstruction of these leptons as jets, however, can result in such events mimicking $t\bar{t}$ events and passing the signal selection, although this contamination is small. Comparisons of data to Monte Carlo simulation, and the composition of the backgrounds, including $W + \text{jets}$ and $Z + \text{jets}$ events, will be shown in Section 8.1.

3.1.4 QCD background

The multijet background from QCD events presents a significant obstacle in many measurements at LHC, including this semi-leptonic $t\bar{t}$ analysis. Gluon-gluon fusion and quark-antiquark annihilation in proton-proton collisions can produce energetic jets. Although these processes have only two jets in their final state, higher order processes, including initial state radiation and final state radiation, can also produce additional jets, leading to potential mimicking of the semi-leptonic $t\bar{t}$ signal. The leptons required for this to happen can come from jets which are misreconstructed and misidentified as leptons, or real leptons in heavy flavour (b and c) jets. Unfortunately the cross section of these processes is several orders of magnitude larger than the signal cross section. Although the lepton (either fake or real) is rarely one that passes selection, the much higher QCD cross section means that its contribution as a background is significant.

In the muon+jets channel, only highly energetic jets ($p_T > 500 \text{ GeV}$) are capable of “punching through” from the calorimeters to leave tracks in the muon chambers. Such events can be removed by isolation requirements (since they deposit significant amounts of energy in the calorimeters). Events with real electrons and muons from heavy quark jets can be identified by the track quality requirements in the selection since they would not begin from the primary vertex and so would have a distinct track signature compared to prompt leptons.

On the other hand, the electron channel poses a more problematic QCD background, due mainly to the conversion of photons, whether produced at the interaction point or through

subsequent decays and radiation, into electrons and positrons. The identification and removal of such events is described in Section 5.3.3. However, the large uncertainty in the cross sections of QCD events, large contamination from higher order processes with additional jets in the signal region of this analysis and the difficulty in modelling such contributions, lead to incorrect event kinematics and significant disagreements in the QCD background distributions in data and in simulation. Therefore, the QCD background is modelled using a data driven method, described in Section 7.3.5, and then normalised to the number of events passing the signal selection in simulation. Comparisons of data to Monte Carlo simulation, and the composition of the backgrounds, including QCD multi-jet events, will be shown in Sections 7.3.5 and 8.1.

3.2 Monte Carlo Simulation

Monte Carlo event simulation is used to simulate the aforementioned signal and background processes, and to compare the theoretical knowledge of the SM incorporated therein with real data. Differences between simulation and data would then indicate the presence of new physics processes which are not present in the theoretical assumptions made in the SM, or perhaps that the simulation process is sub-optimal. Different event generators exist, and samples produced by the MADGRAPH, PYTHIA, POWHEG and HERWIG generators are used in this analysis.

Different generators have characteristics which optimise them for different aspects of the production chain: the initial hard process scattering of the partons in the hadrons (protons), decay showers of the resulting partons, subsequent decays of resulting hadrons and hadronisation of resulting partons, and the underlying event (the parton showers produced from soft scattering between the remaining contents of the colliding protons).

3.2.1 MadGraph

MADGRAPH [28], a matrix element generator, works by taking into account leading-order (LO) Feynman diagrams for a given process and subsequently calculating the matrix elements

for these diagrams with up to three additional partons, over all phase space. The PDFs are used to generate the incoming partons. The cross section of the process and various subprocesses and the structure and contents of the event (such as the partons present and their kinematics) are thus produced. Proton fragmentation and subsequent hadronisation are simulated using the PYTHIA generator, as explained in Section 3.2.3.

The PYTHIA parton showers are then matched with the matrix element partons via the MLM method [80]. This method ensures that parton showers with a highly energetic jet are not double counted. Matching is carried out between parton showers in the hadronisation and the partons from the matrix element calculations. The matching is carried out by satisfying distance requirements in η and ϕ between the parton and parton shower. Only if the parton has a transverse energy above a certain threshold, is it considered for this matching, and if an event contains either too few or too many matching jets, it is discarded. The matching threshold is process dependent as follows:

- $t\bar{t}$: 20 GeV
- $W + \text{jets}$: 10 GeV
- $Z + \text{jets}$: 10 GeV

3.2.2 MC@NLO

The MC@NLO [70, 69] generator is a next-to-leading-order (NLO) generator. These additional corrections provide more accurate simulations of physics processes in comparison to LO generators by including additional partons from the initial hard process in the final state of the event.

3.2.3 PYTHIA

PYTHIA [106] then simulates the proton fragmentation, the subsequent hadronisation of the resulting quarks and gluons resulting from the hard interaction and the underlying event. PYTHIA is considered to be particularly good at multi-particle simulation, modelling

fragmentation and hadronisation. Therefore, PYTHIA carries out these steps after the initial partons are provided by other generators in most simulated samples, if it is not already used for the whole production chain (as is common in QCD multijet simulations).

3.2.4 POWHEG

One problem with the MC@NLO generator is that some events are given negative weights when matching the NLO QCD multijet calculations to parton showers. The Positive Weight Hardest Emission Generator, POWHEG [68, 98, 26], is another NLO generator which generates the hardest processes in the event first, which avoids double counting of softer radiation produced later in the chain, which is the cause of negative event weights.

3.3 Theoretical Systematics

3.3.1 Factorisation and Renormalisation Scale & Matching Threshold

old

The models used in generators use an essentially arbitrary choice for the threshold transverse energy above which matrix-element partons are matched to parton showers. To account for the systematic uncertainties as a result of this threshold, simulated samples in which this matching threshold is increased and decreased by a factor of 2 (see Table 3.2) are used to estimate the effect of this uncertainty on this analysis.

Similarly, the factorisation (μ_F) and renormalisation (μ_R) scale, or Q^2 , at which α_S is evaluated, is varied up and down from the nominal value of $Q^2 = m^2 + \sum p_T^2$ by a factor of 2 (see Table 3.2) to produce simulation samples to evaluate the systematic uncertainty resulting from this. The uncertainty resulting from these variations in both $t\bar{t}$ and $W/Z + \text{jets}$ processes is evaluated.

Process	Matching Threshold			Factorisation Scale		
	nominal / GeV	+ variation / GeV	- variation / GeV	nominal / GeV	+ variation / GeV	- variation
t <bar>t</bar>	20	40	10	$Q^2 = m_T^2 + \Sigma p_T^2$	$(2Q)^2$	$(0.5Q)^2$
W + jets	10	20	5	$Q^2 = m_W^2 + \Sigma p_T^2$	$(2Q)^2$	$(0.5Q)^2$
Z + jets	10	20	5	$Q^2 = m_Z^2 + \Sigma p_T^2$	$(2Q)^2$	$(0.5Q)^2$

Table 3.2: Threshold transverse energy for matching systematic uncertainty

3.3.2 Detector Simulation (GEANT)

Following creation of the physics processes in proton-proton collisions, the simulated events are then put through a detector simulation to evaluate the interaction of the detector with the products of collisions. The Geometry and Tracking (GEANT) package [24, 27] is used for this purpose, which simulates what happens to particles as they travel through the geometry of the detector, including simulation of the detector components and materials and the interaction of particles with the detector such as particle tracks and energy deposits.

4 | The CMS Detector at the LHC

4.1 Introduction to the LHC

The CMS general-purpose detector is one of four detectors located around the LHC, approximately 100 m below ground level. The CERN accelerator complex and the locations of the various experiments around the LHC are shown in Figure 4.1.

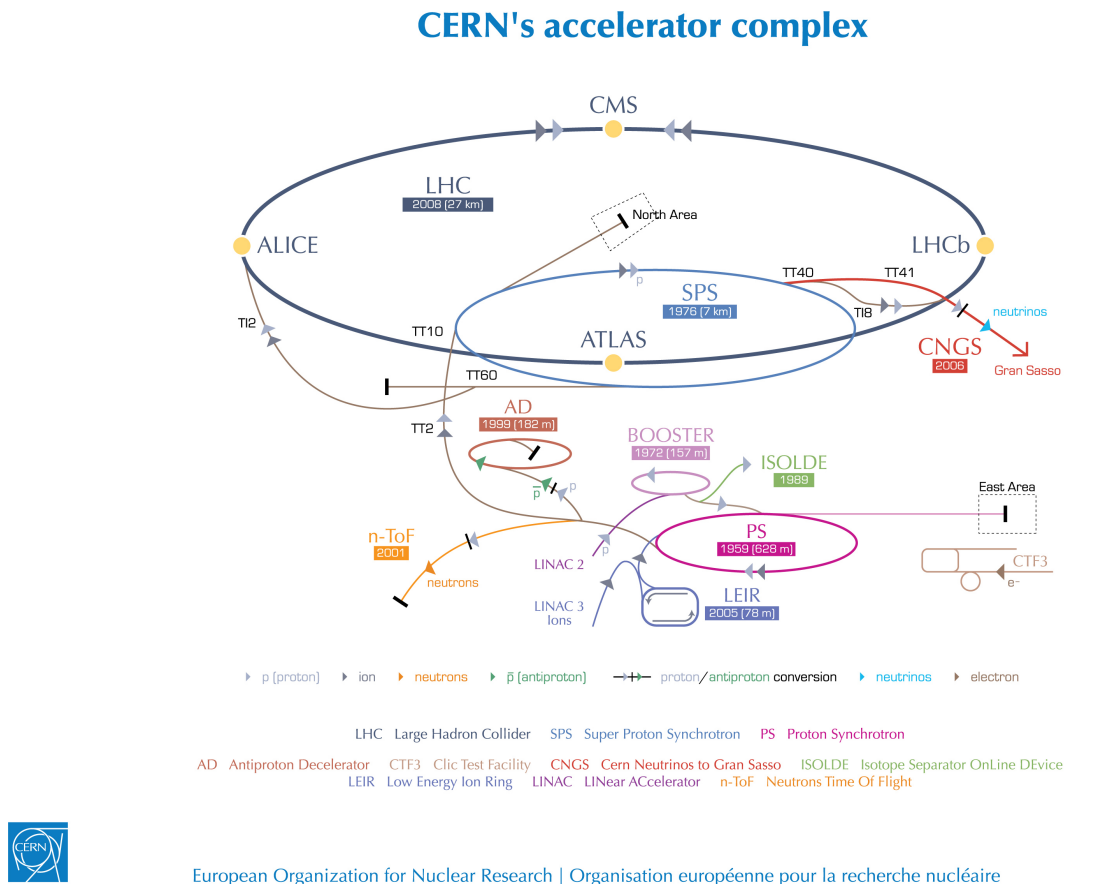


Figure 4.1: Schematic of CERN accelerator complex including the LHC and experiments. CMS is located at Point 5 on the LHC ring.

The 27 km circumference LHC is designed to collide two proton beams, each composed of 2808 bunches, at a design energy of 7 TeV per beam (meaning a 14 TeV centre-of-mass energy, \sqrt{s} , in collisions) with a luminosity \mathcal{L} of $10^{34} \text{ cm}^{-2}\text{s}^{-1}$ at a collision rate of 25 ns

4. The CMS Detector at the LHC

(40 MHz). Each event that is recorded in the CMS detector is one crossing of the bunches of protons of which the beams are comprised. During the first part of Run 1 in 2011 the machine ran at a centre-of-mass-energy of 7 TeV at a bunch spacing of 50 ns (leading to 8 proton-proton interactions per bunch crossing) and CMS recorded a peak instantaneous luminosity of $3.7 \times 10^{33} \text{ cm}^{-2}\text{s}^{-1}$. In 2012 the centre-of-mass energy was increased to 8 TeV (21 proton-proton interactions per bunch crossing) and CMS recorded a peak instantaneous luminosity of $7.7 \times 10^{33} \text{ cm}^{-2}\text{s}^{-1}$. Since Run 2 began in May 2015 after Long Shutdown 1, the LHC has been operating at a collision energy of 13 TeV and CMS recorded a peak instantaneous luminosity of $4.7 \times 10^{33} \text{ cm}^{-2}\text{s}^{-1}$ at a collision rate of 25 ns initially, before switching to 50 ns. The design collision energy and luminosity are scheduled to be attained later in Run 2 and after Long Shutdown 2 (in 2019) respectively. 6.1 fb^{-1} and 23.3 fb^{-1} of data was delivered to CMS during the 2011 and 2012 data taking periods respectively; Figure 4.2 shows the increase in integrated luminosities delivered to CMS over time during 2010–2012.

The acceleration process, or fill, begins with a tank of hydrogen (see Figure 4.1). After stripping electrons off the hydrogen atoms using an electric field, the remaining protons are inserted into the Linear Accelerator 2 (LINAC2) which accelerates them up to 50 MeV. From here, the proton beam is injected into the Proton Synchrotron Booster (PSB) which increases the energy to 1.4 GeV, followed by the Proton Synchrotron (PS) which accelerates the beam to 25 GeV and the Super Proton Synchrotron (SPS) where the beam energy reaches 450 GeV. Finally, the protons are injected into the LHC where two beampipes carry the beams in a clockwise and an anti-clockwise direction while accelerating them up to the required collision energy. Filling the LHC rings takes approximately 4 minutes, followed by approximately 20 minutes until the beams reach energies of 4 TeV (during 2012 data taking). The beams are accelerated by radio frequency cavities, and superconducting dipole magnets bend the beams to maintain their trajectory around the LHC beampipe. Once the collision energy has been attained, the beams are “squeezed” to focus them into a cross sectional area of approximately $16 \mu\text{m}^2$ using superconducting quadrupole magnets. The longitudinal distribution (i.e. in the

z direction) of collision vertices take the form of a gaussian with a width of 3–5 cm, varying from fill to fill, and also gradually with time during fills [6]. Collimators act to scrape away protons, thereby maintaining beam losses to the superconducting magnets below the level that would cause quenching. The counter-circulating beams are brought into collision at the four main LHC experiments CMS, ATLAS, LHCb and ALICE. ATLAS, like CMS, is a general purpose detector, ALICE is specifically designed to investigate heavy ion collisions (as opposed to protons), while LHCb investigates b-meson physics.

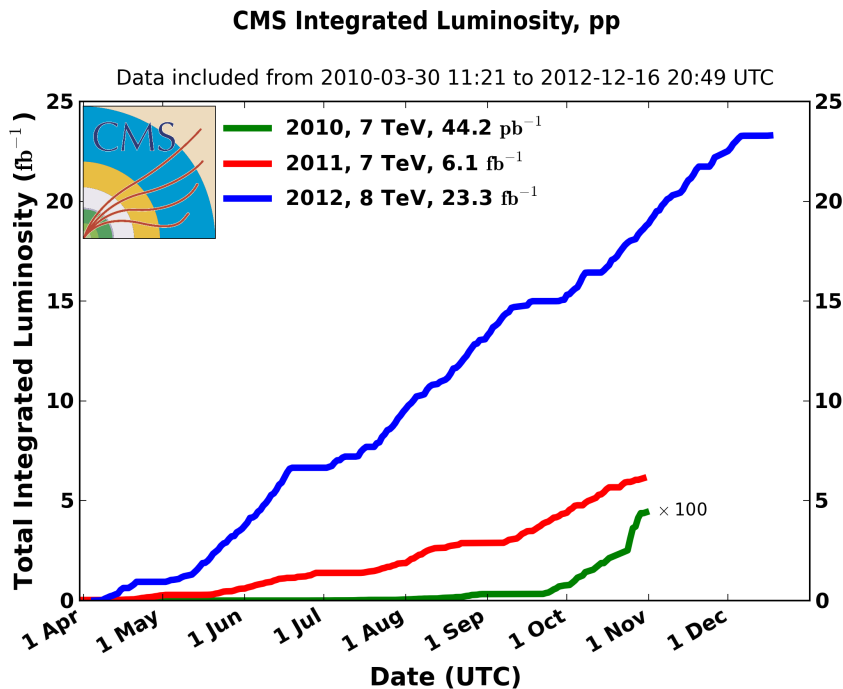


Figure 4.2: Cumulative luminosity delivered to CMS over time during 2010, 2011 and 2012 proton-proton data taking periods.

4.2 Overview of CMS

Compact Muon Solenoid is both the name of the detector at the LHC, and of the collaboration of people worldwide who work to build, operate, maintain and upgrade it, and to analyse the data it records.

CMS is a general-purpose detector, designed to be efficient at detecting new physics with a wide range of signals. The detector measures 14.6 m in diameter and 21.6 m in length, and weighs 12500 tonnes [39]. The different sub-detectors of CMS are arranged in concentric

4. The CMS Detector at the LHC

layers around the point of the beampipe at which the two beams of proton bunches collide, known as the interaction point (see Figure 4.3). As the products of any collisions that occur in the bunch crossing travel outwards from the interaction point, they pass through the sub-detectors depositing energy, resulting in signals being produced. A subset of the information from some sub-detectors (the calorimeters and muon chambers, described in Section 4.3) is then processed by a trigger while information from other sub-detectors is buffered on the detector.

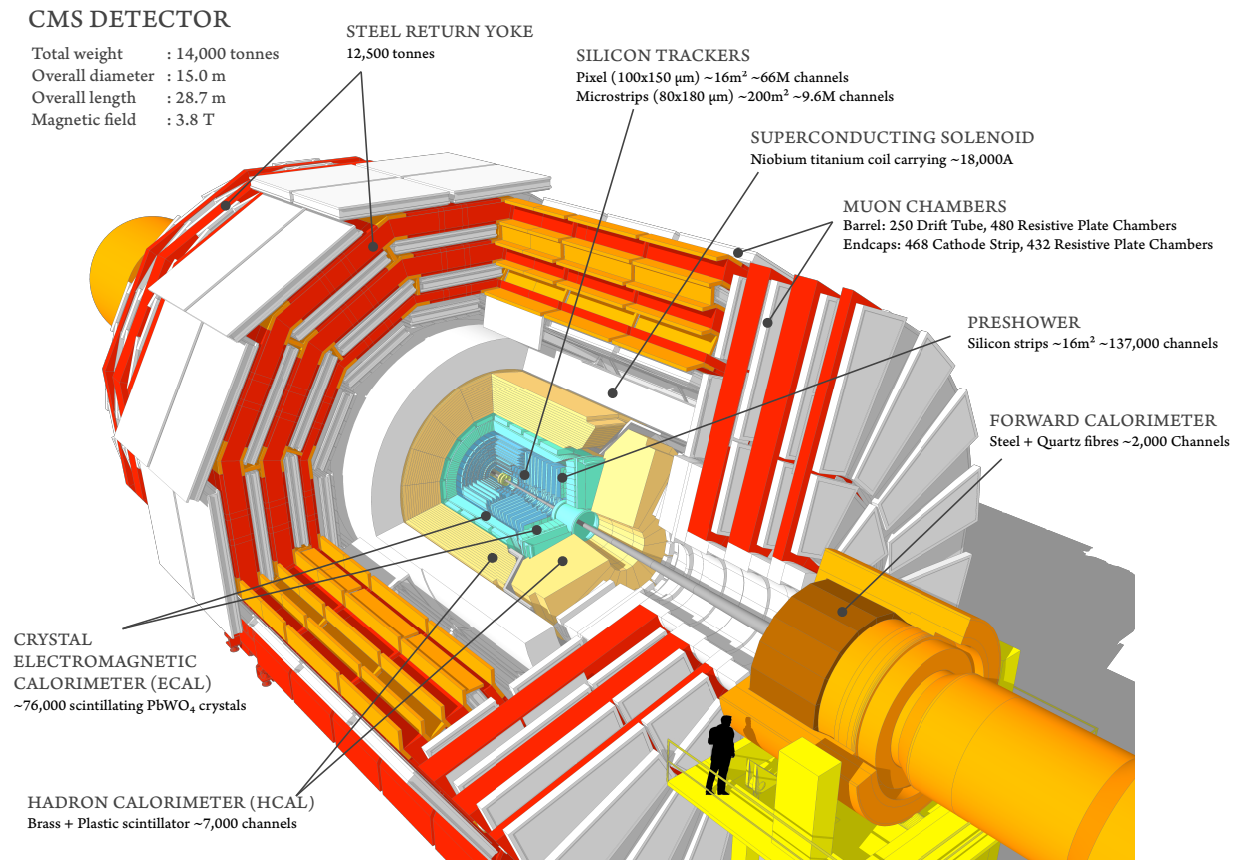


Figure 4.3: Diagrammatic sectional view of the CMS detector [105].

The design of CMS is based firstly around a superconducting solenoid magnet. Around and inside the magnet are the sub-detectors: the pixel and strip tracker, the electromagnetic calorimeter, the hadronic calorimeter, the return yoke for the magnet and the muon detectors. The coordinate system of the detector is designated with the origin as the intersection point of the two beams in the beampipe, the x-axis positive towards the centre of the LHC ring, the y-axis positive vertically upwards and the z-axis pointing along the beampipe in an

anticlockwise direction. The azimuthal angle, ϕ , is defined as the angle in the x-y plane, transverse to the beampipe starting from the x-axis. The polar angle, θ , is defined as the angle in the z-y plane starting from the z-axis (the beampipe). The angle θ is related to the pseudorapidity, η , by the formula $\eta = -\ln(\tan(\theta/2))$, so that η ranges from 0 at $\theta = 90^\circ$ to ∞ at $\theta = 0^\circ$ [109]. The two ends of the detector, at high $|\eta|$ values, are called the endcap regions while the central area at lower $|\eta|$ values is called the barrel region. The detector volume is often denoted in terms of ΔR , with the separation between two particles 1 and 2 being defined as

$$\Delta R = \sqrt{(\eta_1 - \eta_2)^2 + (\phi_1 - \phi_2)^2}. \quad (4.1)$$

4.3 Sub-Detectors

4.3.1 Tracker

The trajectories and charges of particles created in the proton-proton collisions need to be recorded for later use in particle reconstruction. This is achieved using the tracker section of CMS which consists of silicon sensors in two forms: pixels and strips. The purpose of the tracker within the CMS detector is to track the trajectory of charged particles as they travel out from the interaction point. An important requirement of the tracker is that material budget must be low in order to allow charged particles to pass through the tracker to outer sub-detectors while minimising multiple scattering, bremsstrahlung radiation, nuclear interactions and photon conversions. The tracker readout chips must also be capable of distinguishing in which bunch crossing a particle was produced (bunch-crossing identification), in order for the trigger to remove particles from previous bunch crossings (termed out-of-time pileup) and fully reconstruct events.

The tracker is split into two parts, with an inner silicon pixel detector and an outer silicon strip detector. A diagrammatic view of the tracker, including both pixels and strips, is shown in Figure 4.4. The inner pixel detector consists of three layers in the barrel region at distances of 4.4 cm, 7.3 cm and 10.2 cm from the beam line with two endcap discs at each

4. The CMS Detector at the LHC

end. Each pixel measures 100 μm by 150 μm . The entire pixel detector covers an area of only approximately 1 m^2 and contains 66 million pixels in total.

The strip tracker is comprised of ten layers in the barrel region at distances ranging from 20 cm to 1.1 m from the beampipe. The four inner layers (at distances of 26 cm, 34 cm, 42 cm and 50 cm from the beampipe) are collectively named the Tracker Inner Barrel (TIB), while the outer six layers (at distances of 61 cm, 70 cm, 78 cm, 87 cm, 97 cm and 108 cm from the beampipe) are known as the Tracker Outer Barrel (TOB). The endcaps consist of twelve discs, three of which correspond to the Tracker Inner Discs (TID) at z-distances from 75 cm to 100 cm, and nine to the Tracker End Caps (TEC) at z-distances between 120 cm and 280 cm [101]. The largest silicon detector ever constructed, the strip tracker contains about ten million channels and covers an area of approximately 200 m^2 [39, 109]. The operating temperature of the tracker during 2011 and 2012 was 7.4 °C and 0 °C respectively for the pixels, and +4 °C throughout for the strips [83, 36].

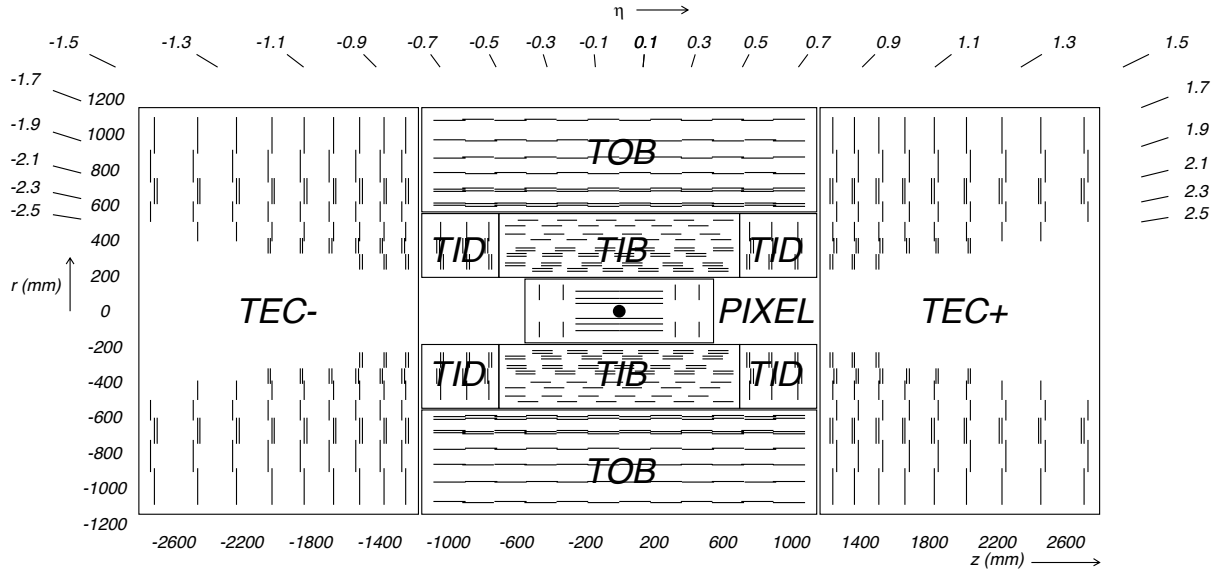


Figure 4.4: Cross sectional diagram of the CMS strip tracker; each line represents a detector module [109].

As charged particles travel through these silicon sensors, electron-hole pairs are produced that induce a current in the sensors and are processed by readout chips. This readout is carried out by the Analogue Pipeline Voltage 25 (APV25) chip. Offline algorithms then use the data relating to which strips and sensors received ‘hits’ to reconstruct the tracks of charged

particles and this information is later used for particle reconstruction and identification [39, 94]. The curving of particle tracks within a magnetic field also allows the calculation of the particle momentum and charge, $mv = RqB$, where mv is the momentum of the particle, R is the radius of curvature, q is the electric charge, and B is the magnetic field strength.

The required tracker characteristics of high granularity and high resolution, fast response to process the high data rate without losing potentially valuable information, radiation hardness and keeping detector material to a minimum to minimise scattering without minimising the signal, resulted in silicon being chosen to construct the tracker.

One of the advantages of using silicon over gaseous detectors is that silicon produces more charge carriers per unit of length travelled by a particle. The silicon sensors that make up the strip tracker in the CMS detector vary in thickness depending on their location. Sensors of 320 μm thickness are utilised in the TIB and TID, 500 μm in the TOB, and a mixture of both thicknesses is used in the TEC. Thicker sensors are used in the outer sections of the strip tracker in order to maintain a high signal to noise ratio, since the increased strip lengths in this region lead to increased electronics noise due to higher capacitance [39].

Silicon also allows fast signal transfer, of the order of about 10 ns, as the charge carriers travel quickly through silicon. Furthermore, the spacing between strips in a silicon sensor, known as the strip pitch, can be manufactured to be extremely fine (<20 μm). The strip pitches in the CMS strip tracker sensors vary from 80 μm to 205 μm , and there are fifteen distinct pitch-length geometries [40].

A further tracker requirement is low occupancy (the fraction of channels with a hit in an event was desired to be 1 % or lower at the nominal LHC luminosity) so that pattern recognition can be carried out efficiently and so that data to be read out is manageable. In order to help maintain such a low occupancy at the nominal LHC luminosity, the strip tracker has a high granularity, with strip lengths less than 20 cm and strip pitches less than 205 μm [101]. While high granularity is beneficial for high precision tracking, it also results in a high number of

channels, which in turn requires a large amount of electronics for readout and leads to a high heat load.

On a global scale, the tracker data is read out using a combination of interoperating systems. The data from the APV25 tracker readout chips is taken via optical fibres to 440 off-detector Front End Drivers (FEDs) (tracker FEDs make up 63 % of the total number of FEDs in CMS). The FEDs then forward the data to the online Data Acquisition System (DAQ). In addition, off-detector Front End Controllers (FECs) control the front-end electronics by means of approximately 350 control rings, including triggers, clock and monitoring [39, 62].

4.3.2 Electromagnetic Calorimeter

The electromagnetic calorimeter (ECAL), is a hermetic, homogeneous sub-detector constructed of scintillating crystals of lead tungstate (PbWO_4), and is the next layer outside the tracker. Any electromagnetic particles such as electrons or photons are absorbed by the ECAL crystals which then scintillate emitting a blue-green coloured light. These signals are then collected and converted to electrical signals by connected photodetectors, and processed by readout electronics.

The signals in the crystals are collected by avalanche photodiodes in the barrel region and vacuum phototriodes in the endcaps. The numbers of photoelectrons produced is dependent on temperature, with increasing temperature resulting in a decrease in the number of electrons at a rate of $-3.8 \pm 0.4\%/\text{ }^\circ\text{C}$. A cooling system is thus employed which maintains a stable operating temperature of the ECAL system to within $\pm 0.05\text{ }^\circ\text{C}$, with a nominal operating temperature of $18\text{ }^\circ\text{C}$ [39]. The energy resolution of the ECAL has been shown to follow $\sigma_E/E = 2.8\%/\sqrt{E} \oplus 12\%/E \oplus 0.3\%$ where the three constant terms come from stochastic fluctuations such as photostatistics, electronics noise and temperature stability and calibration uncertainties [47].

The barrel region of the ECAL consists of 61,200 crystals and extends up to a pseudorapidity η of ± 1.479 . Each individual barrel crystal is $25.8X_0$ thick, where X_0 is the radiation length (the mean distance over which a high energy electron loses all but $1/e$ of its energy

through bremsstrahlung radiation [99]). They have individual cross sectional dimensions of $22 \times 22 \text{ mm}^2$, and are tilted with their front-faces directed towards the nominal interaction point, as can be seen in Figure 4.5, leading to each crystal covering 0.0174×0.0174 in $\eta - \phi$ plane [4]. These crystals are divided into 36 groups, called supermodules, with each supermodule consisting of 4 smaller modules. The endcaps are comprised of 7,324 crystals, cover the range $1.479 \leq \eta \leq 3.0$ and are split into two halves known as “Dees”, each divided into operating segments of 40° each. The endcap crystals have slightly larger dimensions, having a thickness of $24.7X_0$ and cross sectional dimensions of $28.62 \times 28.62 \text{ mm}^2$ [39, 30]. Figure 4.5 shows the layout of the ECAL.

The crystals of high density (8.28 g/cm^3), short radiation length ($X_0 = 0.89 \text{ cm}$), and small Molière radius (a measure of the transverse dimensions of electromagnetic showers in a material [99]) of 2.2 cm lead to a compact calorimeter with fast response time (80 % of the light is emitted within 25 ns) and high granularity, capable of withstanding the radiation levels within CMS.

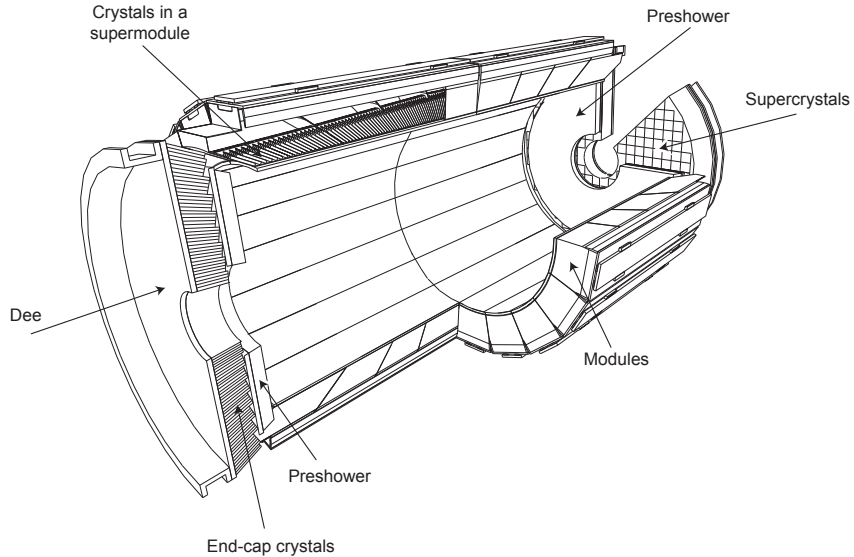


Figure 4.5: Diagram of the ECAL showing barrel supermodules, endcaps and preshower detectors [47].

An ECAL preshower, comprised of two lead plates each followed by a layer of orthogonal silicon strip sensors (thickness 350 mm, strip pitch 2 mm) is located between the tracker and ECAL endcaps to provide a higher spatial resolution than the ECAL. This helps to identify,

for instance, closely spaced photon pairs originating from pion decays which may otherwise be identified as a single high-energy photon based on ECAL energy deposits. As a photon passes through the lead, a shower of electromagnetic particles (e^+e^- pairs) is produced that are detected by the silicon layers to give a measure of the energy of the photon, while the orthogonal strips allow a position measurement. The measured energy can then be combined with the energy measured by the ECAL.

4.3.3 Hadronic Calorimeter

The next sub-detector outside the ECAL is the hadronic calorimeter (HCAL) which works in a similar way to the ECAL, in this case by absorbing hadron jets. The HCAL is located at a distance of 1.77 m to 2.95 m from the beamline, with an additional outer hadronic calorimeter also installed outside the magnet due to radial restrictions imposed by the magnet coil. The HCAL barrel (HB), outer (HO) and endcaps (HE) cover the $|\eta|$ range up to 3.0, with the forward HCAL (HF) placed at $|\eta|$ up to 5.2 increasing the coverage. Figure 4.6 shows a quarter of the HCAL endcap.

The HCAL is a sampling calorimeter, meaning it is composed of alternating absorber layers (made of brass) and scintillator layers (made of plastic). A hadronic particle produces a shower of secondary particles when it strikes an absorber layer. The scintillator layers in between the absorbers emit blue-violet light as the particles traverse them. This process is repeated several times as these secondary particles pass through successive layers of absorber and scintillator. The light in the scintillators is shifted to the green region of the spectrum and fed via optical fibres to readout electronics where photodetectors amplify the signal and the particle energies are measured by summing the measurements over all the layers of the hits in the HCAL, called a “tower”.

4.3.4 Superconducting Magnet

The magnet of the CMS detector is the largest and highest field strength superconducting solenoid constructed for a physics experiment in terms of bending power for physics and total

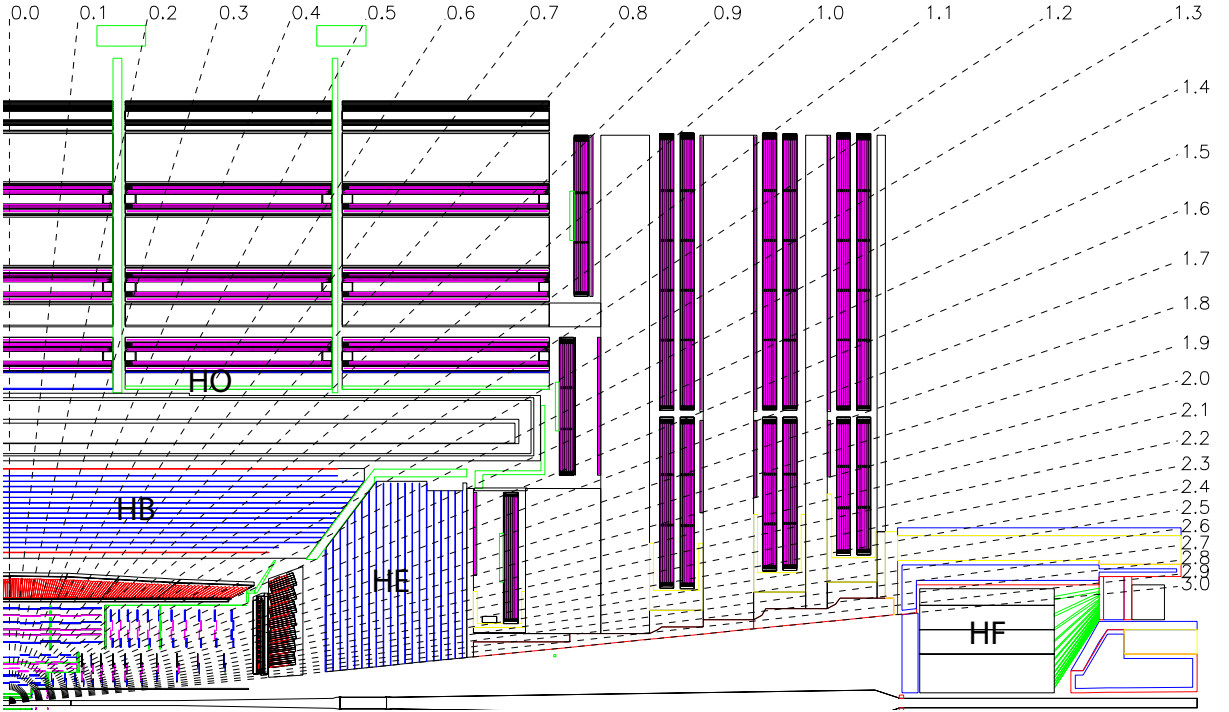


Figure 4.6: A longitudinal schematic of the CMS HCAL showing the location of the hadron barrel (HB), endcap (HE), outer (HO) and forward (HF) calorimeters [39].

stored energy [39]. It can produce a magnetic field up to 4 T (a field strength of 3.8 T is used in normal operation) with a stored energy of 2.7 GJ [109]. The cold bore, cooled to 4.5 K using liquid helium, has dimensions of 12.5 m length and 6 m diameter, and weighs 220 tonnes [64]. Due to design constraints and structural requirements, the magnet itself provides some of the structural strength both to support itself and to withstand its own magnetic bursting force on the coil [39].

The cold bore, pictured in Figure 4.7 in the CMS assembly hall, is enclosed in a steel return yoke weighing 10,000 tonnes with the aim of containing and returning the magnetic field. The yoke is interspersed with the muon chambers and is made up of 5 barrel segments and 6 endcap discs. The magnet was designed in a manner such as to facilitate assembly at ground level prior to lowering into the CMS experimental cavern, UX5. Despite the challenges involved in constructing such a powerful magnet, the high bending-power created by the high magnetic field was desirable in order to provide good momentum resolution of the tracking components.



Figure 4.7: Bore of the CMS solenoid magnet in vertical position in the CMS assembly hall, SX5, prior to installation [39]

4.3.5 Muon Chambers

Muons pass through all the previous inner sub-detectors, losing very little energy as they traverse them (around 1 MeV/mm on average through the whole detector), leading to the muon chambers being located outermost in the detector. There are, in fact, three types of muon detectors in use in CMS. The endcaps contain Cathode Strip Chambers (CSCs), the central barrel regions contain Drift Tubes (DTs), and both regions are equipped with Resistive Plate Chambers (RPCs). These systems, in combination with the silicon tracker, are used to determine the momentum of muons by taking advantage of their curved tracks due to the magnetic field. The different technologies are used due to the different numbers of particles expected in different areas of the detector and because of technological considerations regarding the physical areas to be covered [109]. Figure 4.8 shows a diagrammatic representation of one quarter of the CMS muon detectors. The CSCs are used in the endcaps to cover $|\eta|$ values between 1.2 and 2.4 that experience high muon rates and where the magnetic field of

the solenoid is high [109]. They take the form of four disc layers each made of 2 (inner layer) or 3 (outer three layers) concentric rings. They consist of volumes of gas in which positive wires are placed at right angles to negative copper strips. To relate these to the name given to these detectors, the positive wires are the anodes and the negative strips are the cathodes. As a charged particle passes through the gas it ionises gas atoms and the electrons that are knocked out travel towards the anode wires. At the same time the resulting positively charged ions in the gas travel towards the cathode strips. Since the wires and strips are at right angles to each other, the CSCs provide two position co-ordinates for the passing muon. The CSC detection mechanism is a fast process so their signals are used for muon triggering [39].

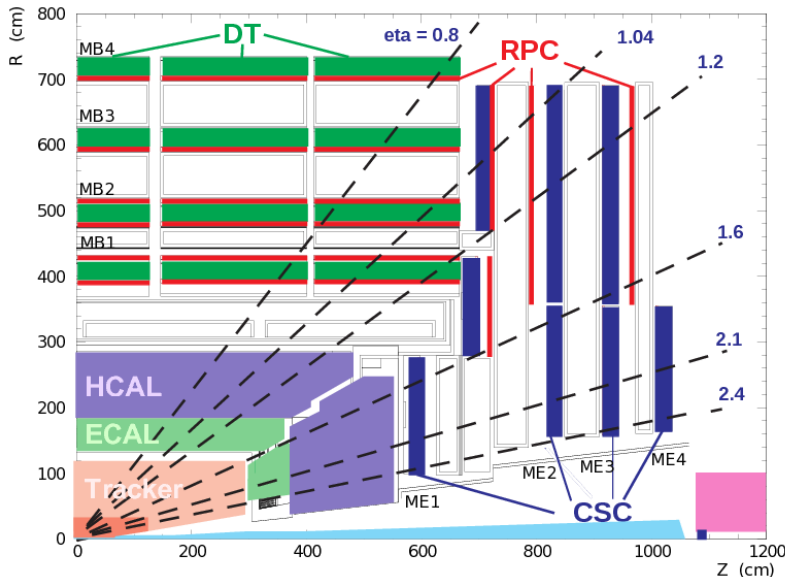


Figure 4.8: Schematic representation of a quarter of the CMS muon system [89]

The barrel region DTs cover $|\eta|$ values of less than 1.2, that encounter low rates of low transverse momentum muons [109]. The drift tube chambers are arranged in four cylindrical layers, or stations, among the layers of the magnet's iron return yoke and RPC layers. The stations are slightly staggered to ensure that even a muon of high transverse momentum will be detected by at least three of the four layers. The drift tubes contain a mixture of argon (85 %) and carbon dioxide (15 %), and a positively charged stretched wire. As a particle with a charge traverses the volume of gas, atoms in the gas are ionised and the resulting free electrons travel along electric field lines towards the positive wire. By using the position

of the electron along the wire and the time taken for the wire to detect the electron, two coordinates of the muon position can be deduced. In comparison to the DTs and CSCs, the RPCs that complement them provide a better resolution in terms of time (1 ns) but a worse resolution in terms of position, and so provide additional trigger information. As their name suggests, they are constructed of plates, one negatively charged (cathode) and one positively charged (anode) and made of a plastic with high resistance. In a similar process to the other muon detectors, a gas that makes up the volume in between the plates is ionised by a passing charged muon. The resulting electrons create an avalanche of electrons by, in turn, ionising other gas atoms; this avalanche of electrons moves towards the anode and metal readout strips outside the plastic anode detect the signal for readout. The hit strips pattern allows a calculation of the muon momentum which is then fed to trigger algorithms.

4.3.6 Trigger and Data Acquisition

At the design bunch crossing frequency of 40 MHz and at the design luminosity of $10^{34} \text{ cm}^{-2}\text{s}^{-1}$, the expected number of proton-proton collisions per second is approximately 10^9 , translating to 21 proton-proton collisions per bunch crossing on average. Each bunch crossing produces approximately 1 MB of data, leading to 40,000 GB/s of data. This extremely large amount of data, which is impractical to record, means that a trigger system is required to filter the events in order to record only data that are of interest for physics analyses.

There are two levels to the CMS trigger, named Level 1 Trigger (L1) and High Level Trigger (HLT). These work with the electronics and readout systems in place in the detector to filter the events to a practically manageable amount for processing. In combination, these triggers reduce the data rate by at least a factor of 10^6 [39].

The L1 Trigger is a pipelined deadtimeless system comprised of calorimeter triggers, muon triggers and a global trigger that works on a combination of data from the former two. The decisions made by the L1 Trigger are carried out by custom-designed hardware processors, consisting mostly of programmable electronics such as Field Programmable Gate Arrays

(FPGAs) [74]. The data from a bunch crossing are held in pipeline buffers in the electronics on the detector (at the front end) whilst the information for the triggers is processed in the CMS service cavern (USC) and the decisions transmitted back to the front end. The maximum time allowed for this process for each event is $3.2\mu\text{s}$, which is the time taken for the signals to be transmitted via optical fibres from the detector to the processors, processing time, and transmitted back again. This time is known as the latency [109]. The L1 Trigger outputs events to the HLT at a rate of 100 kHz [39].

As mentioned, the trigger uses calorimeter and muon chamber data to reach a decision on an event within the required timeframe. Tracker data are not currently used since track reconstruction exceeds the amount of time allowed for the L1 trigger decision. Good trigger performance is related to the quality of the calorimeters and muon systems. Factors such as good momentum resolution of high momentum muons, good charge determination of muons, good ECAL energy resolution and good missing transverse energy resolution are required for the trigger to select interesting events. The trigger was designed as described in order to allow the CMS experiment to meet the goals of the LHC physics programme [39].

Unlike the Level 1 Trigger, the High Level Trigger (HLT) is software-based and runs offline in HLT processor farms of about a thousand commercial processors [109]. If the Level 1 produces an accept decision, the data which was stored in buffers in the front end electronics is read into readout buffers from where the DAQ system accesses it. The L1 output rate of 100 kHz corresponds to a data rate of approximately 100 GB/s. The HLT software processes these events in a computer farm that carries out fast processing of offline algorithms such as selections and object reconstructions to reduce the rate down to approximately 100 Hz. These accepted data are then stored on tape. The HLT algorithms are designed based on the principle of minimising the number of objects that need to be reconstructed in order to arrive at a decision. Events are discarded as early as possible, leading to the HLT consisting of many virtual levels that progressively use more information from, first, the muon chambers and calorimeters, followed by pixel tracker data, and finally full tracker information [109].

Figure 4.9 shows the variation in trigger rates with increasing muon transverse momentum at

luminosities of $2 \times 10^{33} \text{ cm}^{-2}\text{s}^{-1}$ and $10^{34} \text{ cm}^{-2}\text{s}^{-1}$. The rates for different trigger levels are shown. The L1 trigger rate begins to flatten out as the p_T threshold increases because the lack of tracker information at L1 means that low momentum muons mis-measured as having high momentum are not removed. Thus, increasing the threshold would have no discernible effect on reducing the trigger rates while reducing physics performance by rejecting desirable events. In comparison, the L3 trigger rate, which includes tracker information, continues to decrease at high muon momenta, and is able to maintain the rate at the desired level.

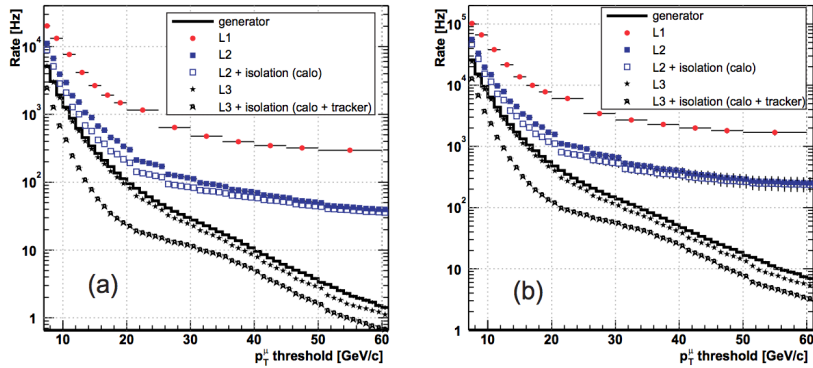


Figure 4.9: Single muon high level trigger rates at (a) $\mathcal{L} = 2 \times 10^{33} \text{ cm}^{-2}\text{s}^{-1}$ and (b) $\mathcal{L} = 10^{34} \text{ cm}^{-2}\text{s}^{-1}$ [53].

A more detailed description of the data acquisition (DAQ) system can be found in [39] and [109].

4.4 Upgrades

The CMS experiment, along with the LHC and the other detectors are in a long term programme of upgrades and maintenance. By 2023 the luminosity provided by the LHC is expected to be $2 \times 10^{34} \text{ cm}^{-2}\text{s}^{-1}$ [56]. The various runs and shutdowns until 2023 are collectively referred to as Phase 1. In phase 2, or after 2023, long shutdown 3 is also planned to bring further improvements and upgrades to the performance of the LHC, after which the luminosity of the LHC is expected to reach $5 \times 10^{34} \text{ cm}^{-2}\text{s}^{-1}$. The machine in this state will be known as the high luminosity LHC, HL-LHC (also sometimes referred to as Super LHC, SLHC).

Naturally, the above dates and schedules are the latest best estimates and are liable to change

over time, particularly those further in the future, as work progresses.

5 | CMS Computing and Offline

5.1 CMS Computing

The CMS offline computing infrastructure takes on the workload of transferring accepted data from the triggers to both permanent and temporary storage, of processing this data for subsequent analysis, in addition to the production of simulated CMS data. The resources needed to process the high volumes of data involved require a distributed computing system. The Worldwide LHC Computing Grid (WLCG) infrastructure, an international collaboration of LHC experiments and computing centres, is employed to carry out these tasks.

CMS computing resources are primarily divided into three tiers. Tier 0 (T0) consists of only one site, at CERN itself. The T0 centre has as its main aim to take accepted data from the detector and transfer it to permanent storage on tape. Tier 0 computing is also responsible for reconstructing the initial RAW data into smaller formats, by passing events through modules to produce physics objects (like electrons and jets) using algorithms to reconstruct tracks in the silicon tracker, clusters of deposits in the calorimeters, primary and secondary vertices, determine particle identification and to correct for detector characteristics such as non-functioning components (see Section 5.2 onwards for more details on data formats). From the T0 centre, copies of the data in RECO and RAW format are transferred to T1 centres around the world. Owing to its crucial role in ensuring the reliable transfer of RAW and RECO data, T0 resources are not available for analysis by CMS users. There are seven Tier 1 centres located in various countries within the CMS collaboration. The UK T1 centre is located at the Rutherford Appleton Laboratory in Harwell, near Oxford. T1 centres provide reliable computing resources for data storage and processing. RAW data is spread between them, providing a second copy of the RAW data stored at CERN. The second reconstruction step, termed REREKO, is also carried out at T1 centres, in addition to the production of

simulated data. These can then be provided to any of the Tier 2 centres at CMS institutes (typically universities) where they may be temporarily stored. T2 centres are also generally used to run users' final analyses and produce simulations [39, 109].

5.2 Event Data Model

Reconstructed data from CMS uses a data model based around an event, called the Event Data Model (EDM), where one event is one crossing of proton bunches at the centre of CMS that passes the triggers. This model is created and manipulated within a CMS software framework (CMSSW) [55] written in C++, with the event and related objects in the object-oriented data analysis framework ROOT [35].

The iterations of data from the initial recorded information to subsequent, more compact formats, are produced by passing events through a sequence of modules. The arrangement of this data takes the form of several layers, with the first of these being RAW. This level contains the full information from the event in CMS and occupies approximately 1.5-2 MB/event. More information than is necessary for user analyses is included at this level, and so the majority of CMS users will not use this data format. Reconstructed level data (RECO) is slightly smaller in size (approximately 0.5 MB/event) and is essentially a compressed subset of the RAW data after modules performing reconstruction have been run.

The third level, Analysis Object Data (AOD), is the smallest of the data formats, requiring approximately 100 kB/event, which is small enough to allow the entire AOD data to be stored at computing centres worldwide. AOD format is a subset of the RECO data, and is produced by further reducing RECO, leaving only high level physics objects (e.g. electrons, jets) which is adequate for most physics analyses.

In the differential cross section analysis presented in this thesis, this AOD data is processed using the Bristol Top Group's NTupleProduction code [92] to produce private ntuples which are yet again smaller in size, at approximately 3 kB/event. These ntuples are then converted to simple ROOT histogram files after applying the required selection criteria and corrections

in the BristolAnalysisTools [90]. Scripts written in Python in DailyPythonScripts [91] are then used to produce final results plots and tables.

5.3 Object Reconstruction and Identification

The process of producing a physics object such as an electron, photon or jet, from the data recorded by CMS is known as reconstruction and is carried out by modules known as EDProducers within CMSSW. The three-step process of reconstructing high level objects consists of local reconstruction within a sub detector, global reconstruction using data from the whole CMS detector, and a final stage combining reconstructed objects from the first two stages. The reconstruction technique used in the majority of CMS analyses is called Particle Flow (PF) [3]. The PF algorithm uses information from all of the sub-detectors in CMS to identify and reconstruct and identify all stable particles produced from a proton-proton collision. There is no lower threshold applied to PF objects, but this is dependent on the resolution of each of the sub-detectors.

5.3.1 Track Reconstruction

Algorithms performing local track reconstruction execute a scan to identify tracker modules that receive a higher than threshold signal. Clusters are then constructed by adding adjacent strips or pixels to the originally identified seed strip or pixel to provide a measurement of the hit position. In order to reconstruct complete tracks to obtain the trajectory and momentum of the charged particle, these clusters are then input to track finding algorithms. These algorithms are based on specific requirements, such as high or low transverse momentum tracks, and are collectively known in CMS as the Combinatorial Track Finder (CTF).

Multiple passes of the CTF reconstruction software are carried out to reconstruct tracks, in a process called iterative tracking. The earliest iterations identify tracks that are easy to find such as high p_T tracks originating near the interaction point. As these tracks are reconstructed, the corresponding hits are removed from consideration in subsequent iterations, making it simpler for later iterations to identify tracks that are more difficult to find such as

those of displaced particles or with low p_T .

Six iterations are carried out in total, and each iteration can be split into four steps. Seeds are created using 2 or 3 hits to produce initial track candidates. The seed gives an estimate of the trajectories of the potential track candidates. A Kalman Filter [71, 108] based track finding algorithm then looks for further hits along an extrapolated path of the seed trajectory. A track fitter is then run using information from the previous steps to produce final values for trajectory parameters. The fourth and final step then rejects tracks which fail specified quality checks [50].

5.3.2 Pileup Subtraction

When reconstructing an event in CMS, all vertices (points from which multiple tracks originate) in the event must be reconstructed. By ordering the vertices by the sum of the transverse momenta of their tracks, it is possible to identify the vertex of interest for physics analyses, known as the primary vertex (PV), as the vertex with the largest transverse momentum. The particle flow algorithm reconstructs objects, starting with those coming from the primary vertex, followed by other vertices (known as pileup). The reconstructed objects from the PV can be affected by the number of other vertices present in the event. For example, the jet momentum and lepton isolation could both increase with high pileup. This can, in turn, lead to signal events not passing selection requirements because a truly isolated lepton from the PV may appear not to be isolated. In addition, a larger number of events from background processes may pass selection requirements due to low energy jets appearing to have a higher energy. Hence, pileup subtraction, the removal of charged particles coming from vertices other than the PV is implemented to reduce these effects.

Neutral particles, however, pose a more difficult problem since they leave no tracker information for the reconstruction algorithms to easily identify their origin. One method of removing such particles from an event, known as the $\Delta\beta$ correction, uses the fact that the estimated average energy in an event from neutral particles from secondary vertices is half that from charged particles from secondary vertices. Thus, it can be estimated that 0.5 times the

charged particle energy comes from neutral particles from secondary vertices. The corrected energy is calculated by Equation 5.1, where $\Delta\beta = 0$.

$$E_{\text{corrected}} = E_{\text{charged hadrons from PV}} + \max(0, (E_{\text{photons+neutral hadrons}}) - \Delta\beta \cdot E_{\text{charged hadrons from PU}}) \quad (5.1)$$

The second method, known as ρ correction, subtracts an average transverse momentum coming from pileup per unit area. While the two methods produce similar results, the ρ correction is used to correct the electron isolation and the $\Delta\beta$ correction is used to correct the muon isolation in the differential cross sections analysis presented in this thesis, as recommended by the CMS TOP physics analysis group.

5.3.3 Electron Reconstruction

ECAL local reconstruction algorithms calculate the time of arrival, position and the energy of deposits. After grouping together deposits in neighbouring crystals to form clusters, deposits are then matched to deposits in the HCAL, forming a Calo Tower. Electrons are, typically, completely stopped in the ECAL and deposit their energy in a narrow cluster of crystals.

However, electrons can interact with the material between the interaction point and the ECAL, emitting a photon via bremsstrahlung radiation. Similarly, photons can convert to an electron-positron pair (e^+e^-). Both of these processes result in ECAL deposits with a larger spread in ϕ because of the strong magnetic field in the inner section of CMS containing the tracker. In the case of photons, several clusters are grouped together to form superclusters, which are then corrected for their energies to obtain the energies of the original photon [87].

Electron reconstruction in the ECAL is carried out by two methods. The first matches superclusters with a trajectory compatible with two or three pixel detector hits and the interaction point. The second matches the supercluster to tracker tracks to identify electrons (and in the case of electrons emitting bremsstrahlung radiation, tracks with a low number of hits) [5]. Combining the seeds from the two methods, a Gaussian-Sum Filter (GSF), a

generalisation of the Kalman Filter (KF) algorithm, is used to reconstruct electron paths [21].

Since other objects can leave similar signatures to electrons in the detector, such as jets or electrons from photon conversions, candidates are required to satisfy additional requirements of identification and isolation. Several electron identification methods exist and are used in CMS analyses. The top cross sections analysis in this thesis uses the multivariate identification (MVA ID). As the name suggests, this approach uses a multivariate analysis to produce a discriminator value, with higher values indicating a higher likelihood for a candidate to be a real electron. The MVA ID algorithm is optimised for identifying electrons from W and Z boson decays, and separately for triggering and non-triggering electrons [5]. The MVA ID algorithm takes the following track, track quality, and supercluster variables as input:

- The measured bremsstrahlung fraction f_{brem} , based on the change in track momentum between the vertex and the outermost hit.
- The χ^2_{GSF} of the GSF track.
- The χ^2_{KF} of the GSF track.
- The number of KF track hits.
- $\Delta\eta_{vtx}$, the distance in η between the supercluster and the track at the vertex.
- $\Delta\phi_{vtx}$, the distance in ϕ between the supercluster and the track at the vertex.
- $\Delta\eta$, the distance in η between the supercluster and the extrapolated track.
- $\Delta\phi$, the distance in ϕ between the supercluster and the extrapolated track.
- $\sigma_{i\eta i\eta}$, the cluster shape in η .
- $\sigma_{i\phi i\phi}$, the cluster shape in ϕ .
- The width in η of the supercluster
- The width in ϕ of the supercluster

- $1 - \frac{E_{1 \times 5}}{E_{5 \times 5}}$, 1 minus the ratio of the energy in the central 1×5 strip of the 5×5 electron cluster, to its total energy.
- $\frac{E_{3 \times 3}}{E_{supercluster(raw)}}$, the ratio of the energy in a 3×3 electron cluster to the raw supercluster energy.
- H/E , the ratio of the energy in the HCAL to the energy in the ECAL.
- $E_{supercluster}/p$, the ratio of the energy of the supercluster to the momentum of the associated track.
- $\frac{1}{E_{ECAL}} - \frac{1}{p}$, the inverse of the ECAL energy minus the inverse of the momentum of the associated track.
- $\frac{E_e}{p_{out}}$, the ratio of the electron cluster energy to the outer track momentum.
- $\frac{E_{preshower}}{E_{supercluster(raw)}}$, the ratio of the preshower energy to the raw supercluster energy.
- η of the supercluster.
- p_T of the associated track.
- d_{xy} , the transverse impact parameter, and the 3D impact parameter.

The isolation of an electron, defined as the activity within a cone surrounding the electron, is used as an additional criterion to select electrons, in particular to identify electrons promptly produced in a proton-proton collision. Such isolated electrons would have less activity in their vicinity than electrons from within a jet, which could originate from leptonically decaying b hadrons, and jets faking electrons. Two methods exist in CMS of calculating the isolation of a particle: detector based isolation and particle based isolation. The detector based method is defined in each sub detector as the sum of the momenta or energies in a cone of $\Delta R = 0.3$ around the electron. The particle based method uses the total transverse energy of PF reconstructed particles within a cone of $\Delta R = 0.3$ and can remove activity coming from collisions other than the hard proton-proton interaction of interest. By normalising this isolation to the momentum or energy of the electron, a relative isolation is obtained, relating the cone activity to the electron. Termed PFRelIso, this method of calculating relative

isolation is used in the cross sections analysis to select electrons.

In order to avoid the selection of electrons originating from a photon conversion, a veto can be placed on a second electron in the event. However, since the two electrons in a photon conversion may not necessarily have equal transverse momentum, i.e. one may have a very low p_T , such a veto may be insufficient, and so further techniques to identify conversion events are used. Firstly, since an electron from a conversion would be produced at some distance from the interaction point and in the detector material, eliminating candidates with missing hits in the pixel tracker helps to distinguish such electrons from promptly produced electrons. In events in which the conversion occurs in the beam pipe or if the electron is matched to unassociated pixel hits, this method can also be insufficient, so an additional track matching step is used. Tracks are matched in pairs and following geometrical cuts, can be removed if they appear to originate from a conversion [5].

5.3.4 Muon Reconstruction

Local reconstruction in the muon chambers provides hit position and time of arrival of a muon. This information from the DTs and CSCs is amalgamated to create muon track hits and segments, which are then used, together with track candidates from the RPCs, by the muon global reconstruction algorithms to reconstruct *standalone-muon tracks* [46]. An inner detector segment from the muon chambers is used as a seed for a Kalman Filter [71, 108] and possible trajectories are generated. By removing hits which are unlikely to have come from the track in question, the likely trajectory is constructed layer-by-layer. A final fit is carried out, including an extrapolation to the interaction point for greater momentum resolution.

Muons are also independently reconstructed in the tracker. These *tracker tracks* can therefore be combined with the aforementioned muon chamber information, where the magnetic field is only 2 T, to improve the p_T resolution of muons, as seen in Figure 5.1.

Two methods are employed to combine the information from the two sub-detectors. *Global muon* reconstruction matches a *tracker track* to a *standalone-muon track* and carries out

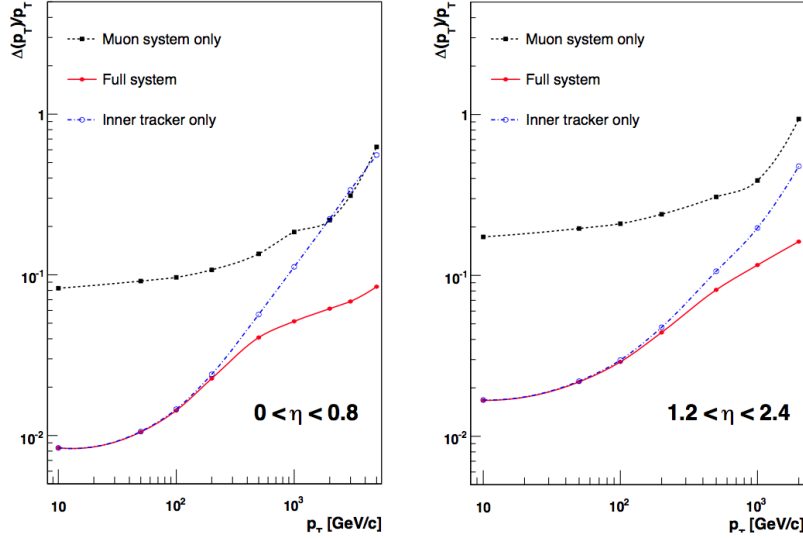


Figure 5.1: Muon transverse momentum resolution as a function of muon transverse momentum using the muon system only, using inner tracking only, and using both [45].

a fit of the resulting *global muon* track. The second method, *tracker muon* reconstruction, extrapolates tracker tracks above a threshold of $p_T > 0.5 \text{ GeV}$ and $p > 2.5 \text{ GeV}$, outwards to the muon chambers. A muon candidate is accepted if a DT or CSC matching track is found and the muon p_T is greater than 0.5 GeV. The *global muon* reconstruction method has a higher efficiency for muons of high p_T while the *tracker muon* reconstructs low momentum muons ($\leq 5 \text{ GeV}/c$) more efficiently [46]. In the case of the semileptonic differential cross sections analysis presented in this thesis, since the signal in the muon channel involves a single highly energetic muon, muons reconstructed using the *global muon* reconstruction method are used.

For triggering, the p_T of a muon is first estimated using the information available at Level 1 from all three types of muon detectors. At HLT level, the muon candidates from Level 1 are further refined using track finding and fitting, but still using only information from muon chambers, leading to Level 2 muons. As mentioned in Section 4.3.6, due to the time constraints required of the L1 trigger, full tracker data are not currently used. However, tracks of Level 2 muons are extrapolated into the tracker systems and a localised track finding algorithm is run to identify only nearby tracker hits. A track matching that of a Level 2 muon leads to a Level 3 muon.

5.3.5 Jet Reconstruction

As quarks produced in proton-proton interactions (except the top quark) hadronise [76], jets of particles are formed in the general direction of travel of the quark. The time of arrival, position and the energy deposited by hadronic objects are locally reconstructed in the HCAL. If the deposit matches an ECAL deposit, a Calo Tower is formed for later use in jet reconstruction algorithms.

The PF algorithm performs the reconstruction of particles, and the anti- k_t algorithm is used to perform the clustering of these particles into jets. The anti- k_t algorithm, explained in detail in [37], is one of several jet algorithms that exist in CMS to combine reconstructed particles into jets. It defines a distance d_{ij} between reconstructed particles as

$$d_{ij} = \min \left(\frac{1}{p_{T,i}^2}, \frac{1}{p_{T,j}^2} \right) \frac{(\eta_i - \eta_j)^2 + (\phi_i - \phi_j)^2}{R^2}. \quad (5.2)$$

$p_{T,i}$ and $p_{T,j}$ are the transverse momenta of the two particles i and j , η_i and η_j are the rapidities, ϕ_i and ϕ_j are the azimuth angles and R is the radius of the jet cone. The anti- k_t algorithm iteratively clusters together particles with the smallest $d_{i,j}$ between them until all PF objects in the event have been clustered into jets. Events will usually consist of a small number of high- p_T (hard) particles and a large number of low- p_T (soft) particles. The distance between hard particles is typically small, and the distance between softer particles is larger. Soft particles tend to cluster around hard particles first, before clustering with other soft particles.

While the PF anti- k_t jets show high jet matching efficiency on Monte Carlo simulation samples, corrections are applied based on the jet p_T and η to correct for mismeasurements in the detector and thereby improve the agreement between the reconstructed PF jet and the particle level generated jet. The factored approach to CMS jet energy corrections is comprised of three parts:

1. L1 Pile Up: corrects for additional energy from charged particles from pile-up in the

event 5.3.2.

2. L2 Relative Jet Correction: corrects the reconstructed energy to match the generated jet with respect to η .
3. L3 Absolute Jet Correction: corrects the reconstructed energy to match the generated jet with respect to p_T .
4. L2L3Residuals: reduces any residual differences between the reconstructed and generated jet due to simulation not being perfectly tuned to data. This correction is applied to data only.

In order to identify jets in the differential cross sections analysis, further identification criteria are used to reduce electronic noise, to reduce the number of electrons mis-identified as jets and, in so doing, to ensure the selection of high quality jets. The requirements, which are known as the loose PF Jet ID, are:

- at least one constituent particle
- the neutral hadron energy fraction (NHF) must be < 0.99
- for jets with $|\eta| < 2.4$, the charged hadron energy fraction (CHF) must be > 0
- the neutral electromagnetic energy fraction (NEF) must be < 0.99
- for jets with $|\eta| < 2.4$, the charged electromagnetic energy fraction (CEF) must be < 0.99
- for jets with $|\eta| < 2.4$, the number of charged hadronic constituents (NCH) must be > 0

B Jets

The process of identifying jets coming from b-quarks is known as b-tagging and is very important in top quark physics due to the decay of the top to a W boson and a b-quark. Effective b-tagging can therefore help to appreciably reduce background processes in an

analysis. A description of b-tagging, the several algorithms available in CMS, relevant event variables, and a performance comparison, is given in Chapter 6.

6 | b-tagging Study

The decay of the t-quark to a W boson and a b-quark necessitates a thorough understanding of these decay products in $t\bar{t}$ events. In particular, methods to identify jets coming from a b-quark, known as b-tagging, are commonly used to increase the efficiency of $t\text{-quark} \rightarrow b\text{-quark}W$ signal selection. CMS has several algorithms for b-tagging: TrackCounting (High Efficiency) and TrackCounting (High Purity) 6.2.1; JetBProbability and JetProbability 6.2.2; SoftMuon, SoftMuonByPt and SoftMuonByIP3d 6.2.3; SimpleSecondaryVertex (High Efficiency) and SimpleSecondaryVertex (High Purity) 6.2.4; CombinedSecondaryVertex and CombinedSecondaryVetexMVA 6.2.5. These algorithms produce a discriminator output for each jet which indicates how likely it is to be a b-quark flavour jet. In all cases, a more positive discriminator value indicates a jet that is more likely to be a b-quark flavour jet.

6.1 Observables used in b-tagging algorithms

The relatively long lifetime (of the order of 10^{-12}s) of b-quarks means that they travel a significant distance (of the order of a few mm) before decaying. This leads to events with b-jets possessing a secondary vertex at a distinguishable distance from the primary interaction vertex, as seen in Figure 6.1. Only tracking detectors are capable of providing the required spatial resolution to identify and measure properties of the secondary vertex and the associated tracks. This therefore means that only charged particle tracks in the b-jet can be used by b-tagging algorithms.

The impact parameter (IP) of a track is defined as the distance between the track and the vertex at the point of closest approach [2]. Figure 6.2 shows a schematic representation of the impact parameter for one single track. The IP measurement can be made in either the plane transverse to the beam line, or in three dimensions. The impact parameter significance

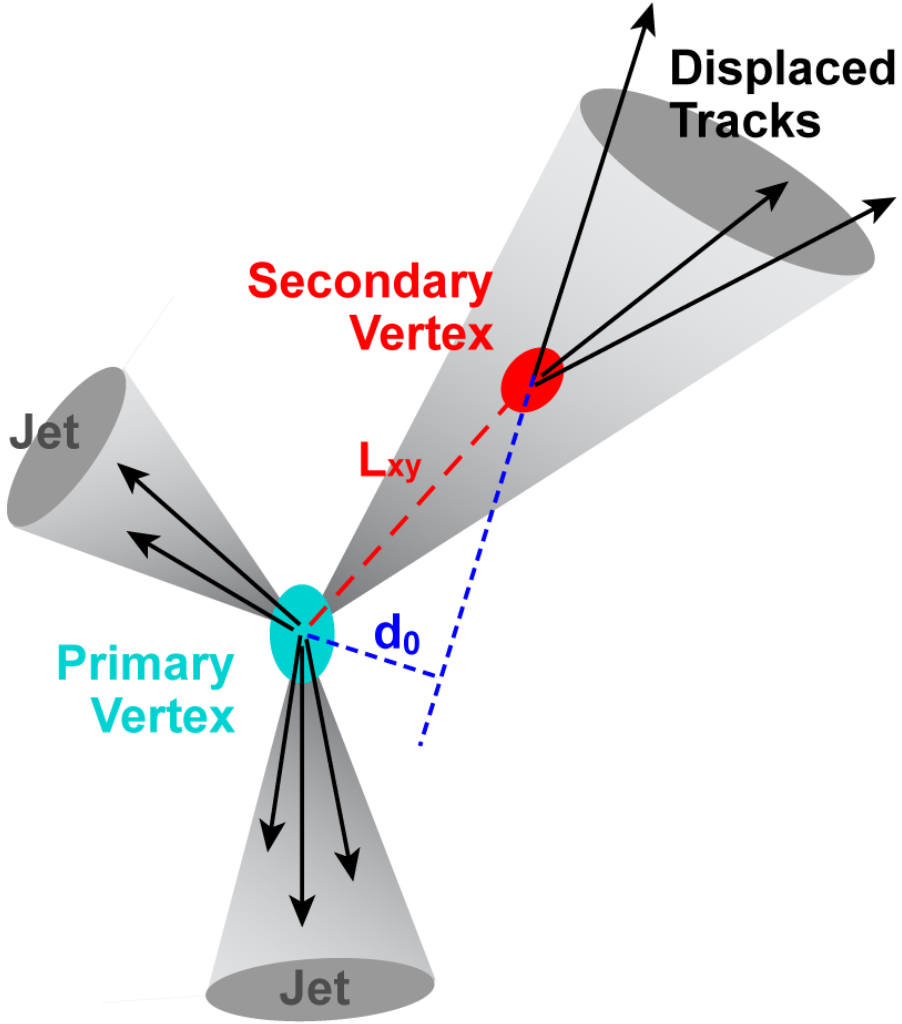


Figure 6.1: Graphical representation of an interaction originating at the primary vertex producing three jets, one of which is a b-jet with a secondary vertex [60].

(IP/σ_{IP}) is often used instead as an input to b-tagging algorithms to allow for the experimental resolution, due to the fact that the uncertainty on the IP value alone can be as large as the IP itself. The IP significance distribution of light jets (u, d, s) and gluon jets form a Gaussian distribution about a mean of zero and width of one, with a slightly extended tail due to tracks from particles in the jet with long lifetimes. The equivalent distribution for c-jets and b-jets show an asymmetric distribution at positive values due to the long lifetime of B and C hadrons, making the IP significance a useful parameter to distinguish between light and heavy flavour jets [1].

The signed IP is also used, in which the sign is obtained from the sign of the scalar product

of the IP vector and the jet direction, so that it is positive if the angle between the IP vector and the jet direction is less than 90° , and negative if the angle is greater than 90° . Tracks belonging in a b-jet would have an IP sign >0 , since the jet direction is an estimate of the direction of travel of the B hadron. However, the sign could be inaccurately calculated in cases with badly reconstructed jet directions or primary vertices, or badly measured track parameters [1]. Another parameter based on track length, the 3D decay length significance (the ratio of the three dimensional distance between the primary vertex and the secondary vertex, and the uncertainty on this value) is also used by some b-tagging algorithms.

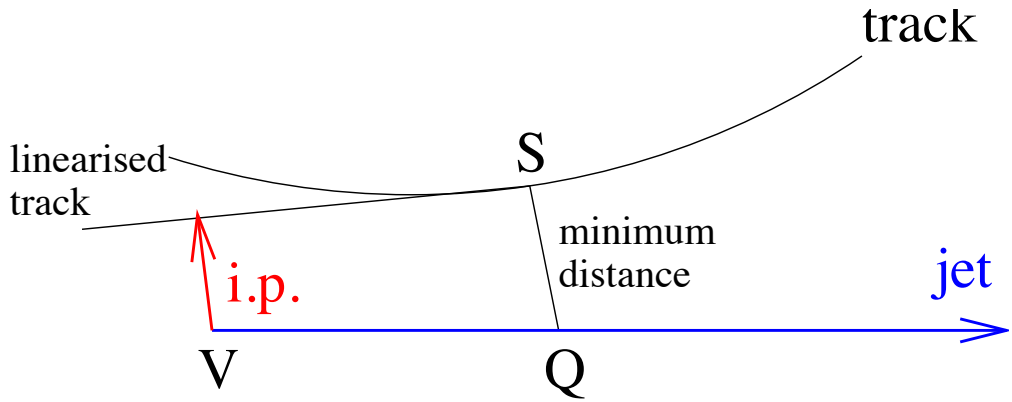


Figure 6.2: Graphical representation of a track impact parameter [2].

Identification of vertices in CMS consists of two stages: vertex finding and vertex fitting. Vertex finding deals with the creation of vertex candidates by grouping reconstructed tracks together. Vertex fitting then deals with obtaining the vertex parameters such as vertex position, track parameters, and quality of the fit. An adaptive vertex fitter [110] calculates an estimate of the vertex position and weights tracks based on their compatibility with the vertex. This fit is initially constrained to the interaction region to identify prompt tracks. After removing tracks with weights >0.5 , subsequent fits are carried out to identify potential decay vertices, until no new vertex is identified.

6.2 b-tagging algorithm descriptions

6.2.1 Track Counting

The simplest b-tagging algorithms available in CMS are the track counting algorithms [2], which positively identifies a b-jet if it contains N or more tracks with IP significance above some threshold value. They function by ordering all good tracks in a jet by order of decreasing IP significance, with the discriminator being the IP significance of the Nth track. The high efficiency version of this algorithm uses N=2, i.e. the second track, and the high purity version uses N=3, i.e. the third track [1].

6.2.2 Jet Probability

The “jet probability” algorithms [2] produce a discriminator based on the probability that the set of tracks come from the primary vertex: a high probability would indicate that the jet is not a b-jet, which would originate at a secondary vertex. These algorithms use all tracks as input and for each track define an individual probability of coming from the primary vertex. By combining these probabilities, a jet probability is produced, and the discriminator is the negative log of this confidence level [1]. The “jet B probability” variant is based on the confidence level that the four most displaced tracks in the jet originate from the primary vertex. The four most displaced tracks are used since the average number of tracks in a b-jet is approximately 5, and the reconstruction of tracks within jets has an average efficiency of approximately 80% [2] (the track reconstruction efficiency is $\approx 80\%$ for tracks of $p_T = 0.5 \text{ GeV}$, increasing to $\approx 90\%$ for tracks of $p_T = 10 \text{ GeV}$ [86]).

6.2.3 Soft Muon

The “soft muon” algorithms make use of global muons reconstructed in the vicinity of the reconstructed jet, which may indicate a semi-leptonic decay of B hadrons to a muon [66]. Two soft muon algorithms exist in CMS. The “soft muon by p_T ” algorithm uses the relative

p_T of the muon with respect to the jet ($p_{T(\text{rel})}$), which is expected to be larger than that for muons in light flavour jets due to the large b-quark mass [66, 67]. A “soft muon by IP algorithm” also exists which uses the IP significance of positive IP muons. In jets containing more than one muon, the muon with the highest discriminator is used.

6.2.4 Simple Secondary Vertex

The simple secondary vertex (SSV) algorithm uses the Adaptive Vertex Fitter to reconstruct the secondary vertex [110]. The discriminator is calculated based on the 3D decay length significance. If no secondary vertex is reconstructed, no discriminator is produced, meaning that the efficiency of this algorithm is limited to the maximum efficiency of secondary vertex reconstruction (approximately 65 %) [48]. There are two variants of the simple secondary vertex algorithm: the high efficiency version uses vertices with at least two compatible tracks, whereas the high purity version uses vertices with at least three tracks.

6.2.5 Combined Secondary Vertex

The current CMS recommendation for physics analyses (and therefore the algorithm used in the differential cross section analysis presented in Chapters 7–9) is the Combined Secondary Vertex (CSV) algorithm [111]. This algorithm reconstructs the event vertices using the Trimmed Kalman Vertex Finder [108], a vertex finding algorithm that fits tracks to a primary vertex after removing incompatible tracks and applies the following cuts to these vertices in order to find a secondary vertex.

- the transverse distance between the primary and secondary vertices, L_T , must be $\geq 100 \mu\text{m}$ and $\leq 2.5 \text{ cm}$.
- L_T divided by its error, σL_T , must be ≥ 3 .
- all charged particles related to the vertex must have an invariant mass of $\leq 6.5 \text{ GeV}/c^2$.
- the vertex is rejected if it has two oppositely charged tracks within a mass window of $50 \text{ MeV}/c^2$, in order to suppress the selection of vertices compatible with a K_S^0 decay.

6. b-tagging Study

The CSV algorithm then combines the following track-based lifetime parameters and secondary vertex information to produce a discriminator [111]:

- IP and IP significance
- Flight distance significance
- Number of charged tracks in the jet (b-jets have a higher track multiplicity than, e.g. c-jets)
- Invariant mass of charged particles related to the secondary vertex (secondary b-jet vertices have a significantly higher invariant mass than c-jets).
- Rapidities of charged particle tracks related to the secondary vertex.

All of the input variables are combined into the final discriminating variable using a likelihood technique. The increased number of input parameters for the CSV algorithm means that even in cases with no reconstructed secondary vertex a discriminator can be produced, thereby increasing the maximum efficiency compared to the SSV algorithms [48].

As with all b-tagging algorithms, a discriminator ranging from 0 to 1 is produced, with larger numbers corresponding to a higher probability of a jet being a b-jet. Three b-tagging working points are used in CMS: tight, medium and loose. The medium working point is used in the differential cross sections analysis, which carries a 1 % mis-tag rate (the rate at which non-b-jets are mistakenly tagged as b-jets) and approximately 70 % b-tag efficiency. The tight and loose working points have mis-tag rates of 0.1 % and 10 % respectively [48]. The CSV MVA algorithm is a variant of this method, in which a multi-variate analysis (MVA) is performed using the CMSSW MVA Tools to produce a discriminator.

6.3 Performance Comparison

Distributions of the discriminators produced by the above algorithms were created for a $t\bar{t}$ **MADGRAPH** Monte Carlo simulation sample (`/TTJets_TuneZ2_7TeV-madgraph-tauola/`, produced in the Fall2011 production cycle using CMSSW version 44X). A comparison of

the discriminator distributions, after normalising to unit area, for the described algorithms were carried out. Figure 6.3 shows a comparison between the distributions obtained by the CSV algorithm for the different jets present in the sample: b-jets, light jets (up, down and strange flavour: uds-jets), gluon jets (g-jets) and charm flavour jets (c-jets). All distributions were normalised to unity in order to facilitate shape comparison. Equivalent plots for other algorithms are included in Figure A.1 in Appendix A. In all cases, it can be seen that higher discriminator values were produced for b-jets than for uds-jets, g-jets and c-jets, as expected.

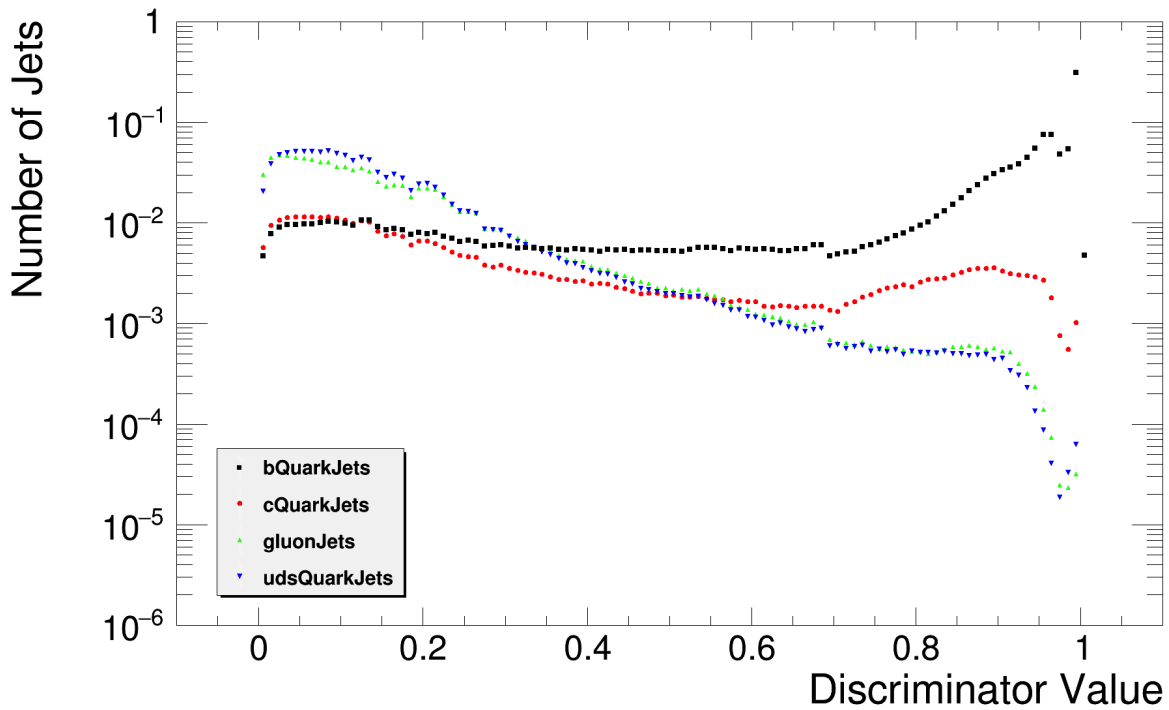


Figure 6.3: Discriminator values produced by the Combined Secondary Vertex algorithm for all b-jets, c-jets, g-jets and uds-jets after normalisation.

6.4 Efficiency

Analyses in CMS make use of b-tagging algorithms by placing cuts on the discriminators. The efficiency of a cut can be defined as the ratio of number of jets passing the selection cut to the total number of jets before the selection cut. The efficiency was calculated for cut values spanning the whole range of discriminator values, and the resulting plot of b-tagging

efficiency for non-b-jets as a function of b-tagging efficiency for b-jets is shown Figure 6.4. In practice, the aim is to achieve a high b-jet efficiency and a low efficiency for all other jet flavours, i.e. the lower right region of the plot. It can be seen that uds-jets and g-jets have similar rates of increase in efficiencies with respect to cut value, owing to their similar discriminator distributions. The c-jet discriminator distribution (Figure 6.3), however, has a noticeably different shape. This leads to the undesirable trend of higher c-jet efficiencies than for uds-jets and g-jets. Equivalent plots for other algorithms can be found in Figure A.2 in Appendix A.

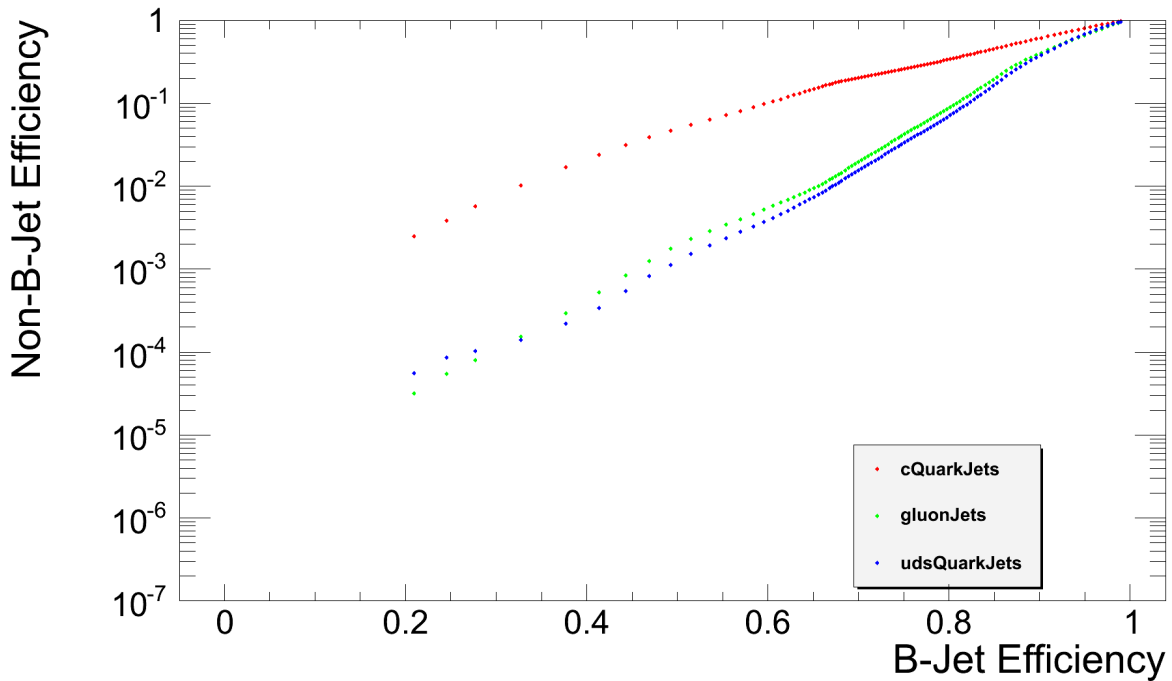


Figure 6.4: b-tagging efficiencies of non-b-jets as a function of b-tagging efficiency for b-jets for the CSV algorithm.

6.5 Algorithm Comparison

The performances of the various algorithms can be compared in Figure 6.5.

It can be seen that not all algorithms reach 100 % b-jet efficiency due to being inherently limited by their methods. For example, the soft muon algorithms are limited by the muon identification efficiency within b-jets and also by the branching fraction of B hadrons to muons. The soft muon algorithms all show low maximum b-jet efficiencies due to the low B

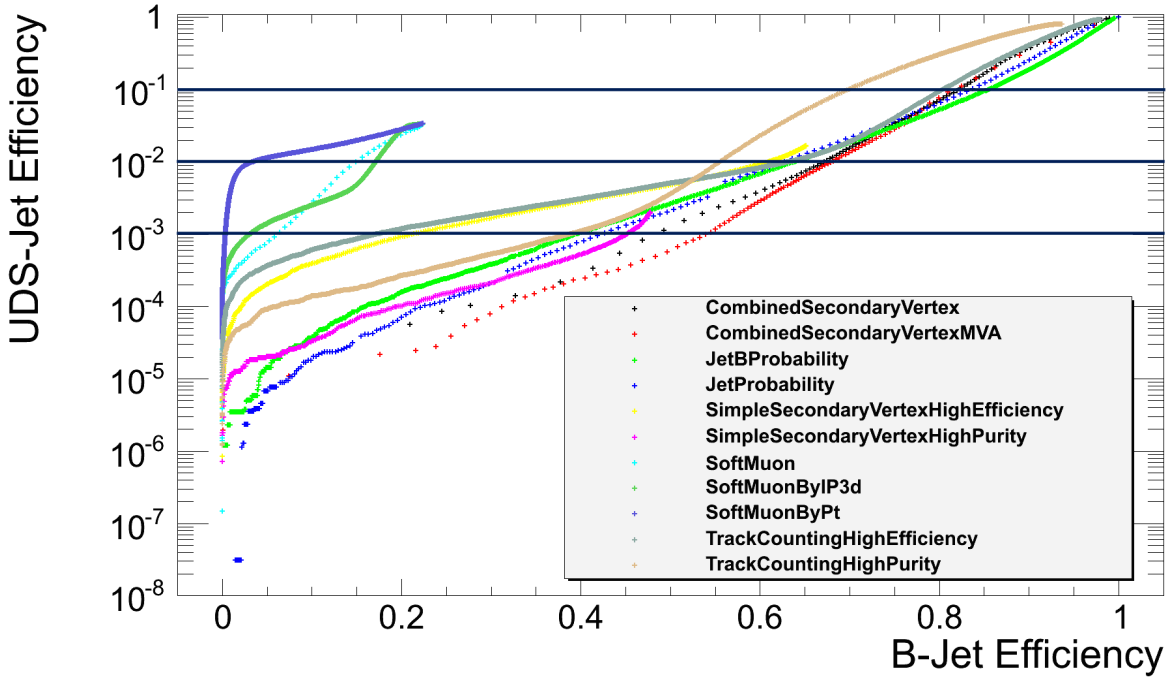


Figure 6.5: uds-jet efficiencies as a function of b-jet efficiencies for all algorithms.

hadron semi-leptonic branching ratio to muons of approximately 11 % (or 20 % when further decays are included such as $b \rightarrow c \rightarrow l$) [67]. Similarly, the SSV algorithms are limited by the efficiency of reconstructing a secondary vertex in the jet of approximately 65 %.

The 2011 and 2012 CMS recommended b-tagger is the CSV algorithm with operating point discriminator cuts of 0.244 (loose), 0.679 (medium) and 0.898 (tight) corresponding to 10%, 1% and 0.1% light jet efficiencies. These cuts are indicated by the horizontal lines on Figure 6.5. It can be seen that for the tight and medium cuts, the CSV MVA algorithm provides the highest b-jet efficiency and lowest light jet efficiency, followed closely by the CSV algorithm. The multiple variables (see Section 6.2.5) that are used as input allow the CSV algorithm to produce higher efficiencies than the SSV algorithms, while the MVA analysis variant provides a slightly improved performance. At approximately 3 % light jet efficiency, there is a convergence of many algorithms that all provide similar performance. At the loose working point also, many of the algorithms provide similar performance with b-jets, with the ‘‘jet probability’’ algorithms marginally outperforming the CSV algorithms. In early CMSSW versions, it was known that the jet probability algorithm provided optimal

6. b-tagging Study

performance, leading to it being recommended for early CMS analyses. Ultimately, the CSV algorithm provides better performance in CMSSW versions after CMSSW_2_X_Y, at which point it became the recommended b-tagging method.

7 | Differential Cross Sections: Data, Simulation and Selection

7.1 Outline and Motivation

This chapter describes the first part of the main $t\bar{t}$ differential cross section analysis in bins of global event variables. Following an introduction to the variables under investigation and motivations, the datasets used and the selection process is explained, including scale factors and corrections applied to ensure agreement between Monte Carlo simulation and data.

The analysis measures the normalised differential $t\bar{t}$ cross section in the semi-leptonic channel and is carried out on 2011 and 2012 data recorded from the CMS detector. The measurement is carried out with respect to the following global, or primary, variables:

- E_T^{miss} , the missing transverse energy in an event, defined as the magnitude of the missing transverse momentum vector \vec{p}_T^{miss} (which is defined as the projection of the negative vector sum of the momenta of all PF objects in the event on the plane perpendicular to the beams).

$$E_T^{\text{miss}} = \left[\left(\sum_i p_x^i \right)^2 + \left(\sum_i p_y^i \right)^2 \right]^{\frac{1}{2}},$$

where p_x^i and p_y^i are momentum components of the i th object in the event, and the sums include all PF objects in the event, with no lower threshold applied. See Section 7.4.4 for details of corrections applied in the calculation of this E_T^{miss} , which include, amongst others, propagation of jet energy corrections and takes account of pileup interactions.

- H_T , the sum of the transverse momenta of all jets with $p_T > 20 \text{ GeV}$ and $|\eta| < 2.5$ in

an event

$$H_T = \sum_{\text{all jets}} p_T^{\text{jet}}$$

- S_T , the sum of all observed transverse momenta in an event, i.e. the scalar sum of H_T , E_T^{miss} , and lepton p_T

$$S_T = H_T + E_T^{\text{miss}} + p_T^{\text{lepton}}.$$

- p_T^W , the transverse momentum of the leptonically decaying W boson, obtained from \vec{p}_T^{miss} and the p_T of the lepton

$$p_T^W = \sqrt{(p_x^{\text{lepton}} + p_x^{\text{miss}})^2 + (p_y^{\text{lepton}} + p_y^{\text{miss}})^2},$$

where p_x^{lepton} and p_y^{lepton} are the transverse components of \vec{p}^{lepton} , and p_x^{miss} and p_y^{miss} are the transverse components of \vec{p}_T^{miss} .

- M_T^W , the transverse mass of the leptonically decaying W boson, also obtained from E_T^{miss} and the p_T of the lepton

$$M_T^W = \sqrt{E_T(\text{lepton}, E_T^{\text{miss}})^2 - (p_T^W)^2},$$

where $E_T(\text{lepton}, E_T^{\text{miss}})$ is the scalar sum of E_T^{miss} and the transverse energy of the lepton, i.e. $E_T^{\text{miss}} + E_T^{\text{lepton}}$

The central objective of these measurements is to verify the models and generators used to produce simulations of the signal and background events in CMS. This understanding is important to provide a good foundation for new physics analyses, where such events constitute a significant background. Comparison of results with predictions using varied choices of the matching threshold of partons, and the renormalisation and factorisation scale (Q^2) allow the verification of these model parameters used in event generation. In addition, the distributions under investigation may be sensitive to rare standard model processes;

for example, the E_T^{miss} and M_T^W distributions could show signs of $t\bar{t} + Z$ (where $Z \rightarrow \nu\bar{\nu}$) and/or $t\bar{t} + W$ (where $W \rightarrow l\nu$) processes, which produce additional E_T^{miss} . The p_T^W and M_T^W distributions are related to the leptonically decaying W boson, and therefore give a handle on modelling of the transverse momentum of the relevant top quark. The H_T and S_T distributions would provide information on $t\bar{t} + X$ production where X is massive and decays to hadrons. Hints of new physics scenarios such as stop pair production, $\tilde{t}\bar{t} \rightarrow t\tilde{\chi}_0\bar{t}\tilde{\chi}_0$, where $\tilde{\chi}_0$ is the lightest supersymmetric particle and a possible dark matter candidate, may also be visible in the distributions of global variables. Cases of rare SM processes or new physics are likely to manifest as observed excesses over predictions in the tails of the primary variables, making this region of the distributions of particular interest.

Note that this analysis on the aforementioned global variables does not require reconstruction of the $t\bar{t}$ decay to identify which decay products are associated with each top quark, and is intended as a complementary analysis to other CMS studies in which such reconstruction is carried out.

7.2 Data and Simulated Samples

7.2.1 Data

Data collected in 2011 at a centre-of-mass energy of 7 TeV corresponding to an integrated luminosity of 5.0 fb^{-1} , and in 2012 at a centre-of-mass energy of 8 TeV corresponding to an integrated luminosity of 19.7 fb^{-1} are used in this analysis. The datasets are determined by the triggers that were used to record them. For 7 TeV, the “ElectronHad” dataset is used in the electron channel, which was recorded with triggers that select events based on at least one, isolated electron and additional jets. At 8 TeV, the “SingleElectron” dataset was used for the electron channel which is based only on at least one, isolated electron. In the muon channel, the “SingleMu” dataset was used for both centre-of-mass energies, requiring a single, isolated muon.

These datasets are produced from CMS data by requiring events to pass a trigger. The

triggers used in both 7 TeV and 8 TeV data are shown in Table B.1 in Appendix B.1. In the electron channel, an electron+jets trigger was used in 2011 with a requirement of at least one electron with $E_T > 25$ GeV and at least three jets with $p_T > 30$ GeV; and a single electron trigger was used in 2012 with at least one electron with $E_T > 27$ GeV. In the muon channel, a single muon trigger was used in both data taking periods with a requirement of at least one muon with $p_T > 24$ GeV. In addition to these kinematic requirements, the triggers also have cuts on the ratio between the HCAL and the ECAL energy (H/E), track matching with ECAL ($\Delta\eta$ and $\Delta\phi$), cluster shape ($\sigma_{inj\eta}$), ECAL isolation ($\frac{ECAL_{iso}}{E_T}$), HCAL isolation ($\frac{HCAL_{iso}}{E_T}$) and tracker isolation ($\frac{tracker_{iso}}{p_T}$). In both channels, the final selection is tighter than these trigger requirements.

The datasets used are shown in Tables 7.1 and 7.2. Only data that is certified as “golden” (data taken with the CMS detector working without any major faults) is used. The masks used to filter out data taken in other periods are specified in Table B.2 in Appendix B.1.

Data set name	Run period	$\mathcal{L}_{int} / \text{pb}^{-1}$	Runs
ElectronHad 12 Oct 2013 ReReco	Run2011A	2,333	160404--173692
ElectronHad 12 Oct 2013 ReReco	Run2011B	2,738	175833--180252
SingleMu 12 Oct 2013 ReReco	Run2011A	2,331	160404--173692
SingleMu 12 Oct 2013 ReReco	Run2011B	2,766	175833--180252

Table 7.1: 7 TeV data sets by run period with the corresponding integrated luminosities (\mathcal{L}_{int}) and run numbers.

Data set name	Run period	$\mathcal{L}_{int} / \text{pb}^{-1}$	Runs
SingleElectron 22 Jan 2013 ReReco	Run2012A	883.3	190456--193621
SingleElectron 22 Jan 2013 ReReco	Run2012B	4,389.0	193834--196531
SingleElectron 22 Jan 2013 ReReco	Run2012C	7,137.0	198022--203742
SingleElectron 22 Jan 2013 ReReco	Run2012D	7,318.0	203777--208686
SingleMu 22 Jan 2013 ReReco	Run2012A	889.4	190456--193621
SingleMu 22 Jan 2013 ReReco	Run2012B	4,424.0	193834--196531
SingleMu 22 Jan 2013 ReReco	Run2012C	7,152.0	198022--203742
SingleMu 22 Jan 2013 ReReco	Run2012D	7,280.0	203777--208686

Table 7.2: 8 TeV data sets by run period with the corresponding integrated luminosities (\mathcal{L}_{int}) and run numbers.

7.2.2 Simulated Samples

The signal event for this analysis is the production of a $t\bar{t}$ pair which decays semi-leptonically, i.e. each of the t-quarks decays to a W boson and a b-jet, with one of the W bosons decaying hadronically to two jets and the other decaying leptonically to a lepton (electron or muon) and an associated neutrino. Section 3 outlines the signal and background events considered. Additional, lower energy jets, can be produced from other scatterings in the same proton-proton interaction and from gluon radiation from quarks in the decay. See Section 3 for detailed descriptions of the signal and backgrounds in this analysis.

The Monte Carlo generators used in this analysis are MADGRAPH v5.1.5.11 [28], PYTHIA v6.426 [106], POWHEG v1.0, r1380 and POWHEG v2.0, r2819 [98, 68, 26], HERWIG v6.520 [75] and MC@NLO v3.41 [70, 69]. See Section 3.2 for details about these Monte Carlo generators. The GEANT4 package [24, 27] is used to simulate the CMS detector response.

Tables 7.3 and 7.4 show the Monte Carlo signal samples used in this analysis at 7 TeV and 8 TeV respectively. Tables 7.5 and 7.6 list the background simulation samples used.

Top pair production is modelled using the MADGRAPH event generator, with PYTHIA modelling the parton showering and hadronisation, with matching between the parton showers and the matrix element performed via the MLM prescription [80] (Section 3.2.1). Two independent $t\bar{t}$ samples are also produced with the POWHEG 2 generator interfaced with PYTHIA and HERWIG for parton showering. At $\sqrt{s} = 7$ TeV, three additional samples are used generated using MC@NLO with HERWIG to model the parton showers, POWHEG 1 with PYTHIA, and POWHEG 1 with HERWIG.

Single top events are modelled with POWHEG, W and Z boson plus jets production is modelled using MADGRAPH and QCD multi-jet events are modelled with PYTHIA. Tables 7.7 and 7.8 show the samples used to evaluate the factorisation scale, matching threshold, and top quark mass uncertainties. W + jets and Z + jets samples were not made available at 7 TeV, so the scaled distributions from 8 TeV were used, as described in Section 9.1.2.

Standard Model cross sections at NNLO of 252.89 pb at $\sqrt{s} = 7 \text{ TeV}$ and 177.31 pb at $\sqrt{s} = 8 \text{ TeV}$ are used for $t\bar{t}$ processes [63]. NNLO cross sections are also applied for W + jets processes and Z+jets processes [95]. Cross sections at NLO are used for single top processes [38] and LO cross sections are used for QCD multi-jet processes. Numerical values for cross sections are included in all abovementioned tables.

The CTEQ6L PDFs [103] are used to generate the MADGRAPH simulations, the CT10 PDFs [93] are used for POWHEG production and CTEQ6M PDFs [103] are used for MC@NLO. The underlying event tunes (sets of theory parameters) used for production of the MADGRAPH and POWHEGv2+PYTHIA samples at $\sqrt{s} = 7 \text{ TeV}$, as well as the MC@NLO+HERWIG sample at $\sqrt{s} = 8 \text{ TeV}$, is the PYTHIA Z2 tune [43]. The PYTHIA Z2* is used for the MADGRAPH, POWHEGv1+PYTHIA and POWHEGv2+PYTHIA samples at $\sqrt{s} = 8 \text{ TeV}$, and the AUET tune [7] is used in all POWHEGvs+HERWIG amplitudes. All simulations are generated with a top quark mass of 172.5 GeV, and in all cases, PYTHIA is used to model parton showering, radiation and hadronisation processes.

Table 7.3: 7 TeV Monte Carlo signal datasets used for this analysis.

Process	Generator	σ / pb	No. events	$\mathcal{L}_{\text{int}} / \text{fb}^{-1}$
$t\bar{t}$	MADGRAPH	177.31	17100187	96.4
$t\bar{t}$	MC@NLO	Not Available	-	-
$t\bar{t}$	POWHEGv1+PYTHIA	Not Available	-	-
$t\bar{t}$	POWHEGv1+HERWIG	Not Available	-	-
$t\bar{t}$	POWHEGv2+PYTHIA	177.31	4833135	27.3
$t\bar{t}$	POWHEGv2+HERWIG	177.31	4480816	25.3

Table 7.4: 8 TeV Monte Carlo signal datasets used for this analysis.

Process	Generator	σ / pb	No. events	$\mathcal{L}_{\text{int}} / \text{fb}^{-1}$
$t\bar{t}$	MADGRAPH	252.89	6706068	26.5
$t\bar{t}$	MC@NLO	252.89	32852517	129.9
$t\bar{t}$	POWHEGv1+PYTHIA	252.89	21675913	85.7
$t\bar{t}$	POWHEGv1+HERWIG	252.89	27684194	109.5
$t\bar{t}$	POWHEGv2+PYTHIA	252.89	9044049	35.8
$t\bar{t}$	POWHEGv2+HERWIG	252.89	8630382	34.1

Table 7.5: 7 TeV Monte Carlo background datasets used for this analysis. All samples are generated inclusively if not marked otherwise (* generator cut on in-flight-decays of b- and c-hadrons, \ominus enriched in conversion electrons; l means all leptonic decays: $l = e, \mu, \tau$; \bullet generator cut on $m_{Z/\gamma} > 50$ GeV).

Process	Generator	σ (pb)	No. events	\mathcal{L}_{int} (fb^{-1})
Single t t-channel ($W \rightarrow l\nu$)	POWHEG	42.6	3249530	76.3
Single \bar{t} t-channel ($W \rightarrow l\nu$)	POWHEG	22.0	1813615	82.4
Single t s-channel ($W \rightarrow l\nu$)	POWHEG	2.72	229786	84.5
Single \bar{t} s-channel ($W \rightarrow l\nu$)	POWHEG	1.49	138187	92.7
Single t tW-channel ($W \rightarrow l\nu$)	POWHEG	5.3	744859	140.5
Single \bar{t} tW-channel ($W \rightarrow l\nu$)	POWHEG	5.3	801626	151.3
$W (\rightarrow l\nu) + 1$ Jet	MADGRAPH	4480.0	70430949	15.7
$W (\rightarrow l\nu) + 2$ Jets	MADGRAPH	1435.0	25069566	17.5
$W (\rightarrow l\nu) + 3$ Jets	MADGRAPH	304.2	6291772	20.7
$W (\rightarrow l\nu) + 4$ Jets	MADGRAPH	172.6	13240209	76.7
$Z/\gamma^* (\rightarrow l^+l^-) + \text{jets } \bullet$	MADGRAPH	3048	32846945	10.8
QCD BCtoE p_T 20-30 *	PYTHIA	139299.0	1927944	1.4×10^{-2}
QCD BCtoE p_T 30-80 *	PYTHIA	143844.8	1946505	1.4×10^{-2}
QCD BCtoE p_T 80-170 *	PYTHIA	9431.1	1002427	0.1
QCD EM p_T 20-30 \ominus	PYTHIA	2502660.0	32976415	1.3×10^{-2}
QCD EM p_T 30-80 \ominus	PYTHIA	3625840.0	71775065	2.0×10^{-2}
QCD EM p_T 80-170 \ominus	PYTHIA	142813.8	7650319	5.4×10^{-2}
QCD EM p_T 170-250 \ominus	PYTHIA	142813.8	2968842	2.1×10^{-2}
QCD EM p_T 250-350 \ominus	PYTHIA	368.0	2952960	8.0
QCD EM p_T 350-inf \ominus	PYTHIA	55.0	2957326	53.8
$\gamma + \text{Jets HT } 40\text{-}100$	MADGRAPH	25690.0	9882860	0.4
$\gamma + \text{Jets HT } 100\text{-}200$	MADGRAPH	5213.0	1514347	0.3
$\gamma + \text{Jets HT } > 200$	MADGRAPH	798.3	9275592	11.6
QCD μ enriched p_T 15-20	PYTHIA	1668096.0	1901684	1.1×10^{-3}
QCD μ enriched p_T 20-30	PYTHIA	1342184.0	10173300	7.6×10^{-3}
QCD μ enriched p_T 30-50	PYTHIA	596506.8	11610111	1.9×10^{-2}
QCD μ enriched p_T 50-80	PYTHIA	140039.55	9870031	7.0×10^{-2}
QCD μ enriched p_T 80-120	PYTHIA	28546.2	9769136	0.3
QCD μ enriched p_T 120-170	PYTHIA	4692.91	7818474	1.7
QCD μ enriched p_T 170-300	PYTHIA	1445.96	8116409	5.6
QCD μ enriched p_T 300-470	PYTHIA	95.4464	7870002	82.5
QCD μ enriched p_T 470-600	PYTHIA	7.41697	3812529	514.0
QCD μ enriched p_T 600-800	PYTHIA	1.69145	4149911	2453.5
QCD μ enriched p_T 800-1000	PYTHIA	0.231869	4036867	17410.1
QCD μ enriched p_T 1000-inf	PYTHIA	0.053385	4133897	77435.6

Table 7.6: 8 TeV Monte Carlo background datasets used for this analysis. All samples are generated inclusively if not marked otherwise (* generator cut on in-flight-decays of b- and c-hadrons, \ominus enriched in conversion electrons; l means all leptonic decays: $l = e, \mu, \tau$; • generator cut on $m_{Z/\gamma} > 50$ GeV).

Process	Generator	σ (pb)	No. events	\mathcal{L}_{int} (fb^{-1})
Single t t-channel ($W \rightarrow l\nu$)	POWHEG	55.53100	3758221	67.7
Single \bar{t} t-channel ($W \rightarrow l\nu$)	POWHEG	30.00420	1906041	63.5
Single t s-channel ($W \rightarrow l\nu$)	POWHEG	3.89394	259960	66.8
Single \bar{t} s-channel ($W \rightarrow l\nu$)	POWHEG	1.75776	139974	79.6
Single t tW-channel ($W \rightarrow l\nu$)	POWHEG	11.17730	497657	44.5
Single \bar{t} tW-channel ($W \rightarrow l\nu$)	POWHEG	11.17730	473721	42.4
$W (\rightarrow l\nu) + 1$ Jet	MADGRAPH	5400.0	23129996	15.7
$W (\rightarrow l\nu) + 2$ Jets	MADGRAPH	1750.0	34027847	17.5
$W (\rightarrow l\nu) + 3$ Jets	MADGRAPH	519.0	15539463	20.7
$W (\rightarrow l\nu) + 4$ Jets	MADGRAPH	214.0	13373865	76.7
$Z/\gamma^* (\rightarrow l^+l^-) + 1$ jet•	MADGRAPH	561.0	24032529	42.8
$Z/\gamma^* (\rightarrow l^+l^-) + 2$ jets•	MADGRAPH	181.0	21840628	0.1
$Z/\gamma^* (\rightarrow l^+l^-) + 3$ jets•	MADGRAPH	51.1	10819603	0.2
$Z/\gamma^* (\rightarrow l^+l^-) + 4$ jets•	MADGRAPH	23.04	6381467	0.3
QCD BCtoE p_T 20-30 *	PYTHIA	167388.0	1731522	1.0×10^{-2}
QCD BCtoE p_T 30-80 *	PYTHIA	167040.0	2037907	1.2×10^{-2}
QCD BCtoE p_T 80-170 *	PYTHIA	12981.9	1945523	0.1
QCD BCtoE p_T 170-250 *	PYTHIA	632.0	1948112	3.1
QCD BCtoE p_T 250-350 *	PYTHIA	103.3	2026516	19.6
QCD BCtoE p_T 350-inf *	PYTHIA	23.9	1948525	81.5
QCD EM p_T 20-30 \ominus	PYTHIA	2914860.0	34830398	1.2×10^{-2}
QCD EM p_T 30-80 \ominus	PYTHIA	4615893.0	32443607	7.0×10^{-3}
QCD EM p_T 80-170 \ominus	PYTHIA	183294.9	34024542	0.2
QCD EM p_T 170-250 \ominus	PYTHIA	4586.5	31696985	6.9
QCD EM p_T 250-350 \ominus	PYTHIA	556.7	33659467	60.5
QCD EM p_T 350-inf \ominus	PYTHIA	89.1	33756727	378.8
$\gamma + \text{Jets HT } 200\text{-}400$	MADGRAPH	960.5	47316433	49.3
$\gamma + \text{Jets HT } 400\text{-inf}$	MADGRAPH	107.5	9491846	88.3
QCD μ enriched p_T 15-20	PYTHIA	2738580.0	1722678	0.6×10^{-3}
QCD μ enriched p_T 20-30	PYTHIA	1865500.0	8486893	4.5×10^{-3}
QCD μ enriched p_T 30-50	PYTHIA	806298.0	9560248	1.2×10^{-2}
QCD μ enriched p_T 50-80	PYTHIA	176187.6	10365209	5.9×10^{-2}
QCD μ enriched p_T 80-120	PYTHIA	40448.0	9238622	0.2
QCD μ enriched p_T 120-170	PYTHIA	7463.94	8501920	1.1
QCD μ enriched p_T 170-300	PYTHIA	2299.752	7669932	3.3
QCD μ enriched p_T 300-470	PYTHIA	151.8048	7832248	51.6
QCD μ enriched p_T 470-600	PYTHIA	11.79648	3783066	320.7
QCD μ enriched p_T 600-800	PYTHIA	2.690196	4118988	1531.1
QCD μ enriched p_T 800-1000	PYTHIA ⁷⁸	0.3687810	4099633	11116.7
QCD μ enriched p_T 1000-inf	PYTHIA	0.0849078	9238622	108807.7

Table 7.7: 7 TeV Monte Carlo systematic datasets used for this analysis. All samples are produced with the MADGRAPH generator. W + jets and Z + jets samples were not available and so have been scaled from available 8 TeV samples.

Process	Variation	Generator	σ (pb)	No. events	\mathcal{L}_{int} (fb $^{-1}$)
t̄t	0.5×Q ² (norm. & fact. scale down)	MADGRAPH	177.31	9426377	53.2
t̄t	2×Q ² (norm. & fact. scale up)	MADGRAPH	177.31	10095984	56.9
t̄t	0.5×matching threshold (down)	MADGRAPH	177.31	4056487	22.9
t̄t	2×matching threshold (up)	MADGRAPH	177.31	16727257	94.3
t̄t	0.5×mass uncertainty (down)	MADGRAPH	177.31	4560762	25.7
t̄t	2×mass uncertainty (up)	MADGRAPH	177.31	9151264	51.6
W + jets	0.5×Q ² (norm. & fact. scale down)	MADGRAPH	31314	20121177	0.6
W + jets	2×Q ² (norm. & fact. scale up)	MADGRAPH	31314	20711338	0.7
W + jets	0.5×matching threshold (down)	MADGRAPH	31314	21341479	0.7
W + jets	2×matching threshold (up)	MADGRAPH	31314	20594331	0.7
Z + jets	0.5×Q ² (norm. & fact. scale down)	MADGRAPH	3048.0	1934895	0.6
Z + jets	2×Q ² (norm. & fact. scale up)	MADGRAPH	3048.0	2159410	0.7
Z + jets	0.5×matching threshold (down)	MADGRAPH	3048.0	2112383	0.7
Z + jets	2×matching threshold (up)	MADGRAPH	3048.0	1985526	0.7

Table 7.8: 8 TeV Monte Carlo systematic datasets used for this analysis. All samples are produced with the MADGRAPH generator.

Process	Variation	Generator	σ (pb)	No. events	\mathcal{L}_{int} (fb $^{-1}$)
$t\bar{t}$	$0.5 \times Q^2$ (norm. & fact. scale down)	MADGRAPH	252.89	5387169	21.3
$t\bar{t}$	$2 \times Q^2$ (norm. & fact. scale up)	MADGRAPH	252.89	5009481	19.8
$t\bar{t}$	$0.5 \times$ matching threshold (down)	MADGRAPH	252.89	5476715	21.7
$t\bar{t}$	$2 \times$ matching threshold (up)	MADGRAPH	252.89	5415003	21.4
$t\bar{t}$	$0.5 \times$ mass uncertainty (down)	MADGRAPH	252.89	39423535	155.9
$t\bar{t}$	$2 \times$ mass uncertainty (up)	MADGRAPH	252.89	26488957	104.7
W + jets	$0.5 \times Q^2$ (norm. & fact. scale down)	MADGRAPH	36257.2	20121177	0.6
W + jets	$2 \times Q^2$ (norm. & fact. scale up)	MADGRAPH	36257.2	20711338	0.6
W + jets	$0.5 \times$ matching threshold (down)	MADGRAPH	36257.2	21341479	0.6
W + jets	$2 \times$ matching threshold (up)	MADGRAPH	36257.2	20594331	0.6
Z + jets	$0.5 \times Q^2$ (norm. & fact. scale down)	MADGRAPH	3503.71	1934895	0.6
Z + jets	$2 \times Q^2$ (norm. & fact. scale up)	MADGRAPH	3503.71	2159410	0.6
Z + jets	$0.5 \times$ matching threshold (down)	MADGRAPH	3503.71	2112383	0.6
Z + jets	$2 \times$ matching threshold (up)	MADGRAPH	3503.71	1985526	0.6

7.3 Selection

Selection algorithms are run on the data and samples listed in Sections 7.2 and 7.2.2 to identify $t\bar{t}$ events. The selection process is performed in two stages: a “preselection” using loose criteria to produce ntuples, and a second, full selection when processing these ntuples to produce the final analysis samples. The selections used follow the criteria recommended by the CMS TOP Physics Analysis Group (PAG), and are the same for $\sqrt{s} = 7 \text{ TeV}$ and $\sqrt{s} = 8 \text{ TeV}$. All objects are reconstructed with the PF algorithms and pileup subtraction is carried out as described in Section 5.3.2. Table 7.9 shows the selection steps and event yields.

	electron channel	muon channel
	preselection	preselection
Trigger	$\sqrt{s}=7 \text{ TeV}$: Electron+3Jets	SingleMuon
	$\sqrt{s}=8 \text{ TeV}$: Single Electron	
	one isolated electron	one isolated muon
	muon veto	second muon veto
	dilepton veto	electron veto
	conversion veto	
jet selection	≥ 4 jets	≥ 4 jets
b-tagging	≥ 2 b-tags	≥ 2 b-tags

Table 7.9: Summary of event selection steps.

7.3.1 Preselection

The preselection is performed on the AOD datasets, with the aim of making the resulting ntuples smaller in size but still versatile enough for adjustments later in the analysis chain.

The preselection requires at least one good primary vertex with at least four degrees of freedom, obtained from the adaptive vertex fit of clustered tracks to identify vertex parameters, and defined as $-3 + 2 \sum_{i=1}^{\#tracks} w_i$ where w_i is the weight of the i th track. The vertex must be located within 24 cm of the centre of the CMS detector in the z direction and within 2 cm of

the centre of the beam trajectory in the transverse plane. In addition, events are required to have at least one lepton candidate. In the case of electrons, a transverse energy of at least 30 GeV and $|\eta| < 2.5$ and in the muon channel a transverse momentum of at least 20 GeV and $|\eta| < 2.1$ are required. At least three jets passing the loose PF jet ID (Section 5.3.5) with $p_T > 30$ GeV and $|\eta| < 2.6$ are also required at this stage, due mainly to the jet requirement in the electron channel trigger at $\sqrt{s} = 7$ TeV.

Several filters are also applied in the preselection stage to remove events with significant levels of noise due to elements of the detector with sub-optimal performance during data-taking. These filters include an HCAL noise filter to remove events with high HCAL noise, a tracking failure filter to remove events with too few tracks, ECAL filters to remove events with signals in dead and/or noisy modules of the ECAL and a beam scraping veto which requires tracks of high purity in events with high track multiplicity.

7.3.2 Electron channel selection

The final selection in the electron+jets channel follows that recommended by the CMS TOP Physics Analysis Group (PAG). After having passed the electron trigger (Section 7.2.1), events are further required to have an electron with an MVA ID, which provides a multivariable-based discriminating variable indicating the likelihood of an object to be an electron (see Section 5.3.3 for details of input variables to the electron MVA ID), of > 0.5 . The electron is also required to have $E_T > 30$ GeV and $|\eta| < 2.5$ (excluding the transition region between the ECAL barrel and endcap of $1.4442 < |\eta| < 1.5660$). The electron E_T cut of 30 GeV is slightly higher than the trigger electron requirements of 25 GeV at 7 TeV and 27 GeV at 8 TeV, to ensure the analysis selects events in the high trigger efficiency p_T region. A transverse impact parameter, the distance between the electron and the primary vertex, of $d_{xy} < 0.02$ cm is also required to ensure an electron promptly produced at the primary vertex. In addition, a ρ corrected (explained in Section 5.3.2) relative isolation of < 0.1 , within a cone of size $\Delta R = 0.3$ is required to remove background events in which the electron is not isolated such as electrons embedded within jets, heavy flavour (b and c) decays, or jets

being misreconstructed, or “faking” an electron. Furthermore, electrons that are matched to a photon conversion are rejected. A veto is placed on additional electrons with looser identification criteria, including an MVA ID of > 0.5 , $E_T > 20 \text{ GeV}$, $|\eta| < 2.5$ and a ρ corrected relative isolation of < 0.15 . A loose muon veto is also enforced, with requirements of $p_T > 10 \text{ GeV}$, $|\eta| < 2.5$ and a $\Delta\beta$ corrected relative isolation of < 0.2 .

7.3.3 Muon channel selection

As in the electron channel, the final selection in the muon channel is taken from the CMS TOP PAG recommendations. In this case, following acceptance by the muon trigger (Section 7.2.1), events must satisfy the muon identification requirement, which comprises several cuts: at least five hits in the tracker and at least one hit in the muon chambers associated to the track, at least one layer of the muon chamber hits must be matched to a global muon (described in Section 5.3.4), and the inner track must include at least one hit in the pixel sub detector. Furthermore, the normalised chi-squared of the track fit should be less than 10. In addition, the muon identification algorithms should identify the particle as a global, PF muon, the muon track should pass within a z-distance of $d_z < 0.5 \text{ cm}$ of the primary vertex, and the transverse impact parameter is required to be $d_{xy} < 0.2 \text{ cm}$. The signal selection also requires that the muon has a $p_T > 26 \text{ GeV}$, $|\eta| < 2.1$ and a $\Delta\beta$ corrected (explained in Section 5.3.2) relative isolation of < 0.12 , within a cone of size $\Delta R = 0.4$. Additional loose muons are vetoed, with looser requirements of passing the PF identification, $p_T > 10 \text{ GeV}$, $|\eta| < 2.5$ and a $\Delta\beta$ corrected relative isolation of < 0.2 . Loose electrons are also vetoed if they have an MVA ID of > 0.5 , $E_T > 20 \text{ GeV}$, $|\eta| < 2.5$ and a ρ corrected relative isolation of < 0.15 .

7.3.4 Jets selection

In addition to the signal lepton, all events must also have at least four PF jets as reconstructed using the anti- k_t algorithm (see Section 5.3.5) with a cone of $\Delta R = 0.5$. The jet collection is “cleaned” with the signal electron, meaning that any jets within a cone of $\Delta R = 0.3$ from the signal electron or muon are excluded, to suppress events in which an electron fakes a jet

due to the calorimeter energy deposits. Jets are also required to have $p_T > 30 \text{ GeV}$, $|\eta| < 2.5$, and satisfy the criteria for the loose PF jet identification. These PF jet criteria are outlined in Section 5.3.5. Candidate PF jets from pileup are removed from the event; this is known as charged hadron subtraction. Events with at least four jets passing these criteria are permitted to have additional lower energy jets passing the same requirements mentioned above, down to $p_T = 20 \text{ GeV}$. At least two of the four primary jets are further required to be identified as originating from b-quarks by the CSV b-tagging algorithm using the medium working point discriminator cut of 0.679 (Section 6.2.5 and 7.4.2.) These jet requirements, in particular the selection of four jets, two b-jets and the minimum p_T criterion of 30 GeV, remove much of the $W + \text{jets}$ background, where jet multiplicity and energy are typically low.

It should be noted that the cut values used are based on official CMS recommendations. The recommendations are obtained after careful study by CMS Physics Object Groups (POG), and are optimised for a wide range of analyses, meaning they may not necessarily be optimal for this particular analysis, since cuts are analysis dependent. However, unless an analysis is adversely affected, it is generally acceptable to use the provided cut values.

7.3.5 Multi-jet background selection

The QCD background to the $t\bar{t}$ signal is difficult to model in simulation, therefore this background shape is modelled from data. Clearly, a different selection from the signal selection is required to run on data and obtain a sample rich in QCD multi-jet events. These changes in cuts, such as b-tag requirement, jet multiplicity and photon conversion requirements, are chosen such that they enhance the QCD background, without changing the shape of the QCD distributions to first order.

In the electron+jets channel, the control region is obtained by applying the standard full event selection, with the exception of an inverted conversion veto i.e. the veto on electrons that are matched to a photon conversion is reversed, such that events will only pass the selection if they are matched to a photon conversion. The ≥ 2 b-tags requirement is also changed to select only events with 0 b-tags to increase statistics and to enrich the selection

with QCD events. An alternative control region is also investigated by applying the signal selection but with the electron isolation requirement changed from < 0.1 to > 0.2 .

Although only these two QCD selections are used in this analysis, the true QCD background distribution is likely to be a mixture of the conversion and non-isolated distributions (plus possibly other additional components). The conversion region is used to provide the QCD shape in the electron+jets channel, and since the contributions from the conversion and non-isolated regions to the true QCD background are unknown, the non-isolated region is used as an alternative QCD shape in order to evaluate a systematic uncertainty on the choice of this QCD background.

The electron $|\eta|$ distributions observed in data in the electron+jets QCD selections are shown in Figure 7.1a and 7.1b. The MC distributions are also shown for comparison. Evidently, the MC simulation does not describe the data distributions well, with low statistics in the simulation leading to peaks in the distribution.

A comparison of the two QCD background selections at $\sqrt{s} = 7\text{ TeV}$ and $\sqrt{s} = 8\text{ TeV}$ is shown in the lower plots in Figure 7.1c. The conversion distribution is comprised primarily of events in the photon conversion region, i.e. in which the electron comes from photon conversions and where the second electron is not rejected by the electron veto. A rise in this distribution at $|\eta| > 1.5$ can be seen, due to more conversion events in these endcap regions as a result of the larger amount of detector material for electrons to traverse. The non-isolated region favours events with jets misreconstructed as electrons or with jets from heavy flavour decays containing electrons. The rise in this distribution between 1.0 and 1.5 is linked to the jet $|\eta|$ distribution. While the general shape of the conversion region is expected to be the same in both signal and QCD selections, the same may not be true of the non-isolated selection due to the isolation requirement in the signal selection. It should be noted, however, that in the case of the non-isolated distribution at $\sqrt{s} = 7\text{ TeV}$, the simulation does not contain the triggers used in this analysis, unlike at $\sqrt{s} = 8\text{ TeV}$, therefore the simulation distribution at $\sqrt{s} = 7\text{ TeV}$ is not affected by the trigger isolation requirements.

7. Differential Cross Sections: Data, Simulation and Selection

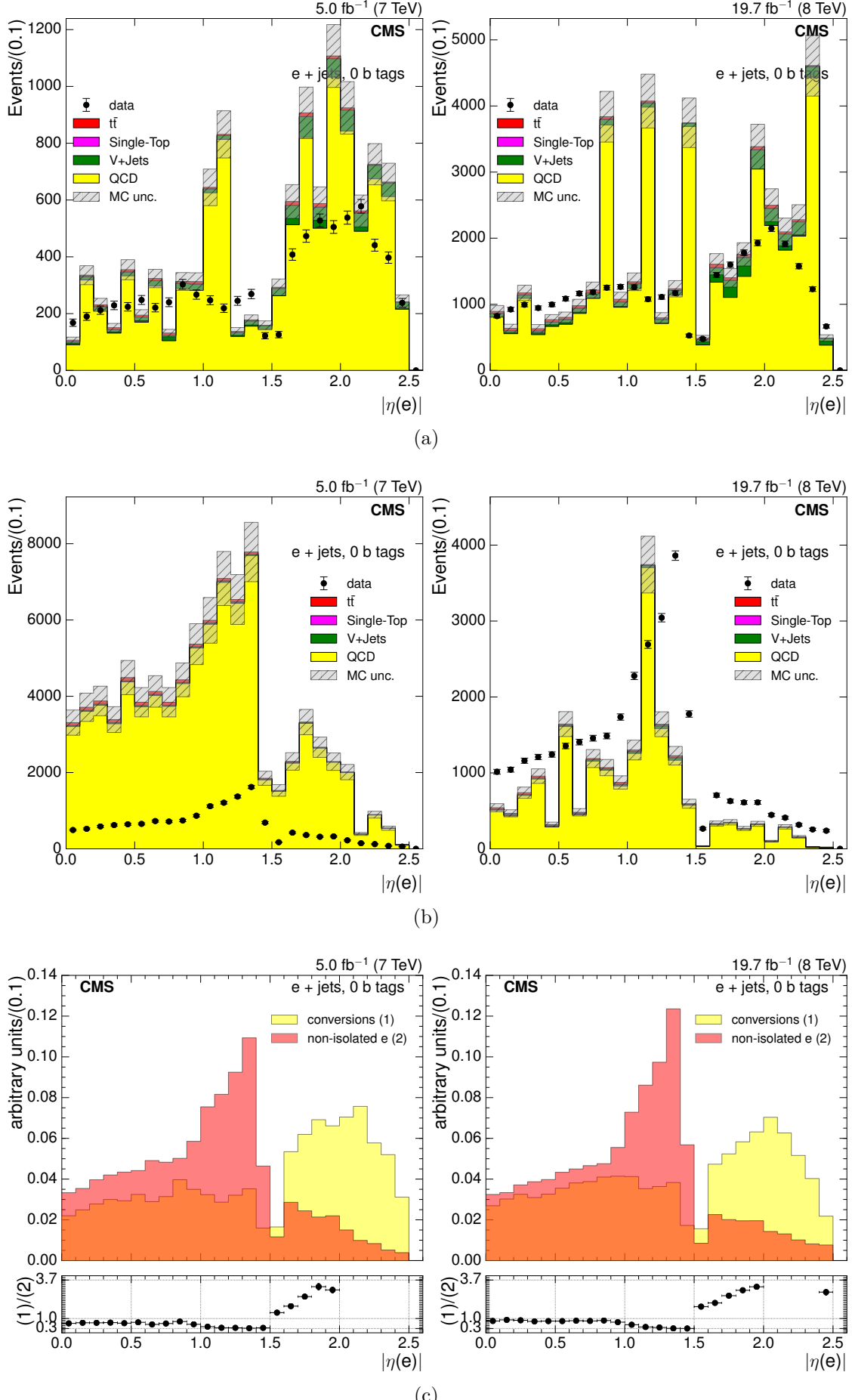


Figure 7.1: Electron $|\eta|$ distributions in QCD selections in the electron+jets channel at $\sqrt{s} = 7 \text{ TeV}$ on the left and at $\sqrt{s} = 8 \text{ TeV}$ on the right, in the conversion region (a) and in the non-isolated region (b). A shape comparison between the two regions in data is shown in (c).

In the case of the muon+jets channel, the full selection is applied with the exception of the muon relative isolation requirement, which is switched from < 0.12 to > 0.3 . This cut value is chosen in order to largely remove most background processes and produce a high purity QCD sample, as can be seen from Figure 7.2. There is a resonable agreement between MC and data here, although again there are some spikes representing the lack of simluation statistics. As in the electron channel, the b-tag requirement is reduced to 0 b-tags and in addition the jet multiplicity requirement is reduced to require at least three jets, to improve statistics and to ensure a purer QCD sample.

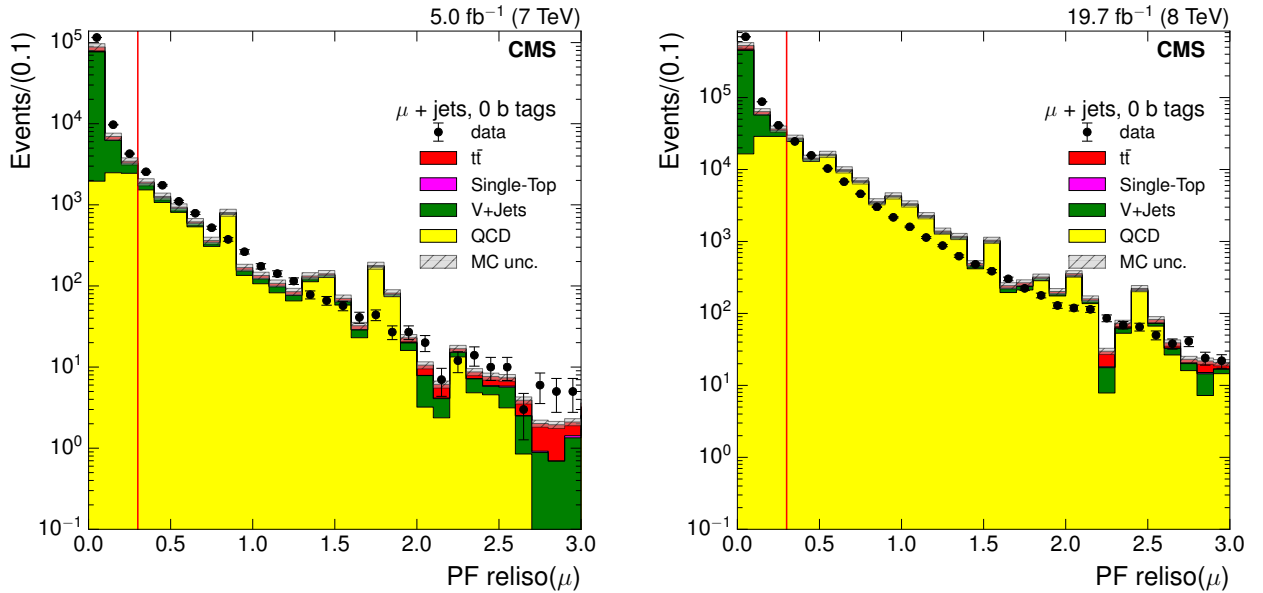


Figure 7.2: PF relative isolation distributions in the muon+jets channel, before subtraction of $t\bar{t}$, single top and $V + \text{jets}$ at $\sqrt{s} = 7 \text{ TeV}$ (left) and $\sqrt{s} = 8 \text{ TeV}$ (right).

Relative to other processes, QCD events are computationally extremely expensive to produce in simulation, owing to their large cross section requiring high numbers of events. Nevertheless, the number of events passing the selection will be very small compared to the number of events passing the signal selection, even with simulated samples with high statistics, meaning there is limited value in obtaining additional statistics for QCD samples. Since the number of events passing the QCD background selections is relatively low, the effect of even large uncertainties in the QCD background on the total number of events will be minimal.

Due to the low statistics of the QCD samples obtained from data, the inclusive QCD shape over all bins is used in every bin for each primary variable (meaning the shape is obtained

over the full range of the primary variables, rather splitting into bins). The remaining contribution from $t\bar{t}$, single-top and $W/Z + \text{jets}$ processes is subtracted from the data sample using the estimation from Monte Carlo simulation. The resulting template of QCD events from data is then used later in the fitting procedure, in place of the equivalent Monte Carlo template (Section 8.1).

7.4 Data-MC scale factors

The following sections describe the small but significant discrepancies that exist between data and simulation regarding pileup modelling 7.4.1; b-tagging 7.4.2; trigger, identification and isolation efficiency 7.4.5; jet energy scale and jet energy resolution 7.4.3; and E_T^{miss} calculation 7.4.4. Scale factors and corrections are applied to both MC and data to account for these differences. The data-MC scale factors used are in accordance with the CMS TOP PAG, and the relevant corrections are implemented for 7 TeV and 8 TeV.

7.4.1 Pileup

Monte Carlo simulation events are produced by first creating the hard proton-proton interaction of interest in a proton bunch crossing, and then introducing the additional interactions, pileup. The pileup distribution in simulation does not reflect the true distribution in data, therefore pileup reweighting is carried out. The estimation of the pileup distribution in data is obtained using the total inelastic proton-proton cross section and the instantaneous luminosity measured in each proton bunch crossing, with a tool provided by the CMS Physics Validation Group. For each number of pileup interactions in simulation, a weight is then produced to match the respective distribution in data.

There is an uncertainty on the measured luminosity which is currently 2.6 % for 2012 data [58] and 2.2 % for 2011 data [57]. The total inelastic cross section has been reported using CMS forward calorimetry [44] and by the TOTEM collaboration [29]. Based on these studies, the CMS recommended central values of 68.0 mb for $\sqrt{s} = 7$ and 69.3 mb for $\sqrt{s} = 8$ have been used, with a ± 5 % uncertainty to account for pileup and physics modelling in

simulation.

The distributions of the number of reconstructed vertices before and after applying pileup reweighting in the electron+jets channel is shown in Figure 7.3, and in the muon+jets channel is shown in Figure B.1 in Appendix B.2. The distributions show good agreement after reweighting.

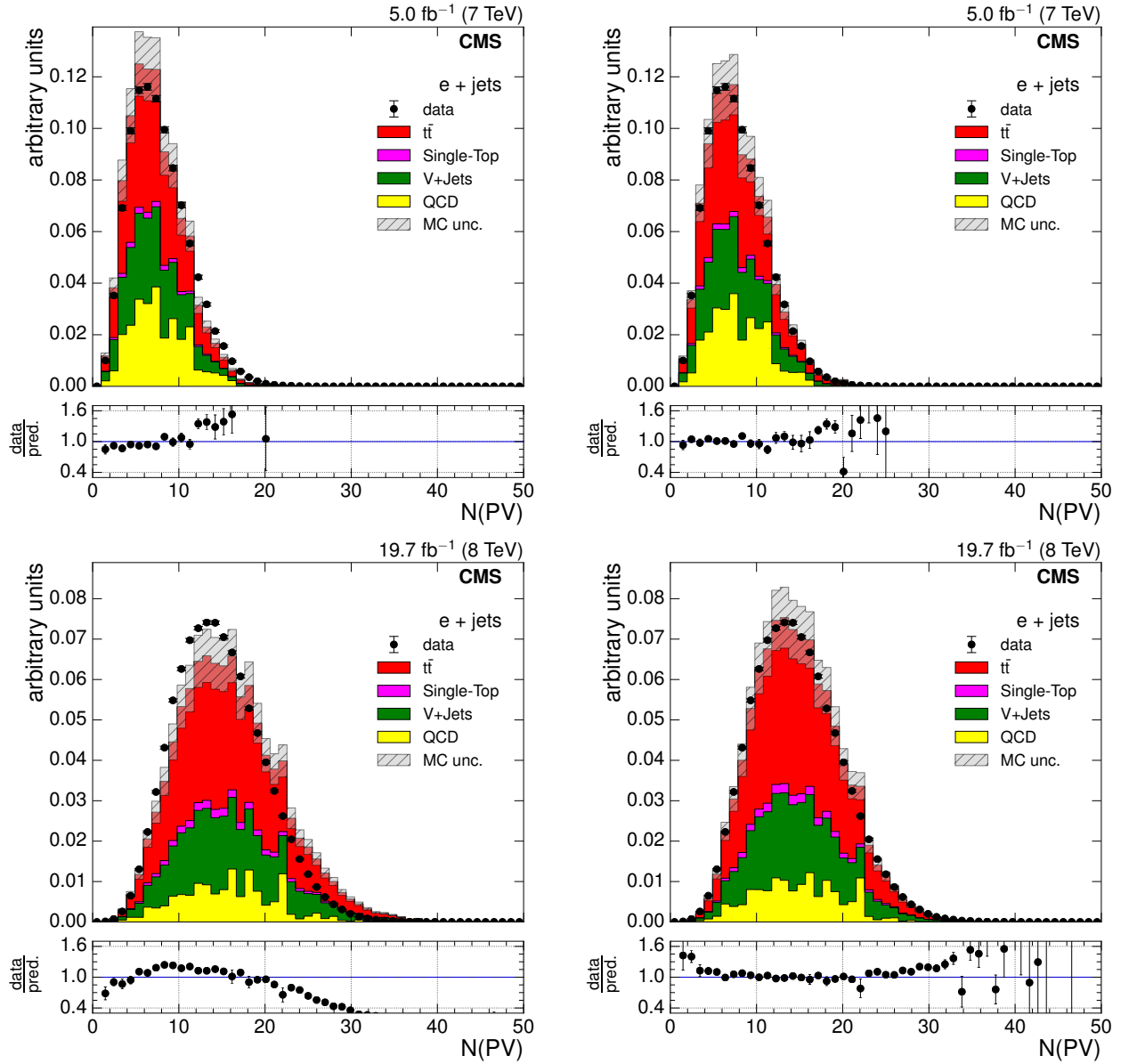


Figure 7.3: Distributions of the number of reconstructed vertices in an event in the electron+jets channel before implementing pileup reweighting (left) and after implementation (right) at $\sqrt{s} = 7$ TeV (upper) and $\sqrt{s} = 8$ TeV (lower). Both data and sum of MC simulations are normalised to one.

7.4.2 b-tagging

The combined secondary vertex b-tagging algorithm (CSV) described in Section 6.2.5 is used in this analysis to identify jets originating from b-quarks in $t\bar{t}$ events. The medium working point, CSVM, which corresponds to a cut on the discriminator output by the algorithm of 0.679, is used in this analysis. This corresponds to a b-tagging efficiency of $\approx 70\%$ and a mis-tag efficiency of 1 % for jets from light quarks (u, d, s) and gluons. Discrepancies between the b-tagging and mis-tagging efficiencies in data and Monte Carlo simulation have been noted in $\sqrt{s} = 7\text{ TeV}$ [48] and $\sqrt{s} = 8\text{ TeV}$ [12]. To account for these differences, events are reweighted as a function of p_T and η , based on the recommendation of the CMS b-tagging POG, with the aim of ensuring that the probability of an event passing selection criteria in simulation matches the probability of an event in data with the same jet(s) passing the same selection. Monte Carlo simulation events are reweighted by a combination of an efficiency, which accounts for tagging efficiencies of b-jets, c-jets and light jets in simulation, and a scale factor, which takes into account the difference in the aforementioned efficiencies in simulation and data. The result of this reweighting in the electron+jets channel is shown in Figure 7.4, and in the muon+jets channel in Figure B.2 in Appendix B.2. The b-tagging efficiency uncertainty is evaluated by varying the scale factors by $\pm 1\sigma$.

7.4.3 Jet Energy Scale

Jet energies are corrected to take into account energy coming from other sources. Level 1 (L1 Pileup) corrections remove energy that comes from pileup collisions, Level 2 (L2 Relative) corrections remove the dependence of jet response on η , and Level 3 (L3 Absolute) corrections correct for the jet response dependence on p_T [41]. These corrections are applied to both data and Monte Carlo simulation events. An additional residual correction (L2L3Residual) is applied to data only for fine tuning of the agreement between data and simulation.

Furthermore, jet energy resolution corrections are applied to simulation (known as jet smearing) to account for the fact that jet energy resolution has been measured to be worse

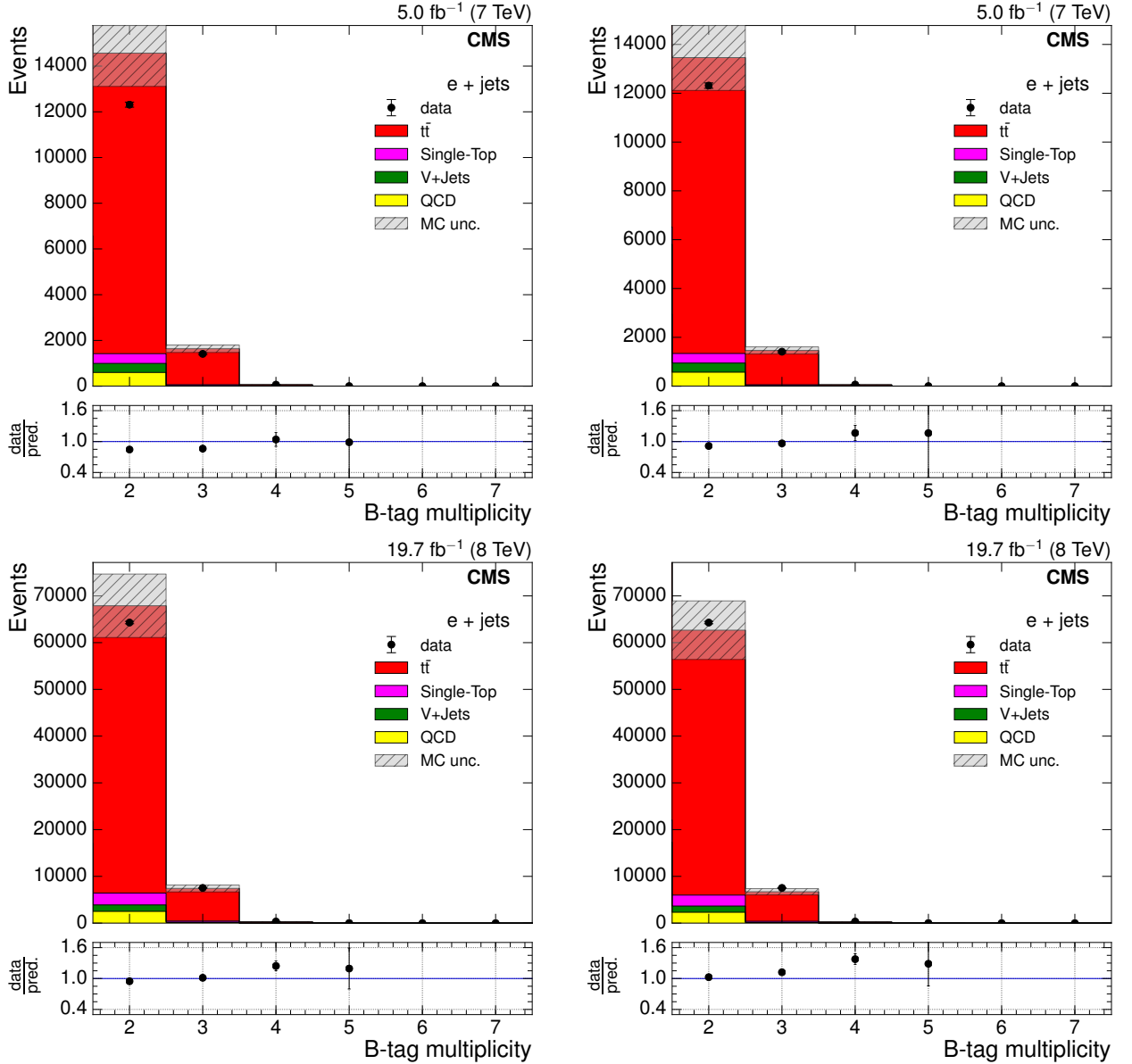


Figure 7.4: Distributions of the number of b-tags in an event in the electron+jets channel before applying b-tag scale factors (left) and after application (right) at $\sqrt{s} = 7 \text{ TeV}$ (upper) and $\sqrt{s} = 8 \text{ TeV}$ (lower).

in data than in simulation. These PF jet corrections are provided by the CMS JETMET Physics Object Group using 0.8 fb^{-1} of dijet data at $\sqrt{s} = 7 \text{ TeV}$ [41] and 19.7 fb^{-1} of dijet data at $\sqrt{s} = 8 \text{ TeV}$ [59].

7.4.4 Missing Transverse Energy Corrections

No selection criteria is placed on missing transverse energy in an event, but corrections are applied to E_T^{miss} as follows. The adjustments to the jet energies as a result of the

corrections mentioned in Section 7.4.3 in turn affect the distributions of E_T^{miss} in the event. Corrections known as Type-I E_T^{miss} corrections are applied to propagate these changes to the E_T^{miss} distributions in the case of jets $\geq 10 \text{ GeV}$. In addition, Type-0 corrections are applied to account for pileup interactions in the event by carrying out charged hadron subtraction (the removal of charged hadrons coming pileup vertices). Finally, a known issue causing a roughly sinusoidal modulation of the E_T^{miss} distribution with respect to ϕ in both simulation and data, is mitigated by applying $E_T^{\text{miss}} \phi$ corrections. This correction ensures the E_T^{miss} distribution is independent of ϕ , due to the rotational symmetry of collisions around the beam axis.

7.4.5 Trigger, Lepton ID and Isolation Efficiencies and Corrections

Corrections are also required for the trigger, identification and isolation efficiencies for muons and electrons. In the muon+jets channel, the corrections were provided by the CMS muon POG for $\sqrt{s} = 8 \text{ TeV}$ and $\sqrt{s} = 7 \text{ TeV}$ [13].

For the electron+jets channel, the corrections were provided by the CMS EGamma Physics Object Group for $\sqrt{s} = 8 \text{ TeV}$, however the corrections for the $\sqrt{s} = 7 \text{ TeV}$ data were not provided and so were derived independently in this analysis using the same tag and probe methods as used by the EGamma POG.

The 7 TeV triggers used (ElectronHad) in this analysis were not present in the 7 TeV simulation, and so the trigger efficiency was calculated with respect to the full selection. This efficiency was then implemented in the Monte Carlo simulation, thereby imitating the trigger. It should be noted that it is assumed that the electron and hadron legs of the trigger are not correlated, since electrons are cleaned from the jet collection at HLT level.

A tag and probe method [42] was used to derive identification, isolation scale factors and electron trigger efficiencies. The full reference selection was first applied with the exception of trigger, b-tagging and electron veto requirements, while in addition, a second loose electron

was required. A Z mass constraint was placed on the two electrons in the event by requiring them to have an invariant mass of between 60 GeV and 120 GeV, thus ensuring that the pair of electrons originated from a Z boson decay. The tight ('tag') electron requirements were $p_T > 30 \text{ GeV}$, $|\eta| < 0.8$, relative isolation < 0.1 , MVA identification > 0.9 , $d_{xy} < 0.02 \text{ cm}$ and reconstructed at HLT level. The loose ('probe') electron requirements were $p_T > 30 \text{ GeV}$, $|\eta| < 2.5$ and $d_{xy} < 2 \text{ cm}$.

Fits were then performed, firstly of the invariant mass of all pairs of tag and probe electrons, and secondly after applying the identification and isolation criteria to the probe electrons, to the invariant mass distribution of pairs of tag and probe electrons in which the probe electron passed the identification and isolation criteria. The fit was implemented in both Monte Carlo simulation and in data, and a Breit-Wigner distribution convoluted with a Crystal Ball function is used to model the invariant mass of the tag and probe electrons, with a falling exponential used to model the background distribution. The Breit-Wigner distribution takes a form similar to that of a Gaussian distribution, with flatter tails [34]. The Crystal Ball function is also based on a Gaussian distribution, but with a power-law tail to the lower end [100, 73, 107]. Both of these functions are commonly used to model the mass peaks of resonances. The result of this fitting procedure in data can be seen in Figure 7.5.

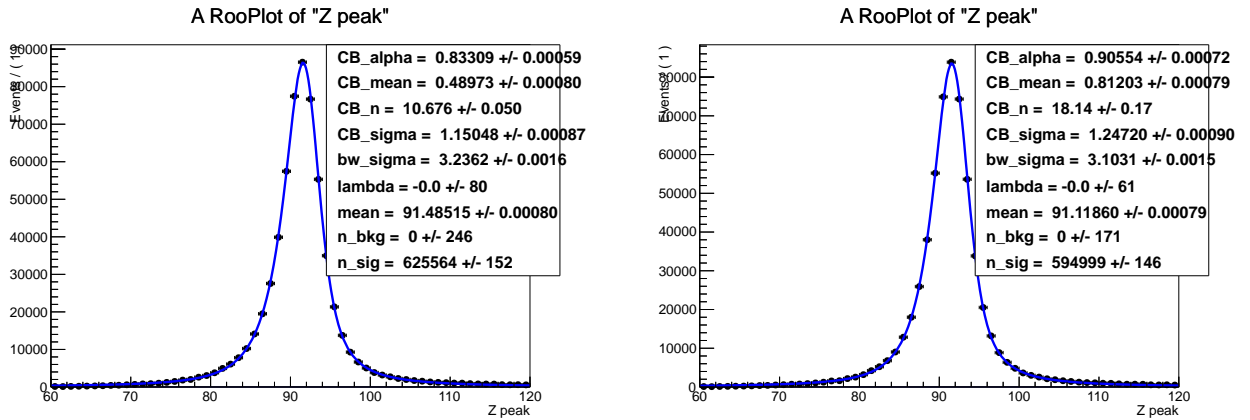


Figure 7.5: Fits of the invariant mass distribution of all tag-and-probe pairs (left) and tag-and-probe pairs in which the probe satisfies the identification and isolation criteria (right).

The efficiency of the identification and isolation process is then calculated using the numbers

extracted from the fits, in bins of p_T and η of the probe electron, as follows:

$$\epsilon(\text{identification and isolation}) = \frac{N_{\text{probe, passing}}^{\text{fit}}}{N_{\text{probe, all}}^{\text{fit}}} \quad (7.1)$$

where $N_{\text{probe, all}}^{\text{fit}}$ is the total number of events with tag and probe electrons and $N_{\text{probe, passing}}^{\text{fit}}$ is the subset in which the probe passes identification and isolation criteria.

The scale factor is then calculated as the ratio between the efficiencies in simulation and in data. The efficiencies in both can be seen to be similar in Figure 7.6, leading to scale factors close to one.

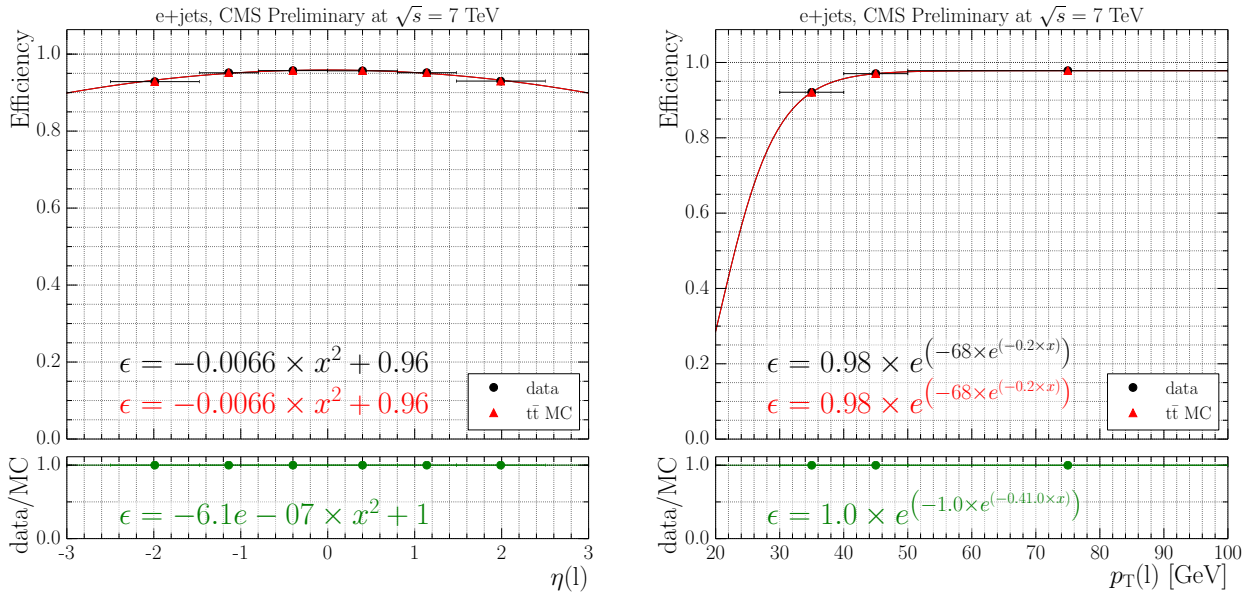


Figure 7.6: Identification and isolation efficiencies as a function of η and p_T in data and $t\bar{t}$ Monte Carlo simulation.

The efficiency of the electron part of the trigger is then similarly calculated, with respect to the identification and isolation requirements, meaning the events passing the identification and isolation requirements in the previous stage are then used as the baseline for the trigger efficiency. The subset of these in which the probe electron matches a HLT electron is then used to calculate the efficiency as follows:

$$\epsilon(\text{trigger}) = \frac{N_{\text{probe, matching HLT}}^{\text{fit}}}{N_{\text{probe, identification and isolation}}^{\text{fit}}} \quad (7.2)$$

where $N_{\text{probe,identification and isolation}}^{\text{fit}}$ is the number of events passing from equation 7.2 and $N_{\text{probe, matching HLT}}^{\text{fit}}$ is the subset in which the probe is matched to an HLT electron object.

In order to calculate the efficiency of the hadron leg of the trigger, the full selection with only the electron part of the trigger and without b-tagging, applied to the SingleElectron dataset, is taken as the baseline. The number of these events passing the hadronic leg of the trigger is then used to calculate the hadronic leg efficiency as follows:

$$\epsilon(\text{hadron leg}) = \frac{N_{\text{hadron leg, passing}}}{N_{\text{passing selection}}} \quad (7.3)$$

where $N_{\text{passing selection}}$ is the number of events passing the baseline selection with the electron leg of the trigger and no b-tagging requirements, and $N_{\text{hadron leg, passing}}$ is the subset in which the hadron leg of the trigger is satisfied.

The scale factors are produced in bins of p_T and η of the fourth most energetic jet, since this is the lowest energy jet that is selected. Parametrising as a function of higher energy jets would lead to a bias towards high efficiencies as the trigger will have a higher efficiency at higher jet energies.

Equivalent fit and efficiency plots for the trigger are included in Figures B.3 and B.4 in Appendix B.2.

8 | Differential Cross Sections: Fitting, Unfolding and Measurement

8.1 Data-MC Comparison

Following the full event selection, the simulated events are scaled to match the luminosity of the data using the scale factor:

$$S = \frac{\mathcal{L} \times \sigma}{N_{\text{processed}}} \quad (8.1)$$

where $N_{\text{processed}}$ is the total number of events processed for each Monte Carlo sample and σ is the production cross section of each process. The numbers of events passing each selection step in data and in Monte Carlo simulation, after scaling to the measured luminosities, are shown for both the electron+jets and muon+jets channels at $\sqrt{s} = 7 \text{ TeV}$ in Table 8.1, and at $\sqrt{s} = 8 \text{ TeV}$ in Table 8.2.

The distributions of the primary variables E_T^{miss} , H_T , S_T , p_T^W and M_T^W after the full selection requirements are applied, are shown in Figures 8.1 and 8.2 for the electron and muon channels respectively at $\sqrt{s} = 7 \text{ TeV}$; and in Figures 8.3 and 8.4 respectively at $\sqrt{s} = 8 \text{ TeV}$. The normalisations and shapes are all obtained from simulation except in the case of QCD, for which only the normalisation is taken from simulation, and the shape is obtained from data, as explained in Section 7.3.5: the conversion region is used in the electron channel and the non-isolated region is used in the muon channel. In general there is good agreement between data and simulation. The distributions in simulation peak at slightly higher energies because event reweighting to account for the p_T mismodelling of the top quark in simulation (see Section 9.1.2) has not yet been carried out at this stage.

8. Differential Cross Sections: Fitting, Unfolding and Measurement

Table 8.1: Expected and observed event yields at several stages of the electron+jets selection (upper) and the muon+jets channel selection (lower) at $\sqrt{s}=7\text{ TeV}$.

Selection step	t̄ + jets	W + jets	Z + jets	Single-Top	QCD	Sum MC	Data
Preselection	248837 \pm 131	296487 \pm 255	87027 \pm 237	26397 \pm 43	24578753 \pm 81165	25237503 \pm 81166	4928736
Event cleaning/HLT	248712 \pm 131	296343 \pm 255	86964 \pm 237	26385 \pm 43	24574668 \pm 81161	25233075 \pm 81162	1103841
One isolated electron	70973 \pm 69	91618 \pm 132	26311 \pm 122	5355 \pm 17	263313 \pm 6601	457572 \pm 6604	299020
Muon veto	67163 \pm 67	91581 \pm 132	26196 \pm 122	5269 \pm 17	263195 \pm 6601	453405 \pm 6604	295961
Dilepton veto	66336 \pm 67	91559 \pm 132	20560 \pm 107	5251 \pm 17	263183 \pm 6601	446892 \pm 6603	289456
Conversion veto	64497 \pm 66	87866 \pm 130	19671 \pm 105	5106 \pm 16	174315 \pm 5761	351458 \pm 5763	243472
≥ 1 jets	64497 \pm 66	87866 \pm 130	19671 \pm 105	5106 \pm 16	174315 \pm 5761	351457 \pm 5763	243471
≥ 2 jets	64489 \pm 66	87789 \pm 130	19633 \pm 105	5104 \pm 16	173680 \pm 5748	350697 \pm 5750	243446
≥ 3 jets	63514 \pm 65	82167 \pm 123	18188 \pm 101	4912 \pm 16	126305 \pm 4416	295088 \pm 4420	236124
≥ 4 jets	35285 \pm 48	17935 \pm 42	3618 \pm 45	1461 \pm 8	21354 \pm 1507	79656 \pm 1509	71414
≥ 1 b-tagged jets	29777 \pm 44	2764 \pm 17	562 \pm 17	1160 \pm 7	3601 \pm 513	37864 \pm 516	34671
≥ 2 b-tagged jets	13777 \pm 30	326 \pm 4	76 \pm 6	434 \pm 4	590 \pm 220	15205 \pm 222	13792
Selection step	t̄ + jets	W + jets	Z + jets	Single-Top	QCD	Sum MC	Data
Preselection	248280 \pm 131	296599 \pm 255	87128 \pm 237	26362 \pm 43	18658866 \pm 41697	19317237 \pm 41699	4201249
Event cleaning/HLT	248155 \pm 131	296455 \pm 255	87065 \pm 237	26350 \pm 43	18655836 \pm 41690	19313864 \pm 41692	444679
One isolated muon	74418 \pm 71	93902 \pm 132	22774 \pm 115	5724 \pm 19	45516 \pm 2160	242336 \pm 2168	206738
Second muon veto	73036 \pm 70	93893 \pm 132	14109 \pm 89	5690 \pm 19	44741 \pm 2153	231470 \pm 2161	194980
Electron veto	69681 \pm 69	93852 \pm 132	14020 \pm 89	5615 \pm 19	44666 \pm 2153	227835 \pm 2160	192335
≥ 1 jets	69680 \pm 69	93851 \pm 132	14020 \pm 89	5615 \pm 19	44648 \pm 2153	227816 \pm 2160	192335
≥ 2 jets	69675 \pm 69	93791 \pm 132	14007 \pm 89	5613 \pm 19	43404 \pm 2139	226492 \pm 2146	192310
≥ 3 jets	69054 \pm 68	89508 \pm 126	13186 \pm 86	5455 \pm 18	14627 \pm 1059	191831 \pm 1072	186061
≥ 4 jets	38222 \pm 50	19234 \pm 42	2707 \pm 38	1573 \pm 8	2028 \pm 242	63766 \pm 254	54684
≥ 1 b-tagged jets	32268 \pm 46	2965 \pm 16	463 \pm 15	1250 \pm 7	873 \pm 148	37821 \pm 157	30852
≥ 2 b-tagged jets	15016 \pm 30	355 \pm 5	60 \pm 5	468 \pm 4	180 \pm 48	16081 \pm 58	13128

Table 8.2: Expected and observed event yields at several stages of the electron+jets selection (upper) and the muon+jets selection (lower) at $\sqrt{s}=8\text{ TeV}$.

Selection step	t̄ + jets	W + jets	Z + jets	Single-Top	QCD	Sum MC	Data
Preselection	1389239 \pm 1071	1748404 \pm 1149	385132 \pm 236	170598 \pm 265	131270649 \pm 477929	134964023 \pm 477932	13219192
Event cleaning/HLT	376950 \pm 547	493785 \pm 573	143253 \pm 138	35559 \pm 122	3844108 \pm 83191	4893656 \pm 83195	5952438
One isolated electron	335908 \pm 515	427471 \pm 520	95501 \pm 111	31520 \pm 115	554050 \pm 27723	1444453 \pm 27733	1754243
Muon veto	316823 \pm 500	427354 \pm 520	95069 \pm 111	30820 \pm 113	553991 \pm 27723	1424058 \pm 27733	1733585
Dilepton veto	312321 \pm 497	427247 \pm 520	70836 \pm 96	30648 \pm 113	553952 \pm 27723	1395005 \pm 27733	1692425
Conversion veto	304300 \pm 490	411661 \pm 510	68005 \pm 94	29849 \pm 111	309968 \pm 20284	1123785 \pm 20297	1447105
≥ 1 jets	304300 \pm 490	411658 \pm 510	68005 \pm 94	29849 \pm 111	309968 \pm 20284	1123781 \pm 20297	1447105
≥ 2 jets	304264 \pm 490	411028 \pm 510	67901 \pm 94	29834 \pm 111	307974 \pm 20200	1121003 \pm 20213	1446970
≥ 3 jets	299232 \pm 486	372483 \pm 472	61904 \pm 87	28518 \pm 109	226054 \pm 16034	988193 \pm 16049	1251530
≥ 4 jets	172557 \pm 369	76326 \pm 175	13484 \pm 35	9524 \pm 64	43901 \pm 4145	315795 \pm 4165	361692
≥ 1 b-tagged jets	142836 \pm 332	10417 \pm 65	2019 \pm 13	7296 \pm 55	8705 \pm 1812	171275 \pm 1845	181705
≥ 2 b-tagged jets	63233 \pm 215	1114 \pm 21	291 \pm 4	2566 \pm 32	2427 \pm 1660	69632 \pm 1675	72176
Selection step	t̄ + jets	W + jets	Z + jets	Single-Top	QCD	Sum MC	Data
Preselection	1400798 \pm 1080	1765900 \pm 1159	389320 \pm 239	171677 \pm 266	104820777 \pm 238065	108548474 \pm 238070	20815265
Event cleaning/HLT	469828 \pm 622	669486 \pm 711	153379 \pm 147	46228 \pm 141	1673119 \pm 33684	3012042 \pm 33698	3166723
One isolated muon	385092 \pm 562	496720 \pm 582	92752 \pm 111	37012 \pm 126	89801 \pm 6391	1101379 \pm 6444	1373749
Second muon veto	377038 \pm 556	496660 \pm 582	54606 \pm 85	36705 \pm 126	89060 \pm 6380	1054070 \pm 6433	1292713
Electron veto	358624 \pm 542	496506 \pm 582	54260 \pm 85	36049 \pm 124	89037 \pm 6380	1034478 \pm 6431	1274884
≥ 1 jets	358624 \pm 542	496498 \pm 582	54259 \pm 85	36049 \pm 124	89037 \pm 6380	1034470 \pm 6431	1274884
≥ 2 jets	358592 \pm 542	495658 \pm 581	54186 \pm 85	36029 \pm 124	88048 \pm 6354	1032515 \pm 6405	1274817
≥ 3 jets	354271 \pm 539	448652 \pm 534	49426 \pm 78	34498 \pm 122	34560 \pm 2810	921409 \pm 2914	1138923
≥ 4 jets	202771 \pm 407	90874 \pm 199	10999 \pm 32	11233 \pm 71	8003 \pm 1304	323883 \pm 1383	351087
≥ 1 b-tagged jets	168125 \pm 367	12499 \pm 73	1715 \pm 12	8660 \pm 61	4252 \pm 1036	195253 \pm 1104	197025
≥ 2 b-tagged jets	74995 \pm 238	1367 \pm 23	229 \pm 4	3023 \pm 35	527 \pm 410	80143 \pm 476	81047

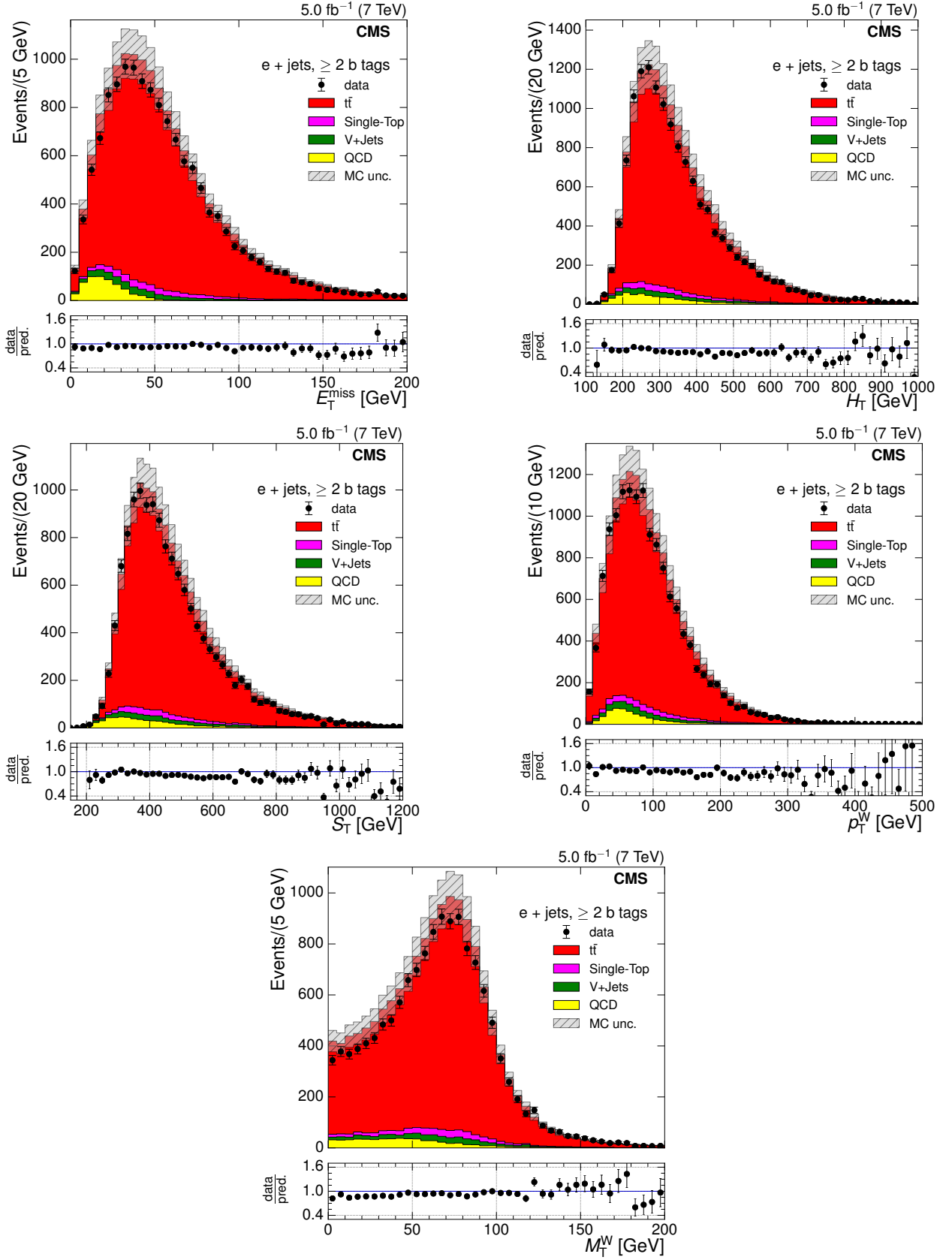


Figure 8.1: Comparison of Monte Carlo simulation to data in the electron+jets channel after final selection at $\sqrt{s} = 7 \text{ TeV}$ for E_T^{miss} (upper left), H_T (upper right), S_T (middle left), p_T^W (middle right) and M_T^W (lower). The shaded region represents the $t\bar{t}$ MC normalisation uncertainty. The lower plots show the ratio of the sum of simulated events to the data.

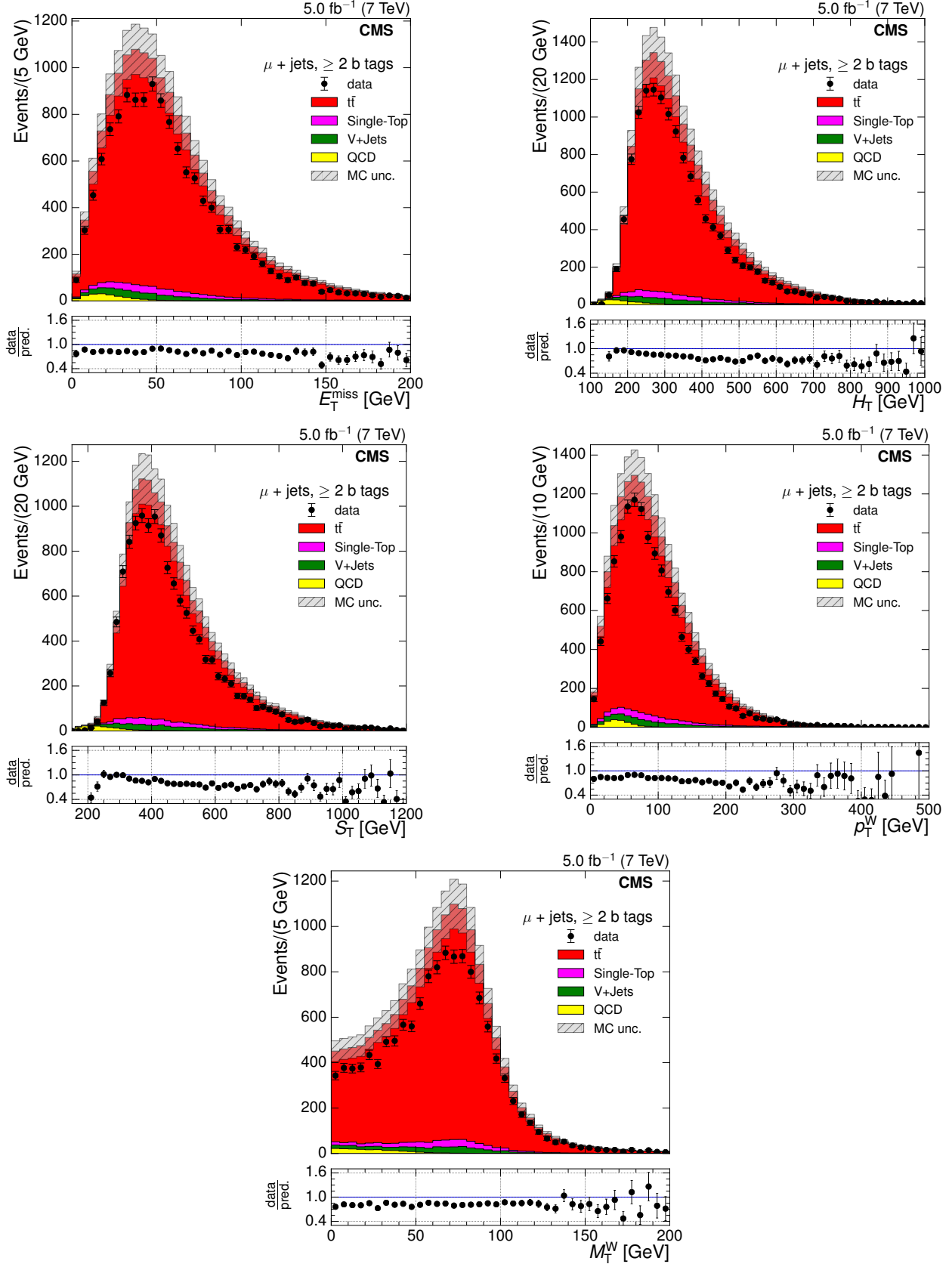


Figure 8.2: Comparison of Monte Carlo simulation to data in the muon+jets channel after final selection at $\sqrt{s} = 7 \text{ TeV}$ for E_T^{miss} (upper left), H_T (upper right), S_T (middle left), p_T^W (middle right) and M_T^W (lower). The shaded region represents the $t\bar{t}$ MC normalisation uncertainty. The lower plots show the ratio of the sum of simulated events to the data.

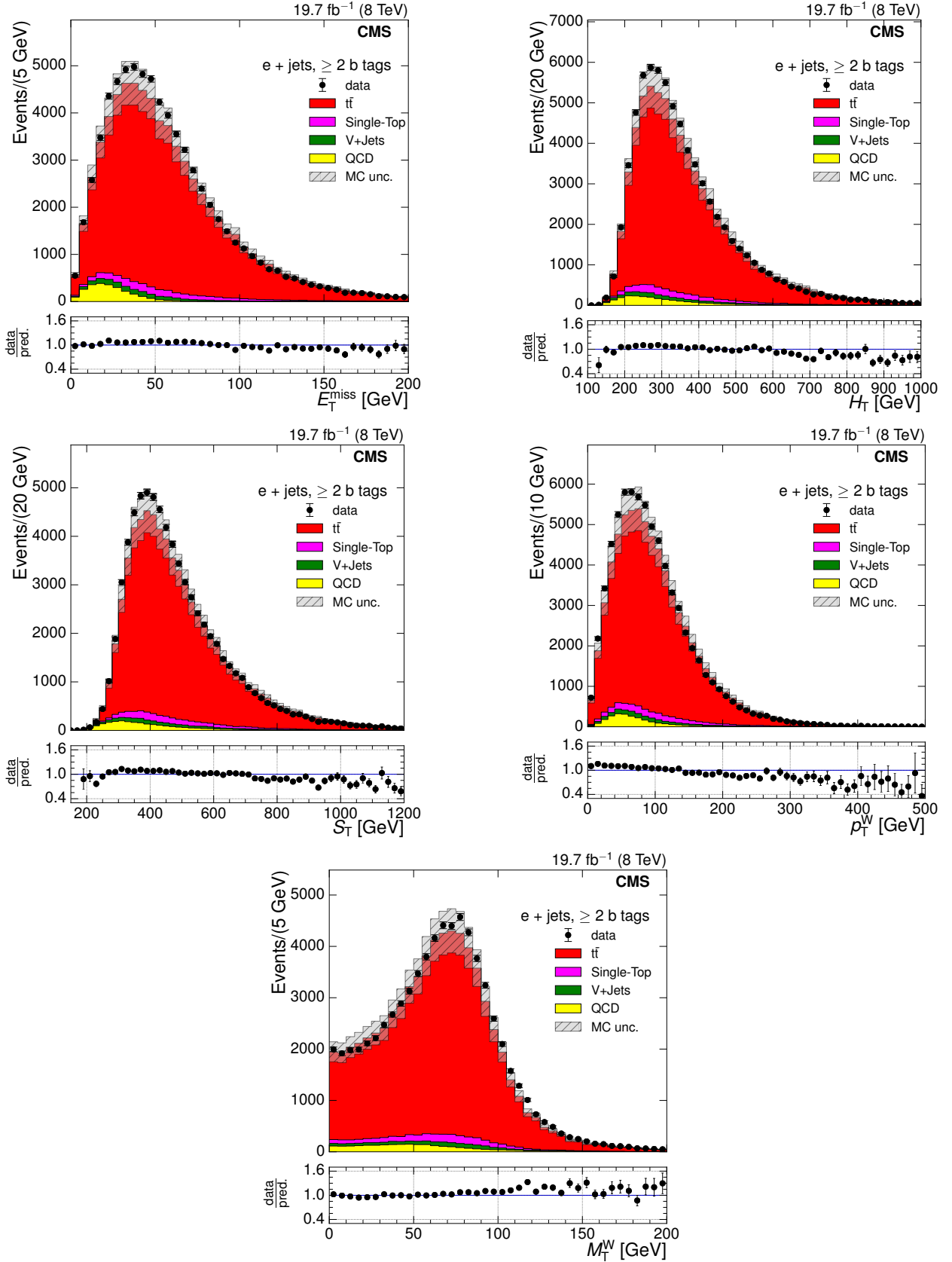


Figure 8.3: Comparison of Monte Carlo simulation to data in the electron+jets channel after final selection at $\sqrt{s} = 8 \text{ TeV}$ for E_T^{miss} (upper left), H_T (upper right), S_T (middle left), p_T^W (middle right) and M_T^W (lower). The shaded region represents the $t\bar{t}$ MC normalisation uncertainty. The lower plots show the ratio of the sum of simulated events to the data.

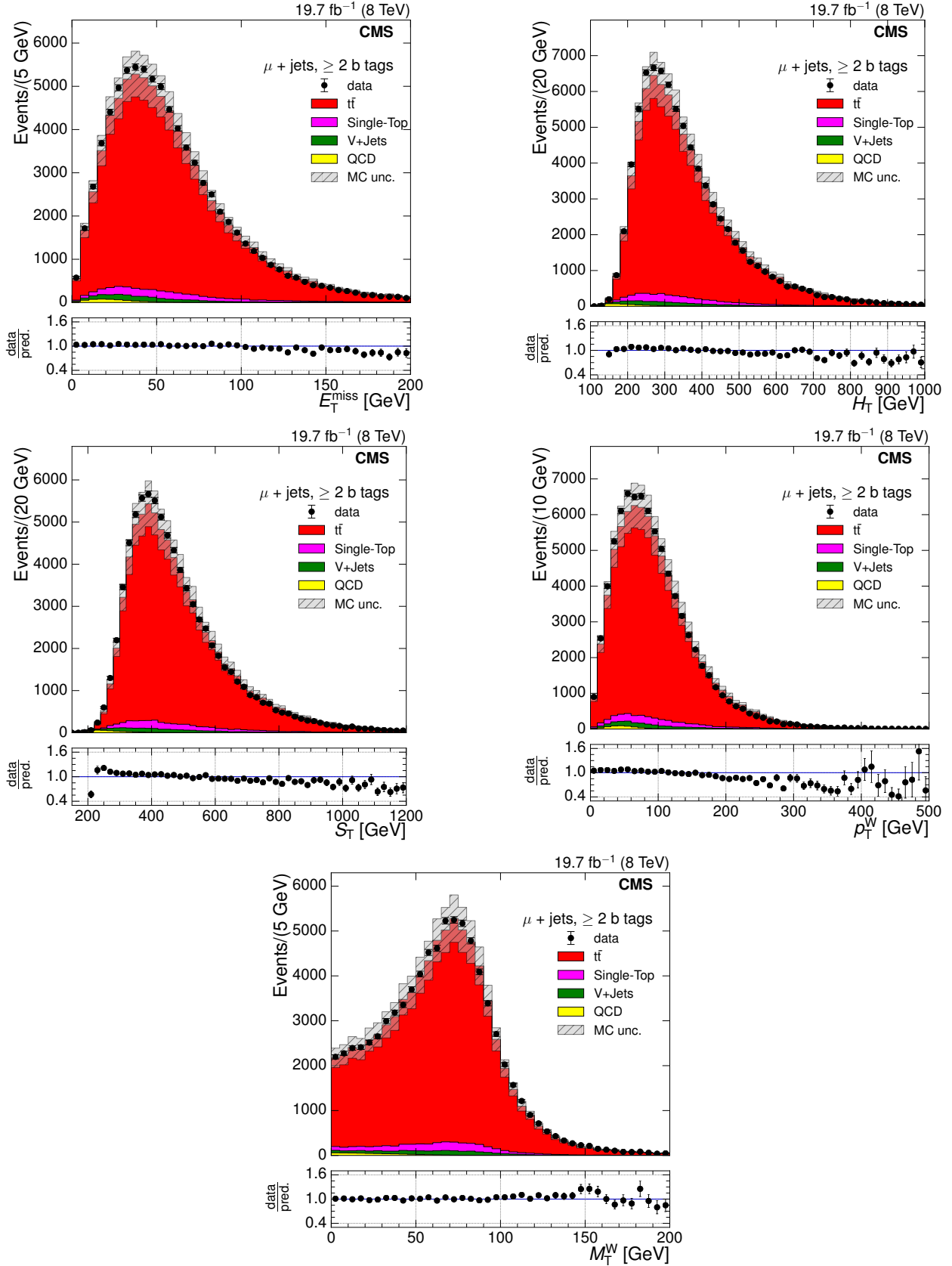


Figure 8.4: Comparison of Monte Carlo simulation to data in the muon+jets channel after final selection at $\sqrt{s} = 8 \text{ TeV}$ for E_T^{miss} (upper left), H_T (upper right), S_T (middle left), p_T^W (middle right) and M_T^W (lower). The shaded region represents the $t\bar{t}$ MC normalisation uncertainty. The lower plots show the ratio of the sum of simulated events to the data.

8.2 Binning Choice

The differential cross sections in this analysis are measured in bins of the primary variable distributions. The choice of bin sizes and boundaries are significant because events generated in one bin can move into another bin after reconstruction due to the finite resolution of the detector. This altering of the number of events, as a result of events moving into and/or out of a bin, is also important to understand so that the final reconstructed distribution can be deconvoluted (unfolded) to the true distribution (Section 8.6). Migration of events between bins is taken into account in the binning choice by evaluating two variables defined as purity (p^k) and stability (s^k), which are functions of how well a variable is reconstructed:

$$p^k = \frac{N_{\text{rec}&\text{gen}}^k}{N_{\text{rec}}^k} \quad (8.2)$$

$$s^k = \frac{N_{\text{rec}&\text{gen}}^k}{N_{\text{gen}}^k}. \quad (8.3)$$

$N_{\text{rec}&\text{gen}}^k$ is the number of events generated and reconstructed in bin k , N_{rec}^k is the number of events reconstructed in bin k and N_{gen}^k is the number of events generated in bin k . The stability of a bin is sensitive to the migration of events out of a bin, while the purity is sensitive to the migration of events into a bin (see Figure 8.5).

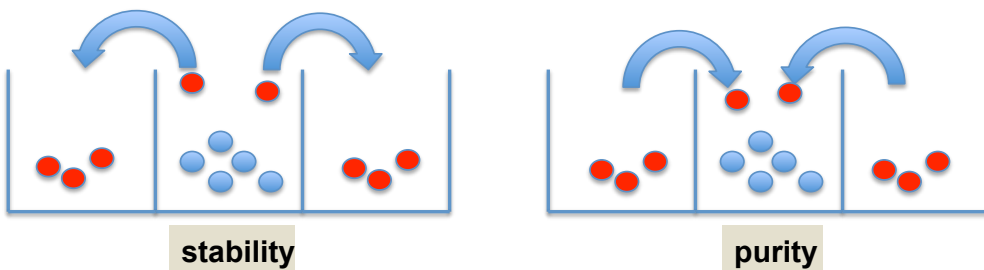


Figure 8.5: Stability quantifies the migration of events out of a bin while purity quantifies the migration of events into a bin. Both quantities compare the bin in which an event is generated to the range in which they are reconstructed.

A high number of bins allows for a fine granularity in the measurement, but bins must also be selected such that good statistics are maintained in all bins, thereby avoiding the large relative statistical error that would result from small bins with few events.

In light of the requirements of minimising event migration between bins and maintaining sufficient numbers of events, the bin boundaries for each primary variable distribution were chosen such that all bins have

- purity and stability values of 0.5 or greater
- at least 100 events

This means that at least half of the events generated in a bin remain in that bin after reconstruction, and that at least half of the events reconstructed in a bin were generated in that bin. Although, ideally, higher values of purity and stability would have been preferable to further minimise bin-to-bin migration, and thereby reduce the unfolding uncertainty and the amount of regularisation needed in the unfolding procedure (Section 8.6), a compromise between minimising migration and adequate statistics was required.

The determination of the bin boundaries following these criteria is carried out simultaneously in (and therefore the binning is identical in) both centre of mass energies and both the electron+jets and muon+jets channel. Plots of generated versus reconstructed events in simulation for all primary variables are shown in the electron+jets channel in Figure 8.6 for $\sqrt{s} = 7 \text{ TeV}$ and in Figure 8.7 for $\sqrt{s} = 8 \text{ TeV}$. The corresponding plots in the muon+jets channel are shown in Figures B.5 and B.6 in Appendix B.3.

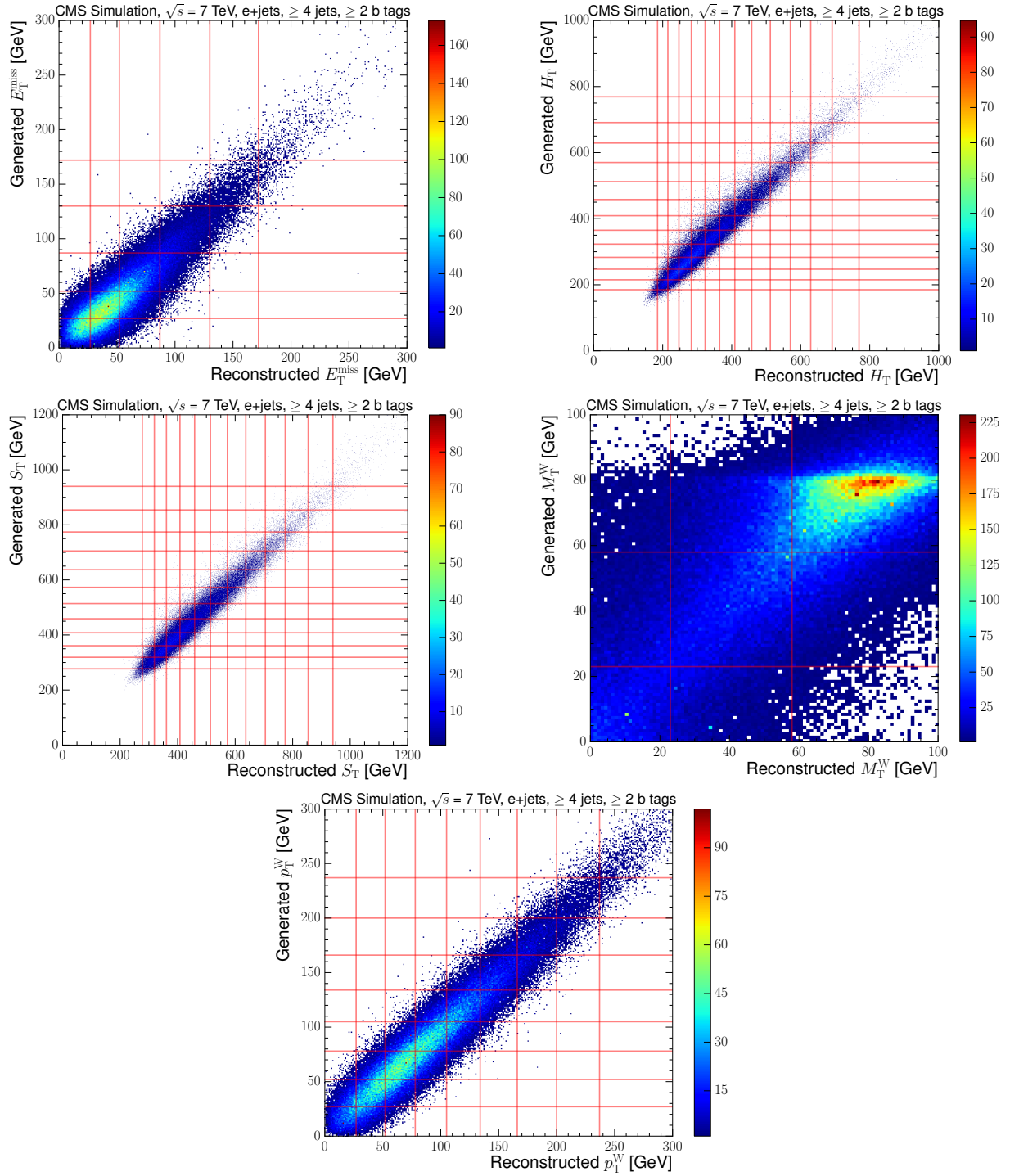


Figure 8.6: Generated versus reconstructed distributions of the primary variables E_T^{miss} (upper left), H_T (upper right), S_T (middle left), M_T^W (middle right) and p_T^W (lower) with horizontal and vertical lines representing the boundaries of the selected bins at $\sqrt{s} = 7$ TeV in the electron+ jets channel. These distributions are obtained using $t\bar{t}$ simulation.

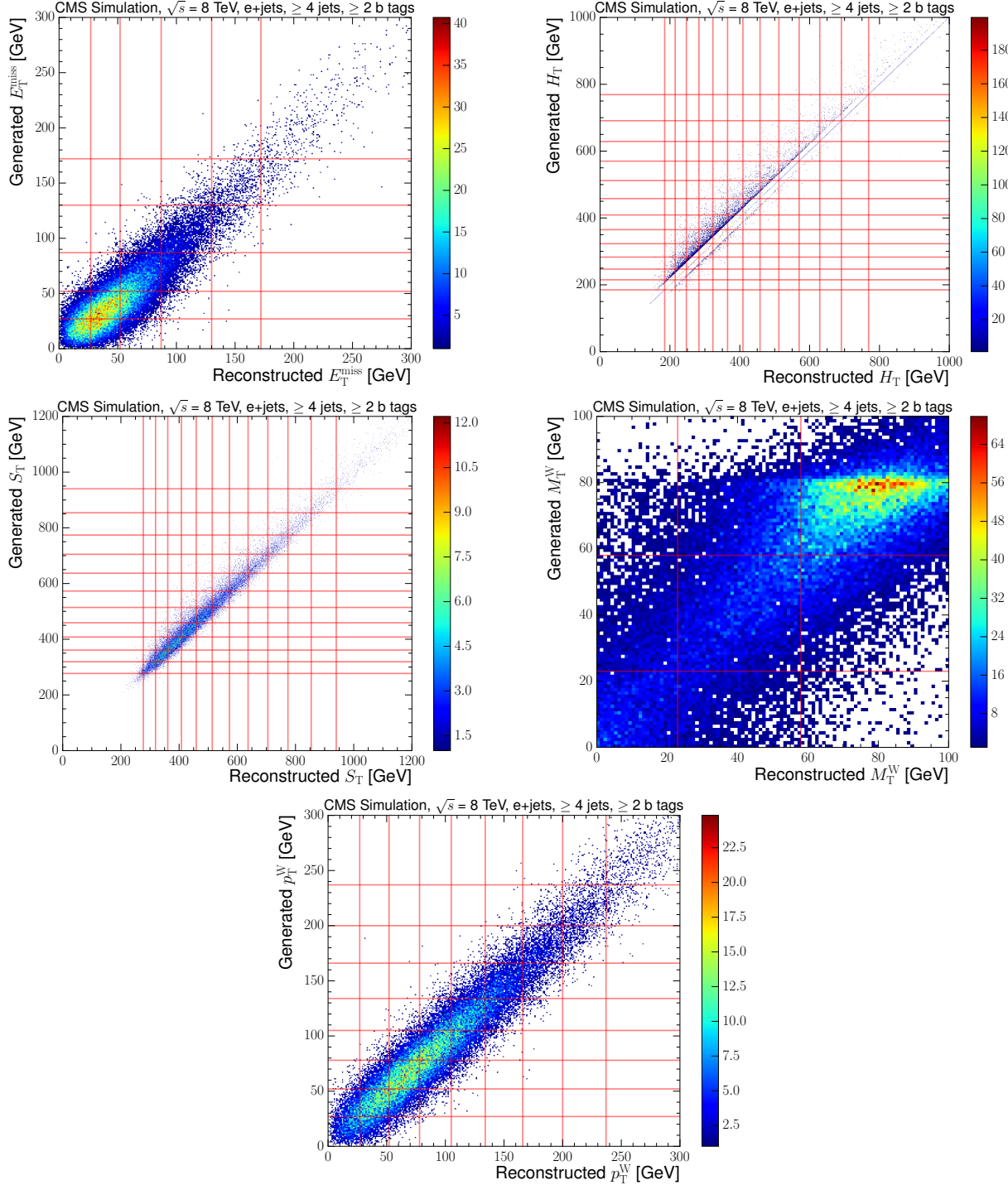


Figure 8.7: Generated versus reconstructed distributions of the primary variables E_T^{miss} (upper left), H_T (upper right), S_T (middle left), M_T^W (middle right) and p_T^W (lower) with horizontal and vertical lines representing the boundaries of the selected bins at $\sqrt{s} = 8 \text{ TeV}$ in the electron+ jets channel. These distributions are obtained using $t\bar{t}$ simulation.

8.3 Maximum Likelihood Fit

A maximum log likelihood fit of four process shapes, or templates, to data in each bin of the primary variables is used to obtain the number of events from each process in each bin. The four templates used are:

- $t\bar{t}$
- single-top
- $V+jets$ ($W+jets + Z+jets$)
- QCD multi-jet

The fit is carried out in three fitting variables, because no individual variable is able to distinguish between all four templates in the fit. The following three fitting variables are used:

- the absolute pseudorapidity of the lepton ($|\eta|$)
- the three-dimensional angle between the lepton and the nearest b-jet (α)
- invariant mass of the three jets with the highest p_T sum ($M3$)

The fit is carried out by maximising the log of the likelihood function (LL):

$$LL(x_i, d_i) = -2 \log \prod_i \frac{x_i^{d_i} \cdot e^{-x_i}}{d_i!} = -2 \sum_i \log \left(\frac{x_i^{d_i} \cdot e^{-x_i}}{d_i!} \right). \quad (8.4)$$

where i is the bin index in the template, x_i is the total of all the templates in bin i , and d_i is the observed number of data events in bin i . x_i is defined to be

$$x_i = \sum_j N_j x_{ij}, \text{ with } \sum_i x_{ij} = 1 \text{ for each process.} \quad (8.5)$$

where x_{ij} represents the templates and N_j represents the normalisations of the templates i.e. the fit parameters. Fitting using more than one variable (the three aforementioned fitting

variables), the log likelihoods are summed:

$$LL(x, d) = -\frac{2}{n} \sum_{k=1,n} \log L_k \quad (8.6)$$

where L_k is the likelihood function of each of the different fit variables. Here the division by n accounts for the fact that the same information is used in all three fit variables, and so full correlation is assumed between the three fitting variables, which provides a conservative estimate of the uncertainties in the resulting fitted parameters. The fit operates by adjusting the normalisation of each template with the aim of equating x_i and d_i in each bin of each template. The starting normalisations in the templates are obtained from simulation after the full selection has been applied (this includes the QCD template, although the shape for this is obtained from data).

8.3.1 Choice of templates

$t\bar{t}$, single-top and V+jets templates are taken from simulation, while the QCD template is extracted from data as described in Section 7.3.5. The W+jets and Z+jets templates are combined firstly due to the similar shapes of the distributions in these two background processes, and secondly due to limited statistics available in simulation. The four template shapes in each of the three fitting variables at $\sqrt{s} = 7$ TeV in both channels are shown in Figure 8.8. The corresponding plots for $\sqrt{s} = 8$ TeV are shown in Appendix B.4.

This combination of fitting variables was selected because they are only weakly correlated to the primary variables under investigation, and they show good discrimination between the four templates. Single top events have similar signatures to $t\bar{t}$ events, with a central lepton from the decay of the single top, leading to a single top template that is similar to the $t\bar{t}$ template in the electron $|\eta|$ and muon $|\eta|$ distributions. In the α distribution, the similarity is attributable to the fact that the closest b-jet from the lepton is generally a b-jet from the decay of a t-quark. However, the average boost for single top events is lower than in $t\bar{t}$ events, leading to a wider single top template. The $M3$ variable will be a combination of the

jets from the hadronically decaying t-quark (a b-jet and two other jets from the W-boson, which may include a second b-jet) in $t\bar{t}$ events, whereas in the other templates, $M3$ will simply correspond to some random combination of jets in the event. Hence, $M3$ shows the best discrimination between the single top and $t\bar{t}$ templates.

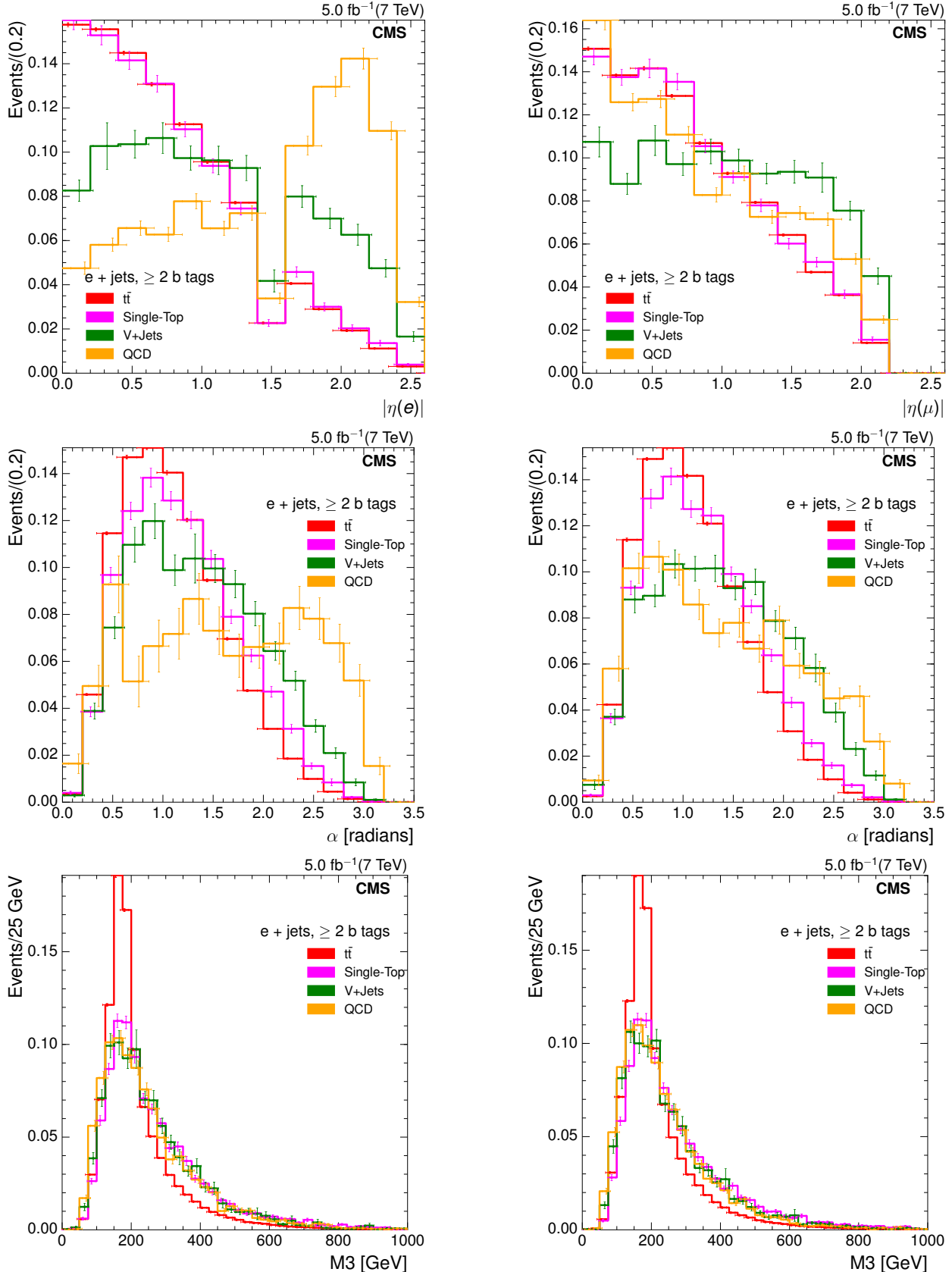


Figure 8.8: Normalised distributions of the templates, normalised to one, for the three fit variables lepton $|\eta|$ (upper), α (middle) and M_3 (lower), inclusive across all primary variable bins, at $\sqrt{s} = 7 \text{ TeV}$ in the electron+jets channel (left) and in the muon+jets channel (right). The marker points are spread along the bin width, and vertical error bars represent the statistical uncertainty.

The QCD templates, in particular those in higher bins of the primary variables, contain lower statistics than those in lower bins. Therefore, the inclusive QCD template shape, i.e. the QCD distribution over all bins, is used for the fitting process in every bin. Figure 8.9 shows a comparison between QCD templates at $\sqrt{s} = 8$ TeV in the lowest three bins of the E_T^{miss} variable and also the inclusive E_T^{miss} QCD template. It can be seen that the third E_T^{miss} bin already shows large statistical errors due to low numbers of events, and that the inclusive template is largely shaped by events in the first two bins. Therefore, the inclusive QCD template is used rather than those in individual bins.

An inclusive template is also used in the V+jets ($W+jets + Z+jets$) template for the same reason. Figure 8.10 shows a comparison between the V+jets templates at $\sqrt{s} = 8$ TeV in each E_T^{miss} bin and also the inclusive E_T^{miss} V+jets template. As is the case for the QCD background template, it can be seen in the V+jets templates that there are diminished statistics available in higher bins, and the inclusive template shape is largely governed by the lower bins.

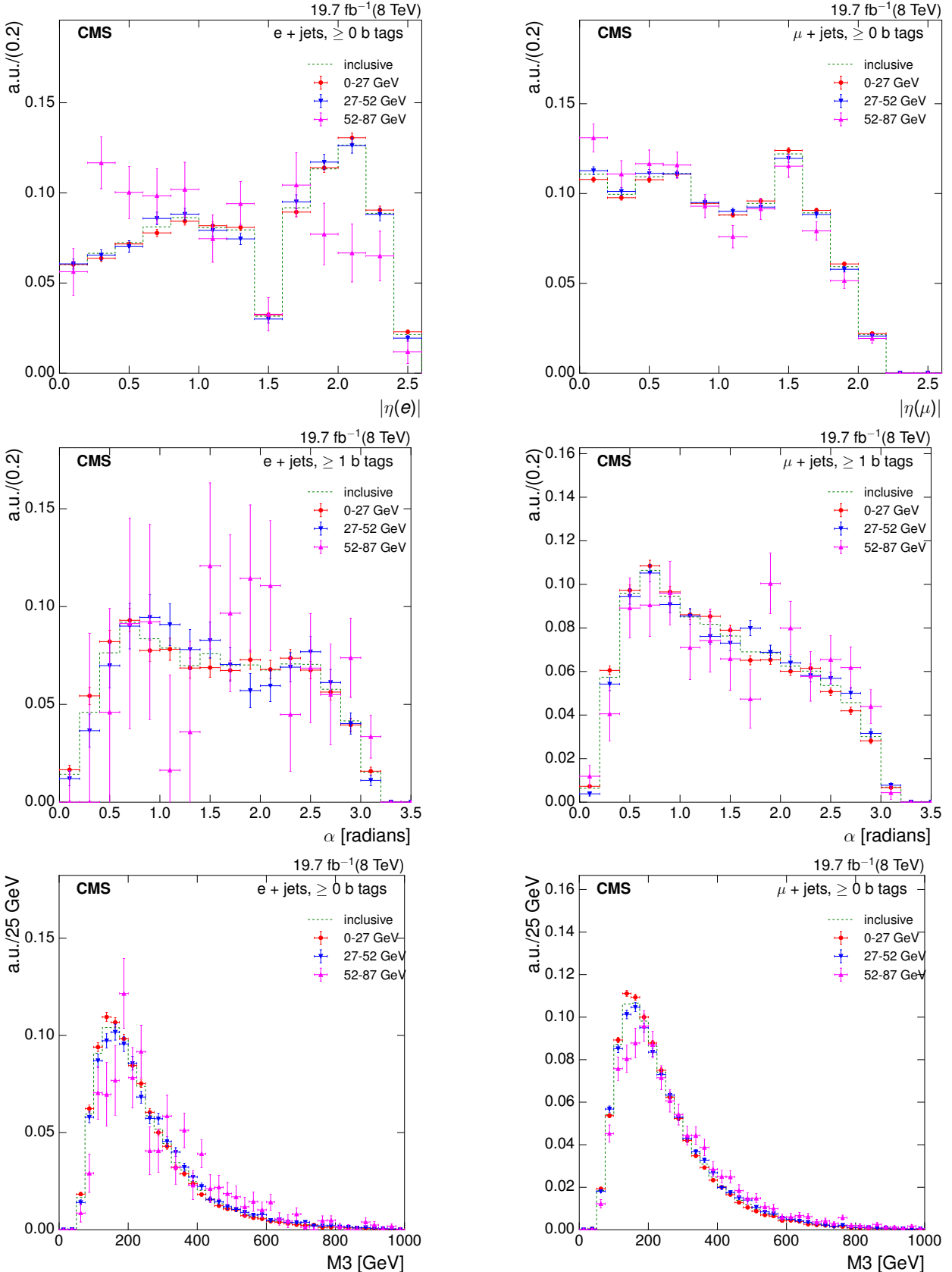


Figure 8.9: Normalised distributions of the QCD templates for the three fit variables lepton $|\eta|$ (upper), α (middle) and $M3$ (lower) inclusive across all E_T^{miss} bins and for the lowest three E_T^{miss} bins at $\sqrt{s} = 8 \text{ TeV}$ in the electron+jets channel (left) and in the muon+jets channel (right).

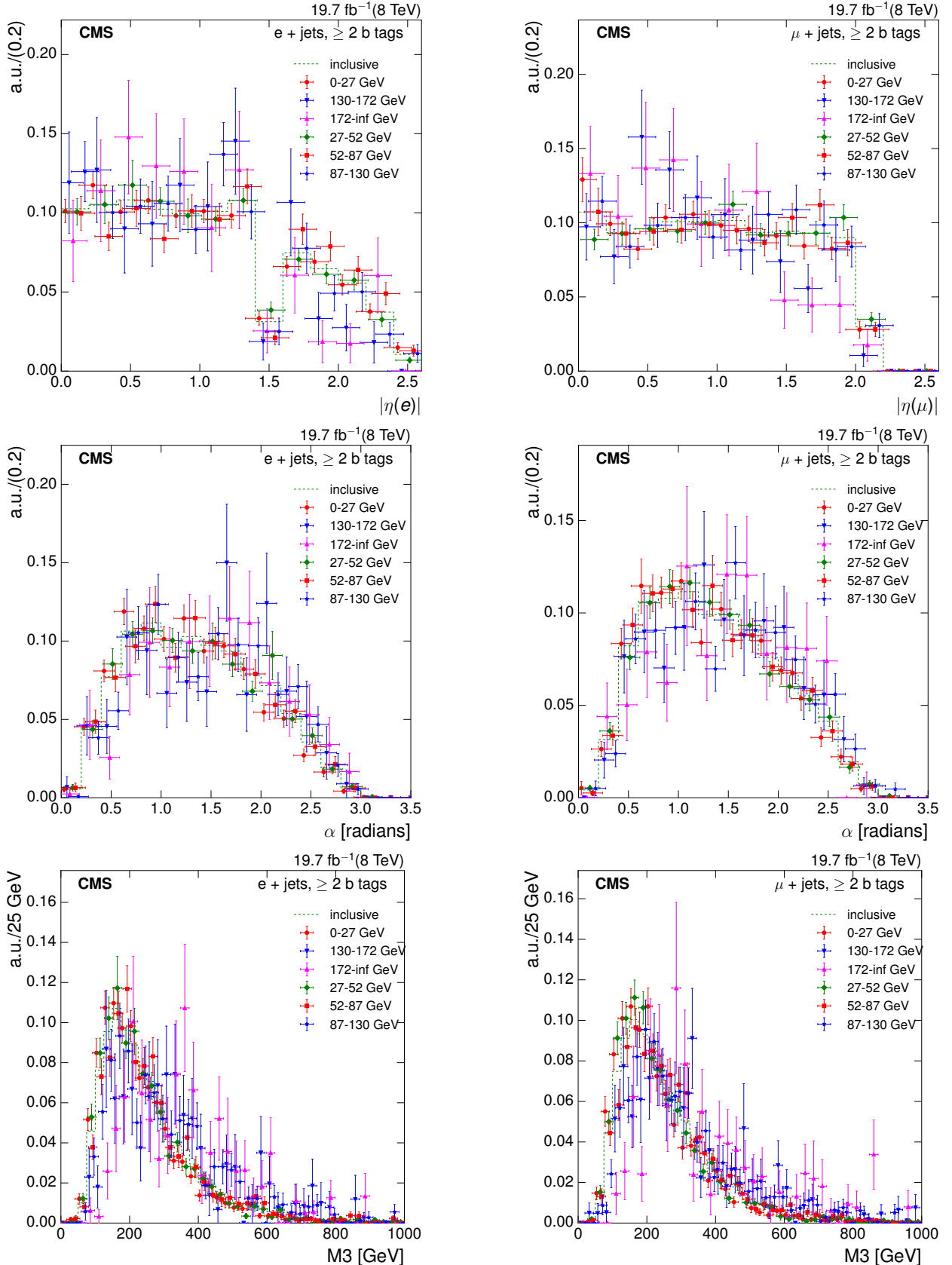


Figure 8.10: Normalised distributions of the $V + \text{jets}$ templates for the three fit variables lepton $|\eta|$ (upper), α (middle) and $M3$ (lower) inclusive across all E_T^{miss} bins and for the lowest three E_T^{miss} bins at $\sqrt{s} = 8 \text{ TeV}$ in the electron+jets channel (left) and in the muon+jets channel (right).

8.3.2 Fit Results

Comparisons of data to Monte Carlo simulation distributions of the primary variables, using normalisation results from the fit, are shown in Figures 8.11 and 8.12 for the electron and muon channels respectively at $\sqrt{s} = 7 \text{ TeV}$, and in Figures 8.13 and 8.14 for the electron and muon channels at $\sqrt{s} = 8 \text{ TeV}$. The corresponding numerical values from the fit can be found in Appendix B.5. Overall, there is broad agreement between the data and the simulation within fit uncertainties.

Similar post-fit comparisons of data to Monte Carlo simulation distributions of selected additional variables lepton $|\eta|$, lepton p_T , α , M_3 and N_{jets} are shown in Figures 8.15 and 8.16 for $\sqrt{s} = 7 \text{ TeV}$, and in Figures 8.17 and 8.18 for $\sqrt{s} = 8 \text{ TeV}$.

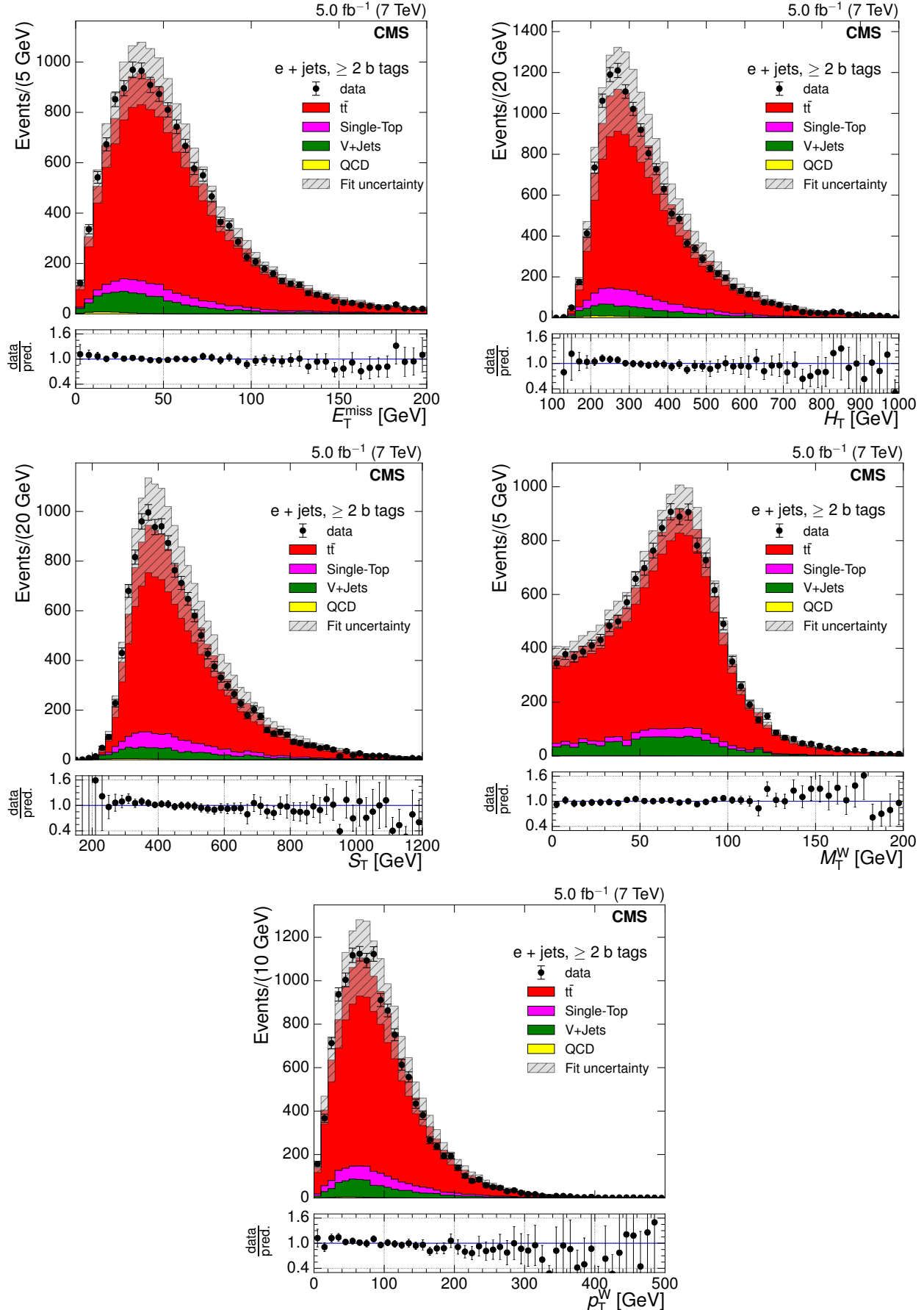


Figure 8.11: Comparison of Monte Carlo simulation to data distributions of primary variables, from top left, E_T^{miss} , H_T , S_T , M_T^W and p_T^W in the electron+jets channel after fitting at $\sqrt{s} = 7 \text{ TeV}$.

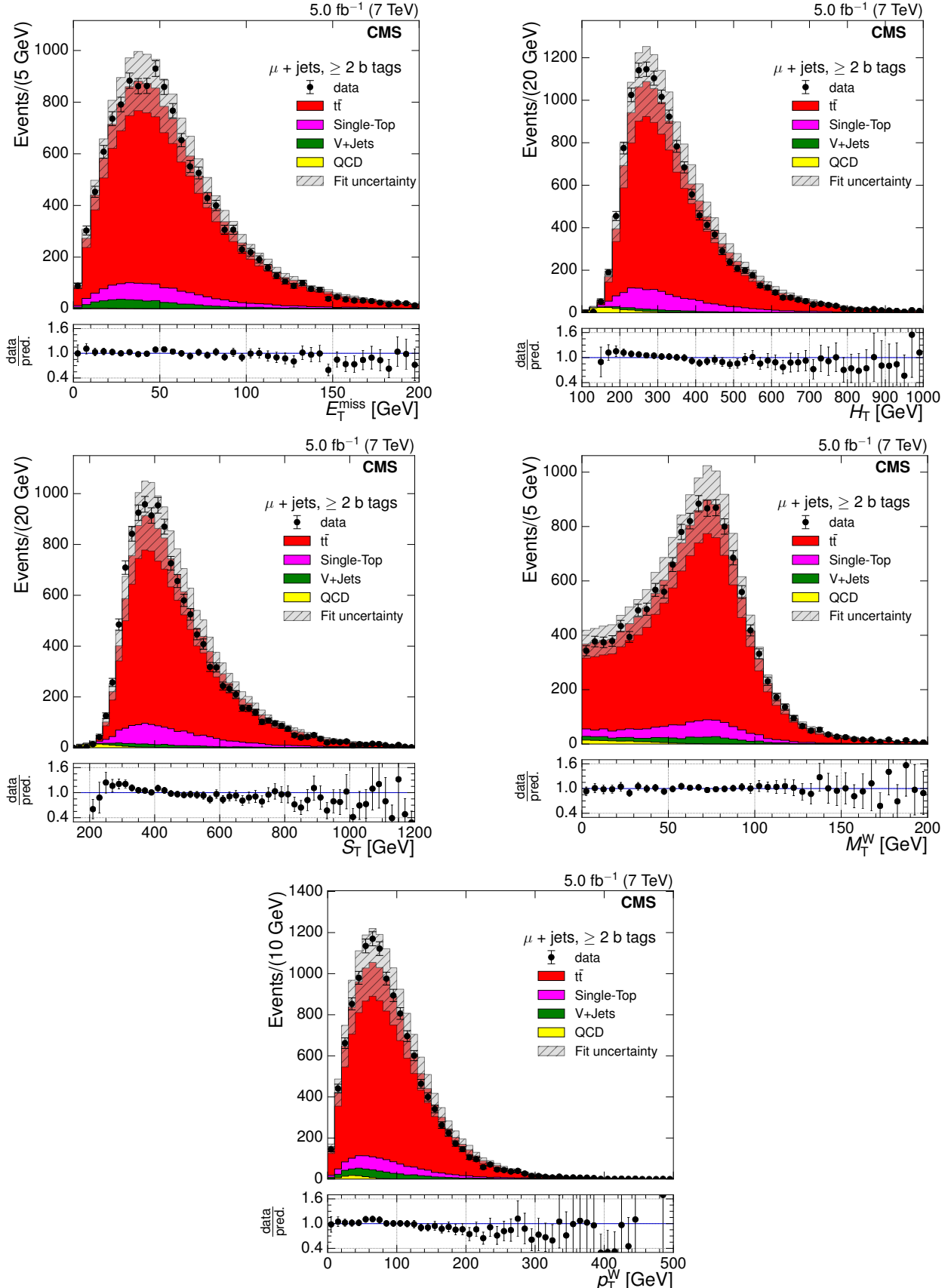


Figure 8.12: Comparison of Monte Carlo simulation to data distributions of primary variables, from top left, E_T^{miss} , H_T , S_T , M_T^W and p_T^W , in the muon+jets channel after fitting at $\sqrt{s} = 7\text{ TeV}$.

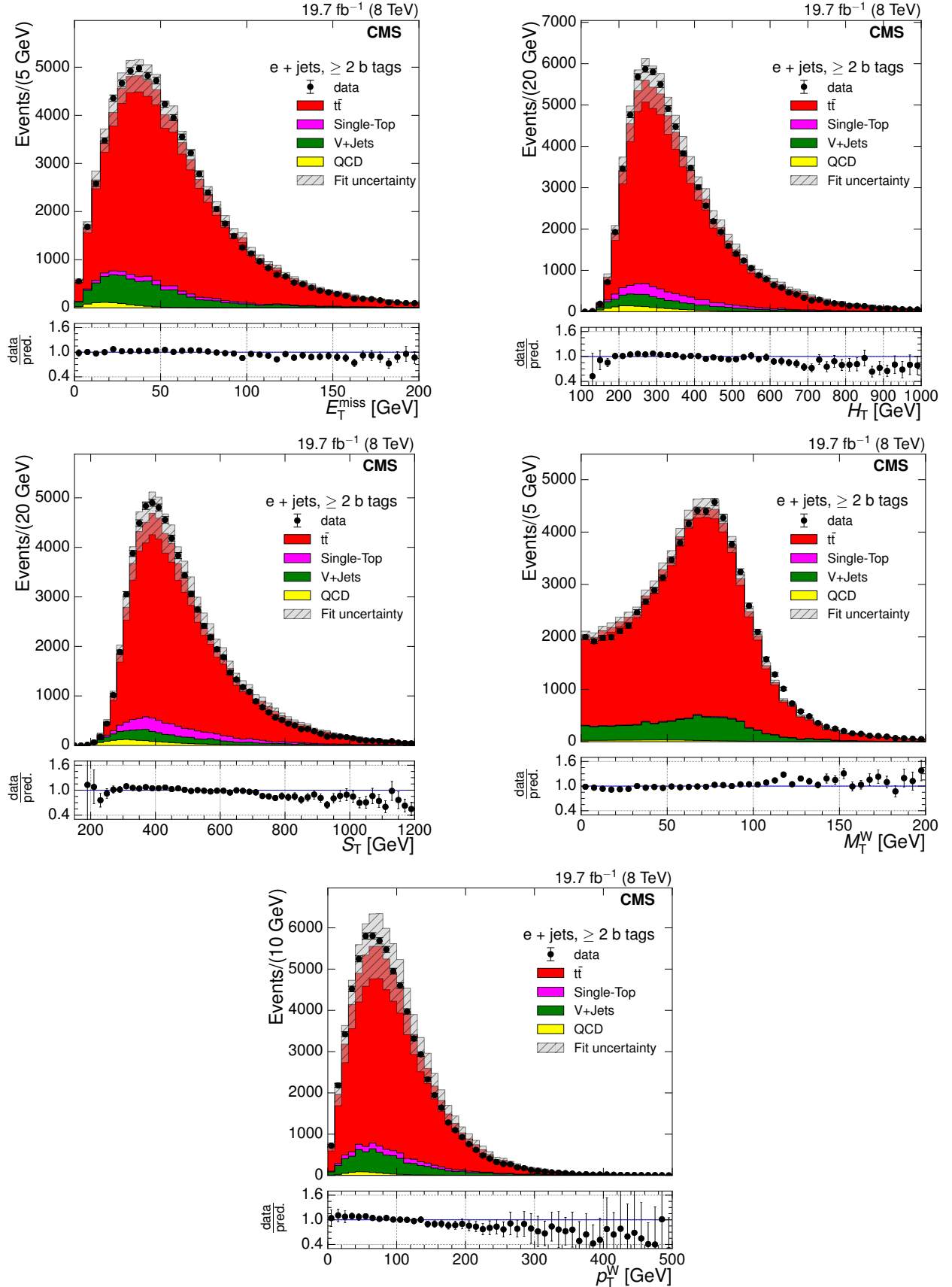


Figure 8.13: Comparison of Monte Carlo simulation to data distributions of primary variables, from top left, E_T^{miss} , H_T , S_T , M_T^W and p_T^W , in the electron+jets channel after fitting at $\sqrt{s} = 8 \text{ TeV}$.

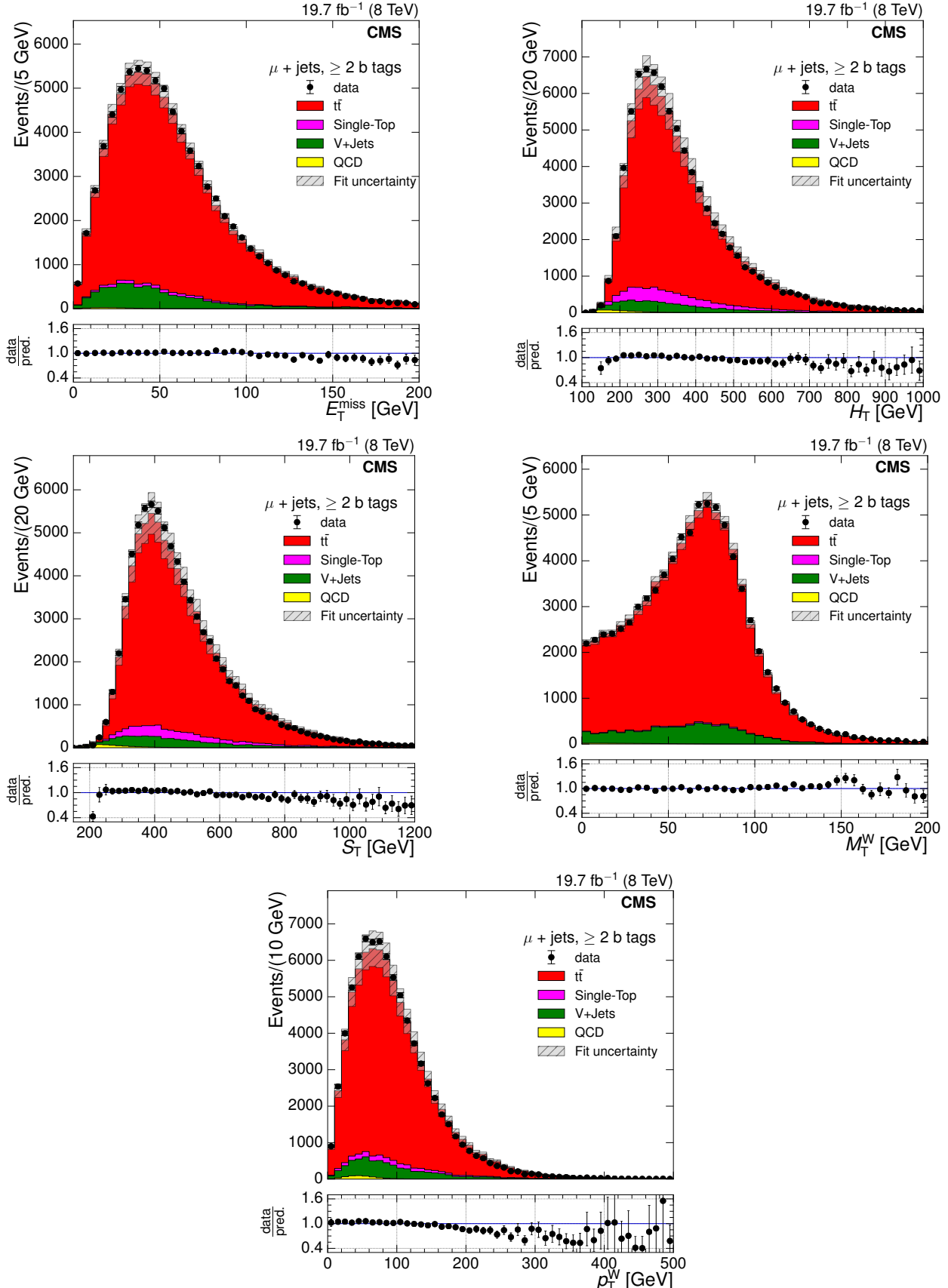


Figure 8.14: Comparison of Monte Carlo simulation to data distributions of primary variables, from top left, E_T^{miss} , H_T , S_T , M_T^W and p_T^W , in the muon+jets channel after fitting at $\sqrt{s} = 8 \text{ TeV}$.

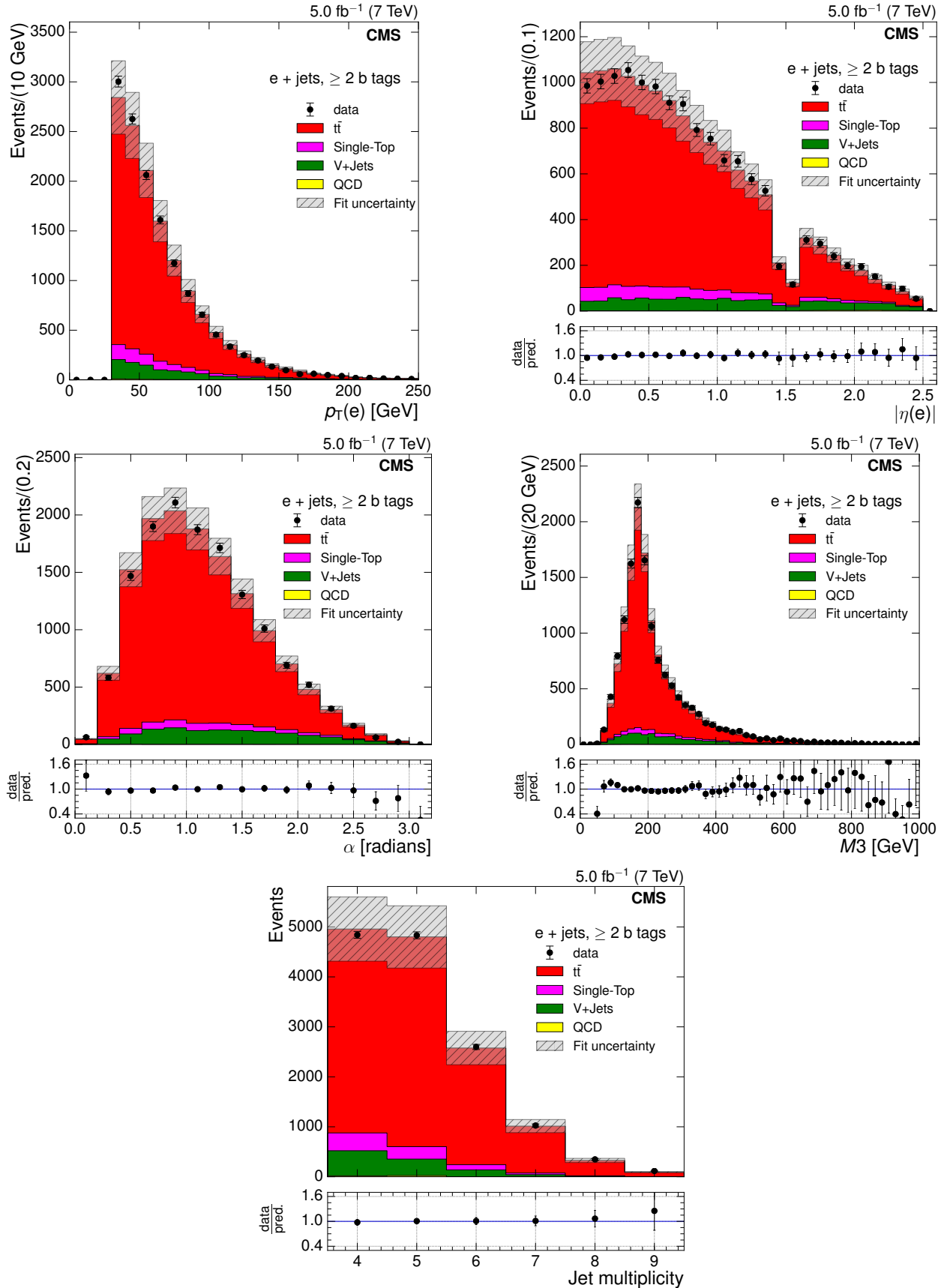


Figure 8.15: Comparison of Monte Carlo simulation to data distributions of kinematic event variables, from top left, electron $|\eta|$, electron p_T , α , M_3 and N_{jets} , in the electron+jets channel after fitting at $\sqrt{s} = 7 \text{ TeV}$.

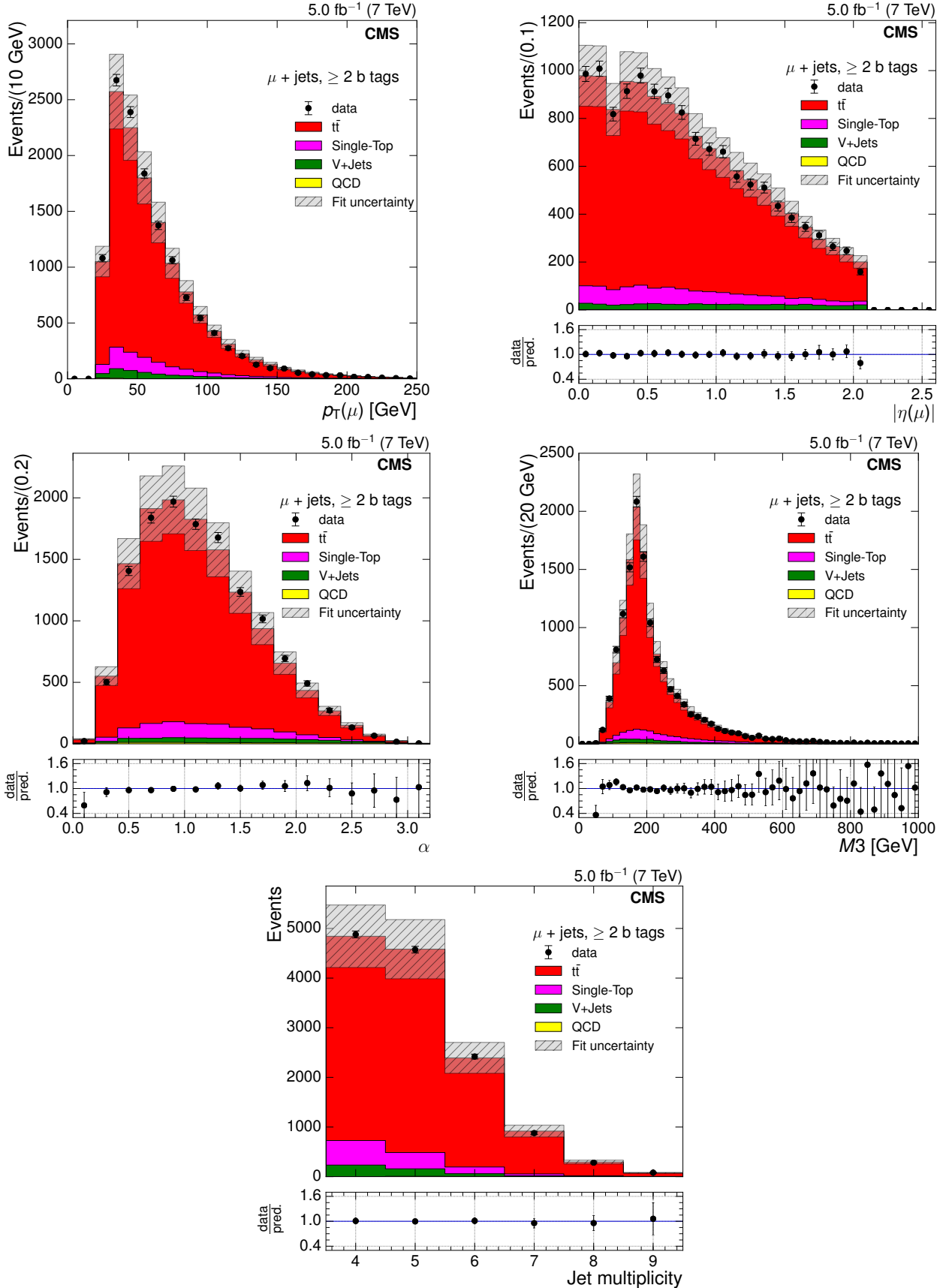


Figure 8.16: Comparison of Monte Carlo simulation to data distributions of kinematic event variables, from top left, electron $|\eta|$, electron p_T , α , $M3$ and N_{jets} , in the muon+jets channel after fitting at $\sqrt{s} = 7 \text{ TeV}$.

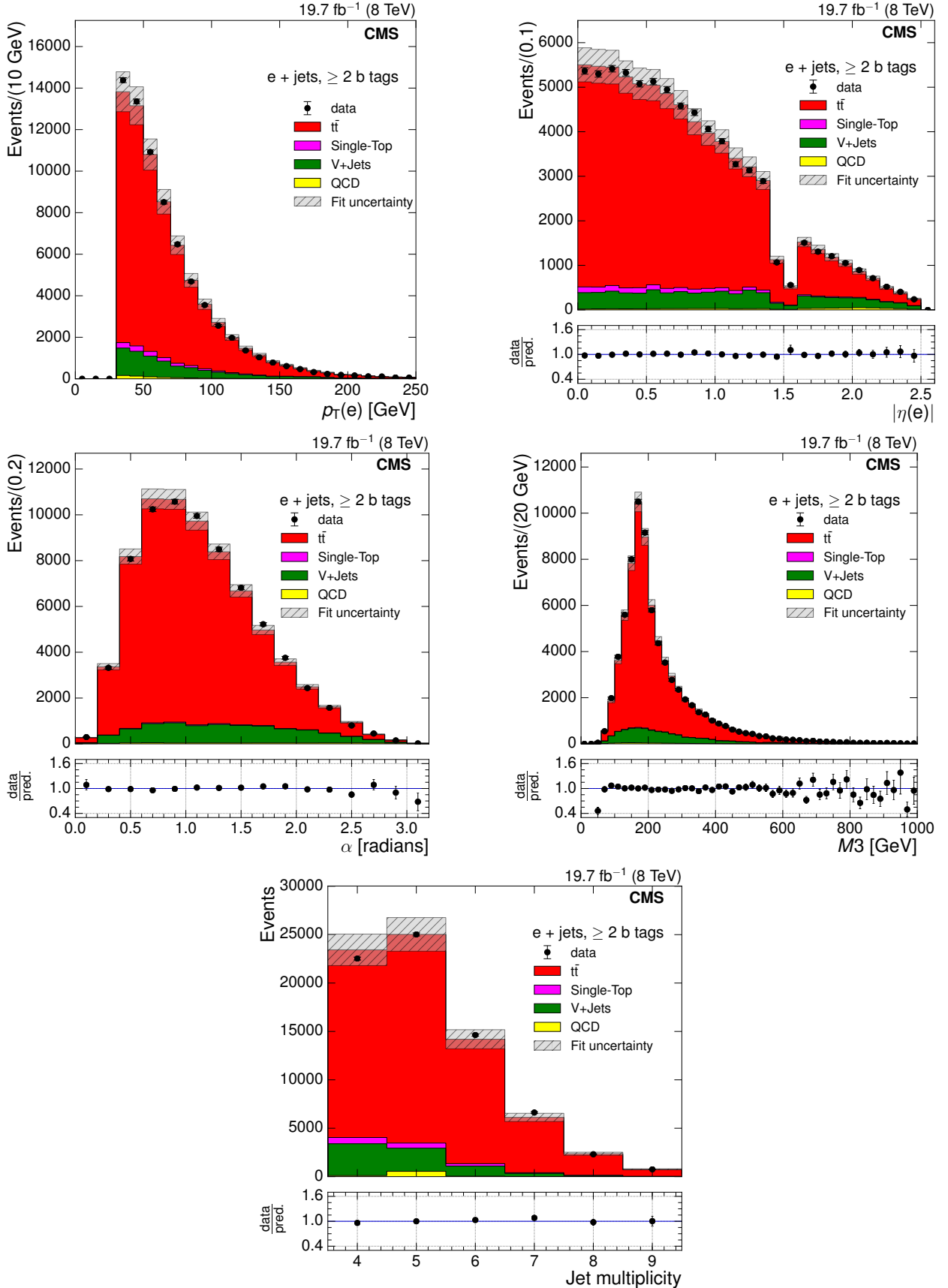


Figure 8.17: Comparison of Monte Carlo simulation to data distributions of kinematic event variables, from top left, electron $|\eta|$, electron p_T , α , $M3$ and N_{jets} , in the electron+jets channel after fitting at $\sqrt{s} = 8 \text{ TeV}$.

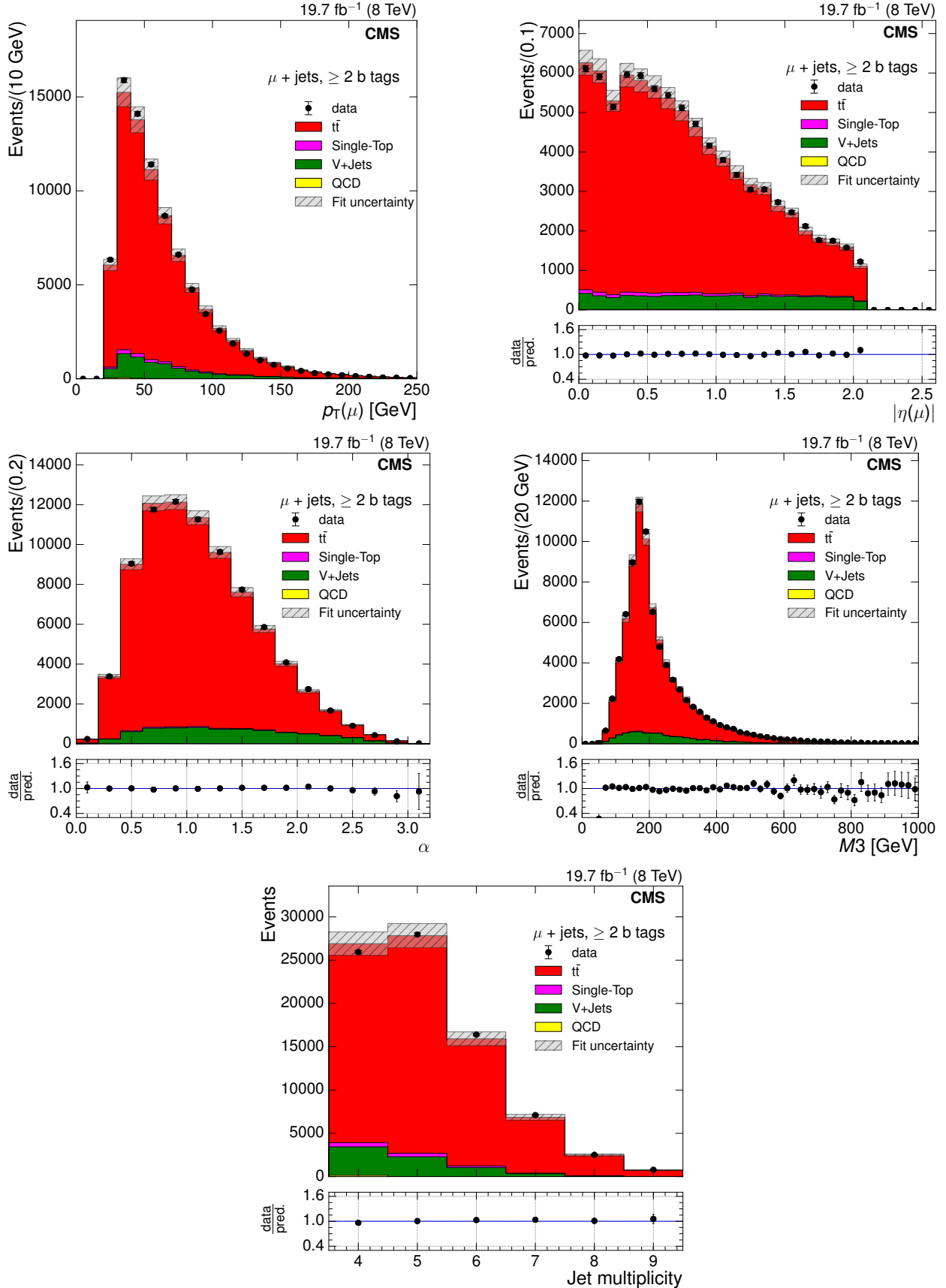


Figure 8.18: Comparison of Monte Carlo simulation to data distributions of kinematic event variables, from top left, electron $|\eta|$, electron p_T , α , M_3 and N_{jets} , in the muon+jets channel after fitting at $\sqrt{s} = 8 \text{ TeV}$.

8.4 Fit cross-checks

The correlations between the fitted processes, $N_{t\bar{t}}$, $N_{\text{singletop}}$, $N_{V+\text{jets}}$ and N_{QCD} , for the $E_{\text{T}}^{\text{miss}}$ variable in the electron+jets channel at $\sqrt{s} = 8 \text{ TeV}$ are shown in Figure 8.19. The equivalent plots for $\sqrt{s} = 7 \text{ TeV}$ are shown in Figure B.8 in Appendix B.6. It can be seen that the correlation between signal and QCD remains very low for all $E_{\text{T}}^{\text{miss}}$ bins. The V+jets template is negatively correlated with the QCD template in low bins, whereas this is not seen in higher bins due to these bins containing very few QCD events.

8.5 Background Subtraction

As a cross-check for the fitting process, an alternative method of extracting the number of $t\bar{t}$ events using the background subtraction method was performed. This method removes, to some extent, the model-dependency present in the fitting method, by not using the $t\bar{t}$ MC simulation. The MC predictions of single top, V + jets and QCD events are subtracted from the data in each bin to provide the $t\bar{t}$ yield. The normalisations of these background processes is the same as previously used in the fitting method, i.e. to their respective cross sections and luminosities. The resulting number of $t\bar{t}$ events is then taken forward to the unfolding process.

8.6 Unfolding

The measurement of the differential cross section will be limited by the finite resolution of the detector, detector acceptance and selection efficiency, and also by the presence of a small number of dilepton and fully hadronic $t\bar{t}$ events, and semi-leptonic events in the tau channel. In order to allow later comparison of results with theory predictions and with measurements from other experiments, deconvolution (unfolding) is employed to provide an estimate of the true distributions of the measured variables.

Generally speaking, any variable can be generated and reconstructed in simulation. Denoting

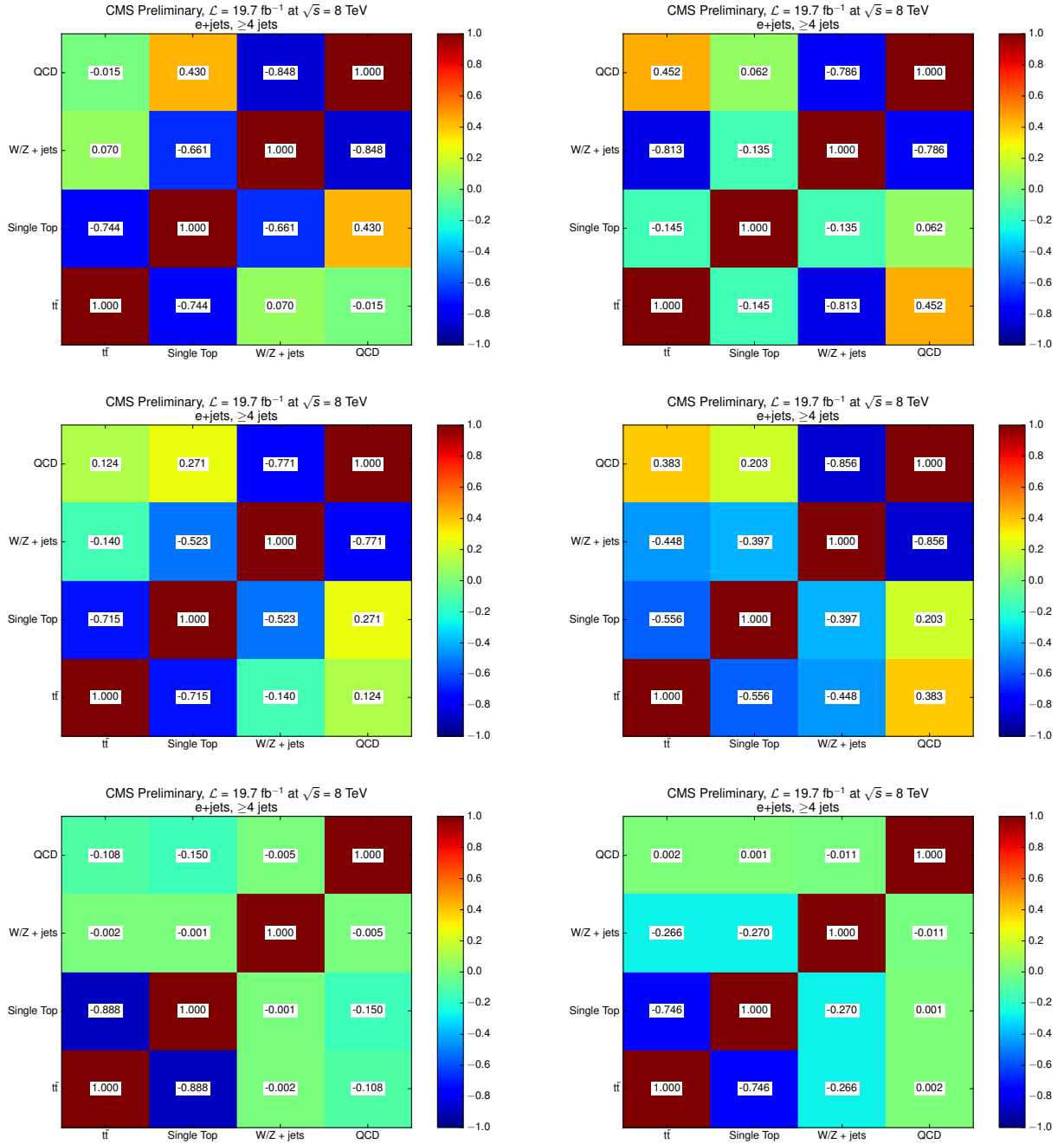


Figure 8.19: Correlation between fit processes for the E_T^{miss} variable in the electron+jets channel at $\sqrt{s} = 8 \text{ TeV}$ in bins 0-27 GeV (upper left), 27-52 GeV (upper right), 52-87 GeV (middle left), 87-130 GeV (middle right), 130-172 GeV (lower left) and $\geq 172 \text{ GeV}$ (lower right).

the generated (“true”) distribution by a vector x_0 , and the corresponding reconstructed distribution by b_0 , these can be related by

$$\hat{A}x_0 = b_0. \quad (8.7)$$

where \hat{A} is the response matrix, containing information about how the true distribution is reconstructed and measured as the distribution obtained in the real world. The variable in question is then measured in reality to have some distribution, b , which is then related to the true distribution by

$$\hat{A}x = b, \quad (8.8)$$

and therefore

$$x = \hat{A}^{-1}b, \quad (8.9)$$

Therefore, in this analysis, the system is solved to identify the true underlying distribution, x , using Singular Value Decomposition (SVD) [81] of the response matrix, with the RooUnfold package [23], and using regularisation to overcome the problem of oscillating solutions. In SVD unfolding, the response matrix is factorised as follows:

$$\hat{A} = USV^T. \quad (8.10)$$

S is a diagonal matrix with non-negative diagonal elements of dimensions $m \times n$, and U and V are orthogonal matrices of dimensions $m \times m$ and $n \times n$ respectively. The diagonal elements of S are called *singular values* of the matrix A and the columns of U and V are called the left and right *singular vectors*. The inverse of the response matrix can then be stated as

$$\hat{A}^{-1} = VS^{-1}U^T. \quad (8.11)$$

In systems in which the response matrix, \hat{A} , is of full rank (all columns and rows are linearly independent of each other) and statistical errors in the bins of the distribution are small, the problem can be solved simply using the inverted response matrix \hat{A}^{-1} . However, in most real

life cases, this is not the case, leading to unphysical fluctuations [81]. Regularisation is used in SVD unfolding to help overcome this problem using a regularisation parameter, k , which specifies the number of statistically significant terms in the system.

The value of k can be obtained by considering a measured variable that follows a smooth distribution, an *a priori* knowledge of the measured distribution, in which only the first few terms of the matrix decomposition are expected to be significant, with the contribution of higher, rapidly oscillating, terms expected to be compatible with zero [81]. The i th component of the vector d , d_i , is the coefficient of the measured distribution b . Using d , a vector obtained by rotating the measured distribution b ,

$$d = U^T \times b. \quad (8.12)$$

A plot of $\log|d_i|$ versus i can be plotted, where the bin number is represented by i . This will show d_i as being statistically significant, i.e. $d_i \gg 1$, for small i , and falling exponentially to a random Gaussian distribution about 0 for larger i . A falling exponential function plus a flat line can be fitted to this distribution, and the value of i at which the d_i changes from exponentially falling to within 10 % of the flat component is taken as the value of the regularisation parameter, k , which represents the number of significant bins in the distribution [81].

The value of k should be between 2 and the number of bins in the distribution, and aims to prevent statistical fluctuations in the distribution being interpreted as real variations in the true data. A low value of k favours the Monte Carlo truth input, while a high value of k favours the measured data which is to be unfolded. The $\log|d_i|$ plots for E_T^{miss} variable at $\sqrt{s} = 7 \text{ TeV}$ is shown in Figure 8.20. The resulting k values for both channels and both centre of mass energies are shown in Table 8.3.

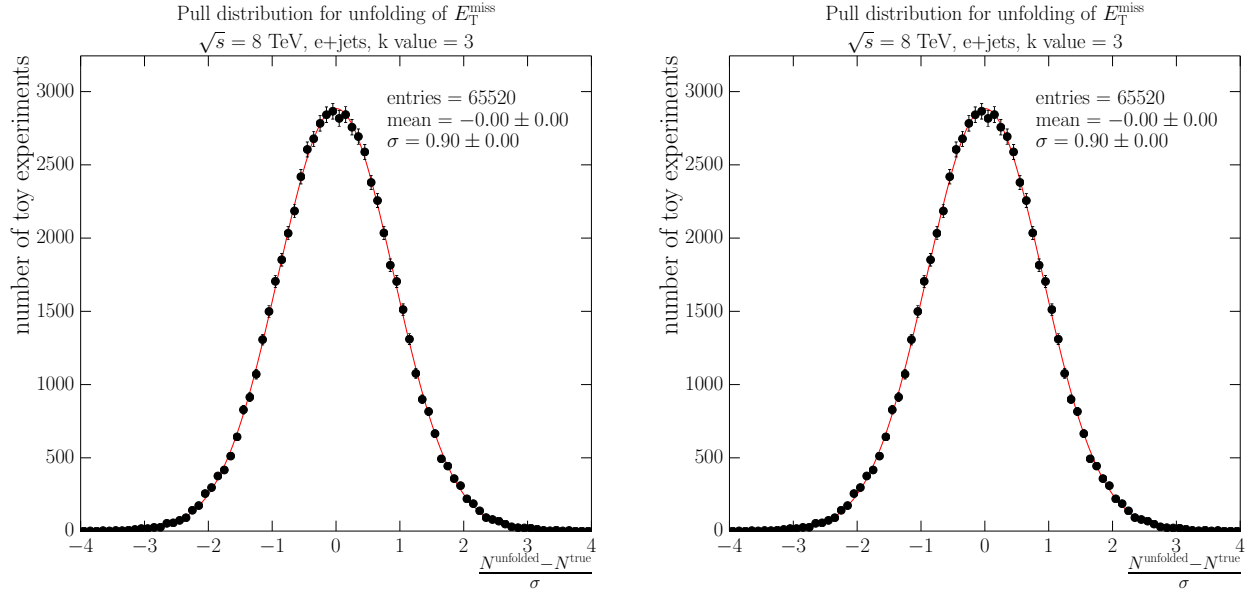


Figure 8.20: $\log|d_i|$ plots at $\sqrt{s} = 8$ TeV for the electron+jets channel (left) and the muon+jets channel (right).

Table 8.3: Optimal k -values for all primary variables at both 7 and 8 TeV.

variable	k-value (electron)	k-value (muon)
$\sqrt{s} = 7$ TeV		
E_T^{miss}	2	2
H_T	3	3
S_T	3	3
M_T^W	2	2
p_T^W	3	3
$\sqrt{s} = 8$ TeV		
E_T^{miss}	3	3
H_T	3	3
S_T	4	4
M_T^W	2	2
p_T^W	3	3

The required inputs to SVD unfolding with the RooUnfold package are:

- the simulated true distribution before selection
- the simulated reconstructed distribution after selection
- the two-dimensional reconstruction matrix of the true distributions after selection versus the measured distributions after selection.

All of the above are obtained from Monte Carlo simulations of $t\bar{t}$ events. Unfolding is carried out to the semi-leptonic phase space, where the lepton is either an electron or a muon. In the cases of E_T^{miss} , p_T^W and M_T^W , unfolding is carried out to the full phase-space where the E_T^{miss} is defined as the p_T of the neutrino from the semi-leptonic decay; and in the cases of H_T and S_T , unfolding is carried out to particle level where the jets in the true distribution have $p_T \geq 20 \text{ GeV}$.

Closure tests were carried out to verify the unfolding method using reconstructed simulated events as pseudo-data. A successful closure test results in the unfolded values matching the simulated truth of the same simulation sample, as can be seen in Figure 8.21 for the E_T^{miss} variable at $\sqrt{s} = 8 \text{ TeV}$.

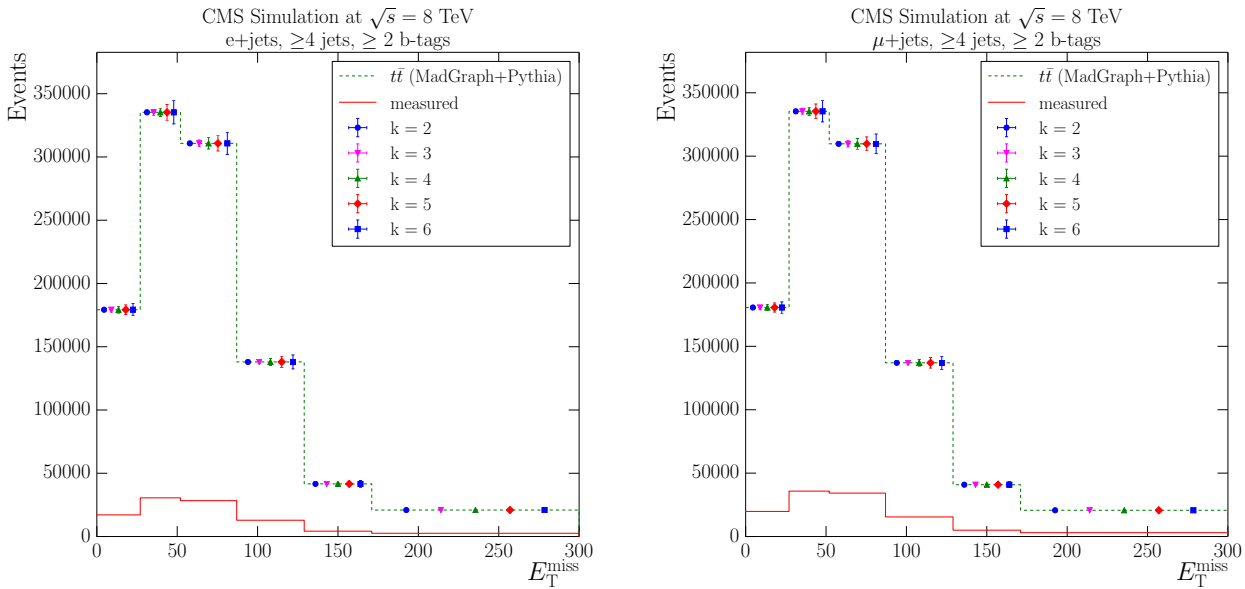


Figure 8.21: Unfolding closure tests performed by unfolding the reconstructed MADGRAPH distribution (“measured”) to generated values for the E_T^{miss} variable in the electron+jets channel (left) and the muon+jets channel (right) at $\sqrt{s} = 8 \text{ TeV}$.

The unfolding method described here was tested using toy Monte Carlo sets and producing pull distributions to investigate any potential bias in the method and to verify the unfolding error is estimated correctly. The central $t\bar{t}$ MADGRAPH sample is used to vary the contents in each bin of each primary variable distribution based on assumed Poissonian behaviour around the observed values. 300 sets of variations (henceforth referred to as models) are created, with the truth and reconstructed distributions varied independently, while another independent variation of the reconstructed distribution is used as the pseudo-data to be unfolded. This therefore creates 300×300 combinations of model and pseudo-data. The pull distributions are created as follows

$$\frac{N^{unfolded} - N^{true}}{\sigma} \quad (8.13)$$

where $N^{unfolded}$ is the number of events in the unfolded result, N^{true} is the number of events in the expected distribution after unfolding (Monte Carlo truth), and σ is the unfolding uncertainty. Provided the unfolding uncertainty is estimated correctly and that there is no bias in the method, the pull distribution is expected to have a Gaussian distribution around a mean of 0 and a σ of 1. Any bias would manifest as a pull distribution centred at a non-zero value, and any miscalculation of the unfolding uncertainty will result in a width of < 1 or > 1 , meaning an overestimation or an underestimation, respectively, of the unfolding uncertainty. Figure 8.22 shows the resulting pull distributions in the E_T^{miss} variable at $\sqrt{s} = 8$ TeV, with a k regularisation value of 3. The distributions can be seen to have means of 0, thereby showing no bias in the unfolding method. The widths are close to 1, but show a very slight overestimation in the unfolding uncertainty. The unfolding procedure was considered sound using this conservative approach as the unfolding is not a dominant source of uncertainty in this analysis.

8.6.1 Measurement

The fitting and unfolding explained in Sections 8.3 and 8.6 is performed individually in the electron+jets and muon+jets channels, resulting in a number of $t\bar{t}$ events, $N_{t\bar{t}}$, in each

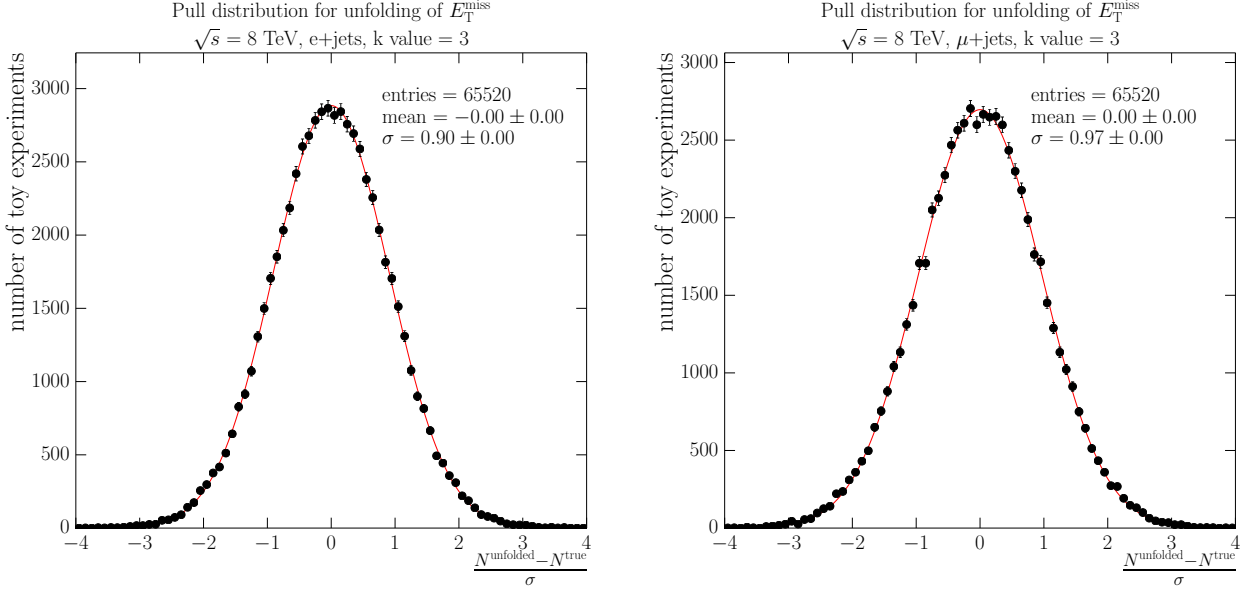


Figure 8.22: Pull distributions using toy Monte Carlo datasets for the E_T^{miss} variable using a k value of 3 in the electron+jets channel (left) and in the muon+jets channel (right) at $\sqrt{s} = 8 \text{ TeV}$.

bin, in each primary variable for each channel. The normalised differential cross section measurement is then carried out in each channel as outlined below using $N_{t\bar{t}}$. In addition, to the sum total $N_{t\bar{t}}$ in the two channels is used to calculate the normalised differential cross section in the combined semileptonic channel.

The number of $t\bar{t}$ events, $N_{t\bar{t}}$ is first used to calculate the average cross section in each bin using

$$\Delta\sigma_{t\bar{t}}^i = \frac{N_{t\bar{t}}^i}{\mathcal{B} \times \mathcal{L}}. \quad (8.14)$$

Here, the theoretical $t\bar{t}$ semi-leptonic branching ratio is denoted by BR , and \mathcal{L} is the luminosity of the recorded dataset. The efficiency is taken account of in the unfolding procedure, and is therefore not included in this calculation. Subsequently, the differential cross section in each primary variable bin is calculated by dividing by the bin width ΔX as follows:

$$\frac{d\sigma_{t\bar{t}}^i}{dX} = \frac{\Delta\sigma_{t\bar{t}}^i}{\Delta X} = \frac{N_{t\bar{t}}^i}{\text{BR} \times \mathcal{L} \times \Delta X}. \quad (8.15)$$

Finally, the normalised differential cross section in each bin is obtained by normalising to

the total measured cross section

$$\frac{1}{\sigma_{tt}^{\text{tot}}} \frac{d\sigma_{tt}^i}{dX} = \frac{1}{\sum_j d\sigma_{tt}^j} \frac{d\sigma_{tt}^j}{dX} = \frac{\text{BR} \times \mathcal{L}}{\sum_j N_{tt}^j} \frac{N_{tt}^i}{\text{BR} \times \mathcal{L} \times \Delta X} = \frac{1}{\sum_j N_{tt}^j} \frac{N_{tt}^i}{\Delta X} \quad (8.16)$$

9 | Differential Cross Sections: Systematic Uncertainties and Results

9.1 Systematic uncertainties

The systematic uncertainties in this analysis are evaluated independently, under the assumption that systematic uncertainty sources are uncorrelated, by changing the inputs by their associated uncertainties (-1σ and $+1\sigma$) and measuring the deviation in the final result from the nominal measurement. The uncertainties from each source are symmetrised by conservatively taking the maximum absolute deviation of the up or down systematic variation. The total systematic uncertainty is obtained by adding each individual systematic uncertainty in quadrature, and this is summed with the fitting and unfolding uncertainties to obtain the total measurement uncertainty. The normalisation of the final differential cross section will cancel systematic uncertainties that are correlated between bins of the primary variables.

In the case of experimental uncertainties, the uncertainty is calculated by changing the templates in the fitting process and/or their normalisations, and using the nominal MADGRAPH response matrix in the unfolding process. In the case of theoretical uncertainties, the nominal fitting templates and normalisation are used, while the response matrix information is changed according to the systematic uncertainty being investigated.

The systematic uncertainties are summarised in Tables B.23 to B.32.

9.1.1 Experimental Uncertainties

Jet energy scale uncertainty is evaluated as a function of jet p_T and jet η , and a 10% jet energy resolution uncertainty is applied. The jet energy scale (JES) directly changes the p_T of jets in the event, and also propagates to the event E_T^{miss} (see Section 7.4.4). Therefore the JES uncertainty becomes significant at higher values of the primary variables, in particular of E_T^{miss} , H_T and S_T .

Together with jet energy scale uncertainty, the E_T^{miss} energy uncertainties are the only systematics applied to both simulation and data. These take account of uncertainty in the lepton energy, and propagate this to the E_T^{miss} in the event. While the electron and muon energy uncertainties are not dominant sources of error in this analysis, the effect of the uncertainty on tau energy has been calculated to be larger. Events with tau leptons can pass the signal selection (a significant component of what are known as fake events, i.e. non semi-leptonic $t\bar{t}$ events which pass our signal selection) if they mimic the signature of an electron+jets or muon+jets $t\bar{t}$ event:

- semi-leptonic tau, where $\tau \rightarrow e/\mu + \bar{\nu}_{e/\mu} + \nu_\tau$ (Figure 9.1a).
- di-leptonic $e\tau$ & $\mu\tau$, where $\tau \rightarrow q\bar{q}' + \nu_\tau$ (Figure 9.1b).
- di-leptonic $\tau\tau$, where $\tau \rightarrow q\bar{q}' + \nu_\tau, \tau \rightarrow e/\mu + \bar{\nu}_{e/\mu}$ (Figure 9.1c).

The first of these, where the leptonically decaying W boson from a semi-leptonic $t\bar{t}$ decay decays to a tau lepton and a tau neutrino, and the tau lepton then decays to another tau neutrino, an electron/muon and an electron neutrino/muon neutrino via a virtual W boson, can be disregarded for the tau energy systematic since the leptonically decaying tau is indistinguishable from the signal electron+jets or muon+jets channels. It is therefore not possible to include such an event in the calculation of the E_T^{miss} uncertainty by varying the τ energy. The other two tau decay channels which potentially fake the signal and pass the $t\bar{t}$ signal selection are distinguishable and are included.

Fake events are removed by subtracting the fake distribution obtained from simulation.

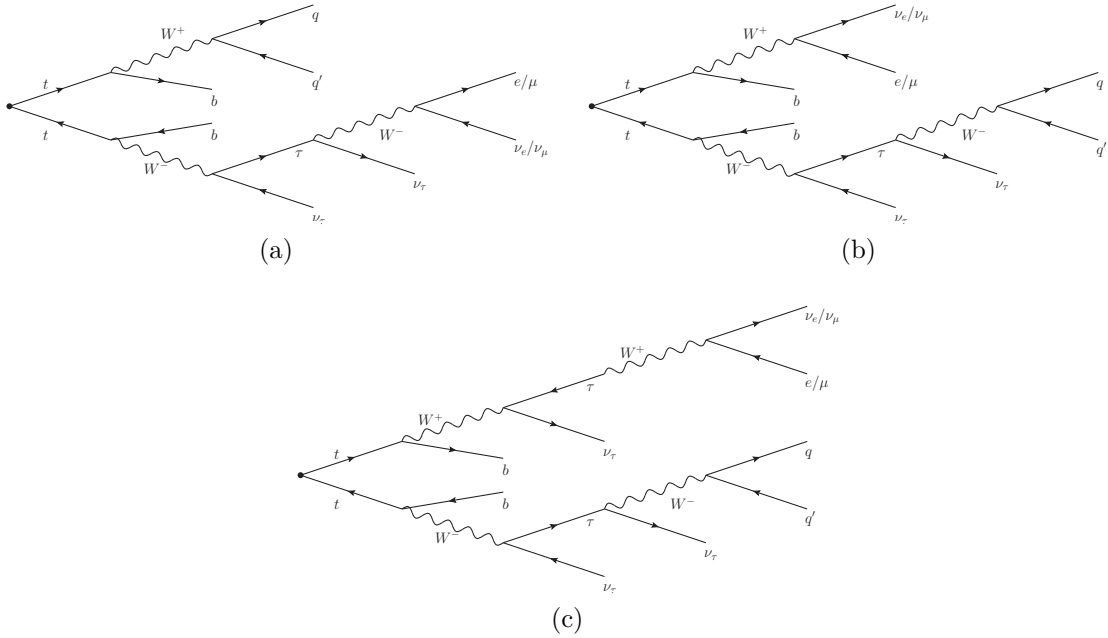


Figure 9.1: Feynman diagrams of semi-leptonic τ events (a), dileptonic events with one τ lepton (b) and dileptonic events with two τ leptons (c).

However, for the systematic measurements with the tau energy varied up and down, the same fake distribution shape is subtracted as in the nominal measurement. The left-hand plot in Figure 9.2 compares the numbers of events in the signal and fake distributions from $t\bar{t}$ simulation after selection. Based on this, an evaluation of the ratio of fake events to the number of reconstructed $t\bar{t}$ events in simulation has been calculated to be approximately 14% (13.5% in electron channel and 13.9% in muon channel). The large component of taus in the fake distribution leads to the larger systematic uncertainties (up to $\approx 6 - 7\%$) as a result of varying the tau energy, while the effect of varying the electron and muon energies is not so pronounced because there are not many electrons or muons in the fake collection (a dileptonic $t\bar{t}$ event with ee , $e\mu$ or $\mu\mu$ would have to be misreconstructed as a semi-leptonic event for this to happen). A comparison of the shapes of the fake and the signal E_T^{miss} distributions from simulation is also shown on the right in Figure 9.2. It can be seen that the relative contribution from fakes increases towards higher values of E_T^{miss} , which leads to the observed increase in the systematic uncertainty due to the uncertainty in the tau energy towards higher bins of E_T^{miss} .

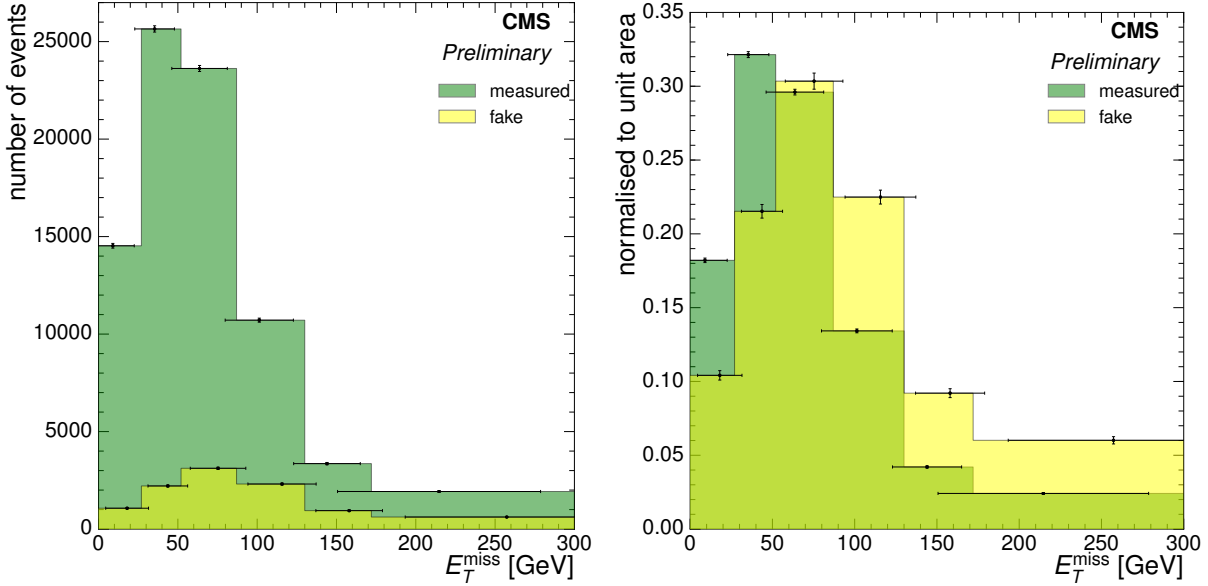


Figure 9.2: Comparison of the signal and fake distributions from semi-leptonic $t\bar{t}$ events after selection in simulation in the electron+jets channel at $\sqrt{s} = 8$ TeV normalised to the numbers of events (left) and normalised to one (right).

Furthermore, the difference between the tau energy down (-1σ) variation and the nominal measurements in the E_T^{miss} variable before fitting and unfolding is shown in Figure 9.3. In the highest E_T^{miss} bin, the difference is approximately 6%, and this value remains approximately constant after fitting and unfolding. The significant effect of varying the tau energy is therefore unlikely to be an artifact of the fitting and/or unfolding procedure, but a real difference in the number of events.

Other small sources of experimental uncertainty include the non-clustered energy uncertainty (which refers to fluctuations in deposits in the electromagnetic calorimeter that are not included in jet clusters), the matching threshold and factorisation and normalisation scale uncertainties in $W + \text{jets}$ and $Z + \text{jets}$ events, pileup uncertainty, the QCD template shape uncertainty, and the efficiency of electron, muon and b-tagging in the selection process.

Rate changing systematics such as the uncertainty on the luminosity and on the theoretical cross sections of the signal and background processes have a negligible effect on the final result, since they cancel in the final normalised measurements.

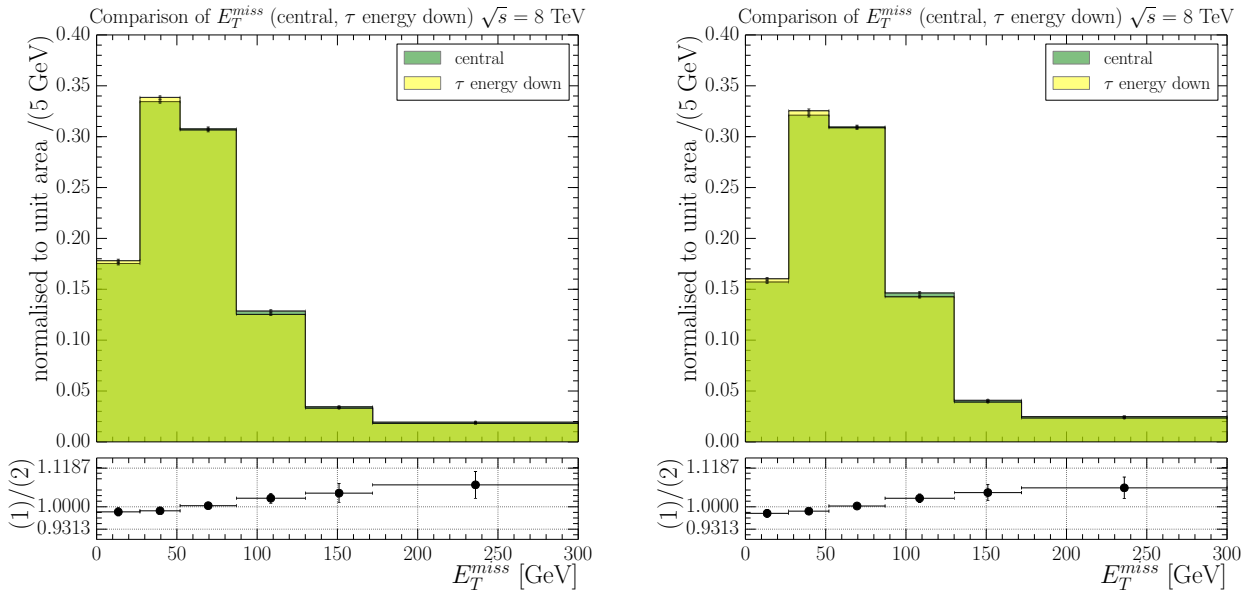


Figure 9.3: Comparison of the E_T^{miss} distributions in the nominal measurement and in the tau energy down variation before fitting and unfolding in data (left) and in $t\bar{t}$ simulation (right) at $\sqrt{s} = 8 \text{ TeV}$

9.1.2 Theoretical Uncertainties

7 TeV V+Jets theory systematic template

The factorisation and normalisation scale (Q^2 up/down) uncertainty is evaluated using simulation samples produced with the scale varied by factors of 2 (up) and 0.5 (down). This has been evaluated to be one of the dominating uncertainties in this analysis. The uncertainty in the matching threshold (matching up/down) for $t\bar{t}$ events is evaluated in the same way.

Unfortunately, Monte Carlo simulation for theoretical systematic uncertainties at $\sqrt{s} = 7 \text{ TeV}$ have not been made available for W+jets and Z+jets processes. However, it can be seen in Figure 9.4 that the W+jets template shapes at $\sqrt{s} = 7 \text{ TeV}$ and $\sqrt{s} = 8 \text{ TeV}$ are similar. The V+jets template shapes used to evaluate these theoretical systematics are therefore obtained from $\sqrt{s} = 8 \text{ TeV}$ theoretical systematic datasets, and then scaled to the normalisation in the nominal sample at $\sqrt{s} = 7 \text{ TeV}$.

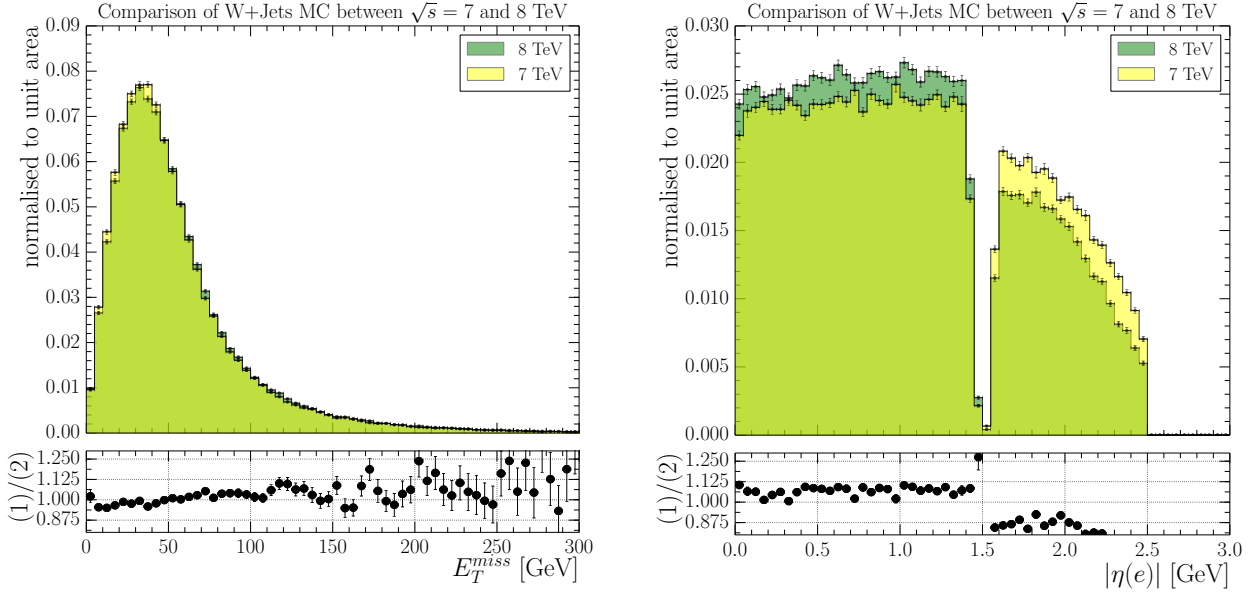


Figure 9.4: Shape comparison of W+jets templates in $\sqrt{s} = 7$ TeV and $\sqrt{s} = 8$ TeV Monte Carlo simulation for E_T^{miss} (left) and electron $|\eta|$ (right) in the electron+jets channel.

Hadronisation Uncertainty

The uncertainty due to hadronisation modelling is evaluated by comparing the results using $t\bar{t}$ simulation from the POWHEG 1 generator with PYTHIA modelling the hadron showering (POWHEGv1+PYTHIA), with a sample generated using the same POWHEG 1 generator with HERWIG carrying out the hadronisation modelling (POWHEGv1+HERWIG). The difference between the PYTHIA and HERWIG samples is scaled to the nominal measurement and taken as the hadronisation uncertainty. At $\sqrt{s} = 7$ TeV, since these samples are not available, the hadronisation uncertainty is obtained by scaling the relative uncertainty at $\sqrt{s} = 8$ TeV to the central $\sqrt{s} = 7$ TeV result. All variables, and in particular those sensitive to hadronic aspects of an event such as H_T and S_T , are significantly affected by this systematic, with a larger uncertainty in lower bins of the primary variables.

PDF Uncertainties

The uncertainty on the measurements as a result of the uncertainty on the choice of proton PDFs is evaluated by reweighting the central MADGRAPH sample with 44 distinct weights (22 orthogonal variables, each of which can be varied up and down according to their uncertainties)

from the CTEQ 6.6 PDF sets [97], according to the PDF4LHC recommendation [33, 25]. The analysis is repeated with each variation, and the maximum of all the up and down variations summed in quadrature is taken as the PDF systematic uncertainty.

Top Quark Mass Uncertainty

The top quark mass uncertainty is evaluated using $t\bar{t}$ samples produced with two different top quark masses of 169.5 GeV and 173.5 GeV, and scaling the error obtained using these samples to the top mass uncertainty of ± 1.0 GeV from the central value of 172.5 GeV.

$t\bar{t}$ p_T Mismodelling

There is a known issue with event generators mismodelling the top quark p_T distribution; the distribution of the transverse momentum of top quarks in data was found to be softer than that in simulation [49, 9, 11]. Scale factors have been centrally derived and provided, as a function of the generated p_T of the top quark, to correct for this disagreement. The effect of this correction on the nominal measurement was evaluated to be negligible for low values of the primary variables, increasing to 3–7% at higher values. The MADGRAPH simulation after applying the t-quark p_T correction is also included in the results plots (Figures 9.5 to 9.8).

The most significant shape changing uncertainties typically arise from the factorisation scale variations in the $t\bar{t}$ process and the hadronisation.

9.1.3 Systematic Uncertainty Tables

Tables 9.2 and 9.4 give typical (median) relative systematic uncertainties for all systematic uncertainty sources, at $\sqrt{s} = 7$ TeV and $\sqrt{s} = 8$ TeV respectively, and are for the combined electron+jets and muon+jets channel, for the fitting method. The sources are grouped into categories, taking only the maximum relative uncertainty between a $+1\sigma / -1\sigma$ variation of each uncertainty source. In categories containing more than one $+1\sigma / -1\sigma$ variation pair (E_T^{miss} uncertainties: electron/muon/tau/unclustered energy; Background (other): $t\bar{t}$ /single

top/V+jets/QCD cross sections and luminosity; Theoretical Systematics: $t\bar{t}/V+jets$ matching and Q^2), the maximum uncertainty of each $+1\sigma$ / -1σ source is added in quadrature. The median values across all of the bins of a primary variable are then taken as the typical systematic uncertainties stated in the tables. Extended uncertainty tables can be found in Appendix B.7.

Table 9.1: Typical systematic uncertainties in percent (median values) for the normalised $t\bar{t}$ differential cross section measurement at $\sqrt{s} = 7$ TeV (combination of electron and muon channels). Typical values of the total systematic uncertainty are also shown.

Uncertainty source	E_T^{miss}	H_T	S_T	p_T^W	M_T^W
Electron trigger and selection efficiencies	< 1	1.30	1.41	< 1	< 1
Muon trigger and selection efficiencies	< 1	< 1	< 1	< 1	< 1
b-tagging	< 1	< 1	2.1	< 1	< 1
Jet Energy Scale	< 1	3.6	1.1	< 1	< 1
Jet Energy Resolution	< 1	3.1	1.6	< 1	< 1
E_T^{miss} uncertainties	1.3	-	2.6	4.3	< 1
Pileup	< 1	0.1	2.4	< 1	< 1
QCD shape	< 1	< 1	2.2	< 1	< 1
Background (other)	< 1	< 1	4.1	< 1	< 1
Theoretical systematics	1.0	4.6	4.7	< 1	1.0
top mass	< 1	< 1	< 1	< 1	< 1
hadronisation	2.1	9.9	8.2	3.8	1.1
PDF uncertainties	< 1	< 1	< 1	< 1	< 1
p_T reweighting	1.6	< 1	1.3	< 1	< 1
Total	3.7	12.4	13.3	6.6	2.9

Table 9.2: Typical systematic uncertainties in percent (median values) for the normalised $t\bar{t}$ differential cross section measurement at $\sqrt{s} = 7$ TeV (combination of electron and muon channels). Typical values of the total systematic uncertainty are also shown.

Uncertainty source	E_T^{miss}	H_T	S_T	p_T^W	M_T^W
Jet Energy Resolution	0.07	3.11	1.58	0.44	0.21
Jet Energy Scale	0.22	3.55	1.13	0.90	0.50
E_T^{miss} uncertainties	1.28	-	2.57	4.31	0.96
PDF uncertainties	0.66	0.79	0.88	0.96	0.82
Pileup	0.05	0.12	2.40	0.65	0.11
QCD shape	0.02	0.16	2.23	0.05	0.06
Background (other)	0.00	0.03	4.07	0.39	0.01
b-tagging	0.03	0.04	2.09	0.23	0.03
Electron trigger efficiency & electron selection	0.01	1.30	1.41	0.85	0.27
Hadronisation	4.23	4.56	7.15	3.06	1.44
Muon trigger efficiency & muon selection	0.00	0.02	0.00	0.01	0.01
p_T reweighting	1.63	0.80	1.25	0.21	0.55
Theoretical systematics	1.01	4.55	4.67	0.84	1.00
Top mass	0.19	0.29	0.41	0.29	0.21

Table 9.3: Typical systematic uncertainties in percent (median values) for the normalised $t\bar{t}$ differential cross section measurement at $\sqrt{s} = 8$ TeV (combination of electron and muon channels). Typical values of the total systematic uncertainty are also shown.

Uncertainty source	E_T^{miss}	H_T	S_T	p_T^W	M_T^W
Electron trigger and selection efficiencies	< 1	< 1	< 1	< 1	< 1
Muon trigger and selection efficiencies	< 1	< 1	< 1	< 1	< 1
b-tagging	< 1	< 1	< 1	< 1	< 1
Jet Energy Scale	< 1	1.7	1.4	0.5	0.7
Jet Energy Resolution	< 1	< 1	< 1	< 1	< 1
E_T^{miss} uncertainties	2.8	-	1.0	2.4	< 1
Pileup	< 1	< 1	< 1	< 1	< 1
QCD shape	< 1	< 1	< 1	< 1	< 1
Background (other)	< 1	< 1	< 1	< 1	< 1
Theoretical systematics	7.2	5.2	3.7	3.2	1.7
Top quark mass	< 1	< 1	< 1	< 1	< 1
Hadronisation	4.2	4.6	7.2	3.1	1.4
PDF uncertainties	< 1	< 1	< 1	< 1	< 1
p_T reweighting	< 1	< 1	< 1	< 1	< 1
Total	9.0	8.7	9.9	4.9	2.8

Table 9.4: Typical systematic uncertainties in percent (median values) for the normalised $t\bar{t}$ differential cross section measurement at $\sqrt{s} = 8$ TeV (combination of electron and muon channels). Typical values of the total systematic uncertainty are also shown.

Uncertainty source	E_T^{miss}	H_T	S_T	p_T^W	M_T^W
Jet Energy Resolution	0.22	0.43	0.59	0.23	0.26
Jet Energy Scale	0.77	1.68	1.38	0.49	0.70
E_T^{miss} uncertainties	2.80	-	1.04	2.42	0.72
PDF uncertainties	0.50	0.50	0.52	0.48	0.15
Pileup	0.22	0.39	0.10	0.58	0.23
QCD shape	0.11	0.24	0.14	0.15	0.28
Background (other)	0.01	0.00	0.03	0.01	0.00
b-tagging	0.21	0.02	0.10	0.11	0.01
Electron trigger efficiency & electron selection	0.20	0.12	0.02	0.62	0.07
Hadronisation	4.23	4.56	7.15	3.06	1.44
Muon trigger efficiency & muon selection	0.01	0.02	0.01	0.02	0.01
p_T reweighting	0.83	0.78	0.53	0.40	0.73
Theoretical systematics	7.19	5.15	3.73	3.16	1.67
Top mass	0.33	0.93	0.72	0.54	0.10

9.2 Results

This section summarises the normalised differential cross sections for the primary variables investigated in this analysis. Figures 9.5 and 9.6 show the distributions at $\sqrt{s} = 7$ TeV; and Figures 9.7 and 9.8 show the distributions at $\sqrt{s} = 8$ TeV. Corresponding numerical results are included in Appendix B.8. Results plots showing the unfolded distributions from the cross check method, in which the less model-dependent technique of background subtraction is used to extract the $t\bar{t}$ event yield, are also shown in Appendix B.8. The results and errors from this method are shown to be compatible with the results obtained using the fitting method.

The normalised cross section distributions are shown compared with predictions from MADGRAPH+PYTHIA, POWHEGv2+PYTHIA, POWHEGv2+HERWIG, and a MADGRAPH+PYTHIA prediction with corrected t-quark p_T in the left hand plots. At $\sqrt{s} = 8$ TeV, additional

predictions from MC@NLO+HERWIG, POWHEGv1+PYTHIA and POWHEGv1+HERWIG are shown for comparison, but these simulated samples were not available at $\sqrt{s} = 7 \text{ TeV}$. The error bars on the data points represent the statistical+unfolding (inner) and systematic uncertainties summed in quadrature (outer). In the right hand plots, the nominal MADGRAPH sample is compared to the top p_T corrected MADGRAPH+PYTHIA sample and modified MADGRAPH samples with the modelling parameters matching threshold, and factorisation and renormalisation scale (Q^2), varied up and down according to their uncertainties. Ratio plots are shown below the distribution plots to allow easier comparison of the distribution in data to the different simulations, with a line at 1.0 for reference. In the ratio plots, the grey error bands represent the statistical+unfolding uncertainty, while the yellow error bands represent the systematic uncertainties added in quadrature.

It can be seen that the data distributions generally show softer spectra than the nominal MADGRAPH generator for all the primary variables. This is likely to be due to the known mismodelling of the top quark p_T in the MADGRAPH event generator [49]. After reweighting the top quark p_T distribution, the MADGRAPH sample describes the data well.

All simulated samples describe the data well in the E_T^{miss} distribution at $\sqrt{s} = 7 \text{ TeV}$, whereas the distributions in the H_T , S_T and p_T^W variables can be seen to be harder in simulation than in data. Nevertheless, the data agrees reasonably well with predictions from POWHEGv2+PYTHIA in H_T , S_T and M_T^W , and from POWHEGv2+HERWIG in p_T^W .

The data at $\sqrt{s} = 8 \text{ TeV}$ agree well with predictions from MC@NLO and POWHEGv2+PYTHIA simulations in all variables. The good performance of the MC@NLO generator is expected since it is an NLO generator, compared to the other LO generators. The POWHEGv1+PYTHIA generator shows similar behaviour to that of the uncorrected MADGRAPH generator, while the POWHEGv1+HERWIG sample provides a spectrum softer than those predicted by the MADGRAPH and POWHEGv1+PYTHIA generators, but harder than data. Predictions from POWHEGv2+HERWIG samples at both $\sqrt{s} = 7 \text{ TeV}$ and $\sqrt{s} = 8 \text{ TeV}$ can be seen to deviate significantly from other predictions and from data in the H_T and S_T variables, with a notably harder distribution in both cases. Since these variables are affected the most by jets in the

event, this seems to suggest that the POWHEGv2+HERWIG samples suffer from some jet p_T mismodelling. The POWHEGv2+HERWIG generator does, however, provide a good description of data in the E_T^{miss} , p_T^W and M_T^W variables.

There is a noticeable trend, in the higher bins of E_T^{miss} , H_T and S_T , of most simulated samples providing an overestimation compared to data, although these bins also tend to have the lowest statistics, leading to a larger uncertainty in these bins.

In comparing the nominal and corrected MADGRAPH distributions with the theoretical modelling uncertainties, it can be seen that predictions from varying the matching threshold up and Q^2 up generally show best agreement with the data. Indeed, the Q^2 up sample better predicts the measured spectrum in the H_T and S_T distributions at $\sqrt{s} = 7\text{ TeV}$, suggesting a possible mismodelling of the factorisation and renormalisation scale in the central MADGRAPH sample (although the top p_T corrected MADGRAPH samples still show best performance). The data in the H_T and S_T distributions at $\sqrt{s} = 8\text{ TeV}$, however, lie between the Q^2 up and down variations, suggesting that the factorisation and renormalisation scale uncertainties may be slightly overestimated, but that the use of the top mass for Q^2 is sound. The samples with matching threshold varied up and down generally follow the same trends as, and lie above and below, the nominal MADGRAPH prediction. This indicates that these varied samples are likely to suffer from the same top quark p_T modelling fault as the central MADGRAPH sample.

The M_T^W variable, being the least well reconstructed, shows data generally agreeing with predictions. However, these distributions provide low measurement granularity in the M_T range, with large bins and high numbers of events resulting in low statistical uncertainties. The M_T^W distributions are therefore of limited use without carrying out further investigations, possibly with a larger number of bins.

This analysis has been carried out as a measurement, and has not been converted into a search. Some deviations from predictions have been observed, but are, in large part, understood and thought to be mismodelling. Naturally, some deviations are to be expected because of the

statistics available for analysis. Therefore everything within these limits is consistant and there is no sign of deviations that have to be explained by new physics. Any theory that involves top coupling to dark matter, an excess in the tail of the distributions investigated here would be expected. Precise measurements were done, but the step of proceeding to place formal limits on new physics was not done. There are no deviations here, but this could be used as a basis to get the modelling right to then build to more specific, targeted searches. And the data agrees well with the MADGRAPH prediction after top p_T reweighting.

9. Differential Cross Sections: Systematic Uncertainties and Results

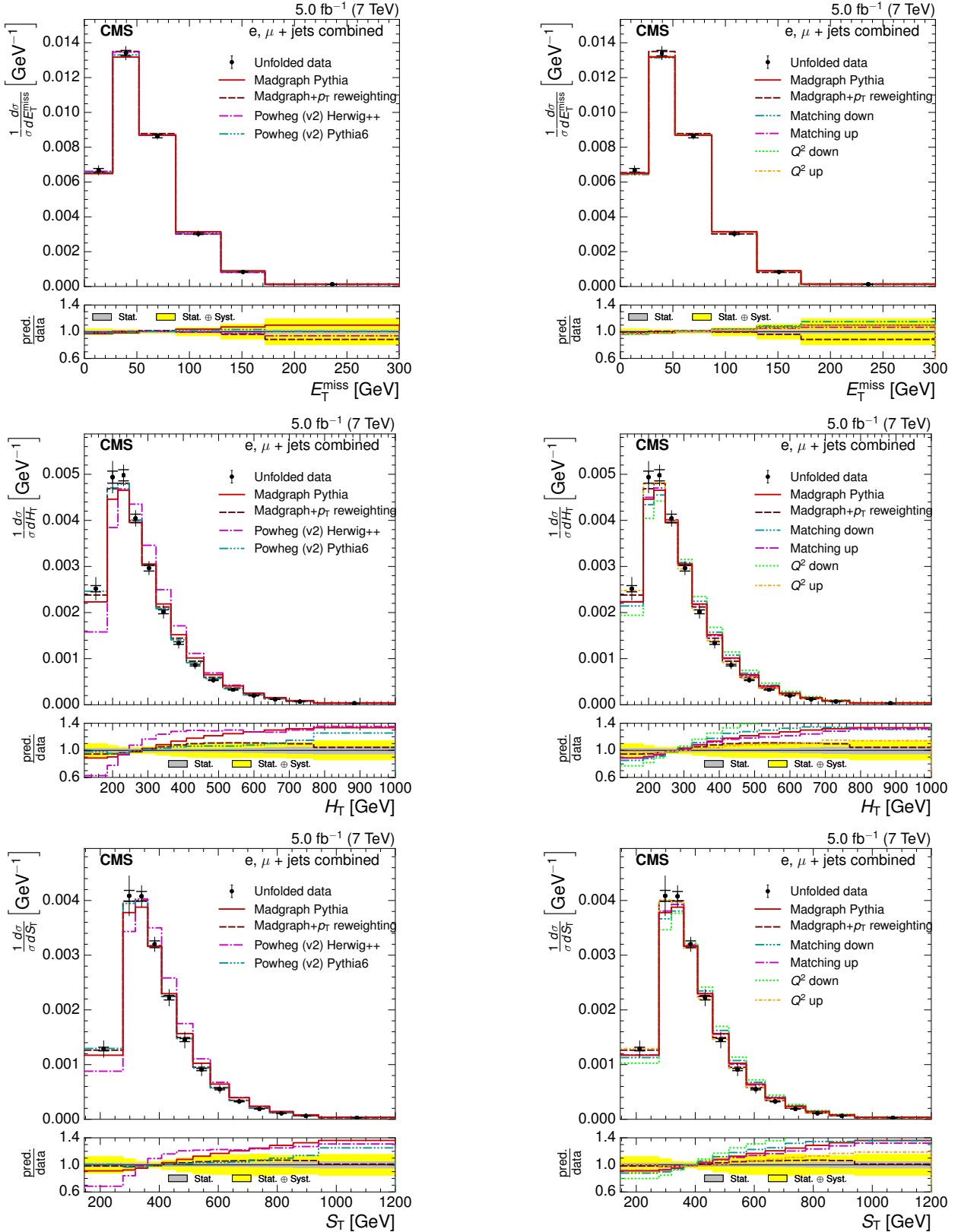


Figure 9.5: Comparison of the measured normalised differential cross section with respect to E_T^{miss} (upper), H_T (middle) and S_T (lower) to different Monte Carlo generators: MADGRAPH, POWHEGv2+HERWIG, POWHEGv2+PYTHIA and MADGRAPH corrected for top p_T mismodelling (left) and to different Monte Carlo predictions matching threshold up/down and factorisation scale up/down (right) in the combined electron+jets and muon+jets channel at $\sqrt{s} = 7 \text{ TeV}$. The lower plots show the ratio of the predictions to the data.

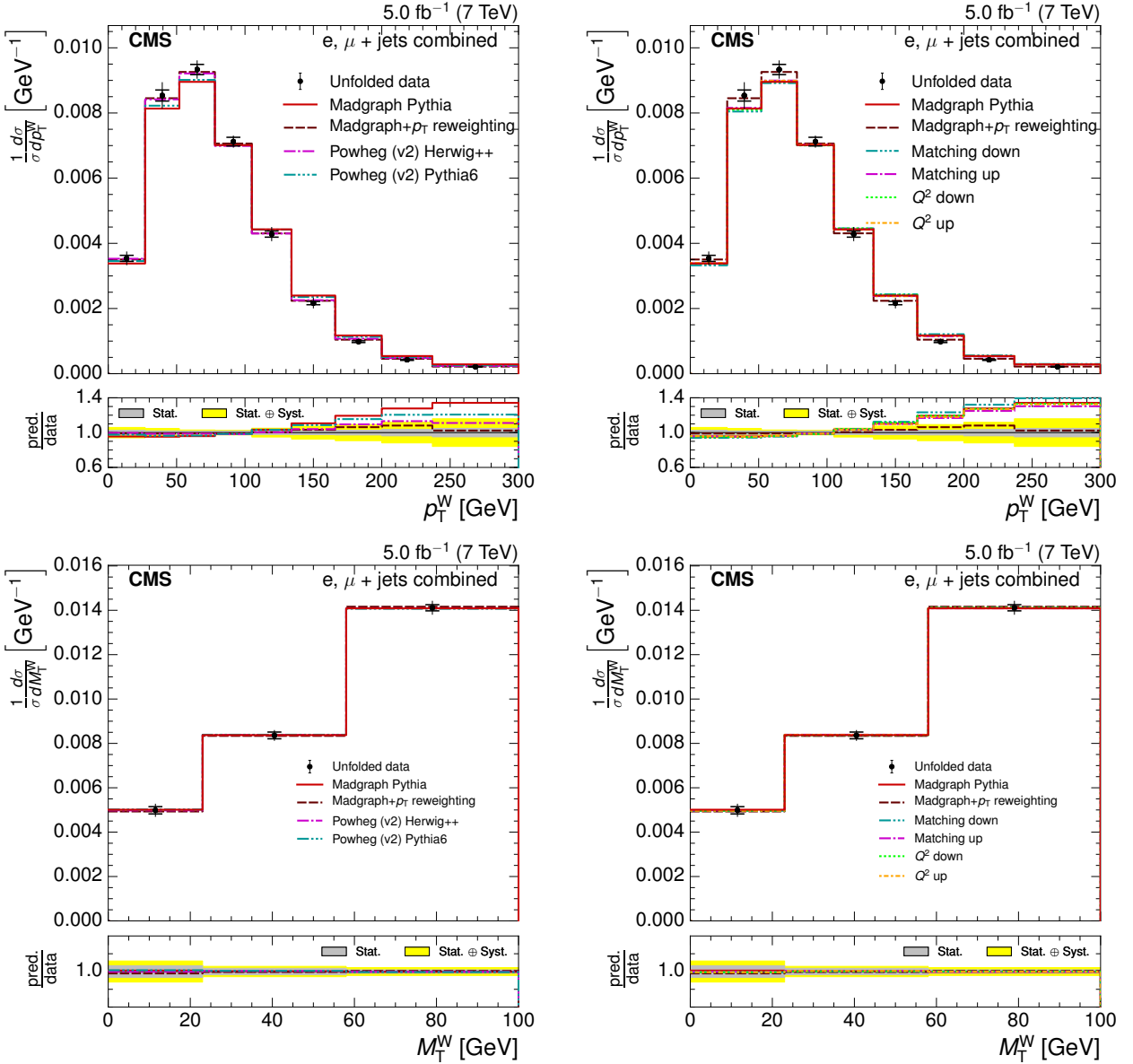


Figure 9.6: Comparison of the measured normalised differential cross section with respect to p_T^W (upper) and M_T^W (lower) to different Monte Carlo generators: MADGRAPH, POWHEGv2+HERWIG, POWHEGv2+PYTHIA and MADGRAPH corrected for top p_T mismodelling (left) and to different Monte Carlo predictions matching threshold up/down and factorisation scale up/down (right) in the combined electron+jets and muon+jets channel at $\sqrt{s} = 7\text{ TeV}$. The lower plots show the ratio of the predictions to the data.

9. Differential Cross Sections: Systematic Uncertainties and Results

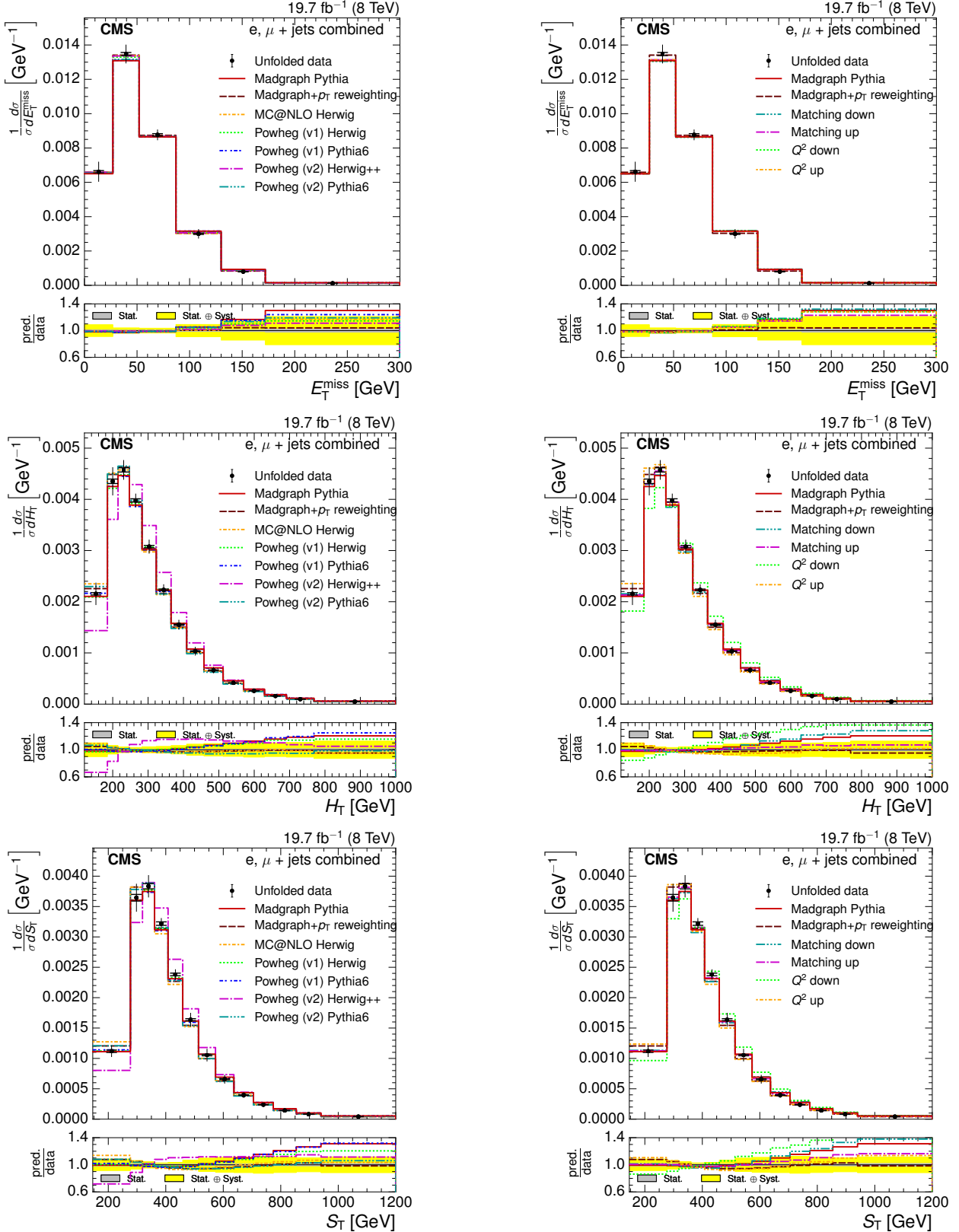


Figure 9.7: Comparison of the measured normalised differential cross section with respect to E_T^{miss} (upper), H_T (middle) and S_T (lower) to different Monte Carlo generators: MADGRAPH, POWHEGv1+HERWIG, POWHEGv1+PYTHIA, POWHEGv2+HERWIG, POWHEGv2+PYTHIA and MADGRAPH corrected for top p_T mismodelling (left) and to different Monte Carlo predictions matching threshold up/down and factorisation scale up/down (right) in the combined electron+jets and muon+jets channel at $\sqrt{s} = 8 \text{ TeV}$. The lower plots show the ratio of the predictions to the data.

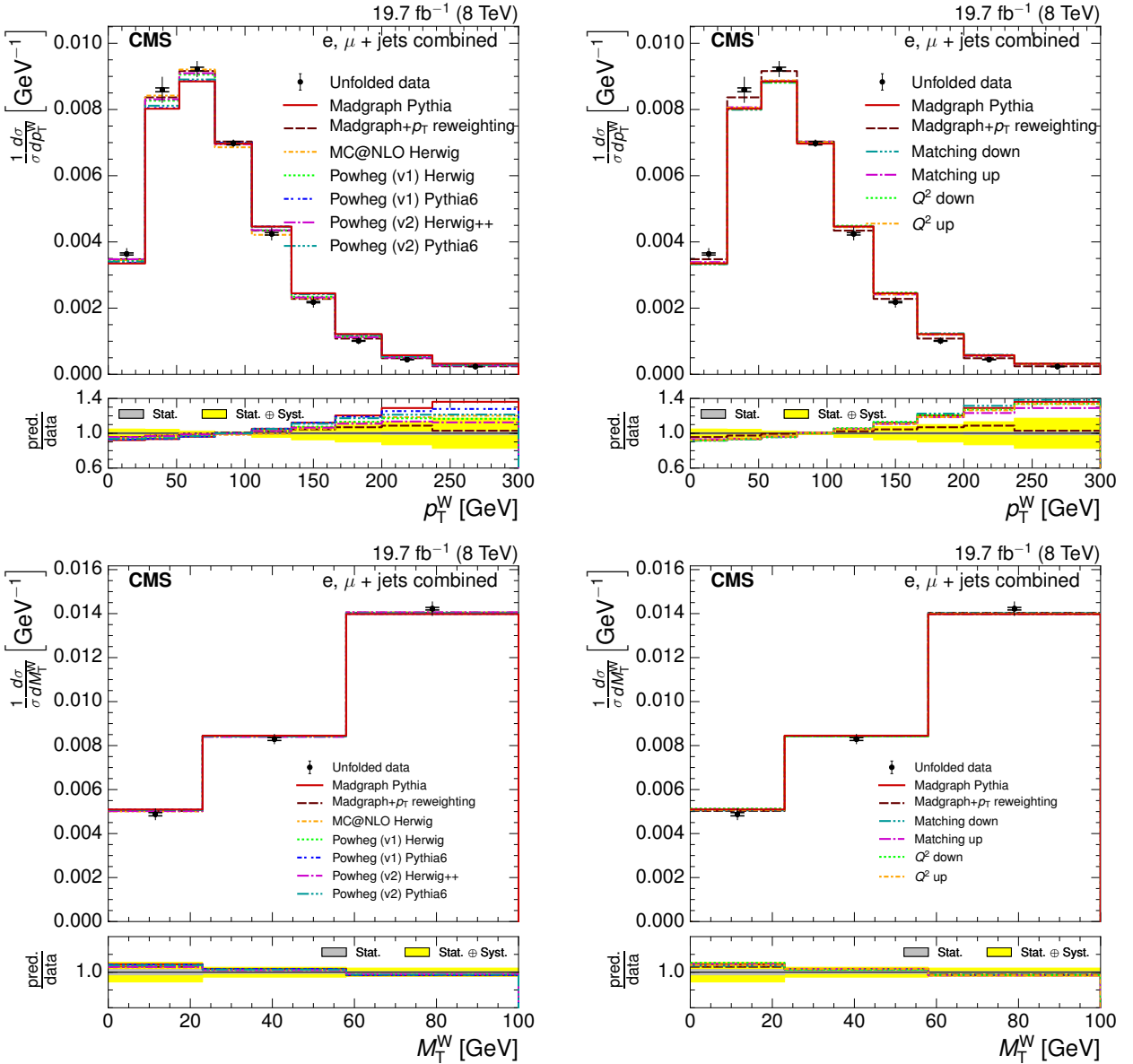


Figure 9.8: Comparison of the measured normalised differential cross section with respect to p_T^W (upper) and M_T^W (lower) to different Monte Carlo generators: MADGRAPH, POWHEGv1+HERWIG, POWHEGv1+PYTHIA, POWHEGv2+HERWIG, POWHEGv2+PYTHIA and MADGRAPH corrected for top p_T mismodelling (left) and to different Monte Carlo predictions matching threshold up/down and factorisation scale up/down (right) in the combined electron+jets and muon+jets channel at $\sqrt{s} = 8$ TeV. The lower plots show the ratio of the predictions to the data.

10 | Summary and Outlook

This thesis has presented an overview of the theoretical background to the Standard Model, a summary of the CMS detector at the LHC, a small scale study of b-tagging algorithms employed in CMS physics analyses, and a measurement of normalised differential $t\bar{t}$ cross sections with respect to global variables E_T^{miss} , H_T , S_T , M_T^W and p_T^W in proton-proton collisions with 5.0 fb^{-1} of data at $\sqrt{s}=7 \text{ TeV}$ and with 19.7 fb^{-1} of data at $\sqrt{s}=8 \text{ TeV}$, collected with the CMS detector.

The results of this analysis confirmed the previously observed characteristic [49] of a p_T distribution that is softer in data than in the simulation from the **MADGRAPH**, **MC@NLO** and **POWHEG** generators. The simulated **MADGRAPH** distribution, which is used as the nominal signal sample in this analysis, once corrected for this mismodelling shows good agreement with data. Otherwise, the data shows good general agreement with predictions, showing that these commonly used Monte Carlo simulation generators can be used with confidence to model $t\bar{t}$ events. The **MC@NLO** generator performs well at $\sqrt{s}=8 \text{ TeV}$ in terms of agreement with measurements, with **POWHEGv2+PYTHIA** also predicting data well at both $\sqrt{s}=7 \text{ TeV}$ and $\sqrt{s}=8 \text{ TeV}$. In Run 2 CMS top analyses at $\sqrt{s}=13 \text{ TeV}$, samples generated with **POWHEGvv+PYTHIA 8** are used as the nominal $t\bar{t}$ signal sample, in which the top p_T mismodelling has been corrected.

Whilst the tendency for maximum deviations of observations from predictions is in the tails of the distributions, the general trend is for simulations to provide overestimations of the data. This appears to rule out signs of rare SM processes or BSM physics described in Sections 2.2 and 7.1 such as such as $t\bar{t} + W, Z$ or X , stop pair production or the existence of a composite top-antitop top field as postulated by the topcolour theory.

Existing analyses using $\sqrt{s}=7 \text{ TeV}$ data investigating E_T^{miss} and using $\sqrt{s}=8 \text{ TeV}$ data investigating all the global variables listed above can be found in [8] and [10] respectively.

The combination of the data from both $\sqrt{s} = 7\text{ TeV}$ and $\sqrt{s} = 8\text{ TeV}$ in this analysis with one single set of methods for both, allows the comparison of normalised differential cross sections between the two centre-of-mass-energies. Potential further work related to this analysis may look at a ratio of the differential cross sections between $\sqrt{s} = 7\text{ TeV}$ and $\sqrt{s} = 8\text{ TeV}$. Such a measurement would cancel many systematic measurements, producing a potentially precise measurement.

This analysis forms part of the output of the CMS top quark group [54], and complements similar analyses within CMS investigating top pair cross sections in various other final states such as the hadronic channel [85], in which both W bosons from the top quarks decay hadronically, leading to a six-jet event signature, and the dileptonic channel [51], in which both W bosons decay leptonically. The technique of top reconstruction, which is not carried out in the analysis presented in this thesis, allows for the identification of the specific top quark from which the decay products originate. Top reconstruction is utilised in CMS studies investigating the top pair cross section as a function of variables such as kinematic properties (like p_T and η) of the top quarks, $t\bar{t}$ pair and charged lepton(s) and $t\bar{t}$ invariant mass in addition to variables related to the b-jets and jets in the $t\bar{t}$ system [84]. Differential cross sections also

Normalised differential cross section measurements have also been performed by the ATLAS collaboration at $\sqrt{s} = 7\text{ TeV}$ [15] and $\sqrt{s} = 8\text{ TeV}$ [17]. While a direct comparison to ATLAS results is not possible since different variables are used and bin selection is not identical between analyses. However, the general observations of a harder distribution in predictions than observed in data, and generator performance such as the good agreement of MC@NLO+HERWIG generated samples with data, have also been noted in ATLAS analyses.

Run 2 of the LHC, after Long Shutdown 1, began in June 2015 with proton-proton collisions occurring at $\sqrt{s} = 13\text{ TeV}$. Further measurements of $t\bar{t}$ events are on-going at the LHC on Run 2 data and are an important component of the future CMS and LHC physics programs. An Early Analysis (EA, analyses aiming to produce early results and to demonstrate that

the detector and simulations are well understood at this early stage of Run 2) has been carried out on 71 pb^{-1} of LHC Run 2 data from CMS, by the same group that worked on the analysis presented in this thesis. As collision energies and luminosities at the LHC increase, the resulting higher statistics and larger cross sections in the coming years could lead to the observation of rare physics processes and/or the production of potential heavier particles than observed to date.

Run 2 is scheduled to continue until Long Shutdown 2 in 2018 when major accelerator and experiment upgrades will take place. Until then, regular technical stops, such as during vacation periods, will allow for routine maintenance to be carried out.

10. Summary and Outlook

A | b-tagging Study Plots

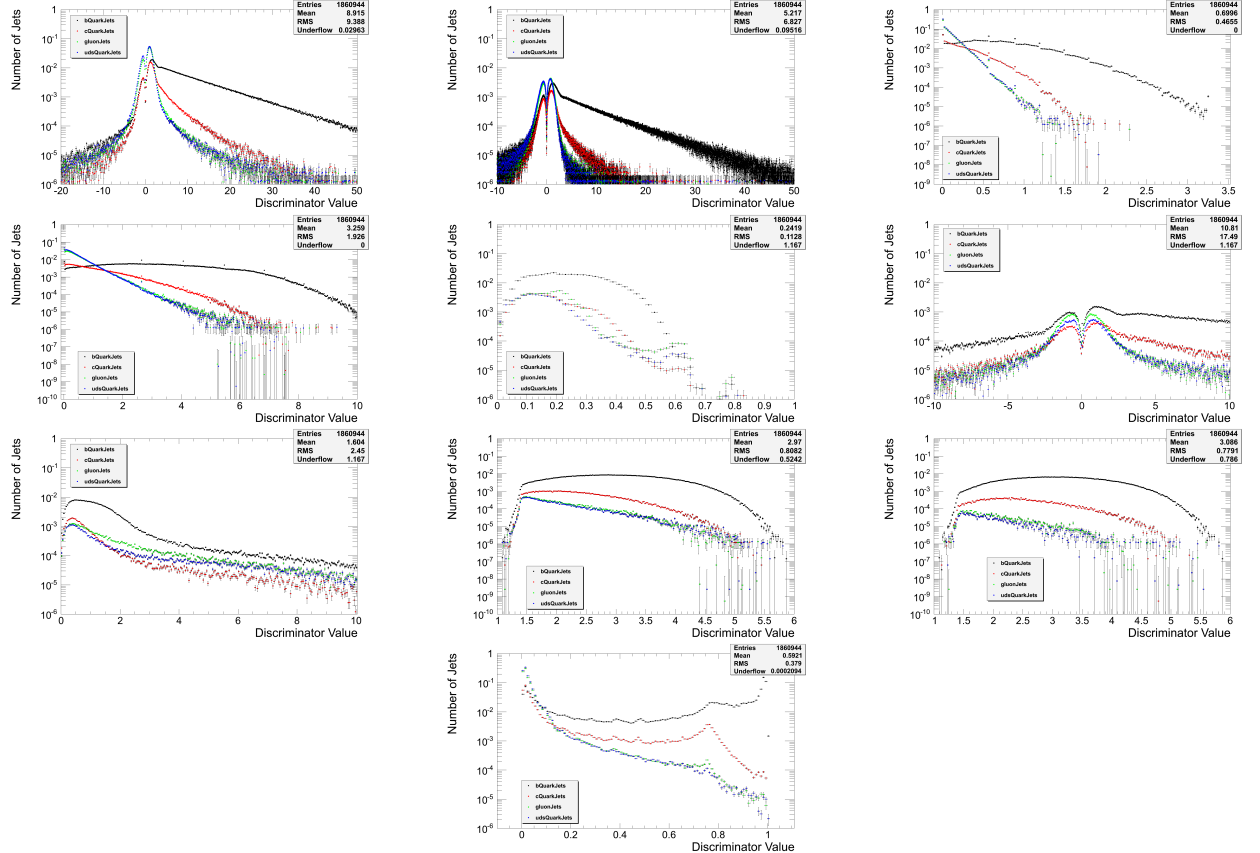


Figure A.1: Discriminator values produced by, from upper left: Track Counting High Efficiency, Track Counting High Purity, Jet Probability, JetBProbability, Soft Muon, Soft Muon by IP, Soft Muon by p_T , SSV High Efficiency, SSV High Purity and the CSV MVA algorithm for b-jets, c-jets, g-jets and uds-jets after normalisation

A. b-tagging Study Plots

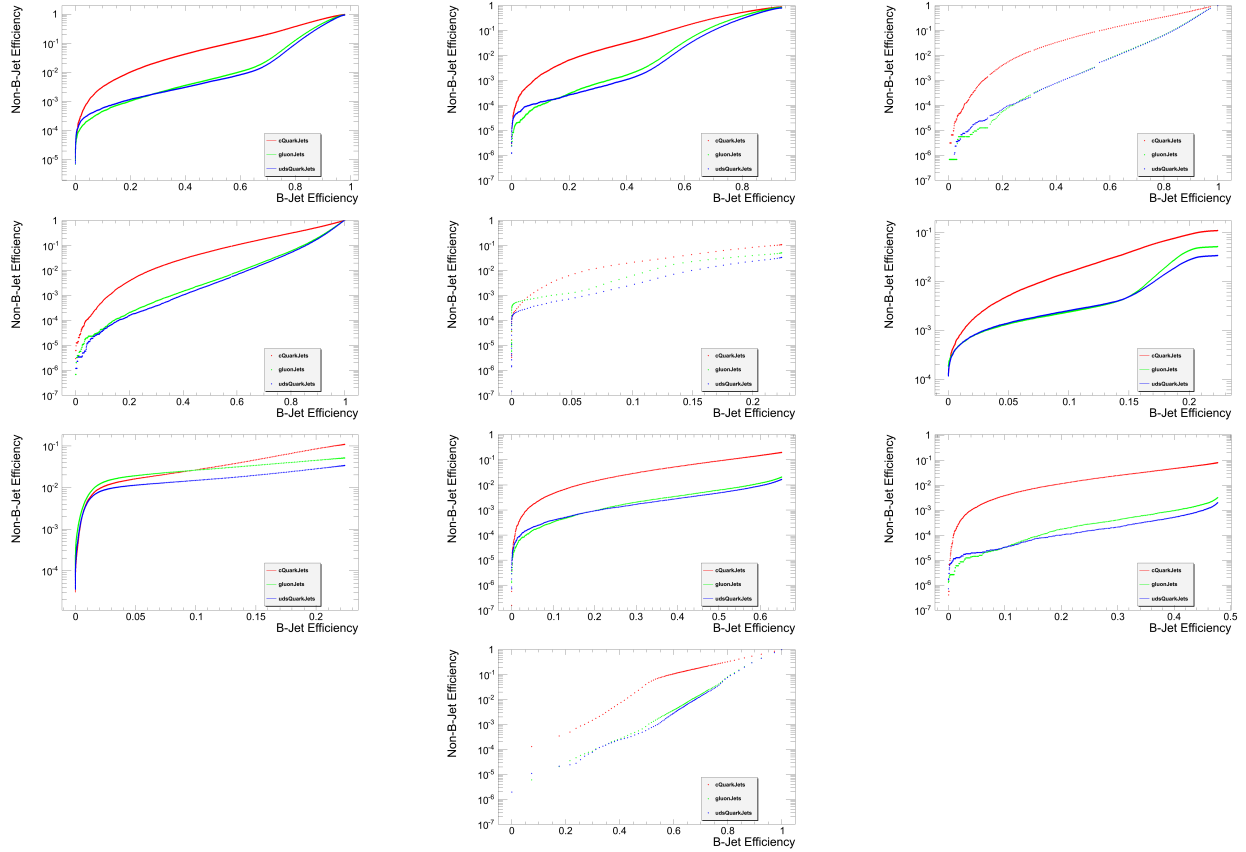


Figure A.2: c-jet, g-jet and uds-jet efficiencies as a function of b-jet efficiency for, from upper left: Track Counting High Efficiency, Track Counting High Purity, Jet Probability, JetBProbability, Soft Muon, Soft Muon by IP, Soft Muon by p_T , SSV High Efficiency, SSV High Purity and the CSV MVA algorithm.

B | $t\bar{t}$ differential cross section

B.1 Datasets in differential cross section analysis

Year	\sqrt{s} (TeV)	Channel	HLT Trigger	Run Range
2011	7	electron	HLT_Ele25_CaloIdVT_TrkIdT_CentralTriJet30	160404–163869
2011	7	electron	HLT_Ele25_CaloIdVT_TrkIdT_TriCentralJet30	163870–165633
2011	7	electron	HLT_Ele25_CaloIdVT_CaloIsoT_TrkIdT_TrkIsoT_TriCentralJet30	165634–178380
2011	7	electron	HLT_Ele25_CaloIdVT_CaloIsoT_TrkIdT_TrkIsoT_TriCentralPFJet30	178381–180252
2012	8	electron	HLT_Ele27_WP80	all
2011	7	muon	HLT_IsoMu24	160404–160404
2011	7	muon	HLT_IsoMu24_eta2p1	173236–190456
2012	8	muon	HLT_IsoMu24_eta2p1_v	all

Table B.1: HLT Triggers used in 2011 and 2012 data in the electron+jets and muon+jets channels.

Data Period	Mask
2011	Cert_160404-180252_7TeV_ReRecoNov08_Collisions11_JSON_v2.txt
2012	Cert_190456-208686_8TeV_22Jan2013ReReco_Collisions12_JSON.txt

Table B.2: JSON files used for the 2011 and 2012 data taking periods.

B.2 Data - Monte Carlo corrections

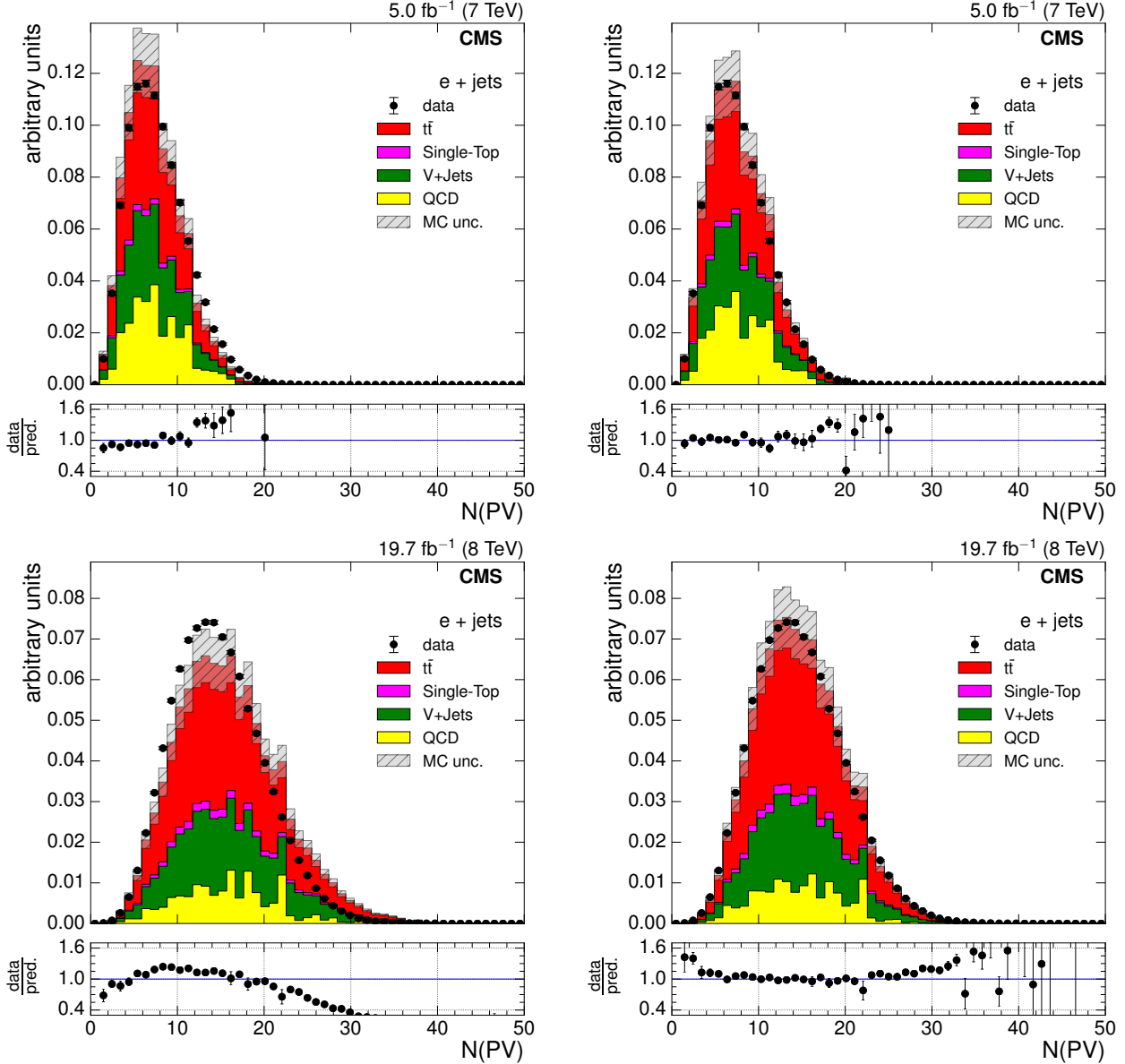


Figure B.1: Distributions of the number of reconstructed vertices in an event in the muon+jets channel before implementing pileup reweighting (left) and after implementation (right) at $\sqrt{s} = 7 \text{ TeV}$ (upper) and $\sqrt{s} = 8 \text{ TeV}$ (lower).

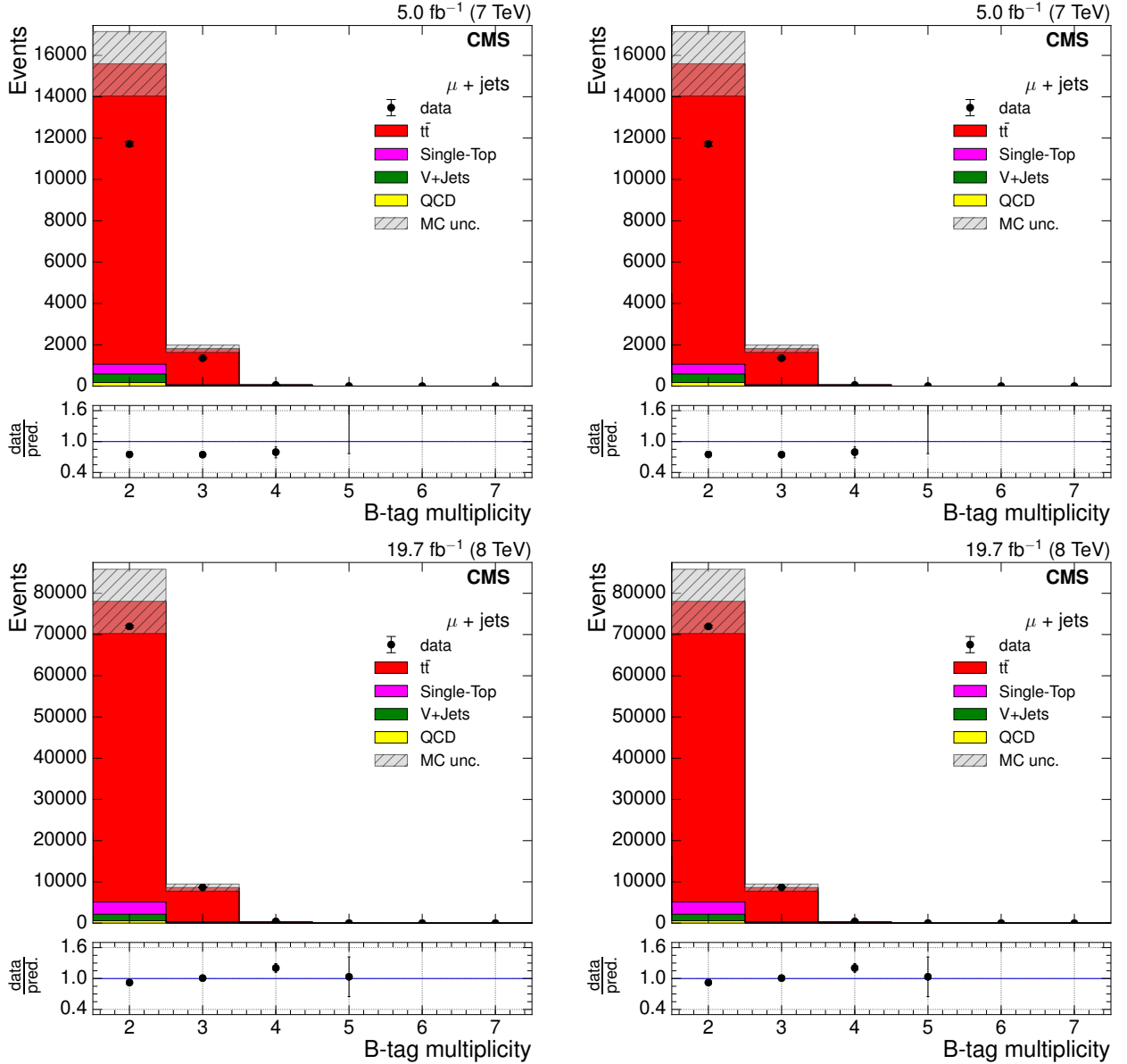


Figure B.2: Distributions of the number of b-tags in an event in the muon+jets channel before applying b-tag scale factors (left) and after application (right) at $\sqrt{s} = 7 \text{ TeV}$ (upper) and $\sqrt{s} = 8 \text{ TeV}$ (lower).

B. $t\bar{t}$ differential cross section

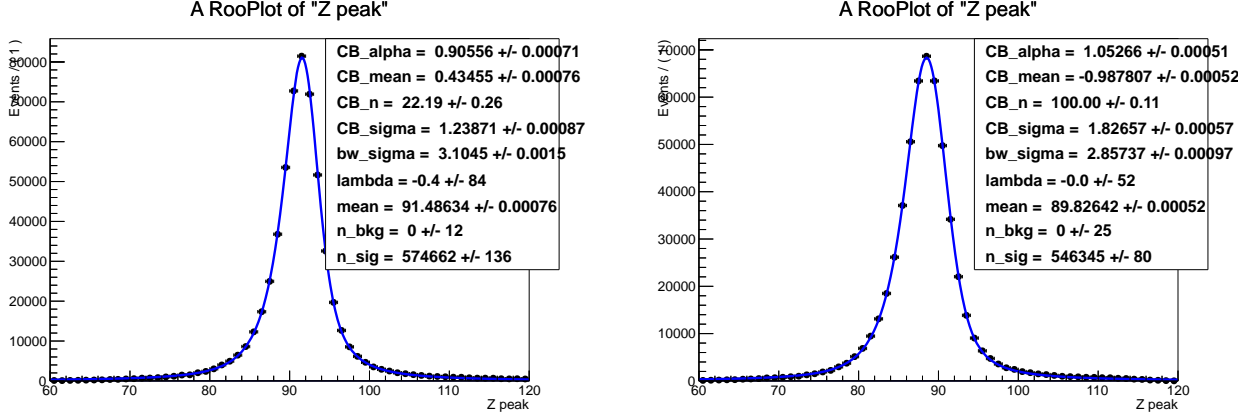


Figure B.3: Fits of the invariant mass distribution of all tag-and-probe pairs (left) and for tag-and-probe pairs in which the probe passes the trigger (right).

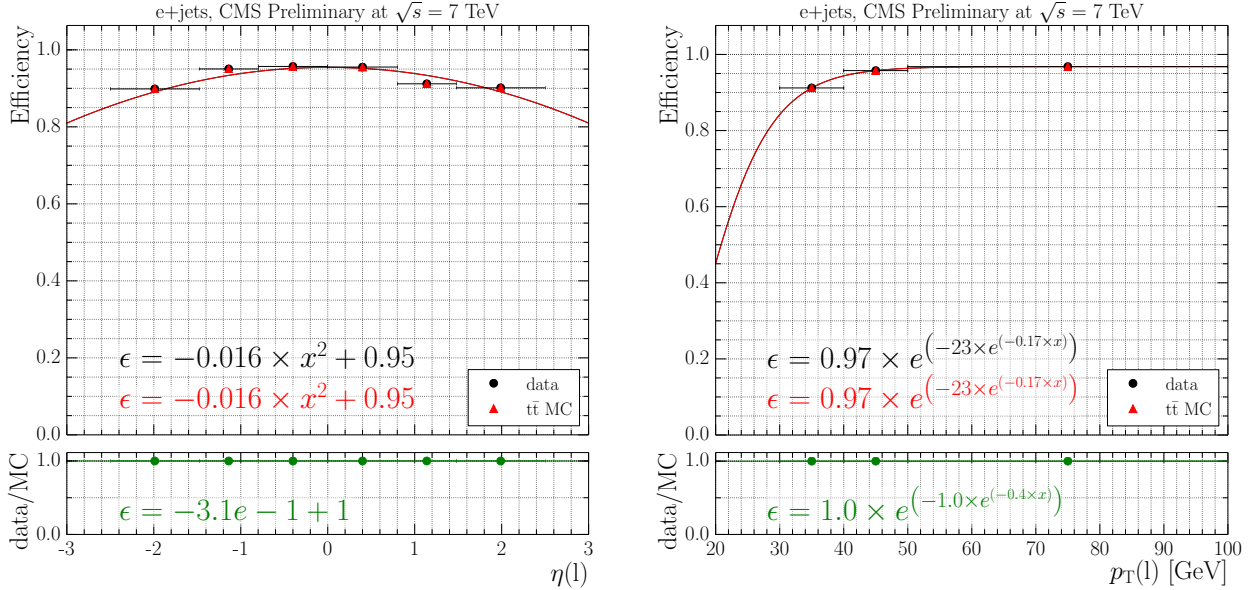


Figure B.4: Trigger efficiencies as a function of η and p_T in data and $t\bar{t}$ Monte Carlo simulation.

B.3 Binning in the muon+jets channel

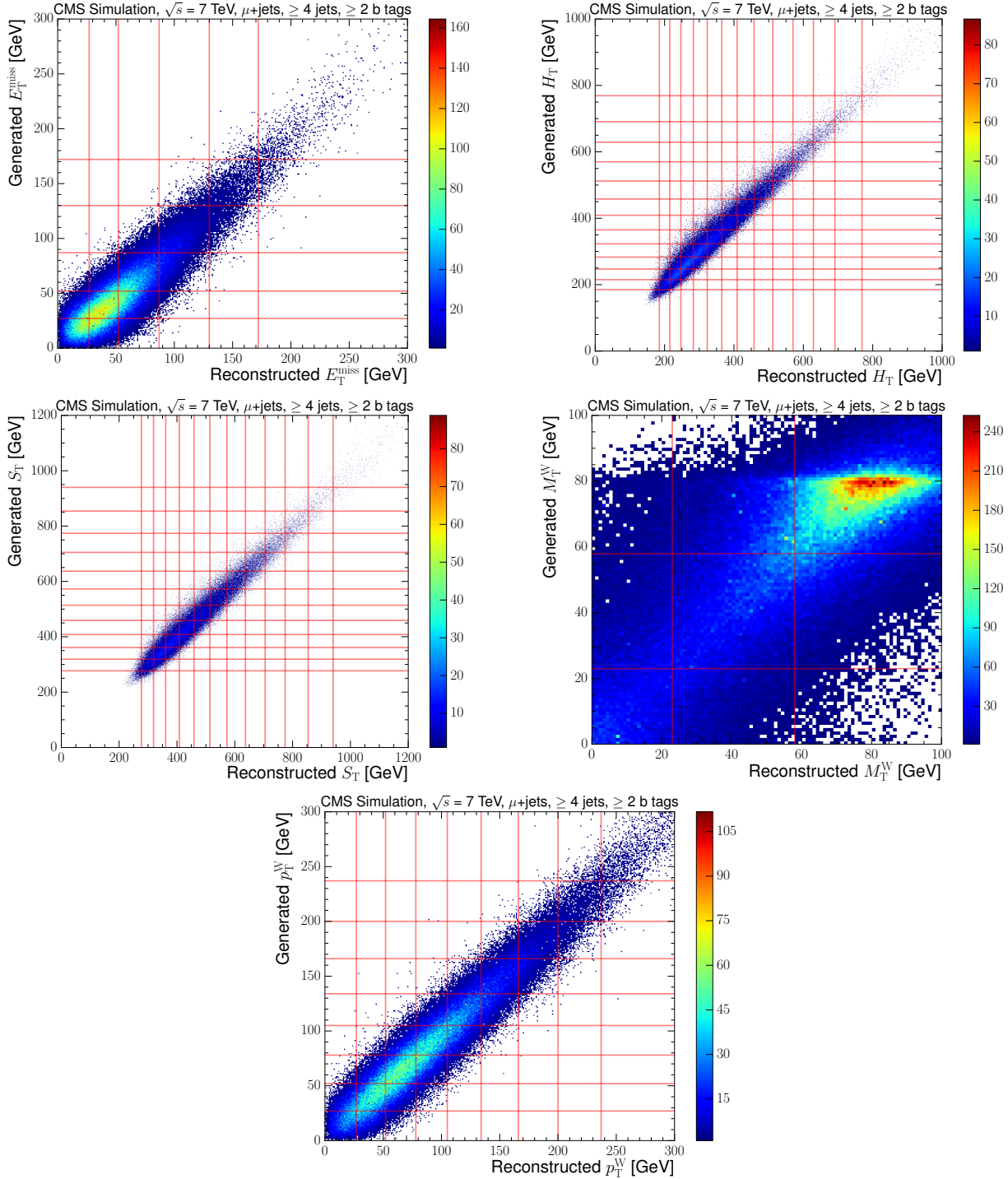


Figure B.5: Generated versus reconstructed distributions of the primary variables E_T^{miss} (upper left), H_T (upper right), S_T (middle left), M_T^W (middle right) and p_T^W (lower) with horizontal and vertical lines representing the boundaries of the selected bins at $\sqrt{s} = 7 \text{ TeV}$ in the muon+jets channel. These distributions are obtained using $t\bar{t}$ simulation.

B. $t\bar{t}$ differential cross section

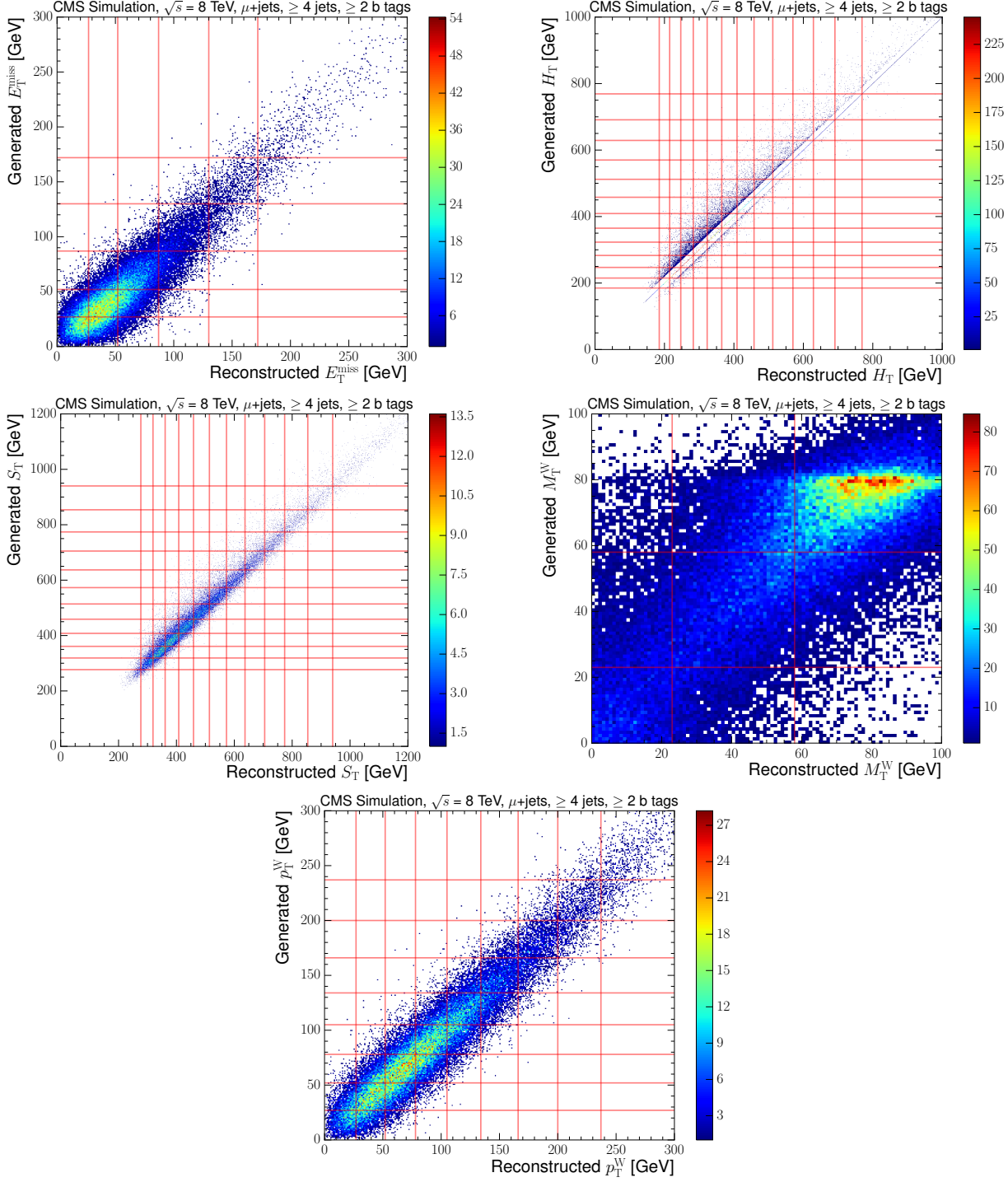


Figure B.6: Generated versus reconstructed distributions of the primary variables E_T^{miss} (upper left), H_T (upper right), S_T (middle left), M_T^W (middle right) and p_T^W (lower) with horizontal and vertical lines representing the boundaries of the selected bins at $\sqrt{s} = 8$ TeV in the muon+jets channel. These distributions are obtained using $t\bar{t}$ simulation.

B.4 Fitting Variable Distributions

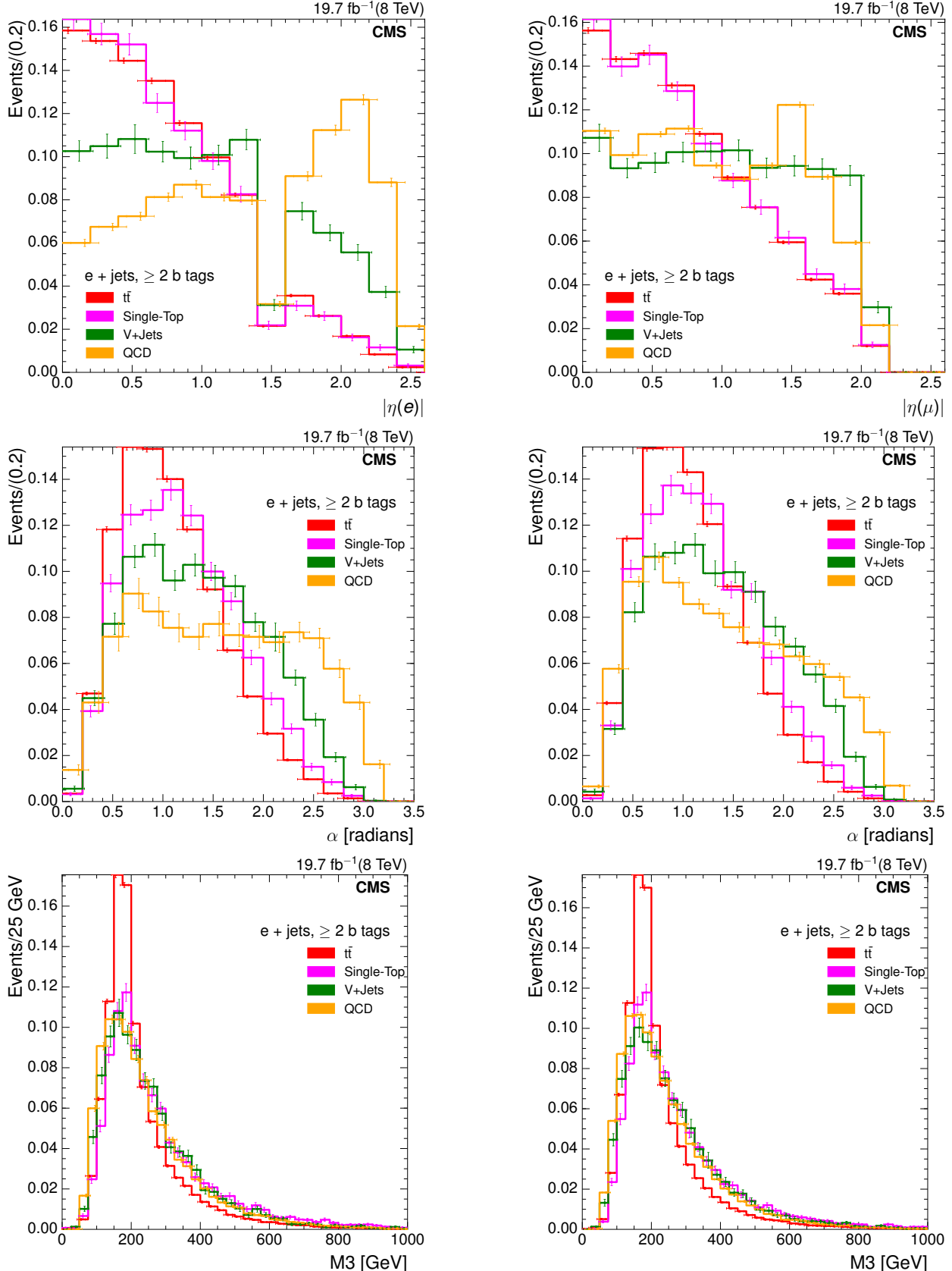


Figure B.7: Normalised distributions of the templates for the three fit variables lepton $|\eta|$ (upper), α (middle) and $M3$ (lower) inclusive¹⁶⁴ across all primary variable bins at $\sqrt{s} = 8 \text{ TeV}$ in the electron+jets channel (left) and in the muon+jets channel (right).

B.5 Fit Results Tables

Table B.3: Fit results for the E_T^{miss} variable at a centre-of-mass energy of 7 TeV (electron channel).

Process	0–27 GeV	27–52 GeV	52–87 GeV	87–130 GeV	130–172 GeV	≥ 172 GeV	Total
t̄t in	2526.0 ± 41.1	4512.2 ± 54.0	4013.3 ± 55.7	1725.2 ± 33.3	518.4 ± 18.5	287.8 ± 12.2	13582.9 ± 214.8
t̄t fit	2444.9 ± 90.2	3902.5 ± 159.0	3610.7 ± 148.6	1447.3 ± 83.5	366.1 ± 34.8	202.0 ± 24.1	11973.6 ± 540.2
Single Top in	82.4 ± 6.7	143.2 ± 8.9	120.1 ± 7.7	50.5 ± 4.9	19.6 ± 3.1	12.0 ± 2.1	427.8 ± 33.4
Single Top fit	0.0 ± 381.7	341.0 ± 197.4	212.6 ± 181.9	82.4 ± 88.3	59.3 ± 33.1	57.1 ± 21.2	752.3 ± 903.6
W/Z + jets in	121.0 ± 8.7	138.7 ± 9.9	82.9 ± 5.9	30.9 ± 2.2	12.8 ± 0.9	9.4 ± 0.7	395.7 ± 28.3
W/Z + jets fit	403.7 ± 125.3	342.4 ± 110.5	160.7 ± 105.0	109.3 ± 58.0	0.0 ± 40.5	4.9 ± 13.6	1021.0 ± 452.9
QCD in	323.3 ± 15.0	242.9 ± 11.3	9.0 ± 0.4	1.3 ± 0.1	1.0 ± 0.0	1.0 ± 0.0	578.5 ± 26.8
QCD fit	31.4 ± 56.6	0.0 ± 25.7	0.0 ± 88.1	0.0 ± 15.5	13.6 ± 11.0	0.0 ± 82.7	45.1 ± 279.6
Sum MC in	3052.7 ± 71.5	5037.0 ± 84.1	4225.3 ± 69.7	1807.8 ± 40.5	551.8 ± 22.6	310.3 ± 15.0	14984.9 ± 303.4
Sum MC fit	2880.0 ± 653.8	4586.0 ± 492.5	3984.0 ± 523.6	1639.0 ± 245.3	439.0 ± 119.5	264.0 ± 141.6	13792.0 ± 2176.3
Data	2880.0 ± 180.1	4586.0 ± 226.1	3984.0 ± 207.8	1639.0 ± 132.0	439.0 ± 66.7	264.0 ± 49.6	13792.0 ± 862.2

Table B.4: Fit results for the E_T^{miss} variable at a centre-of-mass energy of 7 TeV (muon channel).

Process	0–27 GeV	27–52 GeV	52–87 GeV	87–130 GeV	130–172 GeV	≥ 172 GeV	Total
t̄t in	2697.6 ± 41.5	4877.4 ± 57.9	4542.1 ± 52.0	1983.5 ± 34.2	594.9 ± 18.8	320.7 ± 13.0	15016.1 ± 217.4
t̄t fit	2026.2 ± 122.4	3800.8 ± 157.6	3729.3 ± 145.1	1475.9 ± 85.8	413.7 ± 39.0	200.7 ± 24.9	11646.6 ± 574.9
Single Top in	88.4 ± 6.7	150.6 ± 8.4	138.4 ± 8.4	57.6 ± 5.1	20.1 ± 3.0	13.9 ± 2.3	468.9 ± 33.9
Single Top fit	269.5 ± 150.0	397.2 ± 203.6	200.9 ± 164.4	83.5 ± 88.4	21.4 ± 33.7	35.3 ± 24.2	1007.8 ± 664.1
W/Z + jets in	107.9 ± 6.4	144.1 ± 8.6	103.6 ± 6.2	39.0 ± 2.3	11.5 ± 0.7	10.5 ± 0.6	416.5 ± 24.8
W/Z + jets fit	178.6 ± 119.9	198.1 ± 116.8	28.8 ± 101.6	43.6 ± 62.1	0.0 ± 35.8	9.0 ± 15.9	458.0 ± 452.1
QCD in	122.6 ± 5.1	22.6 ± 0.9	34.9 ± 1.5	0.1 ± 0.0	0.1 ± 0.0	0.1 ± 0.0	180.4 ± 7.5
QCD fit	4.7 ± 335.7	0.0 ± 370.4	0.0 ± 714.2	0.0 ± 253.2	10.9 ± 20.4	0.0 ± 18.8	15.6 ± 1712.7
Sum MC in	3016.5 ± 59.8	5194.7 ± 75.9	4819.1 ± 68.1	2080.2 ± 41.6	626.5 ± 22.4	345.1 ± 15.9	16082.0 ± 283.7
Sum MC fit	2479.0 ± 727.9	4396.1 ± 848.5	3959.0 ± 1125.3	1603.0 ± 489.5	446.0 ± 128.9	245.0 ± 83.8	13128.1 ± 3403.9
Data	2479.0 ± 159.2	4396.0 ± 211.6	3959.0 ± 200.7	1603.0 ± 126.7	446.0 ± 65.9	245.0 ± 46.9	13128.0 ± 811.0

Table B.5: Fit results for the H_T variable at a centre-of-mass energy of 7 TeV (electron channel).

Process	120–185 GeV	185–215 GeV	215–247 GeV	247–283 GeV	283–323 GeV	323–365 GeV	365–409 GeV	409–458 GeV	458–512 GeV	512–570 GeV	570–629 GeV	629–691 GeV	691–769 GeV	≥ 769 GeV	Total
$t\bar{t}$ in	220.2 ± 11.4	769.6 ± 24.0	1478.9 ± 29.9	2001.7 ± 40.5	2101.2 ± 37.0	1827.6 ± 37.5	1451.0 ± 31.1	1176.7 ± 25.8	868.9 ± 23.5	602.5 ± 18.7	384.4 ± 14.7	257.2 ± 11.9	193.0 ± 10.5	249.9 ± 12.1	13582.9 ± 328.7
$t\bar{t}$ fit	197.0 ± 42.8	705.9 ± 72.2	1399.3 ± 91.5	1998.6 ± 110.9	1782.1 ± 89.0	1533.8 ± 71.0	1235.2 ± 66.6	934.0 ± 67.5	671.5 ± 49.7	533.4 ± 47.5	342.1 ± 34.4	200.0 ± 23.6	152.7 ± 20.1	188.2 ± 29.3	11873.8 ± 816.0
Single Top in	12.9 ± 2.5	32.2 ± 4.2	49.4 ± 5.0	59.5 ± 5.7	64.1 ± 5.9	53.3 ± 5.4	41.4 ± 4.6	33.6 ± 4.0	27.2 ± 3.6	18.2 ± 2.9	13.0 ± 2.6	7.7 ± 1.8	6.2 ± 1.7	9.2 ± 2.0	427.8 ± 51.7
Single Top fit	106.7 ± 45.0	120.0 ± 83.5	239.4 ± 101.8	13.1 ± 367.3	109.0 ± 121.5	48.5 ± 88.6	64.8 ± 68.8	134.0 ± 68.1	82.5 ± 46.9	31.4 ± 40.3	28.1 ± 30.7	7.2 ± 19.0	11.3 ± 18.0	45.6 ± 27.5	1041.6 ± 1127.1
W/Z + jets in	24.2 ± 1.7	34.0 ± 2.4	47.4 ± 3.4	47.3 ± 3.4	50.7 ± 3.6	43.5 ± 3.1	34.8 ± 2.5	31.8 ± 2.3	24.2 ± 1.7	22.0 ± 1.6	14.1 ± 1.0	6.1 ± 0.4	6.6 ± 0.5	9.1 ± 0.7	395.7 ± 28.3
W/Z + jets fit	0.0 ± 16.7	14.2 ± 47.5	10.2 ± 33.9	181.3 ± 65.1	218.9 ± 76.0	174.6 ± 65.4	21.3 ± 99.6	55.0 ± 36.8	50.0 ± 29.4	11.2 ± 41.9	7.8 ± 16.3	30.8 ± 14.2	0.0 ± 13.1	0.0 ± 16.6	775.4 ± 572.6
QCD in	0.3 ± 0.0	102.4 ± 4.7	46.5 ± 2.2	193.7 ± 9.0	82.0 ± 3.8	86.8 ± 4.0	13.2 ± 0.6	17.5 ± 0.8	2.8 ± 0.1	4.6 ± 0.2	13.1 ± 0.6	5.5 ± 0.3	2.0 ± 0.1	6.0 ± 0.3	576.5 ± 26.7
QCD fit	13.4 ± 10.8	11.9 ± 29.5	0.0 ± 69.3	0.0 ± 14.8	0.0 ± 90.2	0.0 ± 36.5	50.7 ± 40.1	0.0 ± 18.6	0.0 ± 10.9	17.9 ± 19.9	0.0 ± 5.1	0.0 ± 1.9	7.2 ± 5.8	101.1 ± 360.4	
Sum MC in	257.7 ± 15.6	938.2 ± 35.3	1622.1 ± 40.4	2302.1 ± 58.5	2298.0 ± 50.4	2011.2 ± 50.0	1540.4 ± 38.8	1259.6 ± 32.9	923.2 ± 28.9	647.3 ± 23.4	424.6 ± 19.0	276.5 ± 14.4	207.7 ± 12.8	274.1 ± 15.0	14982.9 ± 435.5
Sum MC fit	317.0 ± 115.4	852.0 ± 232.7	1649.0 ± 296.6	2193.0 ± 558.0	2110.0 ± 376.7	1757.0 ± 261.5	1372.0 ± 275.0	1123.0 ± 191.1	804.0 ± 136.8	594.0 ± 149.6	378.0 ± 88.3	238.0 ± 61.9	164.0 ± 53.1	241.0 ± 79.2	13791.9 ± 2876.0
Data	317.0 ± 61.1	852.0 ± 97.6	1649.0 ± 135.2	2193.0 ± 155.3	2110.0 ± 153.2	1757.0 ± 139.5	1372.0 ± 122.7	1123.0 ± 109.6	804.0 ± 92.2	594.0 ± 79.5	378.0 ± 62.2	238.0 ± 49.8	164.0 ± 38.8	241.0 ± 49.6	13792.0 ± 1346.4

Table B.6: Fit results for the H_T variable at a centre-of-mass energy of 7 TeV (muon channel).

Process	120–185 GeV	185–215 GeV	215–247 GeV	247–283 GeV	283–323 GeV	323–365 GeV	365–409 GeV	409–458 GeV	458–512 GeV	512–570 GeV	570–629 GeV	629–691 GeV	691–769 GeV	≥ 769 GeV	Total
$t\bar{t}$ in	253.7 ± 12.0	882.4 ± 22.4	1711.4 ± 31.2	2273.6 ± 37.9	2358.3 ± 40.4	2019.1 ± 35.9	1586.2 ± 34.1	1258.0 ± 27.4	916.9 ± 22.6	636.0 ± 18.5	400.4 ± 14.8	269.7 ± 13.0	196.2 ± 10.4	254.3 ± 12.5	15016.1 ± 333.1
$t\bar{t}$ fit	337.9 ± 18.7	839.0 ± 104.1	1394.6 ± 101.4	1883.0 ± 101.4	1937.2 ± 79.3	1498.0 ± 81.8	1100.7 ± 63.9	901.6 ± 55.1	595.8 ± 48.0	450.8 ± 38.7	253.6 ± 33.4	146.6 ± 24.4	112.7 ± 20.9	127.1 ± 28.9	11578.5 ± 799.9
Single Top in	17.4 ± 3.2	35.4 ± 4.0	56.1 ± 5.3	63.2 ± 5.6	67.6 ± 6.1	55.0 ± 5.0	46.4 ± 4.6	37.4 ± 4.1	29.4 ± 3.7	19.8 ± 2.9	13.5 ± 2.4	8.0 ± 1.8	8.1 ± 1.9	11.6 ± 2.2	468.9 ± 52.8
Single Top fit	0.0 ± 46.2	61.1 ± 110.5	90.4 ± 135.6	121.0 ± 119.8	86.6 ± 93.2	279.0 ± 77.9	157.3 ± 60.1	94.4 ± 51.2	99.2 ± 45.2	63.9 ± 35.5	50.4 ± 31.7	34.2 ± 21.9	29.0 ± 18.5	70.9 ± 28.3	1237.3 ± 875.6
W/Z + jets in	26.6 ± 1.6	37.5 ± 2.2	49.4 ± 2.9	52.9 ± 3.2	57.4 ± 3.4	47.0 ± 2.8	36.9 ± 2.2	30.0 ± 1.8	25.3 ± 1.5	17.5 ± 1.0	9.8 ± 0.6	8.1 ± 0.5	6.3 ± 0.4	11.6 ± 0.7	416.5 ± 24.8
W/Z + jets fit	0.0 ± 39.9	21.9 ± 25.0	32.3 ± 101.5	12.6 ± 248.9	62.7 ± 92.7	0.0 ± 149.0	0.0 ± 108.6	0.0 ± 36.1	0.0 ± 100.7	0.0 ± 18.6	0.0 ± 47.9	4.9 ± 50.0	7.3 ± 8.9	0.0 ± 5.3	141.7 ± 1033.1
QCD in	12.2 ± 0.5	27.3 ± 1.2	30.0 ± 1.3	42.7 ± 1.9	21.7 ± 0.9	19.8 ± 0.9	19.6 ± 0.9	1.4 ± 0.1	1.6 ± 0.1	1.8 ± 0.1	0.8 ± 0.0	0.1 ± 0.0	1.1 ± 0.0	0.3 ± 0.0	180.3 ± 7.9
QCD fit	7.2 ± 13.5	0.0 ± 26.3	106.7 ± 87.2	24.3 ± 100.8	18.6 ± 69.4	0.0 ± 97.9	0.0 ± 42.7	0.0 ± 15.8	0.0 ± 14.0	3.3 ± 12.6	0.0 ± 10.2	10.4 ± 29.6	0.0 ± 24.4	0.0 ± 3.2	170.5 ± 547.6
Sum MC in	309.9 ± 17.3	982.6 ± 29.9	1846.9 ± 40.7	2432.4 ± 48.5	2505.0 ± 50.9	2140.8 ± 44.6	1689.0 ± 41.8	1326.8 ± 33.3	973.3 ± 27.9	675.1 ± 22.6	424.5 ± 17.8	286.0 ± 15.3	211.6 ± 12.7	277.7 ± 15.4	16081.9 ± 418.7
Sum MC fit	345.0 ± 118.3	922.0 ± 265.9	1624.0 ± 425.7	2041.0 ± 570.9	2105.0 ± 334.6	1777.0 ± 406.6	1258.0 ± 275.3	996.0 ± 158.1	695.0 ± 207.9	518.0 ± 105.4	304.0 ± 123.1	196.0 ± 125.9	149.0 ± 72.7	198.0 ± 65.6	13128.0 ± 3256.2
Data	345.0 ± 59.2	922.0 ± 97.6	1624.0 ± 129.6	2041.0 ± 143.7	2105.0 ± 146.0	1777.0 ± 133.9	1258.0 ± 112.8	996.0 ± 100.5	695.0 ± 83.3	518.0 ± 71.0	304.0 ± 53.8	196.0 ± 43.3	149.0 ± 38.4	198.0 ± 43.6	13128.0 ± 1256.8

Table B.7: Fit results for the S_T variable at a centre-of-mass energy of 7 TeV (electron channel).

Process	146–277 GeV	277–319 GeV	319–361 GeV	361–408 GeV	408–459 GeV	459–514 GeV	514–573 GeV	573–637 GeV	637–705 GeV	705–774 GeV	774–854 GeV	854–940 GeV	≥ 940 GeV	Total
t̄t in	243.0 \pm 12.7	925.4 \pm 23.2	1705.6 \pm 38.2	2198.3 \pm 38.3	2139.4 \pm 37.3	1836.8 \pm 38.1	1440.0 \pm 30.2	1057.2 \pm 25.5	726.1 \pm 20.4	466.2 \pm 15.8	341.3 \pm 14.1	210.2 \pm 10.4	293.3 \pm 12.9	13582.9 \pm 317.1
t̄t fit	247.0 \pm 46.2	1009.4 \pm 199.6	1619.0 \pm 97.4	2014.1 \pm 122.4	1943.0 \pm 83.4	1619.5 \pm 82.4	1108.8 \pm 66.6	795.9 \pm 64.0	623.0 \pm 41.9	344.9 \pm 71.7	261.2 \pm 26.4	185.7 \pm 22.8	185.8 \pm 26.5	11957.3 \pm 951.3
Single Top in	15.1 \pm 2.8	34.2 \pm 4.1	56.1 \pm 5.5	61.8 \pm 5.8	62.6 \pm 6.0	54.6 \pm 5.4	40.9 \pm 4.4	31.9 \pm 3.6	23.8 \pm 3.4	16.4 \pm 2.8	11.1 \pm 2.2	7.4 \pm 1.8	11.9 \pm 2.2	427.8 \pm 50.1
Single Top fit	70.6 \pm 53.4	0.0 \pm 2172.9	152.3 \pm 114.4	48.2 \pm 174.0	86.9 \pm 105.7	21.8 \pm 102.5	155.6 \pm 69.8	169.7 \pm 64.4	77.8 \pm 38.8	40.9 \pm 32.9	59.8 \pm 24.3	25.3 \pm 20.9	62.7 \pm 25.5	971.6 \pm 2999.4
W/Z + jets in	29.3 \pm 2.1	41.3 \pm 3.0	45.7 \pm 3.3	51.1 \pm 3.7	52.3 \pm 3.7	39.4 \pm 2.8	38.6 \pm 2.8	28.2 \pm 2.0	25.3 \pm 1.8	15.4 \pm 1.1	10.4 \pm 0.7	6.8 \pm 0.5	12.0 \pm 0.9	395.7 \pm 28.3
W/Z + jets fit	8.2 \pm 31.4	103.5 \pm 95.8	86.7 \pm 46.7	198.7 \pm 87.8	142.1 \pm 69.8	159.7 \pm 61.2	59.5 \pm 44.5	3.0 \pm 416.6	0.0 \pm 999.9	39.0 \pm 142.0	0.0 \pm 53.6	0.0 \pm 22.2	0.0 \pm 390.9	800.5 \pm 2462.5
QCD in	3.1 \pm 0.1	146.2 \pm 6.8	43.6 \pm 2.0	234.5 \pm 10.9	79.1 \pm 3.7	10.6 \pm 0.5	16.5 \pm 0.8	14.3 \pm 0.7	4.0 \pm 0.2	8.7 \pm 0.4	7.8 \pm 0.4	3.5 \pm 0.2	4.7 \pm 0.2	576.5 \pm 26.7
QCD fit	25.2 \pm 21.3	1.0 \pm 206.6	0.0 \pm 60.7	0.0 \pm 32.3	0.0 \pm 20.0	0.0 \pm 47.1	0.0 \pm 26.6	24.5 \pm 31.8	5.2 \pm 9.8	0.2 \pm 514.4	0.0 \pm 3.5	0.0 \pm 5.4	6.5 \pm 6.1	62.6 \pm 985.6
Sum MC in	290.4 \pm 17.7	1147.1 \pm 37.1	1851.0 \pm 49.0	2545.7 \pm 58.6	2333.4 \pm 50.7	1941.3 \pm 46.8	1536.0 \pm 38.2	1131.6 \pm 31.9	779.3 \pm 25.9	506.7 \pm 20.1	370.6 \pm 17.5	228.0 \pm 12.9	321.9 \pm 16.1	14982.9 \pm 422.3
Sum MC fit	351.0 \pm 152.3	1114.0 \pm 2674.9	1858.0 \pm 319.3	2261.0 \pm 416.5	2172.0 \pm 278.9	1801.0 \pm 293.3	1324.0 \pm 207.4	993.0 \pm 576.7	706.0 \pm 1090.5	425.0 \pm 760.9	321.0 \pm 107.8	211.0 \pm 71.3	255.0 \pm 449.1	13792.0 \pm 7398.8
Data	351.0 \pm 64.6	1114.0 \pm 113.2	1858.0 \pm 143.3	2261.0 \pm 158.2	2172.0 \pm 154.8	1801.0 \pm 141.3	1324.0 \pm 119.1	993.0 \pm 102.0	706.0 \pm 86.0	425.0 \pm 66.6	321.0 \pm 54.5	211.0 \pm 46.3	255.0 \pm 50.2	13792.0 \pm 1300.1

Table B.8: Fit results for the S_T variable at a centre-of-mass energy of 7 TeV (muon channel).

Process	146–277 GeV	277–319 GeV	319–361 GeV	361–408 GeV	408–459 GeV	459–514 GeV	514–573 GeV	573–637 GeV	637–705 GeV	705–774 GeV	774–854 GeV	854–940 GeV	≥ 940 GeV	Total
t̄t in	305.9 \pm 13.3	1099.3 \pm 25.8	1979.3 \pm 33.4	2478.8 \pm 39.3	2392.5 \pm 41.7	2008.9 \pm 37.6	1522.1 \pm 30.1	1115.1 \pm 25.3	772.0 \pm 21.3	483.2 \pm 16.1	350.4 \pm 13.8	213.5 \pm 10.5	295.2 \pm 13.4	15016.1 \pm 321.6
t̄t fit	313.1 \pm 53.1	1116.8 \pm 92.5	1713.7 \pm 89.1	1927.7 \pm 105.7	1857.9 \pm 83.2	1396.0 \pm 87.2	1084.6 \pm 64.4	813.8 \pm 52.6	512.4 \pm 44.6	345.3 \pm 31.8	218.7 \pm 26.3	117.8 \pm 22.2	149.5 \pm 26.4	11567.2 \pm 779.1
Single Top in	18.3 \pm 3.2	42.7 \pm 4.6	57.8 \pm 5.3	71.6 \pm 6.3	64.6 \pm 5.4	56.6 \pm 5.1	46.4 \pm 4.6	35.7 \pm 3.9	24.6 \pm 3.4	15.9 \pm 2.6	11.9 \pm 2.2	8.4 \pm 1.8	14.4 \pm 2.3	468.9 \pm 50.9
Single Top fit	47.3 \pm 54.3	48.3 \pm 102.8	87.6 \pm 118.4	197.6 \pm 132.2	181.1 \pm 83.9	257.5 \pm 98.0	111.4 \pm 60.4	57.2 \pm 48.7	63.6 \pm 44.1	34.6 \pm 29.4	50.7 \pm 26.3	32.0 \pm 20.6	67.5 \pm 25.6	1236.6 \pm 844.8
W/Z + jets in	30.2 \pm 1.8	45.8 \pm 2.7	53.8 \pm 3.2	55.2 \pm 3.3	55.6 \pm 3.3	45.7 \pm 2.7	38.6 \pm 2.3	24.3 \pm 1.4	22.1 \pm 1.3	15.6 \pm 0.9	9.6 \pm 0.6	6.5 \pm 0.4	13.6 \pm 0.8	416.5 \pm 24.8
W/Z + jets fit	0.0 \pm 15.6	41.5 \pm 61.3	43.7 \pm 61.2	83.7 \pm 66.0	0.0 \pm 90.6	14.6 \pm 54.8	0.0 \pm 20.3	0.0 \pm 35.1	5.0 \pm 25.7	2.1 \pm 24.7	1.6 \pm 27.4	10.1 \pm 9.3	0.0 \pm 3.8	202.3 \pm 495.9
QCD in	39.5 \pm 1.7	15.2 \pm 0.6	57.3 \pm 2.4	24.5 \pm 1.0	17.2 \pm 0.7	19.6 \pm 0.8	3.9 \pm 0.2	1.0 \pm 0.0	0.8 \pm 0.0	0.1 \pm 0.0	1.1 \pm 0.0	0.1 \pm 0.0	0.2 \pm 0.0	180.4 \pm 7.6
QCD fit	12.6 \pm 16.7	24.4 \pm 65.5	0.0 \pm 122.8	0.0 \pm 68.1	85.0 \pm 43.1	0.0 \pm 169.6	0.0 \pm 12.4	0.0 \pm 13.0	0.0 \pm 755.8	0.0 \pm 17.3	0.0 \pm 427.0	0.0 \pm 30.1	0.0 \pm 2.3	121.9 \pm 1743.7
Sum MC in	393.9 \pm 20.0	1202.9 \pm 33.8	2148.2 \pm 44.4	2630.1 \pm 50.0	2529.9 \pm 51.2	2130.7 \pm 46.2	1611.1 \pm 37.2	1176.1 \pm 30.7	819.4 \pm 26.0	514.8 \pm 19.6	373.0 \pm 16.7	228.5 \pm 12.7	323.5 \pm 16.5	16082.0 \pm 404.9
Sum MC fit	373.0 \pm 139.7	1231.0 \pm 322.0	1845.0 \pm 391.6	2209.0 \pm 372.0	2124.0 \pm 300.8	1668.0 \pm 409.7	1196.0 \pm 157.5	871.0 \pm 149.3	581.0 \pm 870.2	382.0 \pm 103.3	271.0 \pm 507.0	160.0 \pm 82.2	217.0 \pm 58.1	13128.0 \pm 3863.5
Data	373.0 \pm 62.2	1231.0 \pm 112.7	1845.0 \pm 138.4	2209.0 \pm 149.7	2124.0 \pm 147.1	1668.0 \pm 129.1	1196.0 \pm 109.7	871.0 \pm 92.7	581.0 \pm 75.9	382.0 \pm 60.5	271.0 \pm 51.4	160.0 \pm 38.9	217.0 \pm 45.1	13128.0 \pm 1213.5

Table B.9: Fit results for the p_T^W variable at a centre-of-mass energy of 7 TeV (electron channel).

Process	0--27 GeV	27--52 GeV	52--78 GeV	78--105 GeV	105--134 GeV	134--166 GeV	166--200 GeV	200--237 GeV	≥ 237 GeV	Total
$t\bar{t}$ in	953.0 ± 26.1	2150.1 ± 35.2	2788.4 ± 45.5	2617.7 ± 40.9	2058.0 ± 37.0	1379.9 ± 34.1	782.4 ± 22.0	431.9 ± 15.5	421.8 ± 14.8	13582.9 ± 270.9
$t\bar{t}$ fit	821.0 ± 63.4	2182.9 ± 125.8	2544.3 ± 132.8	2380.5 ± 119.5	1781.9 ± 92.8	1139.6 ± 71.2	548.8 ± 51.9	296.2 ± 31.4	277.4 ± 26.2	11972.7 ± 715.1
Single Top in	30.0 ± 4.1	67.8 ± 6.1	80.6 ± 6.8	78.7 ± 6.4	61.7 ± 5.6	43.3 ± 4.6	26.5 ± 3.3	17.2 ± 2.7	22.0 ± 2.8	427.8 ± 42.4
Single Top fit	12.8 ± 112.3	17.6 ± 311.9	159.1 ± 179.7	207.9 ± 134.8	108.6 ± 105.5	68.5 ± 77.6	110.2 ± 54.0	88.8 ± 29.7	93.6 ± 24.4	867.1 ± 1029.8
W/Z + jets in	28.0 ± 2.0	73.6 ± 5.3	89.0 ± 6.4	66.7 ± 4.8	48.3 ± 3.5	34.9 ± 2.5	22.7 ± 1.6	14.3 ± 1.0	18.3 ± 1.3	395.7 ± 28.3
W/Z + jets fit	146.2 ± 50.4	264.5 ± 80.0	122.8 ± 155.1	104.6 ± 78.9	116.5 ± 67.9	111.9 ± 51.8	46.2 ± 67.3	0.0 ± 6.1	0.0 ± 12.3	912.7 ± 569.8
QCD in	6.0 ± 0.3	95.9 ± 4.4	95.7 ± 4.4	268.5 ± 12.4	85.2 ± 3.9	15.9 ± 0.7	3.2 ± 0.1	2.2 ± 0.1	3.9 ± 0.2	576.5 ± 26.7
QCD fit	0.0 ± 42.3	0.0 ± 71.6	32.8 ± 54.2	0.0 ± 14.7	0.0 ± 18.7	0.0 ± 39.5	6.8 ± 30.8	0.0 ± 5.6	0.0 ± 5.2	39.6 ± 282.8
Sum MC in	1017.0 ± 32.4	2387.4 ± 51.0	3053.6 ± 63.1	3031.6 ± 64.5	2253.1 ± 50.0	1474.0 ± 42.0	834.8 ± 27.1	465.6 ± 19.3	465.9 ± 19.1	14982.9 ± 368.4
Sum MC fit	980.0 ± 268.5	2465.0 ± 589.4	2859.0 ± 521.8	2693.0 ± 347.9	2007.0 ± 284.9	1320.0 ± 240.1	712.0 ± 204.0	385.0 ± 72.8	371.0 ± 68.2	13792.0 ± 2597.6
Data	980.0 ± 105.9	2465.0 ± 168.1	2859.0 ± 177.5	2693.0 ± 171.1	2007.0 ± 147.4	1320.0 ± 118.8	712.0 ± 86.4	385.0 ± 60.3	371.0 ± 58.5	13792.0 ± 1094.1

Table B.10: Fit results for the p_T^W variable at a centre-of-mass energy of 7 TeV (muon channel).

Process	0--27 GeV	27--52 GeV	52--78 GeV	78--105 GeV	105--134 GeV	134--166 GeV	166--200 GeV	200--237 GeV	≥ 237 GeV	Total
t̄t in	1123.0 \pm 27.5	2494.5 \pm 38.8	3109.7 \pm 46.3	2846.6 \pm 40.7	2224.3 \pm 37.9	1487.2 \pm 30.4	843.1 \pm 21.4	457.2 \pm 16.4	430.6 \pm 15.5	15016.1 \pm 274.8
t̄t fit	840.6 \pm 64.9	1962.2 \pm 118.8	2766.6 \pm 141.1	2204.6 \pm 118.1	1763.2 \pm 91.6	1084.0 \pm 71.8	569.9 \pm 48.6	278.9 \pm 31.4	269.0 \pm 26.2	11739.0 \pm 712.6
Single Top in	34.2 \pm 4.1	78.6 \pm 6.9	92.3 \pm 6.8	85.6 \pm 6.4	64.2 \pm 5.4	46.5 \pm 4.5	28.1 \pm 3.4	15.7 \pm 2.4	23.9 \pm 2.8	468.9 \pm 42.7
Single Top fit	48.7 \pm 74.0	246.6 \pm 140.4	46.9 \pm 164.3	236.8 \pm 143.3	53.6 \pm 103.3	71.1 \pm 67.7	59.6 \pm 45.8	34.9 \pm 30.1	43.7 \pm 25.4	842.0 \pm 794.3
W/Z + jets in	39.5 \pm 2.4	75.4 \pm 4.5	89.8 \pm 5.4	68.3 \pm 4.1	52.4 \pm 3.1	38.4 \pm 2.3	19.2 \pm 1.1	14.3 \pm 0.9	19.1 \pm 1.1	416.5 \pm 24.8
W/Z + jets fit	77.4 \pm 80.6	71.9 \pm 147.0	183.3 \pm 168.4	48.6 \pm 86.8	77.2 \pm 73.9	0.0 \pm 109.0	0.0 \pm 16.2	0.0 \pm 21.5	5.3 \pm 14.2	463.8 \pm 717.6
QCD in	3.8 \pm 0.2	85.7 \pm 3.6	51.7 \pm 2.2	20.2 \pm 0.8	1.1 \pm 0.0	17.0 \pm 0.7	0.7 \pm 0.0	0.1 \pm 0.0	0.1 \pm 0.0	180.4 \pm 7.5
QCD fit	50.3 \pm 67.6	1.4 \pm 3131.1	4.2 \pm 911.5	0.0 \pm 54.1	0.0 \pm 63.5	15.9 \pm 34.7	8.4 \pm 15.5	3.2 \pm 13.6	0.0 \pm 8.4	83.4 \pm 4300.0
Sum MC in	1200.6 \pm 34.1	2734.1 \pm 53.8	3343.4 \pm 60.6	3020.7 \pm 52.0	2342.0 \pm 46.5	1589.1 \pm 37.9	891.1 \pm 26.0	487.3 \pm 19.6	473.7 \pm 19.5	16082.0 \pm 350.0
Sum MC fit	1017.0 \pm 287.2	2282.1 \pm 3537.4	3001.0 \pm 1385.3	2490.0 \pm 402.3	1894.0 \pm 332.3	1171.0 \pm 283.2	638.0 \pm 126.1	317.0 \pm 96.6	318.0 \pm 74.2	13128.1 \pm 6524.5
Data	1017.0 \pm 102.8	2282.0 \pm 152.9	3001.0 \pm 175.6	2490.0 \pm 159.4	1894.0 \pm 138.0	1171.0 \pm 107.1	638.0 \pm 78.3	317.0 \pm 54.8	318.0 \pm 54.2	13128.0 \pm 1023.1

B. $t\bar{t}$ differential cross section

Table B.11: Fit results for the M_T^W variable at a centre-of-mass energy of 7 TeV (electron channel).

Process	0--23 GeV	23--58 GeV	≥ 58 GeV	Total
$t\bar{t}$ in	1734.8 ± 37.6	3862.1 ± 49.1	7985.4 ± 74.2	13582.3 ± 160.8
$t\bar{t}$ fit	1411.7 ± 85.9	3451.4 ± 145.5	7204.3 ± 215.0	12067.4 ± 446.4
Single Top in	52.9 ± 5.1	126.8 ± 8.3	248.1 ± 11.4	427.8 ± 24.7
Single Top fit	27.6 ± 100.7	151.2 ± 172.1	318.0 ± 264.4	496.8 ± 537.2
W/Z + jets in	58.4 ± 4.2	119.7 ± 8.6	217.6 ± 15.6	395.7 ± 28.3
W/Z + jets fit	242.8 ± 123.3	348.4 ± 103.7	608.6 ± 145.8	1199.8 ± 372.9
QCD in	163.4 ± 7.6	223.6 ± 10.4	189.4 ± 8.8	576.5 ± 26.7
QCD fit	27.9 ± 45.6	0.0 ± 37.5	0.0 ± 34.6	27.9 ± 117.7
Sum MC in	2009.5 ± 54.4	4332.3 ± 76.3	8640.5 ± 110.0	14982.3 ± 240.6
Sum MC fit	1710.0 ± 355.4	3951.0 ± 458.9	8131.0 ± 659.8	13792.0 ± 1474.1
Data	1710.0 ± 138.3	3951.0 ± 208.3	8131.0 ± 298.4	13792.0 ± 645.0

Table B.12: Fit results for the M_T^W variable at a centre-of-mass energy of 7 TeV (muon channel).

Process	0--23 GeV	23--58 GeV	≥ 58 GeV	Total
$t\bar{t}$ in	1937.1 ± 35.5	4372.8 ± 54.9	8706.2 ± 72.1	15016.1 ± 162.5
$t\bar{t}$ fit	1612.1 ± 68.2	3424.7 ± 136.2	6685.5 ± 215.8	11722.2 ± 420.1
Single Top in	63.2 ± 5.6	137.3 ± 7.9	268.4 ± 11.6	468.9 ± 25.1
Single Top fit	0.0 ± 581.2	137.4 ± 165.6	777.2 ± 265.1	914.5 ± 1011.9
W/Z + jets in	65.9 ± 3.9	118.2 ± 7.0	232.4 ± 13.9	416.5 ± 24.8
W/Z + jets fit	121.9 ± 62.3	232.9 ± 110.9	18.6 ± 757.6	373.4 ± 930.8
QCD in	58.5 ± 2.4	106.7 ± 4.5	15.1 ± 0.6	180.3 ± 7.5
QCD fit	0.0 ± 95.8	0.0 ± 55.7	117.8 ± 158.0	117.8 ± 309.5
Sum MC in	2124.6 ± 47.5	4735.1 ± 74.4	9222.1 ± 98.2	16081.8 ± 220.0
Sum MC fit	1734.0 ± 807.5	3795.0 ± 468.3	7599.0 ± 1396.5	13128.0 ± 2672.2
Data	1734.0 ± 132.8	3795.0 ± 197.7	7599.0 ± 276.5	13128.0 ± 607.0

Table B.13: Fit results for the E_T^{miss} variable at a centre-of-mass energy of 8 TeV (electron channel).

Process	0--27 GeV	27--52 GeV	52--87 GeV	87--130 GeV	130--172 GeV	≥ 172 GeV	Total
t̄t in	11394.8 \pm 297.5	20257.4 \pm 397.5	18771.6 \pm 379.9	8534.4 \pm 253.3	2662.8 \pm 141.6	1612.1 \pm 108.5	63233.1 \pm 1578.2
t̄t fit	11258.8 \pm 307.4	21023.0 \pm 265.5	19133.9 \pm 359.0	7721.3 \pm 207.2	2394.7 \pm 92.0	1212.7 \pm 58.0	62744.4 \pm 1289.2
Single Top in	470.0 \pm 44.6	804.0 \pm 58.5	729.8 \pm 55.0	348.6 \pm 38.9	124.1 \pm 21.9	90.5 \pm 18.7	2566.9 \pm 237.6
Single Top fit	610.9 \pm 421.8	0.0 \pm 6921.1	380.7 \pm 413.8	305.3 \pm 199.2	100.3 \pm 85.8	127.1 \pm 52.8	1524.3 \pm 8094.5
W/Z + jets in	418.9 \pm 22.7	493.4 \pm 26.8	309.9 \pm 16.8	110.9 \pm 6.0	37.4 \pm 2.0	35.1 \pm 1.9	1405.6 \pm 76.2
W/Z + jets fit	2165.4 \pm 396.9	2845.1 \pm 346.6	1638.9 \pm 366.8	469.8 \pm 264.5	0.0 \pm 71.6	66.1 \pm 30.8	7185.4 \pm 1477.3
QCD in	2285.7 \pm 54.4	104.0 \pm 2.5	35.5 \pm 0.8	0.8 \pm 0.0	1.0 \pm 0.0	0.4 \pm 0.0	2427.4 \pm 57.8
QCD fit	443.8 \pm 160.7	112.9 \pm 147.8	11.6 \pm 333.2	77.4 \pm 107.0	76.0 \pm 24.4	0.0 \pm 23.7	721.7 \pm 796.9
Sum MC in	14569.4 \pm 419.3	21658.8 \pm 485.2	19846.7 \pm 452.6	8994.7 \pm 298.2	2825.3 \pm 165.5	1738.1 \pm 129.0	69633.0 \pm 1949.8
Sum MC fit	14478.9 \pm 1286.9	23981.0 \pm 7681.0	21165.0 \pm 1472.8	8573.9 \pm 777.9	2570.9 \pm 273.8	1406.0 \pm 165.3	72175.7 \pm 11657.7
Data	14479.0 \pm 402.7	23981.0 \pm 513.6	21165.0 \pm 476.2	8574.0 \pm 301.0	2571.0 \pm 162.1	1406.0 \pm 118.1	72176.0 \pm 1973.6

Table B.14: Fit results for the E_T^{miss} variable at a centre-of-mass energy of 8 TeV (muon channel).

Process	0--27 GeV	27--52 GeV	52--87 GeV	87--130 GeV	130--172 GeV	≥ 172 GeV	Total
t̄t in	13206.5 \pm 318.6	23819.0 \pm 428.4	22684.5 \pm 416.1	10234.5 \pm 279.2	3132.3 \pm 153.1	1918.5 \pm 117.3	74995.1 \pm 1712.8
t̄t fit	12976.6 \pm 179.3	23608.5 \pm 428.3	22339.7 \pm 413.8	9636.1 \pm 215.5	2774.5 \pm 108.0	1343.1 \pm 69.8	72678.4 \pm 1414.7
Single Top in	539.8 \pm 47.6	892.7 \pm 60.6	894.2 \pm 60.9	417.6 \pm 41.8	161.0 \pm 26.2	118.7 \pm 22.5	3024.0 \pm 259.5
Single Top fit	0.0 \pm 193.8	680.4 \pm 539.3	58.4 \pm 1080.7	194.1 \pm 237.3	13.5 \pm 198.0	206.7 \pm 65.0	1153.1 \pm 2314.1
W/Z + jets in	407.9 \pm 20.2	566.7 \pm 28.1	372.4 \pm 18.4	143.3 \pm 7.1	64.2 \pm 3.2	42.3 \pm 2.1	1596.7 \pm 79.1
W/Z + jets fit	1904.6 \pm 272.5	2174.5 \pm 396.5	2037.9 \pm 279.9	627.6 \pm 251.6	229.7 \pm 101.8	73.2 \pm 37.7	7047.5 \pm 1340.0
QCD in	440.9 \pm 6.0	43.4 \pm 0.6	42.5 \pm 0.6	0.1 \pm 0.0	0.5 \pm 0.0	0.1 \pm 0.0	527.6 \pm 7.2
QCD fit	62.8 \pm 206.5	34.6 \pm 315.9	0.0 \pm 135.1	59.2 \pm 157.5	11.4 \pm 52.3	0.0 \pm 82.9	168.1 \pm 950.3
Sum MC in	14595.0 \pm 392.5	25321.8 \pm 517.6	23993.6 \pm 496.0	10795.5 \pm 328.2	3357.9 \pm 182.4	2079.5 \pm 141.9	80143.4 \pm 2058.6
Sum MC fit	14944.0 \pm 852.1	26498.0 \pm 1680.1	24436.1 \pm 1909.5	10517.0 \pm 861.9	3029.0 \pm 460.2	1623.0 \pm 255.4	81047.1 \pm 6019.1
Data	14944.0 \pm 392.0	26498.0 \pm 520.6	24436.0 \pm 499.9	10517.0 \pm 325.7	3029.0 \pm 174.3	1623.0 \pm 125.6	81047.0 \pm 2038.2

Table B.15: Fit results for the H_T variable at a centre-of-mass energy of 8 TeV (electron channel).

Process	120–185 GeV	185–215 GeV	215–247 GeV	247–283 GeV	283–323 GeV	323–365 GeV	365–409 GeV	409–458 GeV	458–512 GeV	512–570 GeV	570–629 GeV	629–691 GeV	691–769 GeV	≥ 769 GeV	Total
tt in	937.5 \pm 85.8	3148.7 \pm 156.7	6333.1 \pm 223.2	8687.4 \pm 259.1	9454.1 \pm 270.1	8372.7 \pm 253.4	6889.5 \pm 231.1	5669.7 \pm 207.2	4326.6 \pm 181.5	2961.6 \pm 150.2	2066.7 \pm 125.1	1465.1 \pm 105.4	1104.5 \pm 90.2	1815.9 \pm 116.3	63233.1 \pm 2455.3
tt fit	1071.7 \pm 67.9	3100.1 \pm 176.4	7037.8 \pm 110.8	9677.3 \pm 138.5	9700.1 \pm 207.8	8309.8 \pm 167.0	6494.9 \pm 171.0	5399.5 \pm 143.9	4263.9 \pm 122.9	3005.0 \pm 104.6	1828.2 \pm 75.7	1289.0 \pm 48.1	898.4 \pm 47.0	1388.5 \pm 72.3	63464.3 \pm 1653.8
Single Top in	64.0 \pm 16.4	182.6 \pm 27.7	260.2 \pm 33.0	360.2 \pm 39.7	359.2 \pm 38.0	297.8 \pm 35.8	279.6 \pm 34.3	210.7 \pm 29.8	164.2 \pm 25.9	128.9 \pm 23.4	78.9 \pm 17.9	52.9 \pm 14.1	47.3 \pm 13.0	80.3 \pm 17.9	2566.9 \pm 366.8
Single Top fit	38.9 \pm 69.0	517.5 \pm 220.5	0.0 \pm 155.1	0.0 \pm 875.3	333.0 \pm 270.7	540.9 \pm 205.6	874.3 \pm 185.9	334.2 \pm 145.7	140.1 \pm 112.1	75.8 \pm 93.9	210.1 \pm 65.7	67.4 \pm 39.1	88.1 \pm 40.2	137.5 \pm 64.8	3357.9 \pm 2543.6
W/Z + jets in	95.7 \pm 5.2	124.4 \pm 6.7	166.0 \pm 9.0	191.1 \pm 10.4	172.8 \pm 9.4	144.5 \pm 7.8	121.6 \pm 6.6	104.3 \pm 5.7	84.1 \pm 4.6	60.1 \pm 3.3	41.6 \pm 2.3	33.0 \pm 1.8	25.1 \pm 1.4	41.1 \pm 2.2	1405.6 \pm 76.2
W/Z + jets fit	0.0 \pm 37.3	121.4 \pm 128.9	280.7 \pm 160.5	665.1 \pm 183.3	884.5 \pm 272.8	861.4 \pm 156.4	304.7 \pm 181.8	397.4 \pm 143.6	88.1 \pm 135.5	149.0 \pm 106.8	43.7 \pm 59.7	0.0 \pm 46.9	0.0 \pm 62.1	80.2 \pm 51.5	3876.1 \pm 1727.1
QCD in	2.6 \pm 0.1	17.4 \pm 0.4	1827.4 \pm 43.5	221.1 \pm 5.3	47.8 \pm 1.1	32.6 \pm 0.8	41.1 \pm 1.0	123.8 \pm 2.9	30.5 \pm 0.7	12.1 \pm 0.3	21.7 \pm 0.5	11.1 \pm 0.3	19.2 \pm 0.5	18.9 \pm 0.5	2427.4 \pm 57.8
QCD fit	178.5 \pm 27.1	287.0 \pm 75.5	329.5 \pm 102.3	228.7 \pm 99.8	167.3 \pm 109.1	0.0 \pm 145.6	21.2 \pm 71.2	28.9 \pm 59.4	91.9 \pm 64.9	36.1 \pm 53.4	28.0 \pm 28.8	29.6 \pm 15.0	42.5 \pm 13.4	8.8 \pm 31.6	1477.8 \pm 897.3
Sum MC in	1099.8 \pm 107.4	3473.2 \pm 191.6	8586.7 \pm 308.7	9459.9 \pm 314.5	10033.9 \pm 318.7	8847.7 \pm 297.8	7331.8 \pm 273.0	6108.5 \pm 245.5	4605.5 \pm 212.7	3162.7 \pm 177.1	2208.9 \pm 145.7	1562.1 \pm 121.5	1196.2 \pm 105.0	1956.1 \pm 136.9	69633.0 \pm 2956.2
Sum MC fit	1289.0 \pm 201.3	4026.0 \pm 601.3	7648.0 \pm 528.7	10571.0 \pm 1296.9	11085.0 \pm 800.5	9712.0 \pm 674.6	7695.0 \pm 609.9	6160.0 \pm 492.6	4584.0 \pm 435.4	3266.0 \pm 358.8	2110.0 \pm 229.9	1386.0 \pm 149.1	1029.0 \pm 162.6	1615.0 \pm 220.2	72176.1 \pm 6821.9
Data	1289.0 \pm 122.5	4026.0 \pm 213.0	7648.0 \pm 292.2	10571.0 \pm 339.5	11085.0 \pm 349.0	9712.0 \pm 323.9	7695.0 \pm 286.5	6160.0 \pm 256.1	4584.0 \pm 219.4	3266.0 \pm 186.4	2110.0 \pm 149.0	1386.0 \pm 120.1	1029.0 \pm 104.2	1615.0 \pm 130.6	72176.0 \pm 3092.5

Table B.16: Fit results for the H_T variable at a centre-of-mass energy of 8 TeV (muon channel).

Process	120–185 GeV	185–215 GeV	215–247 GeV	247–283 GeV	283–323 GeV	323–365 GeV	365–409 GeV	409–458 GeV	458–512 GeV	512–570 GeV	570–629 GeV	629–691 GeV	691–769 GeV	≥ 769 GeV	Total
tt in	1092.4 \pm 92.3	3830.8 \pm 171.8	7685.2 \pm 242.5	10846.7 \pm 288.8	11271.8 \pm 294.2	10014.3 \pm 276.9	8183.4 \pm 250.4	6533.5 \pm 222.4	5036.2 \pm 195.2	3579.8 \pm 164.9	2347.3 \pm 133.4	1507.1 \pm 106.1	1227.8 \pm 95.8	1838.7 \pm 117.5	74995.1 \pm 2652.1
tt fit	1069.3 \pm 81.0	3678.4 \pm 198.3	7970.7 \pm 284.4	10932.2 \pm 139.4	10967.8 \pm 269.3	9560.9 \pm 202.1	7915.8 \pm 167.8	5851.0 \pm 153.5	4440.6 \pm 135.7	2977.4 \pm 105.9	1912.9 \pm 83.0	1386.4 \pm 60.4	1046.2 \pm 53.1	1446.3 \pm 73.3	71155.9 \pm 2007.3
Single Top in	88.6 \pm 18.7	195.9 \pm 28.5	338.8 \pm 37.7	374.5 \pm 39.4	428.9 \pm 42.5	380.3 \pm 39.7	312.5 \pm 35.6	259.8 \pm 32.8	189.5 \pm 27.6	144.4 \pm 24.7	96.0 \pm 20.1	70.5 \pm 17.2	57.6 \pm 15.1	86.7 \pm 18.5	3024.0 \pm 398.2
Single Top fit	248.5 \pm 83.4	671.1 \pm 219.9	410.2 \pm 369.8	0.0 \pm 805.2	1029.7 \pm 346.2	535.0 \pm 267.0	143.3 \pm 191.0	793.0 \pm 153.2	446.6 \pm 132.3	357.8 \pm 92.1	214.4 \pm 75.2	123.5 \pm 52.5	2.5 \pm 191.2	117.2 \pm 68.9	5092.8 \pm 3048.1
W/Z + jets in	101.3 \pm 5.0	143.7 \pm 7.1	172.3 \pm 8.5	200.6 \pm 9.9	209.1 \pm 10.4	179.3 \pm 8.9	144.4 \pm 7.2	117.4 \pm 5.8	97.1 \pm 4.8	65.0 \pm 3.2	52.6 \pm 2.6	37.4 \pm 1.9	25.8 \pm 2.5	1596.7 \pm 79.1	
W/Z + jets fit	72.2 \pm 85.0	0.0 \pm 59.6	391.0 \pm 221.4	982.7 \pm 214.9	585.5 \pm 176.0	718.5 \pm 237.8	672.4 \pm 194.1	188.0 \pm 97.3	224.7 \pm 81.5	155.8 \pm 56.0	85.7 \pm 42.2	73.0 \pm 46.8	78.2 \pm 26.4	20.2 \pm 61.7	4248.1 \pm 1600.8
QCD in	1.0 \pm 0.0	408.5 \pm 5.8	28.0 \pm 0.4	18.9 \pm 0.3	1.0 \pm 0.0	7.5 \pm 0.1	1.0 \pm 0.0	5.4 \pm 0.1	11.8 \pm 0.2	7.9 \pm 0.1	14.1 \pm 0.2	16.3 \pm 0.2	7.7 \pm 0.1	1.3 \pm 0.0	530.4 \pm 7.5
QCD fit	58.0 \pm 83.1	215.6 \pm 69.5	76.9 \pm 159.0	97.2 \pm 176.3	0.0 \pm 477.2	6.6 \pm 587.6	39.5 \pm 111.3	0.0 \pm 51.8	0.0 \pm 60.9	0.0 \pm 80.2	0.0 \pm 885.9	13.1 \pm 28.9	0.0 \pm 22.5	43.3 \pm 48.6	550.2 \pm 2842.7
Sum MC in	1283.3 \pm 116.1	4578.9 \pm 213.2	8224.3 \pm 289.2	11440.7 \pm 338.4	11910.9 \pm 347.1	10581.4 \pm 325.6	8641.4 \pm 293.2	6916.2 \pm 261.1	5334.6 \pm 227.7	3797.1 \pm 192.9	2510.0 \pm 156.3	1631.3 \pm 125.4	1318.9 \pm 112.2	1977.4 \pm 138.5	80146.2 \pm 3136.9
Sum MC fit	1448.0 \pm 332.6	4565.0 \pm 547.3	8848.9 \pm 1034.6	12012.1 \pm 1335.8	12583.0 \pm 1268.7	10821.0 \pm 1294.5	8771.0 \pm 664.2	6832.0 \pm 455.8	5112.0 \pm 410.5	3491.0 \pm 334.2	2213.0 \pm 1086.3	1596.0 \pm 188.6	1127.0 \pm 293.1	1627.0 \pm 252.6	81047.0 \pm 9498.8
Data	1448.0 \pm 123.2	4565.0 \pm 217.3	8849.0 \pm 301.6	12012.0 \pm 351.4	12583.0 \pm 358.7	10821.0 \pm 332.3	8771.0 \pm 298.7	6832.0 \pm 262.3	5112.0 \pm 227.2	3491.0 \pm 188.2	2213.0 \pm 149.1	1596.0 \pm 126.2	1127.0 \pm 106.7	1627.0 \pm 126.2	81047.0 \pm 3169.1

Table B.17: Fit results for the S_T variable at a centre-of-mass energy of 8 TeV (electron channel).

Process	146–277 GeV	277–319 GeV	319–361 GeV	361–408 GeV	408–459 GeV	459–514 GeV	514–573 GeV	573–637 GeV	637–705 GeV	705–774 GeV	774–854 GeV	854–940 GeV	≥ 940 GeV	Total
t̄t in	946.0 \pm 87.2	3777.2 \pm 171.5	7287.4 \pm 239.9	9617.1 \pm 273.1	9713.1 \pm 273.6	8539.6 \pm 256.1	6791.6 \pm 227.5	5216.9 \pm 199.3	3637.8 \pm 166.4	2574.4 \pm 139.5	1838.8 \pm 117.3	1237.2 \pm 94.8	2056.0 \pm 122.6	63233.1 \pm 2368.9
t̄t fit	1066.4 \pm 80.3	4208.8 \pm 192.0	7559.1 \pm 243.6	10629.2 \pm 151.9	9980.6 \pm 202.8	8411.8 \pm 186.3	6401.4 \pm 171.3	4962.8 \pm 143.5	3510.8 \pm 112.5	2237.7 \pm 85.8	1524.8 \pm 59.5	954.0 \pm 48.7	1560.5 \pm 65.4	63007.8 \pm 1743.6
Single Top in	67.0 \pm 16.8	186.6 \pm 27.6	281.6 \pm 34.7	374.4 \pm 39.3	361.5 \pm 39.2	304.1 \pm 35.9	270.3 \pm 33.3	220.0 \pm 30.5	155.8 \pm 25.6	103.9 \pm 21.1	85.7 \pm 18.7	52.3 \pm 14.3	103.6 \pm 20.3	2566.9 \pm 357.2
Single Top fit	167.4 \pm 80.9	309.7 \pm 220.2	551.9 \pm 322.4	0.0 \pm 333.2	116.7 \pm 254.4	600.2 \pm 224.4	617.1 \pm 180.1	664.1 \pm 147.6	444.2 \pm 106.9	205.7 \pm 84.4	167.6 \pm 53.9	128.3 \pm 45.2	224.3 \pm 61.8	4197.3 \pm 2115.5
W/Z + jets in	108.1 \pm 5.9	141.1 \pm 7.6	176.8 \pm 9.6	197.5 \pm 10.7	169.7 \pm 9.2	147.1 \pm 8.0	119.5 \pm 6.5	102.9 \pm 5.6	71.6 \pm 3.9	47.3 \pm 2.6	44.6 \pm 2.4	27.0 \pm 1.5	52.4 \pm 2.8	1405.6 \pm 76.2
W/Z + jets fit	0.0 \pm 171.0	47.1 \pm 146.2	425.7 \pm 216.2	631.1 \pm 203.2	1228.2 \pm 231.7	619.9 \pm 244.3	414.5 \pm 186.8	81.0 \pm 83.0	0.0 \pm 39.6	0.0 \pm 107.6	27.3 \pm 52.0	0.0 \pm 46.0	0.0 \pm 56.4	3474.8 \pm 1784.0
QCD in	8.4 \pm 0.2	1757.3 \pm 41.8	134.9 \pm 3.2	192.2 \pm 4.6	44.0 \pm 1.0	38.0 \pm 0.9	128.6 \pm 3.1	29.8 \pm 0.7	20.8 \pm 0.5	19.0 \pm 0.5	17.3 \pm 0.4	19.8 \pm 0.5	17.2 \pm 0.4	2427.4 \pm 57.8
QCD fit	257.2 \pm 31.9	387.4 \pm 89.5	260.4 \pm 102.1	261.8 \pm 107.3	4.5 \pm 323.7	32.1 \pm 91.7	30.9 \pm 75.6	0.0 \pm 79.0	84.0 \pm 29.7	68.6 \pm 24.9	25.3 \pm 25.7	39.8 \pm 14.0	44.2 \pm 16.1	1496.3 \pm 1011.3
Sum MC in	1129.4 \pm 110.1	5862.2 \pm 248.5	7880.7 \pm 287.4	10381.2 \pm 327.7	10288.3 \pm 323.0	9028.8 \pm 300.9	7310.0 \pm 270.4	5569.5 \pm 236.1	3886.1 \pm 196.3	2744.6 \pm 163.6	1986.4 \pm 138.8	1336.3 \pm 111.0	2229.2 \pm 146.1	69633.0 \pm 2860.1
Sum MC fit	1491.0 \pm 364.2	4953.0 \pm 647.9	8797.1 \pm 884.3	11522.0 \pm 795.6	11330.0 \pm 1012.7	9664.0 \pm 746.7	7463.9 \pm 613.8	5708.0 \pm 453.1	4039.0 \pm 288.7	2512.0 \pm 302.7	1745.0 \pm 191.2	1122.0 \pm 153.9	1829.0 \pm 199.7	72176.2 \pm 6654.4
Data	1491.0 \pm 133.1	4953.0 \pm 237.2	8797.0 \pm 313.0	11522.0 \pm 355.2	11330.0 \pm 351.5	9664.0 \pm 322.3	7464.0 \pm 282.5	5708.0 \pm 244.1	4039.0 \pm 206.4	2512.0 \pm 162.4	1745.0 \pm 134.9	1122.0 \pm 108.3	1829.0 \pm 136.8	72176.0 \pm 2987.6

Table B.18: Fit results for the S_T variable at a centre-of-mass energy of 8 TeV (muon channel).

Process	146–277 GeV	277–319 GeV	319–361 GeV	361–408 GeV	408–459 GeV	459–514 GeV	514–573 GeV	573–637 GeV	637–705 GeV	705–774 GeV	774–854 GeV	854–940 GeV	≥ 940 GeV	Total
t̄t in	1308.6 \pm 101.5	4828.7 \pm 193.7	8949.3 \pm 262.8	11773.4 \pm 300.8	11661.3 \pm 298.9	10029.2 \pm 277.1	7959.9 \pm 246.2	5966.6 \pm 212.4	4245.7 \pm 178.9	2786.3 \pm 144.3	2065.1 \pm 124.2	1313.2 \pm 99.4	2107.8 \pm 123.8	74995.1 \pm 2564.1
t̄t fit	1361.6 \pm 99.9	4983.2 \pm 202.9	9217.9 \pm 363.6	11693.6 \pm 271.8	11405.1 \pm 253.6	9817.7 \pm 202.3	7764.1 \pm 184.3	5374.4 \pm 149.9	3516.8 \pm 119.7	2394.0 \pm 90.7	1767.1 \pm 69.0	1076.0 \pm 48.8	1599.7 \pm 68.7	71971.1 \pm 2125.3
Single Top in	89.5 \pm 18.9	219.7 \pm 30.5	360.3 \pm 38.4	429.6 \pm 42.0	422.2 \pm 41.8	370.2 \pm 39.2	315.7 \pm 36.4	237.0 \pm 31.4	178.6 \pm 26.9	122.3 \pm 22.5	92.1 \pm 20.0	70.6 \pm 16.8	116.2 \pm 21.7	3024.0 \pm 386.5
Single Top fit	418.1 \pm 109.6	447.5 \pm 253.0	129.5 \pm 443.4	546.0 \pm 328.1	490.6 \pm 349.4	93.5 \pm 251.2	188.6 \pm 206.0	586.1 \pm 158.7	596.8 \pm 115.1	194.4 \pm 87.7	161.2 \pm 63.5	76.9 \pm 43.8	125.2 \pm 64.9	4054.4 \pm 2474.5
W/Z + jets in	115.7 \pm 5.7	164.1 \pm 8.1	183.0 \pm 9.1	220.4 \pm 10.9	199.9 \pm 9.9	176.4 \pm 8.7	141.7 \pm 7.0	119.7 \pm 5.9	83.1 \pm 4.1	60.2 \pm 3.0	41.1 \pm 2.0	31.4 \pm 1.6	60.0 \pm 3.0	1596.7 \pm 79.1
W/Z + jets fit	8.7 \pm 259.4	136.3 \pm 143.2	735.4 \pm 229.8	707.6 \pm 254.7	984.1 \pm 273.4	947.7 \pm 169.8	408.3 \pm 126.1	91.5 \pm 90.2	110.4 \pm 65.8	116.6 \pm 46.7	0.0 \pm 140.8	77.9 \pm 82.7	45.3 \pm 62.3	4369.7 \pm 1944.9
QCD in	408.5 \pm 5.6	1.0 \pm 0.0	1.0 \pm 0.0	18.9 \pm 0.3	35.4 \pm 0.5	5.4 \pm 0.1	5.7 \pm 0.1	15.2 \pm 0.2	12.9 \pm 0.2	16.3 \pm 0.2	7.7 \pm 0.1	1.0 \pm 0.0	1.3 \pm 0.0	530.4 \pm 7.3
QCD fit	182.7 \pm 95.6	120.1 \pm 114.8	89.2 \pm 169.1	212.8 \pm 191.5	5.2 \pm 1056.3	0.0 \pm 91.3	0.0 \pm 72.2	0.0 \pm 69.2	0.0 \pm 101.1	0.0 \pm 65.1	17.7 \pm 17.3	2.2 \pm 478.9	21.8 \pm 47.3	651.8 \pm 2569.9
Sum MC in	1922.3 \pm 131.8	5213.5 \pm 232.3	9493.6 \pm 310.2	12442.3 \pm 354.0	12318.8 \pm 351.1	10581.2 \pm 325.1	8423.0 \pm 289.7	6338.6 \pm 250.0	4520.2 \pm 210.1	2985.2 \pm 170.1	2206.0 \pm 146.4	1416.2 \pm 117.8	2285.3 \pm 148.4	80146.2 \pm 3036.9
Sum MC fit	1971.0 \pm 564.5	5687.0 \pm 714.0	10172.0 \pm 1205.9	13160.0 \pm 1046.1	12884.9 \pm 1932.6	10859.0 \pm 714.6	8361.0 \pm 588.6	6052.0 \pm 468.0	4224.0 \pm 401.6	2705.0 \pm 290.1	1946.0 \pm 290.7	1233.0 \pm 654.3	1792.0 \pm 243.3	81047.0 \pm 9114.5
Data	1971.0 \pm 144.0	5687.0 \pm 243.2	10172.0 \pm 324.3	13160.0 \pm 367.7	12885.0 \pm 363.1	10859.0 \pm 332.2	8361.0 \pm 290.6	6052.0 \pm 246.6	4224.0 \pm 206.4	2705.0 \pm 165.0	1946.0 \pm 138.4	1233.0 \pm 110.4	1792.0 \pm 131.4	81047.0 \pm 3063.1

Table B.19: Fit results for the p_T^W variable at a centre-of-mass energy of 8 TeV (electron channel).

Process	0--27 GeV	27--52 GeV	52--78 GeV	78--105 GeV	105--134 GeV	134--166 GeV	166--200 GeV	200--237 GeV	≥ 237 GeV	Total
$t\bar{t}$ in	4063.8 ± 178.3	9575.7 ± 274.6	12466.8 ± 311.8	12054.9 ± 304.4	9721.1 ± 273.6	6755.9 ± 225.8	3958.3 ± 171.7	2289.9 ± 129.7	2346.9 ± 128.0	63233.1 ± 1997.8
$t\bar{t}$ fit	4381.0 ± 159.3	10707.3 ± 189.9	12562.1 ± 298.2	12407.8 ± 206.1	9614.2 ± 232.1	6076.1 ± 179.5	3434.6 ± 126.2	1867.7 ± 76.3	1811.4 ± 61.0	62862.3 ± 1528.7
Single Top in	144.4 ± 24.6	362.1 ± 38.4	461.3 ± 43.5	437.1 ± 43.1	393.5 ± 40.8	289.3 ± 35.8	185.6 ± 27.5	120.5 ± 22.5	173.2 ± 26.5	2566.9 ± 302.8
Single Top fit	125.3 ± 152.4	0.0 ± 1691.4	577.1 ± 377.9	0.0 ± 665.0	351.1 ± 262.5	218.1 ± 203.0	249.3 ± 126.6	259.3 ± 75.6	298.5 ± 57.0	2078.7 ± 3611.4
W/Z + jets in	112.1 ± 6.1	249.4 ± 13.5	292.8 ± 15.9	246.7 ± 13.4	184.1 ± 10.0	127.5 ± 6.9	74.3 ± 4.0	48.4 ± 2.6	70.4 ± 3.8	1405.6 ± 76.2
W/Z + jets fit	581.7 ± 176.4	1129.6 ± 256.9	1781.6 ± 346.7	1408.3 ± 270.2	748.8 ± 298.8	682.9 ± 150.0	221.5 ± 139.2	0.0 ± 4263.1	0.0 ± 35.6	6554.4 ± 5936.9
QCD in	20.4 ± 0.5	150.6 ± 3.6	1811.5 ± 43.1	164.9 ± 3.9	52.4 ± 1.2	177.2 ± 4.2	19.3 ± 0.5	10.7 ± 0.3	20.4 ± 0.5	2427.4 ± 57.8
QCD fit	79.0 ± 80.5	188.2 ± 114.7	167.2 ± 128.2	134.9 ± 114.1	8.8 ± 334.1	0.0 ± 8816.9	29.5 ± 58.5	34.0 ± 29.1	39.1 ± 17.9	680.8 ± 9694.1
Sum MC in	4340.7 ± 209.5	10337.8 ± 330.1	15032.3 ± 414.3	12903.5 ± 364.7	10351.0 ± 325.6	7349.9 ± 272.8	4237.5 ± 203.7	2469.5 ± 155.1	2610.8 ± 158.8	69633.0 ± 2434.6
Sum MC fit	5167.0 ± 568.6	12025.1 ± 2252.9	15088.0 ± 1151.0	13951.1 ± 1255.5	10723.0 ± 1127.5	6977.0 ± 9349.4	3935.0 ± 450.6	2161.0 ± 4444.2	2149.0 ± 171.4	72176.2 ± 20771.1
Data	5167.0 ± 241.9	12025.0 ± 365.6	15088.0 ± 408.6	13951.0 ± 389.9	10723.0 ± 337.9	6977.0 ± 271.7	3935.0 ± 201.7	2161.0 ± 147.2	2149.0 ± 144.2	72176.0 ± 2508.7

Table B.20: Fit results for the p_T^W variable at a centre-of-mass energy of 8 TeV (muon channel).

Process	0--27 GeV	27--52 GeV	52--78 GeV	78--105 GeV	105--134 GeV	134--166 GeV	166--200 GeV	200--237 GeV	≥ 237 GeV	Total
$t\bar{t}$ in	5359.1 ± 204.0	12104.9 ± 307.4	15135.4 ± 341.7	14178.5 ± 329.0	11157.9 ± 291.2	7537.5 ± 238.6	4379.9 ± 181.3	2488.1 ± 134.4	2653.8 ± 136.8	74995.1 ± 2164.4
$t\bar{t}$ fit	5523.7 ± 110.1	12780.5 ± 176.2	14949.0 ± 354.0	13818.3 ± 340.9	10693.5 ± 168.2	7116.8 ± 206.6	3701.0 ± 118.1	1994.8 ± 79.5	1957.0 ± 70.7	72534.6 ± 1624.2
Single Top in	204.1 ± 28.4	449.7 ± 42.5	559.3 ± 48.7	534.4 ± 47.1	439.8 ± 42.4	314.4 ± 36.7	188.7 ± 28.2	126.7 ± 23.1	206.8 ± 29.2	3024.0 ± 326.2
Single Top fit	0.0 ± 658.0	0.0 ± 138.4	565.5 ± 480.5	214.8 ± 439.8	0.0 ± 2205.0	363.6 ± 249.7	483.7 ± 128.7	188.2 ± 84.7	209.1 ± 72.1	2024.9 ± 4457.0
W/Z + jets in	131.6 ± 6.5	289.6 ± 14.3	329.6 ± 16.3	281.7 ± 13.9	190.9 ± 9.5	153.2 ± 7.6	84.9 ± 4.2	59.1 ± 2.9	76.2 ± 3.8	1596.7 ± 79.1
W/Z + jets fit	574.2 ± 98.0	1139.1 ± 237.7	1533.5 ± 260.9	1361.7 ± 359.5	1014.7 ± 242.4	179.1 ± 239.3	14.1 ± 376.4	119.0 ± 56.1	12.9 ± 198.7	5948.4 ± 2069.0
QCD in	5.7 ± 0.1	422.6 ± 5.8	5.7 ± 0.1	39.1 ± 0.5	19.7 ± 0.3	34.0 ± 0.5	0.5 ± 0.0	0.1 ± 0.0	0.1 ± 0.0	527.6 ± 7.2
QCD fit	0.0 ± 23.1	55.4 ± 158.1	0.0 ± 104.4	97.2 ± 209.3	119.9 ± 173.5	181.6 ± 146.0	64.2 ± 94.1	0.0 ± 18.0	21.0 ± 81.9	539.3 ± 1008.5
Sum MC in	5700.5 ± 239.1	13266.8 ± 370.0	16030.0 ± 406.7	15033.8 ± 390.6	11808.2 ± 343.3	8039.2 ± 283.4	4654.0 ± 213.7	2674.0 ± 160.5	2936.9 ± 169.7	80143.4 ± 2576.9
Sum MC fit	6098.0 ± 889.2	13975.1 ± 710.3	17048.0 ± 1199.9	15492.0 ± 1349.6	11828.0 ± 2789.1	7841.0 ± 841.6	4263.0 ± 717.3	2302.1 ± 238.4	2200.0 ± 423.4	81047.2 ± 9158.7
Data	6098.0 ± 251.0	13975.0 ± 380.4	17048.0 ± 419.8	15492.0 ± 398.0	11828.0 ± 346.0	7841.0 ± 279.4	4263.0 ± 205.4	2302.0 ± 150.2	2200.0 ± 143.1	81047.0 ± 2573.4

Table B.21: Fit results for the M_T^W variable at a centre-of-mass energy of 8 TeV (electron channel).

Process	0--23 GeV	23--58 GeV	≥ 58 GeV	Total
t̄t in	8261.6 ± 252.9	17940.6 ± 372.0	37026.8 ± 533.7	63229.0 ± 1158.5
t̄t fit	8012.3 ± 211.3	17460.8 ± 329.3	38017.8 ± 364.2	63491.0 ± 904.8
Single Top in	348.2 ± 39.1	733.5 ± 55.9	1485.2 ± 78.9	2566.9 ± 174.0
Single Top fit	26.9 ± 506.0	245.5 ± 395.8	0.1 ± 4833.9	272.5 ± 5735.7
W/Z + jets in	220.2 ± 11.9	403.2 ± 21.9	782.2 ± 42.4	1405.6 ± 76.2
W/Z + jets fit	959.9 ± 292.4	1784.9 ± 403.2	5102.4 ± 487.8	7847.2 ± 1183.4
QCD in	67.7 ± 1.6	1961.0 ± 46.7	398.7 ± 9.5	2427.4 ± 57.8
QCD fit	169.8 ± 111.3	371.9 ± 146.7	21.8 ± 479.5	563.6 ± 737.5
Sum MC in	8897.6 ± 305.6	21038.3 ± 496.4	39693.0 ± 664.5	69628.8 ± 1466.5
Sum MC fit	9169.0 ± 1121.0	19863.0 ± 1275.0	43142.2 ± 6165.4	72174.2 ± 8561.4
Data	9169.0 ± 316.6	19863.0 ± 465.2	43142.0 ± 684.4	72174.0 ± 1466.2

Table B.22: Fit results for the M_T^W variable at a centre-of-mass energy of 8 TeV (muon channel).

Process	0--23 GeV	23--58 GeV	≥ 58 GeV	Total
t̄t in	9827.5 ± 274.7	21864.3 ± 409.9	43303.4 ± 574.6	74995.1 ± 1259.2
t̄t fit	9392.8 ± 239.2	21147.1 ± 240.7	42723.5 ± 560.5	73263.4 ± 1040.4
Single Top in	409.5 ± 41.6	903.5 ± 61.7	1710.9 ± 84.0	3024.0 ± 187.3
Single Top fit	82.7 ± 277.9	0.0 ± 313.9	303.9 ± 700.1	386.6 ± 1291.9
W/Z + jets in	239.4 ± 11.9	490.2 ± 24.3	867.1 ± 42.9	1596.7 ± 79.1
W/Z + jets fit	1131.5 ± 290.2	2366.8 ± 220.4	3720.6 ± 382.0	7218.8 ± 892.7
QCD in	67.7 ± 0.9	458.8 ± 6.3	0.9 ± 0.0	527.4 ± 7.2
QCD fit	178.0 ± 179.9	0.0 ± 537.4	0.1 ± 177.1	178.2 ± 894.4
Sum MC in	10544.1 ± 329.1	23716.8 ± 502.1	45882.3 ± 701.5	80143.2 ± 1532.8
Sum MC fit	10785.1 ± 987.2	23514.0 ± 1312.3	46748.0 ± 1819.7	81047.1 ± 4119.3
Data	10785.0 ± 333.0	23514.0 ± 491.1	46748.0 ± 689.2	81047.0 ± 1513.3

B.6 Fit correlations

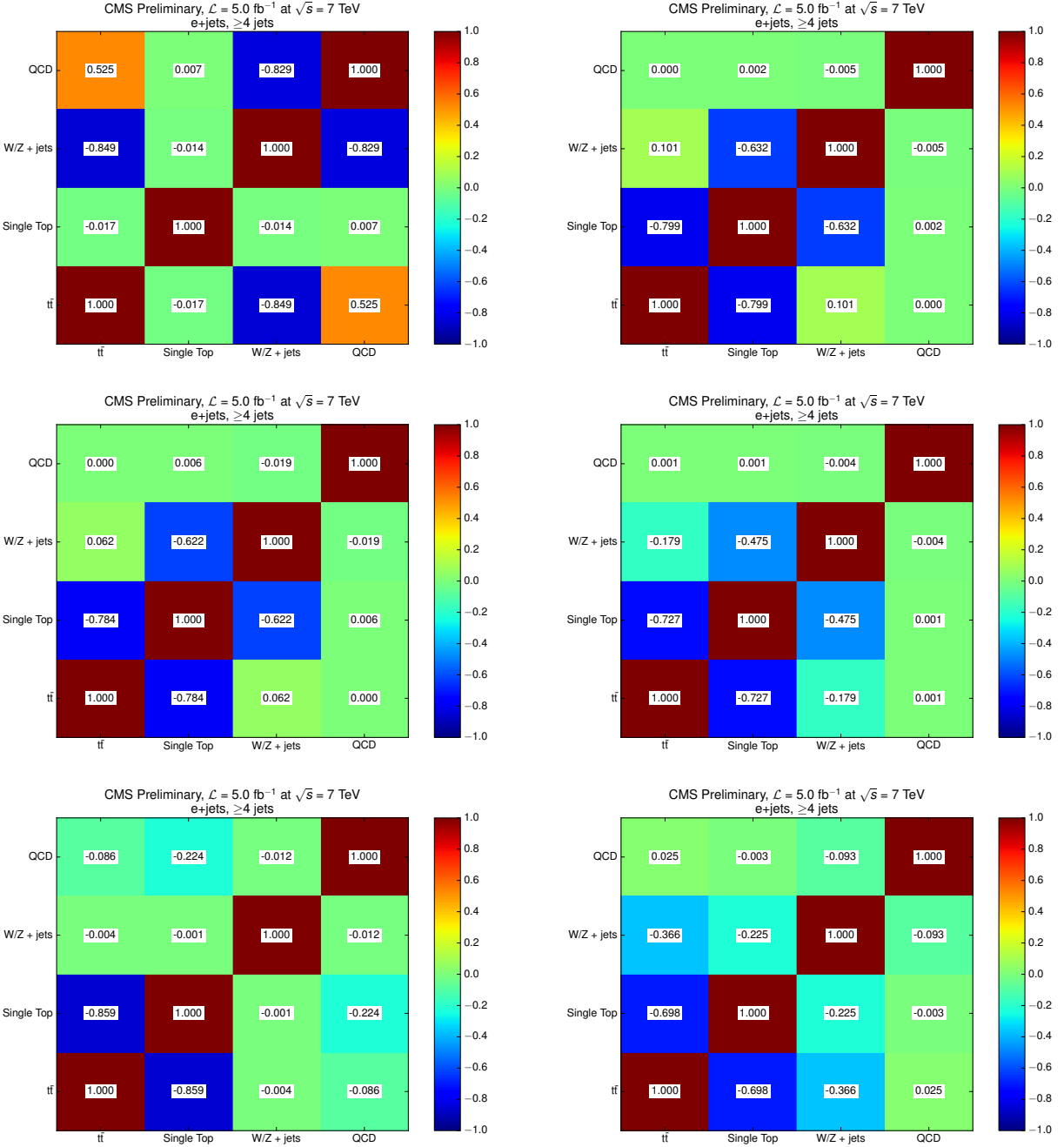


Figure B.8: Correlation between fit processes for the E_T^{miss} variable in the electron+jets channel at $\sqrt{s} = 7 \text{ TeV}$ in bins 0-27 GeV (upper left), 27-52 GeV (upper right), 52-87 GeV (middle left), 87-130 GeV (middle right), 130-172 GeV (lower left) and ≥ 172 GeV (lower right).

B.7 Systematic Uncertainties

B. $t\bar{t}$ differential cross section

Table B.23: Systematic uncertainties for the normalised $t\bar{t}$ cross section measurement with respect to E_T^{miss} variable at a centre-of-mass energy of 7 TeV (combination of electron and muon channels).

Uncertainty source	0--27 GeV	27--52 GeV	52--87 GeV	87--130 GeV	130--172 GeV	≥ 172 GeV
b tagging efficiency -1σ (%)	0.03	0.01	-0.01	-0.03	-0.05	-0.07
b tagging efficiency $+1\sigma$ (%)	-0.03	-0.01	0.01	0.03	0.05	0.07
Electron efficiency -1σ (%)	-0.00	0.00	0.00	-0.00	-0.00	-0.01
Electron efficiency $+1\sigma$ (%)	0.01	0.01	-0.01	-0.02	-0.01	0.01
Jet energy resolution -1σ (%)	-0.00	-0.02	-0.02	0.04	0.14	0.25
Jet energy resolution $+1\sigma$ (%)	0.06	0.03	-0.01	-0.08	-0.14	-0.17
Jet energy scale -1σ (%)	-0.18	-0.11	0.03	0.25	0.51	0.72
Jet energy scale $+1\sigma$ (%)	-0.11	0.02	0.10	-0.01	-0.23	-0.43
Muon efficiency -1σ (%)	-0.00	-0.00	0.00	0.00	0.01	0.01
Muon efficiency $+1\sigma$ (%)	0.00	0.00	-0.00	-0.00	-0.00	-0.01
PDF uncertainty -1σ (%)	1.23	0.57	0.49	0.68	0.65	2.08
PDF uncertainty $+1\sigma$ (%)	1.23	0.57	0.49	0.68	0.65	2.08
Pile-up -1σ (%)	-0.00	-0.00	0.00	0.01	0.01	0.01
Pile-up $+1\sigma$ (%)	0.04	0.03	-0.01	-0.05	-0.10	-0.13
QCD cross section $+1\sigma$ (%)	0.00	0.00	0.00	-0.00	-0.00	-0.00
QCD cross section -1σ (%)	0.00	0.00	-0.00	-0.00	-0.00	-0.00
QCD shape uncertainty (%)	0.02	0.01	-0.01	-0.02	-0.03	-0.04
Single top cross section $+1\sigma$ (%)	-0.00	-0.00	0.00	0.00	0.00	-0.00
Single top cross section -1σ (%)	-0.00	0.00	0.00	0.00	-0.00	-0.00
$t\bar{t}$ cross section $+1\sigma$ (%)	0.00	0.00	0.00	-0.00	-0.00	-0.00
$t\bar{t}$ cross section -1σ (%)	0.00	0.00	-0.00	-0.00	-0.00	-0.00
Top mass down (%)	-0.02	0.02	0.10	-0.18	-0.26	-0.02
Top mass up (%)	0.20	-0.16	0.02	-0.17	1.07	-0.20
Matching down (%)	0.03	0.14	-0.00	-0.66	-0.21	2.55
Matching up (%)	-0.07	-0.12	0.34	0.06	-0.86	-1.57
Q^2 down (%)	-0.09	0.08	0.20	-0.37	-0.24	-1.04
Q^2 up (%)	-0.57	0.03	0.38	-0.26	0.09	0.38
V+jets cross section $+1\sigma$ (%)	-0.00	-0.00	0.00	0.00	0.00	0.00
V+jets cross section -1σ (%)	0.00	0.00	0.00	-0.00	-0.00	-0.00
V+jets (matching down) (%)	-0.31	-0.14	0.11	0.33	0.51	0.63
V+jets (matching up) (%)	-0.42	-0.18	0.16	0.42	0.58	0.69
V+jets (Q^2 down) (%)	-0.62	-0.28	0.21	0.66	1.00	1.25
V+jets (Q^2 up) (%)	-0.39	-0.17	0.14	0.41	0.60	0.72
Hadronisation uncertainty (%)	3.30	2.19	0.93	5.16	7.94	11.30
Luminosity $+1\sigma$ (%)	0.00	0.00	-0.00	-0.00	-0.00	-0.00
Luminosity -1σ (%)	0.00	0.00	-0.00	-0.00	-0.00	-0.00
Electron energy -1σ (%)	-0.07	-0.05	0.01	0.10	0.20	0.27
Electron energy $+1\sigma$ (%)	0.03	0.02	-0.00	-0.05	-0.10	-0.14
Muon energy -1σ (%)	0.00	-0.00	-0.00	0.00	0.01	0.02
Muon energy $+1\sigma$ (%)	0.03	0.02	-0.01	-0.04	-0.07	-0.10
Tau energy -1σ (%)	1.09	0.61	-0.27	-1.36	-2.45	-3.33
Tau energy $+1\sigma$ (%)	-1.07	-0.61	0.24	1.37	2.51	3.41
Unclustered energy -1σ (%)	0.29	0.19	-0.05	-0.41	-0.79	-1.11
Unclustered energy $+1\sigma$ (%)	-0.17	-0.11	0.02	0.24	0.48	0.66
$p_T(t, \bar{t})$ reweighting (%)	0.91	1.36	1.41	1.86	6.51	14.73
Total (%)	4.26	2.99	2.23	6.05	11.01	19.45

Table B.24: Systematic uncertainties for the normalised $t\bar{t}$ cross section measurement with respect to H_T variable at a centre-of-mass energy of 7 TeV (combination of electron and muon channels).

Uncertainty source	120–185 GeV	185–215 GeV	215–247 GeV	247–283 GeV	283–323 GeV	323–365 GeV	365–409 GeV	409–458 GeV	458–512 GeV	512–570 GeV	570–629 GeV	629–691 GeV	691–769 GeV	≥ 769 GeV
b tagging efficiency -1σ (%)	-0.02	-0.02	-0.02	-0.03	-0.03	-0.01	0.01	0.06	0.11	0.16	0.20	0.24	0.26	0.27
b tagging efficiency $+1\sigma$ (%)	0.02	0.02	0.02	0.02	0.01	0.00	-0.02	-0.06	-0.10	-0.14	-0.17	-0.20	-0.21	-0.22
Electron efficiency -1σ (%)	-0.23	-0.23	-0.21	-0.14	0.02	0.22	0.41	0.56	0.66	0.72	0.75	0.75	0.74	0.74
Electron efficiency $+1\sigma$ (%)	0.65	0.62	0.55	0.35	-0.07	-0.60	-1.10	-1.50	-1.78	-1.94	-1.99	-1.95	-1.89	-1.83
Jet energy resolution -1σ (%)	0.67	0.53	0.29	-0.02	-0.33	-0.60	-0.81	-0.90	-0.90	-0.80	-0.66	-0.50	-0.35	-0.21
Jet energy resolution $+1\sigma$ (%)	-3.46	-2.71	-1.41	0.16	1.72	3.01	3.88	4.29	4.32	4.08	3.66	3.21	2.76	2.44
Jet energy scale -1σ (%)	-3.16	-2.47	-1.27	0.11	1.37	2.41	3.24	3.87	4.28	4.49	4.55	4.53	4.39	4.25
Jet energy scale $+1\sigma$ (%)	-1.54	-1.00	-0.13	0.67	1.09	1.23	1.16	0.94	0.57	0.10	-0.48	-1.07	-1.60	-1.99
Muon efficiency -1σ (%)	0.02	0.01	0.00	-0.00	-0.01	-0.01	-0.02	-0.02	-0.01	-0.01	0.00	0.01	0.02	0.03
Muon efficiency $+1\sigma$ (%)	0.00	0.00	0.00	0.00	0.00	0.00	0.00	-0.00	-0.01	-0.01	-0.02	-0.03	-0.03	-0.04
PDF uncertainty -1σ (%)	0.79	0.32	0.34	0.48	0.61	0.81	0.63	0.63	0.79	1.02	1.27	1.41	1.58	1.21
PDF uncertainty $+1\sigma$ (%)	0.79	0.32	0.34	0.48	0.61	0.81	0.63	0.63	0.79	1.02	1.27	1.41	1.58	1.21
Pile-up -1σ (%)	0.05	0.02	-0.02	-0.07	-0.09	-0.07	-0.01	0.08	0.16	0.23	0.28	0.32	0.32	0.30
Pile-up $+1\sigma$ (%)	-0.13	-0.09	-0.01	0.06	0.12	0.12	0.08	0.03	-0.01	-0.05	-0.07	-0.08	-0.07	-0.04
QCD cross section $+1\sigma$ (%)	-0.01	-0.01	-0.01	-0.00	0.00	0.01	0.01	0.01	0.02	0.02	0.02	0.02	0.02	0.02
QCD cross section -1σ (%)	0.02	0.02	0.01	-0.00	-0.01	-0.02	-0.03	-0.03	-0.03	-0.03	-0.03	-0.03	-0.03	-0.03
QCD shape uncertainty (%)	0.10	0.09	0.07	0.04	-0.01	-0.08	-0.14	-0.18	-0.21	-0.24	-0.27	-0.31	-0.36	-0.41
Single top cross section $+1\sigma$ (%)	-0.00	-0.00	-0.00	-0.00	0.00	0.00	0.00	0.01	0.01	0.01	0.01	0.01	0.01	0.01
Single top cross section -1σ (%)	-0.01	-0.01	-0.00	-0.00	0.00	0.01	0.01	0.01	0.01	0.01	0.01	0.01	0.01	0.01
$t\bar{t}$ cross section $+1\sigma$ (%)	0.00	0.00	-0.00	-0.00	-0.00	-0.00	0.00	0.00	0.00	0.00	0.00	0.00	0.00	0.00
$t\bar{t}$ cross section -1σ (%)	0.01	0.00	-0.00	-0.01	-0.01	-0.01	-0.00	-0.00	0.00	0.00	0.01	0.01	0.01	0.01
Top mass down (%)	-0.12	0.11	-0.10	0.20	-0.01	-0.00	0.02	-0.07	-0.14	-0.11	-0.03	0.20	0.12	-0.27
Top mass up (%)	0.11	0.09	-0.17	0.39	-0.46	0.40	-0.22	-0.29	0.28	-0.79	-1.67	0.18	1.16	0.21
Matching down (%)	-1.21	-0.21	-0.38	0.72	0.58	0.73	0.36	1.69	0.26	-0.56	-0.08	0.14	-1.38	-3.95
Matching up (%)	-1.26	-0.44	-0.01	0.88	0.14	0.23	0.33	1.21	0.43	-0.17	-0.41	-0.19	1.66	3.68
Q^2 down (%)	-7.76	-4.32	-0.85	2.30	3.62	5.13	5.49	5.26	4.81	4.33	2.72	2.50	3.04	2.12
Q^2 up (%)	5.26	2.43	-0.12	-1.07	-2.97	-3.04	-3.31	-2.32	-1.89	-2.29	-2.20	-2.36	0.53	-0.66
V+jets cross section $+1\sigma$ (%)	-0.00	-0.00	-0.00	-0.00	0.00	0.00	0.01	0.01	0.01	0.01	0.02	0.02	0.02	0.02
V+jets cross section -1σ (%)	-0.01	-0.01	-0.00	-0.00	0.00	0.01	0.01	0.01	0.01	0.01	0.02	0.01	0.01	0.01
V+jets (matching down) (%)	-0.41	-0.42	-0.40	-0.26	0.04	0.41	0.76	1.03	1.21	1.31	1.37	1.39	1.42	1.44
V+jets (matching up) (%)	0.87	0.59	0.15	-0.24	-0.46	-0.54	-0.57	-0.60	-0.69	-0.80	-0.86	-0.85	-0.80	-0.74
V+jets (Q^2 down) (%)	1.19	0.79	0.14	-0.49	-0.90	-1.02	-0.92	-0.68	-0.36	0.00	0.39	0.73	1.04	1.28
V+jets (Q^2 up) (%)	-0.16	-0.21	-0.26	-0.23	-0.07	0.19	0.47	0.70	0.84	0.89	0.86	0.84	0.84	0.84
Hadronisation uncertainty (%)	1.13	2.96	3.29	2.32	0.27	1.74	3.66	5.46	6.60	7.17	7.54	7.48	7.96	9.89
Luminosity $+1\sigma$ (%)	0.02	0.01	0.01	-0.00	-0.01	-0.01	-0.02	-0.02	-0.02	-0.02	-0.01	-0.01	-0.01	-0.01
Luminosity -1σ (%)	0.01	0.01	0.00	-0.00	-0.01	-0.01	-0.01	-0.02	-0.02	-0.01	-0.01	-0.01	-0.00	-0.00
$p_T(t, \bar{t})$ reweighting (%)	1.91	0.76	0.22	0.96	1.22	1.06	0.57	0.05	0.57	0.84	0.93	0.65	0.01	4.85
Total (%)	10.03	7.08	4.65	4.40	5.10	7.27	8.76	10.13	10.60	10.87	10.69	10.72	11.54	14.09

Table B.25: Systematic uncertainties for the normalised $t\bar{t}$ cross section measurement with respect to S_T variable at a centre-of-mass energy of 7 TeV (combination of electron and muon channels).

Uncertainty source	146–277 GeV	277–319 GeV	319–361 GeV	361–408 GeV	408–459 GeV	459–514 GeV	514–573 GeV	573–637 GeV	637–705 GeV	705–774 GeV	774–854 GeV	854–940 GeV	≥ 940 GeV
b tagging efficiency -1σ (%)	0.05	0.05	0.04	0.02	-0.03	-0.09	-0.17	-0.21	-0.20	-0.12	0.06	0.27	0.46
b tagging efficiency $+1\sigma$ (%)	1.78	1.41	0.64	-0.26	-1.07	-1.67	-2.09	-2.43	-2.72	-2.89	-2.96	-2.93	-2.85
Electron efficiency -1σ (%)	0.33	0.27	0.13	-0.03	-0.18	-0.31	-0.42	-0.52	-0.60	-0.64	-0.61	-0.55	-0.48
Electron efficiency $+1\sigma$ (%)	1.41	1.11	0.47	-0.29	-0.97	-1.43	-1.66	-1.76	-1.79	-1.70	-1.50	-1.22	-0.96
Jet energy resolution -1σ (%)	1.17	0.96	0.54	-0.04	-0.69	-1.27	-1.69	-1.94	-2.06	-2.05	-1.94	-1.77	-1.58
Jet energy resolution $+1\sigma$ (%)	-0.06	-0.03	0.00	0.04	0.08	0.09	0.01	-0.15	-0.26	-0.22	-0.01	0.31	0.62
Jet energy scale -1σ (%)	0.38	0.26	0.04	-0.17	-0.36	-0.46	-0.42	-0.25	0.03	0.31	0.52	0.68	0.86
Jet energy scale $+1\sigma$ (%)	0.47	0.49	0.48	0.30	-0.05	-0.52	-1.13	-1.76	-2.24	-2.39	-2.22	-1.90	-1.62
Muon efficiency -1σ (%)	-0.00	-0.00	-0.00	-0.00	-0.00	-0.00	0.00	0.01	0.01	0.02	0.03	0.03	0.03
Muon efficiency $+1\sigma$ (%)	0.00	0.00	0.00	0.00	0.00	-0.00	-0.00	-0.01	-0.02	-0.03	-0.03	-0.04	-0.05
PDF uncertainty -1σ (%)	0.88	0.48	0.39	0.51	0.82	0.94	0.77	0.77	0.93	1.30	1.66	1.71	1.49
PDF uncertainty $+1\sigma$ (%)	0.88	0.48	0.39	0.51	0.82	0.94	0.77	0.77	0.93	1.30	1.66	1.71	1.49
Pile-up -1σ (%)	0.13	0.12	0.08	0.06	0.04	-0.01	-0.12	-0.31	-0.57	-0.85	-1.12	-1.35	-1.50
Pile-up $+1\sigma$ (%)	2.08	1.65	0.76	-0.31	-1.31	-2.04	-2.54	-2.90	-3.12	-3.13	-2.96	-2.68	-2.40
QCD cross section $+1\sigma$ (%)	-0.05	-0.04	-0.02	0.01	0.03	0.05	0.06	0.06	0.07	0.07	0.06	0.06	0.05
QCD cross section -1σ (%)	-0.04	-0.03	-0.01	0.01	0.02	0.04	0.04	0.05	0.05	0.05	0.04	0.04	0.04
QCD shape uncertainty (%)	1.84	1.48	0.71	-0.21	-1.06	-1.73	-2.23	-2.67	-3.02	-3.26	-3.37	-3.41	-3.37
Single top cross section $+1\sigma$ (%)	1.59	1.25	0.56	-0.25	-0.99	-1.51	-1.86	-2.12	-2.31	-2.41	-2.43	-2.37	-2.27
Single top cross section -1σ (%)	1.77	1.40	0.63	-0.28	-1.11	-1.70	-2.08	-2.37	-2.57	-2.67	-2.68	-2.61	-2.50
$t\bar{t}$ cross section $+1\sigma$ (%)	1.61	1.27	0.56	-0.27	-1.02	-1.55	-1.88	-2.12	-2.29	-2.37	-2.36	-2.30	-2.19
$t\bar{t}$ cross section -1σ (%)	1.78	1.41	0.63	-0.28	-1.10	-1.70	-2.10	-2.39	-2.61	-2.73	-2.74	-2.68	-2.57
Top mass down (%)	-0.13	-0.08	0.00	0.05	0.22	0.07	-0.10	-0.20	0.07	0.22	0.29	0.40	0.13
Top mass up (%)	-0.35	-0.41	0.06	0.40	0.20	0.26	-0.52	0.82	-0.23	-0.41	1.44	0.97	1.00
Matching down (%)	-0.85	-0.53	-0.17	0.59	0.95	0.91	0.72	0.05	-1.26	0.89	0.28	-2.05	-2.88
Matching up (%)	-1.04	-0.47	0.37	0.34	0.32	0.32	0.31	0.20	0.18	1.02	0.78	1.94	2.98
Q^2 down (%)	-8.15	-4.40	0.17	3.23	4.38	5.37	5.75	4.98	3.97	4.55	3.03	2.71	2.13
Q^2 up (%)	5.43	2.06	-0.32	-2.00	-2.96	-3.20	-3.46	-2.03	-1.93	-1.14	-1.21	0.16	0.38
V+jets cross section $+1\sigma$ (%)	-0.02	-0.01	0.01	0.02	0.03	0.03	0.01	-0.02	-0.06	-0.10	-0.11	-0.12	-0.11
V+jets cross section -1σ (%)	1.61	1.27	0.57	-0.25	-0.99	-1.53	-1.89	-2.15	-2.36	-2.47	-2.49	-2.43	-2.33
V+jets (matching down) (%)	-1.03	-0.83	-0.43	0.12	0.70	1.18	1.46	1.48	1.35	1.21	1.11	1.07	1.08
V+jets (matching up) (%)	0.03	0.01	-0.04	-0.05	0.05	0.16	0.15	0.01	-0.18	-0.35	-0.48	-0.56	-0.59
V+jets (Q^2 down) (%)	-1.47	-1.21	-0.69	0.03	0.89	1.66	2.19	2.44	2.47	2.38	2.24	2.11	2.02
V+jets (Q^2 up) (%)	-1.25	-1.05	-0.63	-0.01	0.73	1.42	1.91	2.15	2.22	2.23	2.19	2.16	2.14
Hadronisation uncertainty (%)	5.03	5.37	3.73	0.73	2.38	5.73	8.74	9.40	10.10	10.95	8.49	7.15	8.22
Luminosity $+1\sigma$ (%)	1.76	1.40	0.63	-0.28	-1.09	-1.69	-2.08	-2.37	-2.58	-2.70	-2.71	-2.64	-2.53
Luminosity -1σ (%)	1.74	1.38	0.61	-0.28	-1.09	-1.67	-2.04	-2.31	-2.50	-2.60	-2.60	-2.53	-2.43
Electron energy -1σ (%)	1.65	1.30	0.58	-0.28	-1.03	-1.55	-1.89	-2.17	-2.40	-2.52	-2.53	-2.46	-2.35
Electron energy $+1\sigma$ (%)	0.33	0.27	0.15	-0.02	-0.18	-0.33	-0.47	-0.60	-0.65	-0.62	-0.52	-0.41	-0.31
Muon energy -1σ (%)	0.01	0.01	0.01	-0.00	-0.02	-0.03	-0.03	-0.02	0.00	0.03	0.06	0.08	0.11
Muon energy $+1\sigma$ (%)	0.04	0.04	0.03	0.02	-0.00	-0.03	-0.05	-0.09	-0.13	-0.19	-0.24	-0.29	-0.32
Tau energy -1σ (%)	0.90	0.73	0.38	-0.08	-0.52	-0.85	-1.09	-1.31	-1.55	-1.77	-1.89	-1.87	-1.80
Tau energy $+1\sigma$ (%)	1.35	1.04	0.37	-0.40	-1.03	-1.38	-1.47	-1.44	-1.29	-1.02	-0.69	-0.39	-0.15
Unclustered energy -1σ (%)	0.21	0.18	0.08	-0.03	-0.14	-0.18	-0.20	-0.24	-0.33	-0.44	-0.55	-0.64	-0.68
Unclustered energy $+1\sigma$ (%)	0.66	0.55	0.31	-0.02	-0.35	-0.65	-0.91	-1.17	-1.38	-1.46	-1.35	-1.14	-0.92
$p_T(t, \bar{t})$ reweighting (%)	2.98	1.24	0.20	1.25	1.67	1.61	1.32	0.88	0.53	0.21	0.24	1.29	6.80
Total (%)	12.27	9.06	4.95	4.28	7.02	10.42	13.26	14.08	14.81	15.95	14.13	13.40	15.43

Table B.26: Systematic uncertainties for the normalised $t\bar{t}$ cross section measurement with respect to p_T^W variable at a centre-of-mass energy of 7 TeV (combination of electron and muon channels).

Uncertainty source	0–27 GeV	27–52 GeV	52–78 GeV	78–105 GeV	105–134 GeV	134–166 GeV	166–200 GeV	200–237 GeV	≥ 237 GeV
b tagging efficiency -1σ (%)	0.06	0.05	0.03	-0.01	-0.06	-0.09	-0.12	-0.14	-0.16
b tagging efficiency $+1\sigma$ (%)	-0.23	-0.20	-0.09	0.06	0.21	0.32	0.40	0.45	0.48
Electron efficiency -1σ (%)	-0.02	-0.02	-0.01	0.01	0.02	0.02	0.02	0.01	0.01
Electron efficiency $+1\sigma$ (%)	-1.13	-0.63	-0.10	0.26	0.54	0.85	1.22	1.56	1.80
Jet energy resolution -1σ (%)	0.39	0.21	-0.07	-0.30	-0.37	-0.12	0.39	0.96	1.44
Jet energy resolution $+1\sigma$ (%)	0.56	0.40	0.07	-0.23	-0.44	-0.48	-0.43	-0.35	-0.31
Jet energy scale -1σ (%)	0.29	-0.02	-0.31	-0.31	-0.02	0.46	1.02	1.51	1.82
Jet energy scale $+1\sigma$ (%)	0.60	0.85	0.76	0.10	-0.90	-1.93	-2.81	-3.38	-3.63
Muon efficiency -1σ (%)	-0.00	-0.00	-0.00	-0.00	0.00	0.00	0.01	0.02	0.02
Muon efficiency $+1\sigma$ (%)	0.01	0.01	0.00	-0.00	-0.01	-0.01	-0.02	-0.02	-0.03
PDF uncertainty -1σ (%)	1.07	0.63	0.10	0.45	0.38	0.96	1.15	1.38	1.25
PDF uncertainty $+1\sigma$ (%)	1.07	0.63	0.10	0.45	0.38	0.96	1.15	1.38	1.25
Pile-up -1σ (%)	-0.65	-0.45	-0.14	0.18	0.47	0.70	0.82	0.84	0.82
Pile-up $+1\sigma$ (%)	-0.32	-0.17	0.01	0.10	0.12	0.14	0.23	0.36	0.45
QCD cross section $+1\sigma$ (%)	0.07	0.07	0.06	-0.01	-0.09	-0.16	-0.20	-0.22	-0.23
QCD cross section -1σ (%)	0.07	0.05	0.01	-0.02	-0.05	-0.06	-0.07	-0.07	-0.08
QCD shape uncertainty (%)	0.05	0.05	0.04	0.02	-0.03	-0.11	-0.20	-0.28	-0.34
Single top cross section $+1\sigma$ (%)	0.02	0.01	-0.01	-0.01	-0.01	-0.00	0.00	0.00	0.01
Single top cross section -1σ (%)	0.19	0.13	0.03	-0.08	-0.14	-0.17	-0.17	-0.16	-0.15
$t\bar{t}$ cross section $+1\sigma$ (%)	-0.58	-0.20	0.23	0.38	0.27	-0.08	-0.60	-1.12	-1.51
$t\bar{t}$ cross section -1σ (%)	0.02	0.02	0.01	-0.01	-0.02	-0.03	-0.03	-0.03	-0.03
Top mass down (%)	-0.09	-0.14	0.04	-0.03	0.07	0.29	0.09	0.15	0.24
Top mass up (%)	0.26	-0.14	-0.02	-0.30	0.42	0.08	-0.36	-0.25	1.83
Matching down (%)	0.45	0.44	0.22	-0.45	-0.75	-0.62	0.59	0.27	0.48
Matching up (%)	-0.12	-0.11	0.02	-0.15	0.17	0.18	-0.13	0.96	1.12
Q^2 down (%)	0.33	-0.15	-0.06	-0.53	0.20	0.71	0.47	0.85	1.04
Q^2 up (%)	-0.13	-0.58	0.09	0.22	0.15	0.03	0.32	1.43	1.25
V+jets cross section $+1\sigma$ (%)	0.02	0.02	0.00	-0.01	-0.02	-0.02	-0.03	-0.03	-0.03
V+jets cross section -1σ (%)	0.03	0.02	0.01	-0.01	-0.02	-0.03	-0.04	-0.04	-0.04
V+jets (matching down) (%)	0.02	-0.02	-0.02	0.02	0.08	0.07	-0.04	-0.22	-0.39
V+jets (matching up) (%)	0.45	0.28	0.08	-0.07	-0.20	-0.39	-0.69	-1.00	-1.25
V+jets (Q^2 down) (%)	-0.03	-0.13	-0.17	-0.01	0.23	0.39	0.37	0.26	0.14
V+jets (Q^2 up) (%)	0.32	0.20	0.04	-0.11	-0.26	-0.34	-0.22	-0.02	0.18
Hadronisation uncertainty (%)	2.30	2.79	1.98	0.75	3.06	4.92	5.97	7.85	10.28
Luminosity $+1\sigma$ (%)	0.01	0.01	0.00	-0.01	-0.01	-0.01	-0.01	-0.01	-0.01
Luminosity -1σ (%)	0.03	0.02	0.00	-0.01	-0.02	-0.02	-0.03	-0.02	-0.02
Electron energy -1σ (%)	-0.55	-0.39	-0.14	0.11	0.35	0.59	0.85	1.11	1.33
Electron energy $+1\sigma$ (%)	0.37	0.24	0.06	-0.07	-0.17	-0.32	-0.53	-0.83	-1.13
Muon energy -1σ (%)	-0.14	-0.12	-0.07	0.01	0.12	0.23	0.32	0.40	0.48
Muon energy $+1\sigma$ (%)	0.19	0.13	0.03	-0.06	-0.14	-0.18	-0.19	-0.18	-0.16
Tau energy -1σ (%)	3.55	2.62	0.97	-0.88	-2.56	-3.95	-5.15	-6.36	-7.53
Tau energy $+1\sigma$ (%)	-0.74	-0.87	-0.91	-0.48	0.58	2.25	4.31	6.20	7.54
Unclustered energy -1σ (%)	2.37	1.57	0.30	-0.83	-1.64	-2.07	-2.17	-2.03	-1.76
Unclustered energy $+1\sigma$ (%)	-0.44	-0.32	-0.11	0.14	0.36	0.47	0.53	0.52	0.40
$p_T(t, \bar{t})$ reweighting (%)	1.10	0.14	0.75	0.22	0.10	0.07	0.21	0.20	5.96
Total (%)	5.96	4.79	3.01	2.60	5.07	7.51	9.27	11.86	15.91

B. $t\bar{t}$ differential cross section

Table B.27: Systematic uncertainties for the normalised $t\bar{t}$ cross section measurement with respect to M_T^W variable at a centre-of-mass energy of 7 TeV (combination of electron and muon channels).

Uncertainty source	0--23 GeV	23--58 GeV	≥ 58 GeV
b tagging efficiency -1σ (%)	0.08	0.03	-0.03
b tagging efficiency $+1\sigma$ (%)	-0.06	-0.02	0.02
Electron efficiency -1σ (%)	0.01	0.00	-0.00
Electron efficiency $+1\sigma$ (%)	-0.68	-0.27	0.27
Jet energy resolution -1σ (%)	-0.58	-0.19	0.21
Jet energy resolution $+1\sigma$ (%)	-0.47	-0.00	0.09
Jet energy scale -1σ (%)	-1.48	-0.44	0.50
Jet energy scale $+1\sigma$ (%)	-1.13	-0.39	0.41
Muon efficiency -1σ (%)	0.02	0.01	-0.01
Muon efficiency $+1\sigma$ (%)	-0.02	-0.01	0.01
PDF uncertainty -1σ (%)	1.23	0.82	0.64
PDF uncertainty $+1\sigma$ (%)	1.23	0.82	0.64
Pile-up -1σ (%)	-0.36	-0.08	0.11
Pile-up $+1\sigma$ (%)	-0.00	-0.03	0.02
QCD cross section $+1\sigma$ (%)	0.00	0.00	-0.00
QCD cross section -1σ (%)	0.01	0.00	-0.00
QCD shape uncertainty (%)	-0.15	-0.05	0.06
Single top cross section $+1\sigma$ (%)	0.01	0.00	-0.00
Single top cross section -1σ (%)	0.01	0.00	-0.00
$t\bar{t}$ cross section $+1\sigma$ (%)	0.00	0.00	-0.00
$t\bar{t}$ cross section -1σ (%)	0.01	0.00	-0.00
Top mass down (%)	0.00	0.06	-0.03
Top mass up (%)	-0.32	0.21	-0.04
Matching down (%)	-0.95	0.02	0.17
Matching up (%)	-0.29	0.31	-0.10
Q^2 down (%)	0.40	0.47	-0.31
Q^2 up (%)	-1.25	-0.00	0.24
V+jets cross section $+1\sigma$ (%)	0.00	-0.00	-0.00
V+jets cross section -1σ (%)	0.01	0.00	-0.00
V+jets (matching down) (%)	1.19	0.45	-0.45
V+jets (matching up) (%)	-0.49	-0.17	0.18
V+jets (Q^2 down) (%)	1.74	0.67	-0.67
V+jets (Q^2 up) (%)	1.65	0.69	-0.66
Hadronisation uncertainty (%)	2.87	1.44	1.26
Luminosity $+1\sigma$ (%)	0.01	0.00	-0.00
Luminosity -1σ (%)	0.00	0.00	-0.00
Electron energy -1σ (%)	1.20	0.52	-0.49
Electron energy $+1\sigma$ (%)	-0.78	-0.38	0.34
Muon energy -1σ (%)	0.05	0.03	-0.03
Muon energy $+1\sigma$ (%)	-0.17	-0.07	0.07
Tau energy -1σ (%)	-1.92	-0.64	0.69
Tau energy $+1\sigma$ (%)	0.67	0.18	-0.22
Unclustered energy -1σ (%)	-0.32	-0.24	0.18
Unclustered energy $+1\sigma$ (%)	1.32	0.38	-0.44
$p_T(t, \bar{t})$ reweighting (%)	182	0.76	0.42
Total (%)		5.93	2.91
			2.23

Table B.28: Systematic uncertainties for the normalised $t\bar{t}$ cross section measurement with respect to E_T^{miss} variable at a centre-of-mass energy of 8 TeV (combination of electron and muon channels).

Uncertainty source	0–27 GeV	27–52 GeV	52–87 GeV	87–130 GeV	130–172 GeV	≥ 172 GeV
b tagging efficiency -1σ (%)	0.07	0.03	-0.03	-0.07	-0.06	-0.02
b tagging efficiency $+1\sigma$ (%)	-0.32	-0.16	0.18	0.40	0.24	-0.16
Electron efficiency -1σ (%)	-0.03	-0.02	0.02	0.03	0.03	0.04
Electron efficiency $+1\sigma$ (%)	-0.19	-0.10	0.10	0.21	0.23	0.21
Jet energy resolution -1σ (%)	0.13	-0.12	-0.13	0.19	0.59	0.92
Jet energy resolution $+1\sigma$ (%)	-0.26	-0.07	0.11	0.12	0.30	0.75
Jet energy scale -1σ (%)	-0.11	-0.55	-0.17	0.99	2.26	3.43
Jet energy scale $+1\sigma$ (%)	0.09	0.12	0.01	-0.33	-0.44	-0.14
Muon efficiency -1σ (%)	0.01	0.00	-0.01	-0.01	0.02	0.06
Muon efficiency $+1\sigma$ (%)	-0.01	-0.00	0.01	0.01	-0.02	-0.06
PDF uncertainty -1σ (%)	0.56	0.19	0.24	0.43	0.82	0.75
PDF uncertainty $+1\sigma$ (%)	0.56	0.19	0.24	0.43	0.82	0.75
Pile-up -1σ (%)	-0.18	-0.13	0.10	0.26	0.27	0.26
Pile-up $+1\sigma$ (%)	0.09	0.05	-0.08	-0.21	0.16	0.81
QCD cross section $+1\sigma$ (%)	0.00	0.00	-0.00	-0.00	-0.00	-0.00
QCD cross section -1σ (%)	-0.01	-0.00	0.01	0.01	0.00	0.00
QCD shape uncertainty (%)	0.23	0.06	-0.11	-0.21	-0.12	0.06
Single top cross section $+1\sigma$ (%)	-0.00	-0.00	0.00	0.00	0.00	-0.00
Single top cross section -1σ (%)	0.00	0.00	-0.00	-0.00	-0.00	0.00
$t\bar{t}$ cross section $+1\sigma$ (%)	-0.00	-0.00	0.00	0.00	-0.00	-0.01
$t\bar{t}$ cross section -1σ (%)	0.00	0.00	-0.00	-0.00	-0.00	0.01
Top mass down (%)	-0.39	-0.03	0.08	0.26	0.41	0.43
Top mass up (%)	0.38	-0.07	-0.26	-0.10	0.95	1.16
Matching down (%)	0.82	0.03	-0.40	0.05	-0.64	-1.31
Matching up (%)	-0.85	-0.61	0.04	1.90	2.35	1.39
Q^2 down (%)	7.37	2.72	-2.98	-6.29	-9.25	-12.96
Q^2 up (%)	-0.15	-0.19	-0.06	0.41	0.64	2.22
V+jets cross section $+1\sigma$ (%)	0.00	0.00	0.00	-0.00	-0.00	-0.01
V+jets cross section -1σ (%)	0.00	0.00	-0.00	-0.00	0.00	0.01
V+jets (matching down) (%)	-0.99	-0.55	0.45	1.28	1.36	1.03
V+jets (matching up) (%)	-0.26	-0.27	0.22	0.51	0.21	-0.32
V+jets (Q^2 down) (%)	-1.21	-0.48	0.62	1.18	0.89	0.29
V+jets (Q^2 up) (%)	-0.92	-0.44	0.45	1.04	0.92	0.60
Hadronisation uncertainty (%)	3.30	2.19	0.93	5.16	7.94	11.30
Luminosity $+1\sigma$ (%)	0.00	0.00	-0.00	-0.00	0.00	0.01
Luminosity -1σ (%)	-0.00	-0.00	0.00	0.00	0.01	0.01
Electron energy -1σ (%)	-0.15	-0.17	0.03	0.32	0.62	0.87
Electron energy $+1\sigma$ (%)	-0.07	0.00	0.08	-0.03	-0.12	-0.19
Muon energy -1σ (%)	0.05	-0.01	-0.05	0.00	0.11	0.24
Muon energy $+1\sigma$ (%)	-0.05	0.01	0.03	0.01	-0.07	-0.16
Tau energy -1σ (%)	2.14	1.05	-0.65	-2.37	-4.18	-6.05
Tau energy $+1\sigma$ (%)	-2.13	-1.33	0.54	2.86	5.28	7.44
Unclustered energy -1σ (%)	1.22	0.48	-0.43	-1.24	-1.75	-1.94
Unclustered energy $+1\sigma$ (%)	-1.13	-0.55	0.40	1.22	1.93	2.65
$p_T(t, \bar{t})$ reweighting (%)	0.86	0.69	0.74	0.79	2.55	7.89
Total (%)	8.82	4.05	3.57	9.19	14.21	21.14

Table B.29: Systematic uncertainties for the normalised $t\bar{t}$ cross section measurement with respect to H_T variable at a centre-of-mass energy of 8 TeV (combination of electron and muon channels).

Uncertainty source	120–185 GeV	185–215 GeV	215–247 GeV	247–283 GeV	283–323 GeV	323–365 GeV	365–409 GeV	409–458 GeV	458–512 GeV	512–570 GeV	570–629 GeV	629–691 GeV	691–769 GeV	≥ 769 GeV
b tagging efficiency -1σ (%)	0.02	0.01	0.01	0.00	-0.00	-0.01	-0.03	-0.03	-0.03	-0.02	-0.01	0.01	0.02	0.03
b tagging efficiency $+1\sigma$ (%)	-0.03	-0.02	-0.01	-0.00	0.01	0.03	0.04	0.04	0.03	0.02	0.00	-0.02	-0.04	-0.06
Electron efficiency -1σ (%)	-0.00	-0.00	-0.00	-0.00	-0.00	-0.00	0.00	0.01	0.01	0.01	0.01	0.02	0.02	0.02
Electron efficiency $+1\sigma$ (%)	-0.07	-0.07	-0.07	-0.06	-0.02	0.04	0.10	0.15	0.19	0.21	0.23	0.24	0.24	0.24
Jet energy resolution -1σ (%)	-0.25	-0.26	-0.26	-0.24	-0.07	0.14	0.34	0.51	0.64	0.77	0.90	1.03	1.14	1.23
Jet energy resolution $+1\sigma$ (%)	0.01	0.00	-0.01	0.01	0.07	0.11	0.08	0.00	-0.09	-0.18	-0.28	-0.39	-0.48	-0.54
Jet energy scale -1σ (%)	-1.44	-1.26	-0.89	-0.39	0.22	0.85	1.43	1.92	2.32	2.51	2.55	2.46	2.33	2.23
Jet energy scale $+1\sigma$ (%)	-0.16	-0.12	-0.03	0.08	0.27	0.39	0.36	0.18	-0.09	-0.44	-0.84	-1.27	-1.63	-1.89
Muon efficiency -1σ (%)	-0.01	-0.01	-0.01	-0.01	-0.00	0.01	0.01	0.02	0.03	0.03	0.04	0.05	0.05	0.06
Muon efficiency $+1\sigma$ (%)	0.01	0.01	0.01	0.01	0.00	-0.01	-0.01	-0.02	-0.02	-0.03	-0.03	-0.04	-0.05	-0.05
PDF uncertainty -1σ (%)	0.44	0.39	0.32	0.28	0.24	0.18	0.34	0.56	0.80	1.25	1.54	1.88	2.04	0.90
PDF uncertainty $+1\sigma$ (%)	0.44	0.39	0.32	0.28	0.24	0.18	0.34	0.56	0.80	1.25	1.54	1.88	2.04	0.90
Pile-up -1σ (%)	-0.16	-0.19	-0.23	-0.25	-0.14	0.05	0.28	0.50	0.67	0.80	0.89	0.95	0.99	1.01
Pile-up $+1\sigma$ (%)	-0.05	-0.03	0.01	0.04	0.06	0.05	0.02	-0.02	-0.07	-0.10	-0.12	-0.13	-0.14	-0.13
QCD cross section $+1\sigma$ (%)	-0.00	-0.00	0.00	0.00	0.00	-0.00	-0.00	-0.00	-0.00	-0.00	-0.00	-0.00	-0.00	-0.00
QCD cross section -1σ (%)	-0.00	-0.00	-0.00	0.00	0.00	0.00	0.00	0.00	0.00	0.00	-0.00	-0.00	-0.00	-0.00
QCD shape uncertainty (%)	-0.30	-0.25	-0.16	-0.03	0.12	0.24	0.31	0.34	0.33	0.30	0.24	0.18	0.12	0.08
Single top cross section $+1\sigma$ (%)	-0.00	-0.00	-0.00	-0.00	-0.00	0.00	0.00	0.00	0.00	0.00	0.01	0.01	0.01	0.01
Single top cross section -1σ (%)	-0.00	-0.00	-0.00	-0.00	-0.00	0.00	0.00	0.00	0.00	0.00	0.00	0.00	0.00	0.00
$t\bar{t}$ cross section $+1\sigma$ (%)	-0.00	-0.00	-0.00	-0.00	0.00	0.00	0.00	0.00	0.00	0.00	-0.00	-0.00	-0.00	-0.00
$t\bar{t}$ cross section -1σ (%)	0.00	0.00	0.00	-0.00	-0.00	-0.00	-0.00	-0.00	0.00	0.00	0.00	0.00	0.00	0.01
Top mass down (%)	1.77	0.19	-0.43	-0.62	-0.43	-0.42	-0.30	0.10	0.09	0.28	0.13	0.53	-0.23	-2.44
Top mass up (%)	-2.31	-0.86	0.63	0.67	1.08	0.59	0.38	1.12	0.91	0.95	0.15	0.97	-1.20	-7.22
Matching down (%)	3.57	2.12	1.35	-0.21	-1.28	-1.77	-2.77	-3.35	-2.60	-1.40	-3.25	-2.09	-4.27	-2.79
Matching up (%)	-1.44	-1.23	0.03	0.29	0.99	0.68	0.49	0.44	1.02	0.71	0.15	1.82	-0.24	0.33
Q^2 down (%)	-8.03	-4.88	-1.11	1.79	4.07	4.25	4.15	4.75	4.11	3.18	1.90	1.46	0.11	-1.91
Q^2 up (%)	4.85	2.57	0.87	-0.84	-1.74	-2.27	-2.39	-3.21	-2.55	-3.36	-4.11	-0.72	-1.09	-1.72
V+jets cross section $+1\sigma$ (%)	-0.00	-0.00	0.00	0.00	0.00	0.00	-0.00	-0.00	-0.00	-0.00	-0.00	-0.00	0.00	0.00
V+jets cross section -1σ (%)	-0.00	-0.00	-0.00	-0.00	-0.00	-0.00	0.00	0.00	0.00	0.01	0.01	0.01	0.01	0.02
V+jets (matching down) (%)	-1.15	-1.05	-0.83	-0.50	0.01	0.62	1.24	1.79	2.23	2.51	2.64	2.67	2.64	2.61
V+jets (matching up) (%)	-0.44	-0.40	-0.33	-0.20	0.08	0.41	0.69	0.81	0.78	0.64	0.45	0.26	0.11	0.01
V+jets (Q^2 down) (%)	-0.73	-0.68	-0.58	-0.41	-0.07	0.39	0.86	1.25	1.55	1.76	1.88	1.95	1.99	2.00
V+jets (Q^2 up) (%)	-1.02	-0.95	-0.77	-0.50	-0.04	0.52	1.11	1.65	2.10	2.43	2.60	2.64	2.62	2.59
Hadronisation uncertainty (%)	1.13	2.96	3.29	2.32	0.27	1.74	3.66	5.46	6.60	7.17	7.54	7.48	7.96	9.89
Luminosity $+1\sigma$ (%)	0.00	0.00	-0.00	-0.00	-0.00	-0.00	-0.00	-0.00	0.00	0.00	0.00	0.00	0.01	0.01
Luminosity -1σ (%)	-0.00	-0.00	-0.00	-0.00	-0.00	-0.00	0.00	0.00	0.00	0.00	0.00	0.00	0.00	0.00
$p_T(t, \bar{t})$ reweighting (%)	0.51	0.29	0.55	0.57	0.37	0.06	0.46	1.00	1.36	1.65	1.68	1.76	1.03	3.59
Total (%)	10.14	6.33	4.20	3.34	4.43	4.94	6.19	8.27	9.18	9.72	10.79	9.96	10.77	12.87

Table B.30: Systematic uncertainties for the normalised $t\bar{t}$ cross section measurement with respect to S_T variable at a centre-of-mass energy of 8 TeV (combination of electron and muon channels).

Uncertainty source	146–277 GeV	277–319 GeV	319–361 GeV	361–408 GeV	408–459 GeV	459–514 GeV	514–573 GeV	573–637 GeV	637–705 GeV	705–774 GeV	774–854 GeV	854–940 GeV	≥ 940 GeV
b tagging efficiency -1σ (%)	0.07	0.07	0.06	0.02	-0.03	-0.07	-0.10	-0.13	-0.16	-0.18	-0.20	-0.23	-0.25
b tagging efficiency $+1\sigma$ (%)	-0.04	-0.05	-0.04	-0.02	0.01	0.04	0.07	0.10	0.12	0.13	0.15	0.16	0.18
Electron efficiency -1σ (%)	0.02	0.02	0.00	-0.02	-0.02	-0.02	-0.01	0.00	0.01	0.01	0.01	0.01	0.01
Electron efficiency $+1\sigma$ (%)	-0.01	-0.00	0.01	0.02	0.02	0.00	-0.02	-0.03	-0.04	-0.04	-0.04	-0.04	-0.04
Jet energy resolution -1σ (%)	0.67	0.52	0.26	0.01	-0.28	-0.60	-0.85	-1.00	-1.02	-0.79	-0.38	0.15	0.59
Jet energy resolution $+1\sigma$ (%)	-0.21	-0.10	0.07	0.09	-0.01	-0.08	0.01	0.23	0.44	0.45	0.29	0.00	-0.26
Jet energy scale -1σ (%)	-0.91	-0.91	-0.85	-0.47	0.23	0.80	1.38	2.07	2.58	3.02	3.15	3.02	3.01
Jet energy scale $+1\sigma$ (%)	0.56	0.38	0.14	-0.02	-0.17	-0.39	-0.49	-0.43	-0.42	-0.58	-0.82	-1.21	-1.59
Muon efficiency -1σ (%)	0.01	0.01	0.00	-0.01	-0.01	-0.01	-0.01	-0.00	0.01	0.03	0.05	0.06	0.08
Muon efficiency $+1\sigma$ (%)	-0.01	-0.00	-0.00	0.01	0.01	0.01	0.01	-0.00	-0.01	-0.03	-0.04	-0.05	-0.07
PDF uncertainty -1σ (%)	0.48	0.45	0.33	0.18	0.16	0.35	0.52	0.69	0.91	1.26	1.78	2.30	1.63
PDF uncertainty $+1\sigma$ (%)	0.48	0.45	0.33	0.18	0.16	0.35	0.52	0.69	0.91	1.26	1.78	2.30	1.63
Pile-up -1σ (%)	0.19	0.10	-0.04	-0.14	-0.14	-0.06	0.02	0.08	0.13	0.06	-0.03	-0.05	-0.01
Pile-up $+1\sigma$ (%)	-0.21	-0.12	0.01	0.13	0.16	0.10	0.02	-0.04	-0.07	-0.01	0.08	0.10	0.05
QCD cross section $+1\sigma$ (%)	0.01	0.01	0.01	-0.00	-0.01	-0.01	-0.01	-0.01	-0.01	-0.01	-0.01	-0.01	-0.02
QCD cross section -1σ (%)	0.01	0.01	0.01	-0.00	-0.01	-0.01	-0.01	-0.01	-0.01	-0.01	-0.01	-0.01	-0.01
QCD shape uncertainty (%)	0.22	0.17	0.03	-0.13	-0.14	-0.08	-0.02	0.01	-0.04	-0.18	-0.35	-0.53	-0.65
Single top cross section $+1\sigma$ (%)	0.00	0.00	0.00	-0.00	-0.00	-0.00	-0.00	-0.00	-0.00	-0.00	-0.00	-0.00	-0.01
Single top cross section -1σ (%)	0.01	0.01	0.01	-0.00	-0.01	-0.01	-0.01	-0.01	-0.01	-0.01	-0.01	-0.01	-0.01
$t\bar{t}$ cross section $+1\sigma$ (%)	0.01	0.01	0.01	-0.00	-0.01	-0.01	-0.01	-0.01	-0.01	-0.01	-0.01	-0.01	-0.01
$t\bar{t}$ cross section -1σ (%)	0.01	0.01	0.01	-0.00	-0.01	-0.01	-0.01	-0.01	-0.01	-0.01	-0.01	-0.01	-0.01
Top mass down (%)	1.16	-0.36	-0.57	-0.25	0.10	-0.10	0.06	-0.10	0.03	0.25	0.36	0.98	-0.29
Top mass up (%)	-1.24	0.42	1.19	0.72	0.15	-0.72	-0.52	-1.13	-0.59	-1.08	-0.55	1.87	-2.84
Matching down (%)	2.65	1.73	0.72	-0.11	-1.26	-1.92	-2.13	-2.45	-1.81	-1.99	-4.58	-3.05	-3.50
Matching up (%)	-1.70	-0.94	0.44	0.90	0.84	0.21	0.08	-0.35	0.56	0.21	1.10	2.64	2.22
Q^2 down (%)	-4.81	-1.10	1.28	2.06	2.11	0.85	1.36	-0.04	0.40	-1.64	-1.03	-0.82	-2.31
Q^2 up (%)	3.15	0.90	-0.14	-0.70	-0.85	-1.61	-0.82	-2.11	-1.55	-0.80	-2.32	-0.56	0.45
V+jets cross section $+1\sigma$ (%)	0.01	0.01	0.01	-0.00	-0.01	-0.01	-0.01	-0.01	-0.01	-0.01	-0.01	-0.01	-0.01
V+jets cross section -1σ (%)	0.01	0.01	0.01	-0.00	-0.01	-0.01	-0.01	-0.01	-0.01	-0.01	-0.01	-0.01	-0.01
V+jets (matching down) (%)	-0.78	-0.83	-0.84	-0.52	0.23	1.09	1.69	1.98	2.04	1.99	1.88	1.79	1.73
V+jets (matching up) (%)	-0.88	-0.86	-0.74	-0.25	0.62	1.37	1.66	1.57	1.24	0.82	0.41	0.09	-0.12
V+jets (Q^2 down) (%)	-0.90	-0.91	-0.84	-0.44	0.37	1.22	1.76	1.95	1.91	1.79	1.63	1.53	1.54
V+jets (Q^2 up) (%)	-0.85	-0.88	-0.84	-0.47	0.27	1.06	1.58	1.86	2.01	2.14	2.30	2.49	2.66
Hadronisation uncertainty (%)	5.03	5.37	3.73	0.73	2.38	5.73	8.74	9.40	10.10	10.95	8.49	7.15	8.22
Luminosity $+1\sigma$ (%)	0.01	0.01	0.01	-0.00	-0.01	-0.01	-0.01	-0.01	-0.01	-0.01	-0.01	-0.01	-0.02
Luminosity -1σ (%)	0.01	0.01	0.01	-0.00	-0.01	-0.01	-0.01	-0.01	-0.01	-0.01	-0.01	-0.01	-0.01
Electron energy -1σ (%)	0.16	0.10	-0.00	-0.08	-0.12	-0.12	-0.06	0.02	0.07	0.06	0.01	-0.08	-0.15
Electron energy $+1\sigma$ (%)	0.00	0.03	0.06	0.04	-0.02	-0.05	-0.03	-0.03	-0.07	-0.12	-0.15	-0.16	-0.16
Muon energy -1σ (%)	0.09	0.06	0.00	-0.05	-0.06	-0.06	-0.04	-0.01	0.00	-0.01	-0.01	0.01	0.03
Muon energy $+1\sigma$ (%)	0.05	0.05	0.03	0.00	-0.03	-0.05	-0.07	-0.07	-0.06	-0.04	-0.05	-0.08	-0.11
Tau energy -1σ (%)	0.94	0.74	0.39	-0.04	-0.42	-0.72	-0.91	-1.05	-1.18	-1.28	-1.29	-1.29	-1.23
Tau energy $+1\sigma$ (%)	-0.62	-0.51	-0.29	-0.05	0.18	0.42	0.64	0.84	1.01	1.14	1.33	1.49	1.53
Unclustered energy -1σ (%)	0.34	0.32	0.25	0.07	-0.18	-0.38	-0.48	-0.52	-0.56	-0.60	-0.60	-0.58	-0.58
Unclustered energy $+1\sigma$ (%)	0.13	0.04	-0.09	-0.18	-0.16	-0.07	0.05	0.19	0.31	0.42	0.54	0.57	0.55
$p_T(t, \bar{t})$ reweighting (%)	0.53	0.43	0.49	0.22	0.08	0.30	0.46	0.62	0.68	0.81	1.10	1.14	4.18
Total (%)	8.48	6.33	4.79	2.83	3.58	6.90	9.88	10.99	11.52	12.47	11.42	10.30	11.61

B. $t\bar{t}$ differential cross section

Table B.31: Systematic uncertainties for the normalised $t\bar{t}$ cross section measurement with respect to p_T^W variable at a centre-of-mass energy of 8 TeV (combination of electron and muon channels).

Uncertainty source	0--27 GeV	27--52 GeV	52--78 GeV	78--105 GeV	105--134 GeV	134--166 GeV	166--200 GeV	200--237 GeV	≥ 237 GeV
b tagging efficiency -1σ (%)	0.08	0.06	0.03	-0.01	-0.05	-0.11	-0.17	-0.24	-0.30
b tagging efficiency $+1\sigma$ (%)	-0.11	-0.09	-0.04	0.02	0.08	0.14	0.20	0.24	0.27
Electron efficiency -1σ (%)	0.01	0.00	-0.01	-0.01	-0.00	0.01	0.02	0.02	0.02
Electron efficiency $+1\sigma$ (%)	-0.86	-0.62	-0.13	0.39	0.69	0.75	0.67	0.51	0.34
Jet energy resolution -1σ (%)	0.40	0.24	-0.01	-0.19	-0.23	-0.19	-0.16	-0.18	-0.25
Jet energy resolution $+1\sigma$ (%)	-0.29	-0.17	-0.00	0.11	0.21	0.27	0.17	-0.06	-0.32
Jet energy scale -1σ (%)	-0.27	-0.32	-0.34	-0.22	0.13	0.79	1.73	2.61	3.18
Jet energy scale $+1\sigma$ (%)	-0.49	-0.33	-0.02	0.29	0.45	0.33	0.04	-0.26	-0.46
Muon efficiency -1σ (%)	-0.02	-0.01	-0.01	-0.00	0.01	0.03	0.05	0.08	0.10
Muon efficiency $+1\sigma$ (%)	0.02	0.02	0.01	0.00	-0.01	-0.03	-0.06	-0.09	-0.12
PDF uncertainty -1σ (%)	0.50	0.25	0.22	0.10	0.30	0.48	0.78	1.07	0.69
PDF uncertainty $+1\sigma$ (%)	0.50	0.25	0.22	0.10	0.30	0.48	0.78	1.07	0.69
Pile-up -1σ (%)	-0.81	-0.58	-0.13	0.34	0.64	0.76	0.73	0.58	0.39
Pile-up $+1\sigma$ (%)	0.18	0.10	0.01	-0.04	-0.06	-0.10	-0.21	-0.34	-0.46
QCD cross section $+1\sigma$ (%)	0.00	0.00	-0.00	-0.00	-0.00	-0.00	0.00	0.00	0.00
QCD cross section -1σ (%)	0.00	0.00	0.00	0.00	-0.00	-0.00	-0.00	-0.00	-0.00
QCD shape uncertainty (%)	-0.15	-0.11	-0.03	0.04	0.12	0.17	0.18	0.17	0.15
Single top cross section $+1\sigma$ (%)	0.00	0.00	0.00	-0.00	-0.00	-0.00	-0.00	-0.00	-0.00
Single top cross section -1σ (%)	0.00	0.00	0.00	0.00	-0.00	-0.00	-0.00	-0.01	-0.00
$t\bar{t}$ cross section $+1\sigma$ (%)	-0.00	-0.00	-0.00	0.00	0.00	0.01	0.00	-0.00	-0.01
$t\bar{t}$ cross section -1σ (%)	0.00	0.00	0.00	-0.00	-0.00	-0.00	-0.00	-0.00	-0.00
Top mass down (%)	0.03	-0.06	-0.09	0.02	-0.01	0.10	0.39	0.29	0.32
Top mass up (%)	-0.76	-0.47	0.03	0.41	-0.15	0.54	1.14	0.92	1.05
Matching down (%)	-0.13	0.18	0.04	0.40	-0.27	-0.77	0.01	-0.38	-1.15
Matching up (%)	-0.33	-0.70	-0.64	0.64	0.61	0.47	1.87	0.96	1.83
Q^2 down (%)	3.11	2.81	0.99	-0.36	-2.53	-4.09	-6.03	-8.38	-9.23
Q^2 up (%)	-0.24	-0.01	-0.00	0.41	-0.35	-0.57	0.08	0.54	1.39
V+jets cross section $+1\sigma$ (%)	0.00	0.00	0.00	0.00	-0.00	-0.01	-0.01	-0.01	-0.01
V+jets cross section -1σ (%)	0.00	0.00	0.00	-0.00	-0.00	-0.00	-0.00	-0.00	-0.00
V+jets (matching down) (%)	-0.24	-0.36	-0.32	0.07	0.61	0.89	0.75	0.30	-0.22
V+jets (matching up) (%)	-0.25	-0.29	-0.20	0.13	0.55	0.69	0.36	-0.28	-0.94
V+jets (Q^2 down) (%)	-0.33	-0.40	-0.32	0.08	0.62	0.94	0.84	0.45	0.01
V+jets (Q^2 up) (%)	-0.10	-0.27	-0.34	-0.02	0.49	0.81	0.76	0.47	0.14
Hadronisation uncertainty (%)	2.30	2.79	1.98	0.75	3.06	4.92	5.97	7.85	10.28
Luminosity $+1\sigma$ (%)	-0.00	-0.00	-0.00	0.00	0.00	0.00	0.00	-0.00	-0.01
Luminosity -1σ (%)	0.00	0.00	0.00	-0.00	-0.00	-0.00	-0.01	-0.01	-0.01
Electron energy -1σ (%)	-0.71	-0.52	-0.15	0.26	0.59	0.75	0.74	0.65	0.56
Electron energy $+1\sigma$ (%)	0.36	0.26	0.10	-0.08	-0.26	-0.42	-0.53	-0.63	-0.71
Muon energy -1σ (%)	0.02	0.02	0.01	-0.01	0.00	0.01	-0.05	-0.15	-0.25
Muon energy $+1\sigma$ (%)	0.18	0.14	0.04	-0.05	-0.11	-0.16	-0.25	-0.39	-0.54
Tau energy -1σ (%)	2.06	1.59	0.74	-0.28	-1.39	-2.63	-3.95	-5.19	-6.19
Tau energy $+1\sigma$ (%)	-1.12	-0.99	-0.70	-0.11	0.81	1.99	3.27	4.55	5.64
Unclustered energy -1σ (%)	1.05	0.79	0.32	-0.24	-0.78	-1.27	-1.67	-1.93	-2.05
Unclustered energy $+1\sigma$ (%)	-0.55	-0.44	-0.25	0.07	0.48	0.86	1.09	1.19	1.23
$p_T(t, \bar{t})$ reweighting (%)	0.51	0.34	0.65	0.11	0.40	0.45	0.26	0.35	6.93
Total (%)	4.89	4.58	2.63	1.59	4.69	7.56	10.06	13.27	17.31

Table B.32: Systematic uncertainties for the normalised $t\bar{t}$ cross section measurement with respect to M_T^W variable at a centre-of-mass energy of 8 TeV (combination of electron and muon channels).

Uncertainty source	0–23 GeV	23–58 GeV	≥ 58 GeV
b tagging efficiency -1σ (%)	-0.04	-0.01	0.01
b tagging efficiency $+1\sigma$ (%)	-0.01	-0.01	0.01
Electron efficiency -1σ (%)	0.03	0.01	-0.01
Electron efficiency $+1\sigma$ (%)	0.19	0.07	-0.07
Jet energy resolution -1σ (%)	0.54	0.26	-0.23
Jet energy resolution $+1\sigma$ (%)	0.22	0.10	-0.09
Jet energy scale -1σ (%)	1.63	0.70	-0.65
Jet energy scale $+1\sigma$ (%)	0.03	0.01	-0.01
Muon efficiency -1σ (%)	0.02	0.01	-0.01
Muon efficiency $+1\sigma$ (%)	-0.02	-0.01	0.01
PDF uncertainty -1σ (%)	0.14	0.27	0.15
PDF uncertainty $+1\sigma$ (%)	0.14	0.27	0.15
Pile-up -1σ (%)	0.51	0.23	-0.21
Pile-up $+1\sigma$ (%)	0.08	0.04	-0.04
QCD cross section $+1\sigma$ (%)	-0.01	-0.00	0.00
QCD cross section -1σ (%)	-0.01	-0.00	0.00
QCD shape uncertainty (%)	-0.67	-0.28	0.26
Single top cross section $+1\sigma$ (%)	-0.00	-0.00	0.00
Single top cross section -1σ (%)	-0.00	-0.00	0.00
$t\bar{t}$ cross section $+1\sigma$ (%)	0.00	0.00	-0.00
$t\bar{t}$ cross section -1σ (%)	0.00	0.00	-0.00
Top mass down (%)	0.06	0.13	-0.07
Top mass up (%)	0.10	0.04	-0.04
Matching down (%)	-0.32	-0.01	0.06
Matching up (%)	1.11	0.29	-0.35
Q^2 down (%)	-1.56	-1.31	0.93
Q^2 up (%)	-0.57	-0.14	0.18
V+jets cross section $+1\sigma$ (%)	0.00	0.00	-0.00
V+jets cross section -1σ (%)	0.00	0.00	-0.00
V+jets (matching down) (%)	1.95	0.77	-0.74
V+jets (matching up) (%)	1.13	0.45	-0.43
V+jets (Q^2 down) (%)	1.36	0.53	-0.51
V+jets (Q^2 up) (%)	1.66	0.64	-0.62
Hadronisation uncertainty (%)	2.87	1.44	1.26
Luminosity $+1\sigma$ (%)	0.00	0.00	-0.00
Luminosity -1σ (%)	-0.00	-0.00	0.00
Electron energy -1σ (%)	0.70	0.31	-0.28
Electron energy $+1\sigma$ (%)	-0.42	-0.16	0.15
Muon energy -1σ (%)	0.18	0.09	-0.08
Muon energy $+1\sigma$ (%)	-0.14	-0.06	0.05
Tau energy -1σ (%)	-1.08	-0.41	0.40
Tau energy $+1\sigma$ (%)	0.85	0.38	-0.34
Unclustered energy -1σ (%)	-0.29	-0.06	0.09
Unclustered energy $+1\sigma$ (%)	1.17	0.50	-0.46
$p_T(t, \bar{t})$ reweighting (%)	187	1.20	0.73
Total (%)		5.52	2.79
			0.58
			2.31

B.8 Results

B.8.1 7 TeV

Table B.33: Normalised $t\bar{t}$ cross section measurement with respect to E_T^{miss} variable at a centre-of-mass energy of 7 TeV (combination of electron and muon channels). The errors shown are combined statistical, fit and unfolding errors (\dagger) and systematic uncertainty (*).

E_T^{miss} bin [GeV]	$\sigma_{\text{meas}} (\times 10^3)$
0--27 GeV	$6.68 \pm 0.10^\dagger \pm 0.27^* (4.26\%)$
27--52 GeV	$13.41 \pm 0.15^\dagger \pm 0.37^* (2.99\%)$
52--87 GeV	$8.64 \pm 0.10^\dagger \pm 0.17^* (2.23\%)$
87--130 GeV	$3.03 \pm 0.05^\dagger \pm 0.18^* (6.05\%)$
130--172 GeV	$0.84 \pm 0.02^\dagger \pm 0.09^* (11.01\%)$
≥ 172 GeV	$0.13 \pm 0.00^\dagger \pm 0.02^* (19.45\%)$

Table B.34: Normalised $t\bar{t}$ cross section measurement with respect to H_T variable at a centre-of-mass energy of 7 TeV (combination of electron and muon channels). The errors shown are combined statistical, fit and unfolding errors (\dagger) and systematic uncertainty (*).

H_T bin [GeV]	$\sigma_{\text{meas}} (\times 10^3)$
120--185 GeV	$2.52 \pm 0.07^\dagger \pm 0.24^* (10.03\%)$
185--215 GeV	$4.94 \pm 0.13^\dagger \pm 0.32^* (7.08\%)$
215--247 GeV	$4.98 \pm 0.12^\dagger \pm 0.20^* (4.65\%)$
247--283 GeV	$4.04 \pm 0.09^\dagger \pm 0.15^* (4.40\%)$
283--323 GeV	$2.96 \pm 0.06^\dagger \pm 0.14^* (5.10\%)$
323--365 GeV	$2.02 \pm 0.04^\dagger \pm 0.14^* (7.27\%)$
365--409 GeV	$1.34 \pm 0.03^\dagger \pm 0.11^* (8.76\%)$
409--458 GeV	$0.86 \pm 0.02^\dagger \pm 0.09^* (10.13\%)$
458--512 GeV	$0.54 \pm 0.01^\dagger \pm 0.06^* (10.60\%)$
512--570 GeV	$0.33 \pm 0.01^\dagger \pm 0.03^* (10.87\%)$
570--629 GeV	$0.20 \pm 0.01^\dagger \pm 0.02^* (10.69\%)$
629--691 GeV	$0.12 \pm 0.00^\dagger \pm 0.01^* (10.72\%)$
691--769 GeV	$0.07 \pm 0.00^\dagger \pm 0.01^* (11.54\%)$
≥ 769 GeV	$0.03 \pm 0.00^\dagger \pm 0.00^* (14.09\%)$

Table B.35: Normalised $t\bar{t}$ cross section measurement with respect to S_T variable at a centre-of-mass energy of 7 TeV (combination of electron and muon channels). The errors shown are combined statistical, fit and unfolding errors (\dagger) and systematic uncertainty (*).

S_T bin [GeV]	$\sigma_{meas} (\times 10^3)$
146--277 GeV	$1.28 \pm 0.03^\dagger \pm 0.15^* (12.27\%)$
277--319 GeV	$4.09 \pm 0.10^\dagger \pm 0.36^* (9.06\%)$
319--361 GeV	$4.08 \pm 0.09^\dagger \pm 0.18^* (4.95\%)$
361--408 GeV	$3.20 \pm 0.06^\dagger \pm 0.12^* (4.28\%)$
408--459 GeV	$2.22 \pm 0.04^\dagger \pm 0.15^* (7.02\%)$
459--514 GeV	$1.45 \pm 0.03^\dagger \pm 0.15^* (10.42\%)$
514--573 GeV	$0.91 \pm 0.02^\dagger \pm 0.12^* (13.26\%)$
573--637 GeV	$0.55 \pm 0.01^\dagger \pm 0.08^* (14.08\%)$
637--705 GeV	$0.33 \pm 0.01^\dagger \pm 0.05^* (14.81\%)$
705--774 GeV	$0.19 \pm 0.01^\dagger \pm 0.03^* (15.95\%)$
774--854 GeV	$0.11 \pm 0.00^\dagger \pm 0.02^* (14.13\%)$
854--940 GeV	$0.06 \pm 0.00^\dagger \pm 0.01^* (13.40\%)$
≥ 940 GeV	$0.03 \pm 0.00^\dagger \pm 0.00^* (15.43\%)$

Table B.36: Normalised $t\bar{t}$ cross section measurement with respect to p_T^W variable at a centre-of-mass energy of 7 TeV (combination of electron and muon channels). The errors shown are combined statistical, fit and unfolding errors (\dagger) and systematic uncertainty (*).

p_T^W bin [GeV]	$\sigma_{meas} (\times 10^3)$
0--27 GeV	$3.54 \pm 0.09^\dagger \pm 0.19^* (5.96\%)$
27--52 GeV	$8.54 \pm 0.17^\dagger \pm 0.37^* (4.79\%)$
52--78 GeV	$9.33 \pm 0.16^\dagger \pm 0.23^* (3.01\%)$
78--105 GeV	$7.12 \pm 0.13^\dagger \pm 0.13^* (2.60\%)$
105--134 GeV	$4.28 \pm 0.09^\dagger \pm 0.20^* (5.07\%)$
134--166 GeV	$2.17 \pm 0.05^\dagger \pm 0.15^* (7.51\%)$
166--200 GeV	$0.98 \pm 0.03^\dagger \pm 0.09^* (9.27\%)$
200--237 GeV	$0.42 \pm 0.02^\dagger \pm 0.05^* (11.86\%)$
≥ 237 GeV	$0.21 \pm 0.01^\dagger \pm 0.03^* (15.91\%)$

Table B.37: Normalised $t\bar{t}$ cross section measurement with respect to M_T^W variable at a centre-of-mass energy of 7 TeV (combination of electron and muon channels). The errors shown are combined statistical, fit and unfolding errors (\dagger) and systematic uncertainty (*).

M_T^W bin [GeV]	$\sigma_{meas} (\times 10^3)$
0--23 GeV	$4.98 \pm 0.16^\dagger \pm 0.25^* (5.93\%)$
23--58 GeV	$8.36 \pm 0.15^\dagger \pm 0.19^* (2.91\%)$
≥ 58 GeV	$14.11 \pm 0.14^\dagger \pm 0.28^* (2.23\%)$

B. $t\bar{t}$ differential cross section

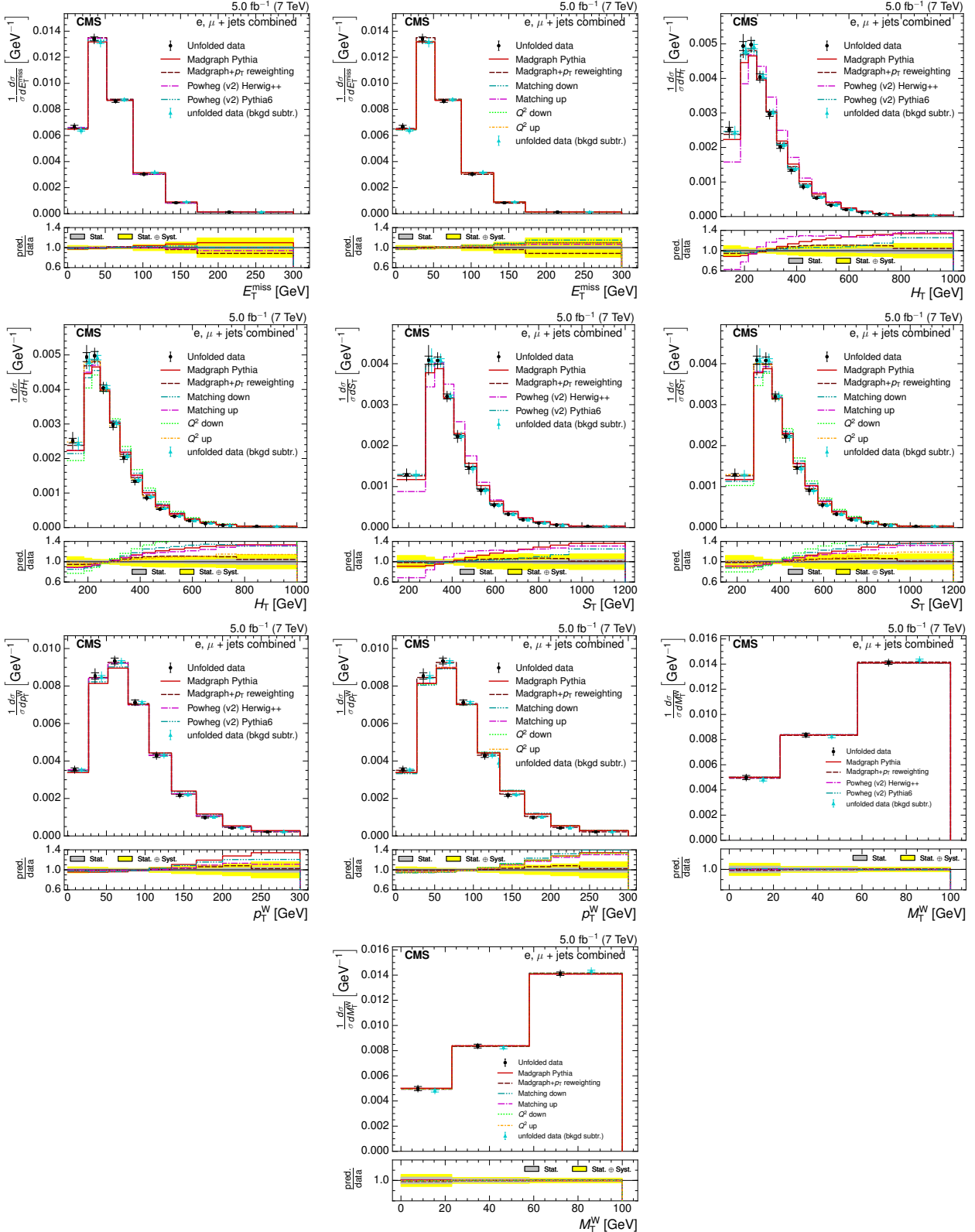


Figure B.9: Comparison of the measured normalised differential cross section, including from the background subtraction method, with respect to E_T^{miss} , H_T , S_T , p_T^W and M_T^W to different Monte Carlo generators: MADGRAPH, POWHEGv+,+HERWIG POWHEGva+PYTHIA and MADGRAPH corrected for top p_T mismodelling (left) and to different Monte Carlo predictions matching threshold up/down and factorisation scale up/down (right) in the combined electron+jets and muon+jets channel at $\sqrt{s} = 7$ TeV. The lower plots show the ratio of the predictions to the data.

B.8.2 8 TeV

Table B.38: Normalised $t\bar{t}$ cross section measurement with respect to E_T^{miss} variable at a centre-of-mass energy of 8 TeV (combination of electron and muon channels). The errors shown are combined statistical, fit and unfolding errors (\dagger) and systematic uncertainty (*).

E_T^{miss} bin [GeV]	$\sigma_{\text{meas}} (\times 10^3)$
0--27 GeV	$6.62 \pm 0.07^\dagger \pm 0.58^* (8.82\%)$
27--52 GeV	$13.47 \pm 0.09^\dagger \pm 0.54^* (4.05\%)$
52--87 GeV	$8.76 \pm 0.07^\dagger \pm 0.30^* (3.57\%)$
87--130 GeV	$3.00 \pm 0.03^\dagger \pm 0.27^* (9.19\%)$
130--172 GeV	$0.80 \pm 0.01^\dagger \pm 0.11^* (14.21\%)$
≥ 172 GeV	$0.12 \pm 0.00^\dagger \pm 0.02^* (21.14\%)$

Table B.39: Normalised $t\bar{t}$ cross section measurement with respect to H_T variable at a centre-of-mass energy of 8 TeV (combination of electron and muon channels). The errors shown are combined statistical, fit and unfolding errors (\dagger) and systematic uncertainty (*).

H_T bin [GeV]	$\sigma_{\text{meas}} (\times 10^3)$
120--185 GeV	$2.15 \pm 0.02^\dagger \pm 0.22^* (10.14\%)$
185--215 GeV	$4.35 \pm 0.04^\dagger \pm 0.27^* (6.33\%)$
215--247 GeV	$4.58 \pm 0.04^\dagger \pm 0.19^* (4.20\%)$
247--283 GeV	$3.98 \pm 0.03^\dagger \pm 0.13^* (3.34\%)$
283--323 GeV	$3.08 \pm 0.02^\dagger \pm 0.13^* (4.43\%)$
323--365 GeV	$2.23 \pm 0.02^\dagger \pm 0.11^* (4.94\%)$
365--409 GeV	$1.55 \pm 0.01^\dagger \pm 0.10^* (6.19\%)$
409--458 GeV	$1.03 \pm 0.01^\dagger \pm 0.09^* (8.27\%)$
458--512 GeV	$0.66 \pm 0.01^\dagger \pm 0.06^* (9.18\%)$
512--570 GeV	$0.41 \pm 0.00^\dagger \pm 0.04^* (9.72\%)$
570--629 GeV	$0.26 \pm 0.00^\dagger \pm 0.03^* (10.79\%)$
629--691 GeV	$0.16 \pm 0.00^\dagger \pm 0.02^* (9.96\%)$
691--769 GeV	$0.10 \pm 0.00^\dagger \pm 0.01^* (10.77\%)$
≥ 769 GeV	$0.05 \pm 0.00^\dagger \pm 0.01^* (12.87\%)$

B. $t\bar{t}$ differential cross section

Table B.40: Normalised $t\bar{t}$ cross section measurement with respect to S_T variable at a centre-of-mass energy of 8 TeV (combination of electron and muon channels). The errors shown are combined statistical, fit and unfolding errors (\dagger) and systematic uncertainty (*).

S_T bin [GeV]	$\sigma_{meas} (\times 10^3)$
146--277 GeV	$1.12 \pm 0.02^\dagger \pm 0.09^* \text{ (8.48\%)}$
277--319 GeV	$3.64 \pm 0.05^\dagger \pm 0.22^* \text{ (6.33\%)}$
319--361 GeV	$3.83 \pm 0.04^\dagger \pm 0.18^* \text{ (4.79\%)}$
361--408 GeV	$3.22 \pm 0.03^\dagger \pm 0.09^* \text{ (2.83\%)}$
408--459 GeV	$2.38 \pm 0.02^\dagger \pm 0.08^* \text{ (3.58\%)}$
459--514 GeV	$1.64 \pm 0.02^\dagger \pm 0.11^* \text{ (6.90\%)}$
514--573 GeV	$1.05 \pm 0.01^\dagger \pm 0.10^* \text{ (9.88\%)}$
573--637 GeV	$0.66 \pm 0.01^\dagger \pm 0.07^* \text{ (10.99\%)}$
637--705 GeV	$0.40 \pm 0.00^\dagger \pm 0.05^* \text{ (11.52\%)}$
705--774 GeV	$0.24 \pm 0.00^\dagger \pm 0.03^* \text{ (12.47\%)}$
774--854 GeV	$0.14 \pm 0.00^\dagger \pm 0.02^* \text{ (11.42\%)}$
854--940 GeV	$0.08 \pm 0.00^\dagger \pm 0.01^* \text{ (10.30\%)}$
≥ 940 GeV	$0.04 \pm 0.00^\dagger \pm 0.00^* \text{ (11.61\%)}$

Table B.41: Normalised $t\bar{t}$ cross section measurement with respect to p_T^W variable at a centre-of-mass energy of 8 TeV (combination of electron and muon channels). The errors shown are combined statistical, fit and unfolding errors (\dagger) and systematic uncertainty (*).

p_T^W bin [GeV]	$\sigma_{meas} (\times 10^3)$
0--27 GeV	$3.64 \pm 0.03^\dagger \pm 0.17^* \text{ (4.89\%)}$
27--52 GeV	$8.59 \pm 0.06^\dagger \pm 0.39^* \text{ (4.58\%)}$
52--78 GeV	$9.22 \pm 0.06^\dagger \pm 0.24^* \text{ (2.63\%)}$
78--105 GeV	$6.98 \pm 0.05^\dagger \pm 0.10^* \text{ (1.59\%)}$
105--134 GeV	$4.24 \pm 0.04^\dagger \pm 0.20^* \text{ (4.69\%)}$
134--166 GeV	$2.18 \pm 0.02^\dagger \pm 0.16^* \text{ (7.56\%)}$
166--200 GeV	$1.01 \pm 0.01^\dagger \pm 0.10^* \text{ (10.06\%)}$
200--237 GeV	$0.45 \pm 0.01^\dagger \pm 0.06^* \text{ (13.27\%)}$
≥ 237 GeV	$0.24 \pm 0.00^\dagger \pm 0.04^* \text{ (17.31\%)}$

Table B.42: Normalised $t\bar{t}$ cross section measurement with respect to M_T^W variable at a centre-of-mass energy of 8 TeV (combination of electron and muon channels). The errors shown are combined statistical, fit and unfolding errors (\dagger) and systematic uncertainty (*).

M_T^W bin [GeV]	$\sigma_{meas} (\times 10^3)$
0--23 GeV	$4.88 \pm 0.07^\dagger \pm 0.26^* \text{ (5.52\%)}$
23--58 GeV	$8.30 \pm 0.06^\dagger \pm 0.22^* \text{ (2.79\%)}$
≥ 58 GeV	$14.22 \pm 0.06^\dagger \pm 0.32^* \text{ (2.31\%)}$

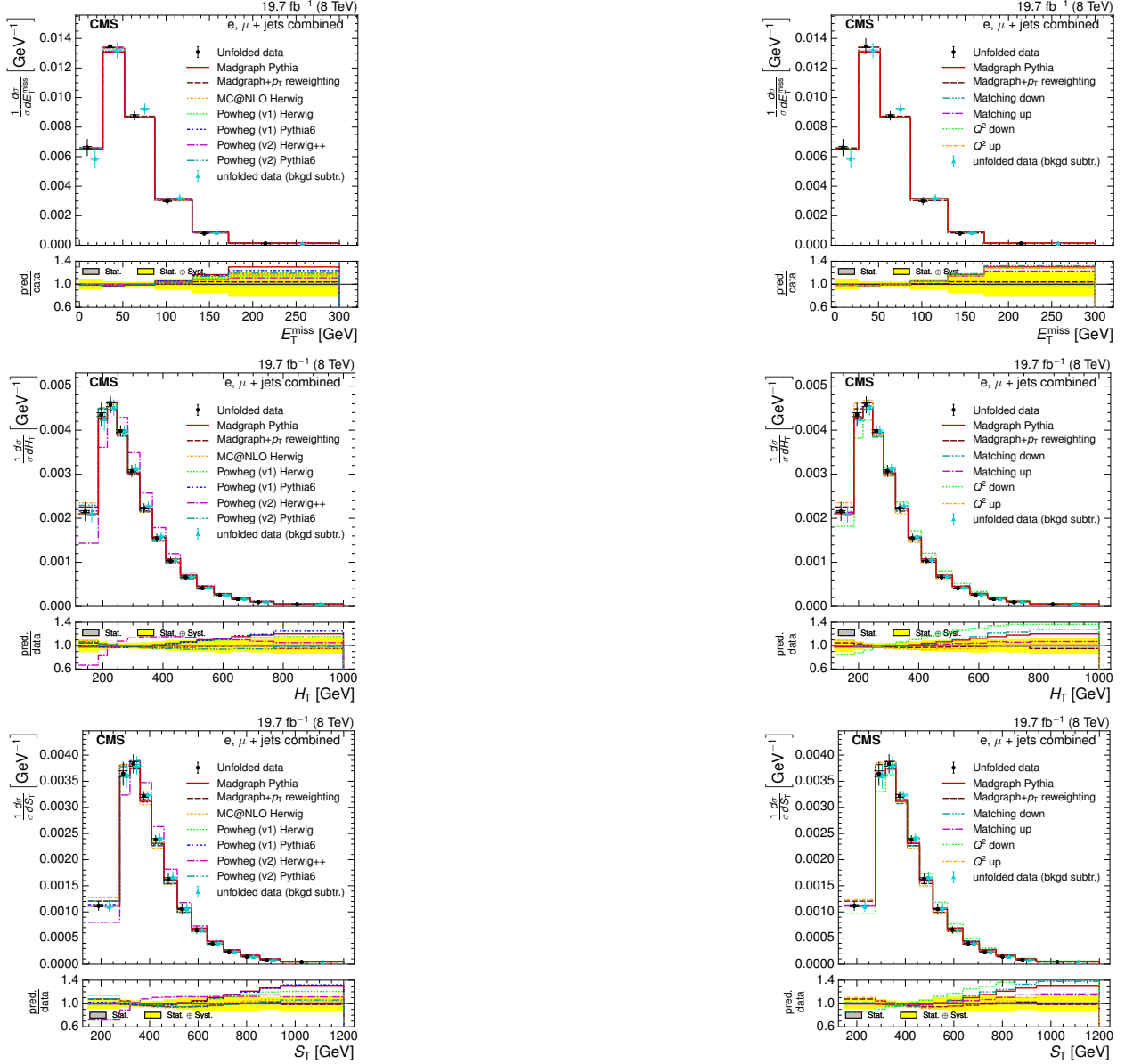


Figure B.10: Comparison of the measured normalised differential cross section, including from the background subtraction method, with respect to E_T^{miss} , H_T and S_T , to different Monte Carlo generators: MADGRAPH, POWHEGv_v+HERWIG POWHEGva+PYTHIA and MADGRAPH corrected for top p_T mismodelling (left) and to different Monte Carlo predictions matching threshold up/down and factorisation scale up/down (right) in the combined electron+jets and muon+jets channel at $\sqrt{s} = 8 \text{ TeV}$. The lower plots show the ratio of the predictions to the data.

B. $t\bar{t}$ differential cross section

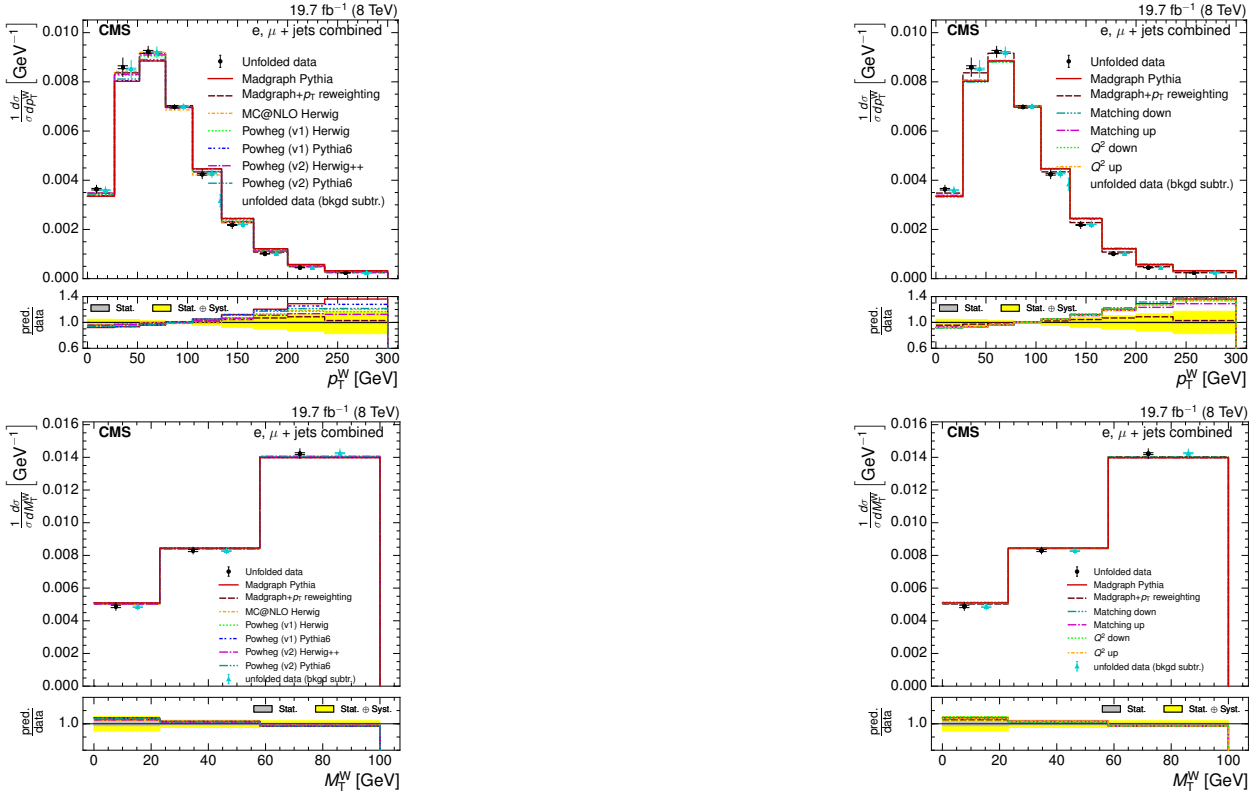


Figure B.11: Comparison of the measured normalised differential cross section, including from the background subtraction method, with respect to p_T^W and M_T^W , to different Monte Carlo generators: MADGRAPH, POWHEGV,+HERWIG POWHEGva+PYTHIA nd MADGRAPH corrected for top p_T mismodelling (left) and to different Monte Carlo predictions matching threshold up/down and factorisation scale up/down (right) in the combined electron+jets and muon+jets channel at $\sqrt{s} = 8$ TeV. The lower plots show the ratio of the predictions to the data.

References

- [1] Track impact parameter based b-tagging with CMS. Technical Report CMS-AN-2005-041, CERN, 2005. Geneva, Nov 2005.
- [2] Algorithms for b Jet identification in CMS. Technical Report CMS-PAS-BTV-09-001, CERN, 2009. Geneva, Jul 2009.
- [3] Particle-Flow Event Reconstruction in CMS and Performance for Jets, Taus, and MET. Technical Report CMS-PAS-PFT-09-001, CERN, 2009. Geneva, Apr 2009.
- [4] Electromagnetic calorimeter calibration with 7 TeV data. 2010.
- [5] Electron reconstruction and identification at $\sqrt{s} = 7$ TeV. Technical Report CMS-PAS-EGM-10-004, CERN, Geneva, 2010.
- [6] Tracking and Primary Vertex Results in First 7 TeV Collisions. Technical Report CMS-PAS-TRK-10-005, CERN, 2010. Geneva, 2010.
- [7] ATLAS tunes of PYTHIA 6 and Pythia 8 for MC11. Technical Report ATL-PHYS-PUB-2011-009, CERN, Geneva, Jul 2011.
- [8] Measurement of missing transverse energy in top pair events. Technical Report CMS-PAS-TOP-12-019, CERN, Geneva, 2012.
- [9] Measurement of differential top-quark pair production cross sections in the lepton+jets channel in pp collisions at 8 TeV. Technical Report CMS-PAS-TOP-12-027, CERN, Geneva, 2013.
- [10] Measurement of MET and other global distributions in top pair events. Technical Report CMS-PAS-TOP-12-042, CERN, Geneva, 2013.
- [11] Measurement of the differential ttbar cross section in the dilepton channel at 8 TeV. Technical Report CMS-PAS-TOP-12-028, CERN, Geneva, 2013.

- [12] Performance of b tagging at $\sqrt{s}=8$ TeV in multijet, ttbar and boosted topology events. Technical Report CMS-PAS-BTV-13-001, CERN, Geneva, 2013.
- [13] Measurement of Z production as a function of pT, Y. Technical Report CMS-PAS-SMP-13-013, CERN, Geneva, 2014.
- [14] Georges Aad et al. Observation of a new particle in the search for the Standard Model Higgs boson with the ATLAS detector at the LHC. *Phys. Lett.*, B716:1--29, 2012.
- [15] Georges Aad et al. Measurements of normalized differential cross sections for $t\bar{t}$ production in pp collisions at $\sqrt{s} = 7$ – 8 TeV using the ATLAS detector. *Phys. Rev.*, D90(7):072004, 2014.
- [16] Georges Aad et al. Combined Measurement of the Higgs Boson Mass in pp Collisions at $\sqrt{s} = 7$ and 8 TeV with the ATLAS and CMS Experiments. *Phys. Rev. Lett.*, 114:191803, 2015.
- [17] Georges Aad et al. Measurements of top-quark pair differential cross-sections in the lepton+jets channel in pp collisions at $\sqrt{s} = 8$ TeV using the ATLAS detector. 2015.
- [18] Roel Aaij et al. Observation of $J/\psi p$ resonances consistent with pentaquark states in $\Lambda_b^0 \rightarrow J/\psi K^- p$ decays. 2015.
- [19] S. Abachi et al. Observation of the top quark. *Phys.Rev.Lett.*, 74:2632--2637, 1995.
- [20] F. Abe et al. Observation of top quark production in $\bar{p}p$ collisions. *Phys.Rev.Lett.*, 74:2626--2631, 1995.
- [21] Wolfgang Adam, R FrÄijhwirth, Are Strandlie, and T Todor. Reconstruction of Electrons with the Gaussian-Sum Filter in the CMS Tracker at the LHC. Technical Report CMS-NOTE-2005-001, CERN, Geneva, Jan 2005.
- [22] P.A.R. Ade et al. Planck 2013 results. I. Overview of products and scientific results. *Astron.Astrophys.*, 571:A1, 2014.
- [23] Tim Adye. Unfolding algorithms and tests using RooUnfold. pages 313--318, 2011.

- [24] S. Agostinelli et al. GEANT4: A Simulation toolkit. *Nucl. Instrum. Meth.*, A506:250--303, 2003.
- [25] Sergey Alekhin et al. The PDF4LHC Working Group Interim Report. 2011.
- [26] Simone Alioli, Paolo Nason, Carlo Oleari, and Emanuele Re. A general framework for implementing NLO calculations in shower Monte Carlo programs: the POWHEG BOX. *JHEP*, 1006:043, 2010.
- [27] John Allison et al. Geant4 developments and applications. *IEEE Trans. Nucl. Sci.*, 53:270, 2006.
- [28] J. Alwall, R. Frederix, S. Frixione, V. Hirschi, F. Maltoni, et al. The automated computation of tree-level and next-to-leading order differential cross sections, and their matching to parton shower simulations. *JHEP*, 1407:079, 2014.
- [29] G. Antchev, P. Aspell, I. Atanassov, V. Avati, J. Baechler, et al. First measurement of the total proton-proton cross section at the LHC energy of $\sqrt{s} = 7$ TeV. *Europhys.Lett.*, 96:21002, 2011.
- [30] Roberta Arcidiacono, Angela Brett, Francesca Cavallari, André David, Nicholas Scott Eggert, Giovanni Franzoni, Matteo Marone, Pasquale Musella, Giovanni Organtini, Paolo Rumerio, Alessandro Thea, and Evgeni Vlassov. ECAL Front-End Monitoring in the CMS experiment. Technical Report CMS-CR-2009-181, CERN, Geneva, Jul 2009.
- [31] Nima Arkani-Hamed, Savas Dimopoulos, and G. R. Dvali. The Hierarchy problem and new dimensions at a millimeter. *Phys. Lett.*, B429:263--272, 1998.
- [32] W. A. Bardeen, C. T. Hill, and M. Lindner. Minimal dynamical symmetry breaking of the standard model. *Physical Review D*, 41:1647--1660, March 1990.
- [33] Michiel Botje, Jon Butterworth, Amanda Cooper-Sarkar, Albert de Roeck, Joel Feltesse, et al. The PDF4LHC Working Group Interim Recommendations. 2011.
- [34] G. Breit and E. Wigner. Capture of slow neutrons. *Phys. Rev.*, 49:519--531, Apr 1936.

- [35] Rene Brun and Fons Rademakers. ROOT -- An object oriented data analysis framework. *Nuclear Instruments and Methods in Physics Research Section A: Accelerators, Spectrometers, Detectors and Associated Equipment*, 389(1-2):81--86, 1997. New Computing Techniques in Physics Research V.
- [36] Erik Manuel Butz. Operation and Performance of the CMS Silicon Tracker. Technical Report CMS-CR-2012-357, CERN, Geneva, Nov 2012.
- [37] Matteo Cacciari, Gavin P. Salam, and Gregory Soyez. The Anti-k(t) jet clustering algorithm. *JHEP*, 0804:063, 2008.
- [38] John M. Campbell, Rikkert Frederix, Fabio Maltoni, and Francesco Tramontano. Next-to-Leading-Order Predictions for t-Channel Single-Top Production at Hadron Colliders. *Phys. Rev. Lett.*, 102:182003, 2009.
- [39] S. Chatrchyan et al. The CMS experiment at the CERN LHC. *JINST*, 3:S08004, 2008.
- [40] S Chatrchyan et al. Commissioning and Performance of the CMS Silicon Strip Tracker with Cosmic Ray Muons. *JINST*, 5:T03008, 2010.
- [41] Serguei Chatrchyan et al. Determination of Jet Energy Calibration and Transverse Momentum Resolution in CMS. *JINST*, 6:P11002, 2011.
- [42] Serguei Chatrchyan et al. Measurement of the Inclusive W and Z Production Cross Sections in pp Collisions at $\sqrt{s} = 7$ TeV. *JHEP*, 10:132, 2011.
- [43] Serguei Chatrchyan et al. Measurement of the Underlying Event Activity at the LHC with $\sqrt{s} = 7$ TeV and Comparison with $\sqrt{s} = 0.9$ TeV. *JHEP*, 09:109, 2011.
- [44] Serguei Chatrchyan et al. Measurement of the inclusive production cross sections for forward jets and for dijet events with one forward and one central jet in pp collisions at $\sqrt{s} = 7$ TeV. *JHEP*, 1206:036, 2012.
- [45] Serguei Chatrchyan et al. Observation of a new boson at a mass of 125 GeV with the CMS experiment at the LHC. *Phys. Lett.*, B716:30--61, 2012.

- [46] Serguei Chatrchyan et al. Performance of CMS muon reconstruction in pp collision events at $\sqrt{s} = 7$ TeV. *JINST*, 7:P10002, 2012.
- [47] Serguei Chatrchyan et al. Energy Calibration and Resolution of the CMS Electromagnetic Calorimeter in pp Collisions at $\sqrt{s} = 7$ TeV. *JINST*, 8:P09009, 2013.
- [48] Serguei Chatrchyan et al. Identification of b-quark jets with the CMS experiment. *JINST*, 8:P04013, 2013.
- [49] Serguei Chatrchyan et al. Measurement of differential top-quark pair production cross sections in pp collisions at $\sqrt{s} = 7$ TeV. *Eur.Phys.J.*, C73(3):2339, 2013.
- [50] Serguei Chatrchyan et al. Description and performance of track and primary-vertex reconstruction with the CMS tracker. *JINST*, 9(10):P10009, 2014.
- [51] Serguei Chatrchyan et al. Measurement of the $t\bar{t}$ production cross section in the dilepton channel in pp collisions at $\sqrt{s} = 8$ TeV. *JHEP*, 02:024, 2014. [Erratum: JHEP02,102(2014)].
- [52] J. H. Christenson, J. W. Cronin, V. L. Fitch, and R. Turlay. Evidence for the 2 pi Decay of the k(2)0 Meson. *Phys. Rev. Lett.*, 13:138--140, 1964.
- [53] Sergio Cittolin, Attila RÃ¡cz, and Paris Sphicas. *CMS The TriDAS Project: Technical Design Report, Volume 2: Data Acquisition and High-Level Trigger. CMS trigger and data-acquisition project*. Technical Design Report CMS. CERN, Geneva, 2002.
- [54] CMS Collaboration. Cms top physics results.
- [55] CMS Collaboration. Cmssw framework.
- [56] CMS Collaboration. Technical proposal for the upgrade of the CMS detector through 2020. Technical Report CERN-LHCC-2011-006. LHCC-P-004, CERN, Geneva, Jun 2011.
- [57] CMS Collaboration. Absolute Calibration of the Luminosity Measurement at CMS: Winter 2012 Update. 2012.

- [58] CMS Collaboration. CMS Luminosity Based on Pixel Cluster Counting - Summer 2013 Update. 2013.
- [59] CMS Collaboration. Jet transverse momentum resolution measurement using dijet events. *AN-13-416, work in progress*, 2013.
- [60] DØ Collaboration. B jet identification.
- [61] The ATLAS collaboration. Combination of ATLAS and CMS results on the mass of the top-quark using up to 4.9 fb^{-1} of $\sqrt{s} = 7 \text{ TeV}$ LHC data. 2013.
- [62] E P Corrin. *Development of Digital Readout Electronics for the CMS Tracker*. PhD thesis, Imperial College, London, 2002.
- [63] Michał Czakon, Paul Fiedler, and Alexander Mitov. Total Top-Quark Pair-Production Cross Section at Hadron Colliders Through $O(\alpha_S^4)$. *Phys. Rev. Lett.*, 110:252004, 2013.
- [64] D. Delikaris, J.P. Dauvergne, G. Passardi, J.C. Lottin, J.P. Lottin, et al. The Cryogenic system for the superconducting solenoid magnet of the CMS experiment. 1998.
- [65] P. A. M. Dirac. The quantum theory of the electron. *Proceedings of the Royal Society of London A: Mathematical, Physical and Engineering Sciences*, 117(778):610–624, 1928.
- [66] T.Speer et al. Algorithms for b jet identification in CMS. Technical Report CMS-AN-2009-085, CERN, 2009. Geneva, Aug 2009.
- [67] Cristina Ferro. B-tagging in CMS. *EPJ Web Conf.*, 28:12055, 2012.
- [68] Stefano Frixione, Paolo Nason, and Carlo Oleari. Matching NLO QCD computations with Parton Shower simulations: the POWHEG method. *JHEP*, 0711:070, 2007.
- [69] Stefano Frixione, Paolo Nason, and Bryan R. Webber. Matching NLO QCD and parton showers in heavy flavor production. *JHEP*, 08:007, 2003.

-
- [70] Stefano Frixione and Bryan R. Webber. Matching NLO QCD computations and parton shower simulations. *JHEP*, 06:029, 2002.
 - [71] R. Fröhwirth. Application of Kalman filtering to track and vertex fitting. *Nucl.Instrum.Meth.*, A262:444–450, 1987.
 - [72] Y. Fukuda et al. Evidence for oscillation of atmospheric neutrinos. *Phys. Rev. Lett.*, 81:1562–1567, 1998.
 - [73] J E Gaiser. *Charmonium Spectroscopy from Radiative Decays of the J/ψ and ψ'* . PhD thesis, Stanford Linear Accelerator Center (SLAC), Stanford, California, U.S.A., August 1982.
 - [74] V M Ghete and Cms Collaboration. The cms 11 trigger emulation software. *Journal of Physics: Conference Series*, 219(3):032009, 2010.
 - [75] Martyn Gigg and Peter Richardson. Herwig++. 2007.
 - [76] D. Griffiths. *Introduction to Elementary Particles*. John Wiley & Sons, New York, USA, 1987.
 - [77] TOPLHC Working Group. Toplhc wg summary plots.
 - [78] Peter W. Higgs. Broken Symmetries and the Masses of Gauge Bosons. *Phys. Rev. Lett.*, 13:508–509, 1964.
 - [79] C. T. Hill. Topcolor: top quark condensation in a gauge extension of the standard model. *Physics Letters B*, 266:419–424, August 1991.
 - [80] Stefan Höche, Frank Krauss, Nils Lavesson, Leif Lonnblad, Michelangelo Mangano, Andreas Schalicke, and Steffen Schumann. Matching parton showers and matrix elements. In *HERA and the LHC: A Workshop on the implications of HERA for LHC physics: Proceedings Part A*, 2006.
 - [81] Andreas Hocker and Vakhtang Kartvelishvili. SVD approach to data unfolding. *Nucl.Instrum.Meth.*, A372:469–481, 1996.

- [82] Takaaki Kajita. Atmospheric neutrino results from Super-Kamiokande and Kamiokande: Evidence for neutrino(mu) oscillations. *Nucl. Phys. Proc. Suppl.*, 77:123--132, 1999.
- [83] JÁnos Karancsi. Operational Experience with the CMS Pixel Detector. *JINST*, 10(05):C05016, 2015.
- [84] Vardan Khachatryan et al. Measurement of the differential cross section for top quark pair production in pp collisions at $\sqrt{s} = 8$ TeV. *Eur. Phys. J.*, C75(11):542, 2015.
- [85] Vardan Khachatryan et al. Measurement of the ttbar Production Cross Section in the All-Jets Final State in pp Collisions at $\sqrt{s}=8$ TeV. 2015.
- [86] Vardan Khachatryan et al. Measurement of transverse momentum relative to dijet systems in PbPb and pp collisions at $\sqrt{s_{NN}} = 2.76$ TeV. 2015.
- [87] Vardan Khachatryan et al. Performance of photon reconstruction and identification with the CMS detector in proton-proton collisions at $\sqrt{s} = 8$ TeV. 2015.
- [88] Vardan Khachatryan et al. Precise determination of the mass of the Higgs boson and tests of compatibility of its couplings with the standard model predictions using proton collisions at 7 and 8 TeV. *Eur. Phys. J.*, C75(5):212, 2015.
- [89] Min Suk Kim et al. CMS reconstruction improvement for the muon tracking by the RPC chambers. *PoS*, RPC2012:045, 2012.
- [90] Luke Kreczko, Jeson Jacob, Sergey Senkin, and EmryrClement. Analysissoftware: Analysissoftware version for top-12-042 paper, 2015.
- [91] Luke Kreczko, Sergey Senkin, Jeson Jacob, and EmryrClement. Dailypythonscripts: Dailypythonscript version for top-12-042 paper, 2015.
- [92] Luke Kreczko, Sergey Senkin, Jeson Jacob, and EmryrClement. Ntupleproduction: Ntupleproduction version for top-12-042 paper, 2015.
- [93] Hung-Liang Lai, Marco Guzzi, Joey Huston, Zhao Li, Pavel M. Nadolsky, Jon Pumplin, and C. P. Yuan. New parton distributions for collider physics. *Phys. Rev.*, D82:074024,

2010.

- [94] Christos Leonidopoulos and The CMS Collaboration. Cms tracking performance results from early lhc operation. *The European Physical Journal C - Particles and Fields*, C70:1165–1192, 2010.
- [95] Kirill Melnikov and Frank Petriello. Electroweak gauge boson production at hadron colliders through O(alpha(s)**2). *Phys. Rev.*, D74:114017, 2006.
- [96] Ian G. Moss. Higgs boson cosmology. 2015.
- [97] Pavel M. Nadolsky, Hung-Liang Lai, Qing-Hong Cao, Joey Huston, Jon Pumplin, Daniel Stump, Wu-Ki Tung, and C. P. Yuan. Implications of CTEQ global analysis for collider observables. *Phys. Rev.*, D78:013004, 2008.
- [98] Paolo Nason. A New method for combining NLO QCD with shower Monte Carlo algorithms. *JHEP*, 0411:040, 2004.
- [99] K.A. Olive et al. Review of Particle Physics. *Chin.Phys.*, C38:090001, 2014.
- [100] M Oreglia. *A Study of the Reactions $\psi' \rightarrow \gamma\gamma\psi$* . PhD thesis, Stanford Linear Accelerator Center (SLAC), Stanford, California, U.S.A., December 1980.
- [101] F M Palmonari. CMS Silicon Strip Tracker Commissioning and Preliminary Performances. *Nucl. Phys. B, Proc. Suppl.*, 197(1):121–124, 2009.
- [102] Ringaile Placakyte. Parton Distribution Functions. In *Proceedings, 31st International Conference on Physics in collisions (PIC 2011)*, 2011.
- [103] J. Pumplin, D. R. Stump, J. Huston, H. L. Lai, Pavel M. Nadolsky, and W. K. Tung. New generation of parton distributions with uncertainties from global QCD analysis. *JHEP*, 07:012, 2002.
- [104] William B. Rolnick. “*The Fundamental Particles and Their Interactions*”. Addison Wesley, 1993.

- [105] Tai Sakuma and Thomas McCauley. Detector and Event Visualization with SketchUp at the CMS Experiment. *J.Phys.Conf.Ser.*, 513:022032, 2014.
- [106] Torbjorn Sjöstrand, Stephen Mrenna, and Peter Z. Skands. PYTHIA 6.4 Physics and Manual. *JHEP*, 05:026, 2006.
- [107] T Skwarnicki. *A Study of the Radiative Cascade Transitions between the Upsilon-Prime and Upsilonon Resonances*. PhD thesis, Deutsches Elektronen-Synchrotron (DESY), Hamburg, Germany, April 1986.
- [108] Thomas Speer, Kirill Prokofiev, R FrÃijhwirth, Wolfgang Waltenberger, and Pascal Vanlaer. Vertex Fitting in the CMS Tracker. Technical Report CMS-NOTE-2006-032, CERN, Geneva, Feb 2006.
- [109] The CMS Collaboration. *CMS Physics: Technical Design Report Volume 1: Detector Performance and Software*. Technical Design Report CMS. CERN, Geneva, Switzerland, 2006.
- [110] Wolfgang Waltenberger, Rudolf FrâĽŽâžhwirth, and Pascal Vanlaer. Adaptive vertex fitting. *Journal of Physics G: Nuclear and Particle Physics*, 34(12):N343, 2007.
- [111] Christian Weiser. A Combined Secondary Vertex Based B-Tagging Algorithm in CMS. Technical Report CMS-NOTE-2006-014, CERN, Geneva, Jan 2006.